Magdalena Malankowska

Membrane Integration in Biomedical Microdevices

Departamento

Ingeniería Química y Tecnologías del Medio Ambiente

Director/es

GARDENIERS, HAN
PINA IRITIA, Mª PILAR
COELHOSO, ISABEL

Tesis Doctoral

MEMBRANE INTEGRATION IN BIOMEDICAL MICRODEVICES

Autor

Magdalena Malankowska

Director/es

GARDENIERS, HAN
PINA IRITIA, Mª PILAR
COELHOSO, ISABEL

UNIVERSIDAD DE ZARAGOZA

Ingeniería Química y Tecnologías del Medio Ambiente

2018

"Membrane integration in biomedical microdevices"

Magdalena Malankowska

Summary and Thesis outline

The present work has been performed under the Erasmus Mundus Doctorate in Membrane Engineering program. The home institute was the Chemical Engineering and Environmental Technologies Department at the University of Zaragoza, within the Nanostructured Films and Particles (NFP) group. The NFP is a member of the Nanoscience Institute of Aragon (INA). Two host universities were: Faculdade de Ciências e Tecnologia at the University Nova de Lisboa (Portugal) and Mesoscale Chemical Systems group at the University of Twente, The Netherlands. This research has been carried out for approximately 4 years (2013-2017). This research was part of the research project EUDIME, which was funded by the European Union.

The target of the research presented in this thesis is a design, development and fabrication of a microfluidic device with integrated membrane in the form of a membrane contactor for various biological applications. The microfluidic devices are fabricated and tested for oxygenation of blood and separation of anaesthetic gas.

In the first part of the work, the microfluidic system for blood oxygenation, so called lung-on-a-chip, is introduced. In such system, one chamber is devoted to pure oxygen, and the other chamber is designed for blood and they are separated by a dense permeable membrane. Computer modelling is performed in order to design the liquid chamber with homogenous liquid flow, low pressure drop of the system and low shear stress without compensation of high oxygenation. Two different microdevice geometries are proposed: alveolar and meander type design with vertical membrane arrangement. Fabricated devices as well as integrated membranes are made of PDMS by soft-lithography and their surface is modified in order to make them more hydrophilic. The experiments of blood oxygenation are performed and the oxygen concentration is measured by an oximeter electrode and compared to the mathematically modelled values. The parameters sensitivity and the possible improvements of the proposed architectures based on the mathematical simulations are presented as well.

The second part of the thesis, introduces the concept of an alveolar microfluidic device as gas-ionic liquid contactor for removal of CO_2 from anaesthesia gas, containing Xe. The working principle involves the transport of CO_2 through a flat PDMS membrane followed by the capture and enzymatic bioconversion in the ionic liquid solvent. As proof of concept demonstration, simple gas permeability experiments are performed followed by the experiments with ionic liquid and ionic liquid with the enzyme.

Finally, an alternative concept of a microfluidic device with an integrated membrane in the form of a fractal geometry with nanonozzles as pores at the vertices of the third-level octahedra

for the controlled addition of gaseous species is introduced. Fractal geometry, that is a three-dimensional repetitive unit, is fabricated by a combination of anisotropic etching of silicon and corner lithography. As a proof of concept, simple gas permeation experiments are performed and the achieved results are compared to the gas permeation obtained by a dense PDMS membrane.

Resumen y Esquema de Tesis

El objetivo principal de esta tesis es el desarrollo y fabricación de un dispositivo microfluídico basado en membranas integradas y el estudio de diversos "contactores de membrana" para las diversas aplicaciones biomedicas. Los dispositivos microfluídicos se fabricaron y se aplicarón en la oxigenación de la sangre y separación de la mezcla de gas anestésico.

En la primera parte del trabajo, se introduce el dispositivo microfluídico propuesto para oxigenación de la sangre, también denominado *"lung-on-a-chip"*. Este sistema consta de dos cámaras independientes, una alimentada con oxígeno puro y otra a la que se bombea sangre, separadas por una membrana densa de espesor controlado. El uso de herramientas de fluidodinámica computacional y la revisión del estado del arte, ha permitido el diseño de microdispositivos que cumplan los requisitos hemodinámicos exigidos en cuanto a distribución del flujo de sangre, pérdida de carga y esfuerzo rasante y aseguren una alta velocidad de oxigenación por unidad de superficie. A la vista de los resultados de simulación se han fabricado microdispositivos con dos geometrías bien diferenciadas: diseño tipo "alveolar" con arreglo horizontal de membrana y diseño tipo "meandro" con arreglo vertical de membrana. La fabricación de estos microdispositivos y de la membrana densa integrada se ha llevado a cabo utilizando herramientas clásicas de microfabricación y PDMS como material. La superficie de los microcanales por donde circula la sangre fue modificada para aumentar su hidrofilicidad y de este modo reducir la adhesión de las proteínas y minimizar el riesgo de coagulación. Todos los microdispositivos fabricados han sido aplicados para oxigenación de sangre de oveja bajo condiciones de operación equivalentes que permitieran la comparación de resultados. En paralelo, se ha desarrollado un modelo matemático para describir la transferencia de oxígeno desde la fase gas a la sangre a través de la membrana permeable de PDMS. Dicho modelo, una vez validado con los resultados experimentales obtenidos en los microdispositivos tipo "meandro", ha sido utilizado para realizar un análisis de sensibilidad de parámetros clave como: concentración de oxígeno en fase gas, permeación de membrana, ancho de microcanal. Además, el modelo matemático se ha utilizado para determinar el impacto que ejerce sobre el rendimiento de oxigenación el miniaturizar tanto el microcanal por donde circula la sangre como el espesor de la membrana y de este modo identificar arquitecturas mejoradas.

La segunda parte del trabajo se dedica a la aplicación del dispositivo microfluídico con diseño tipo alveolar como contactor de membrana gas- líquido iónico para la separación selectiva de CO_2 de una mezcla anestésica enriquecida en Xe. En esta aplicación, la cámara del

gas es presurizada con una corriente de CO_2 o Xe y a la cámara de líquido se bombea la fase solvente basada en un líquido iónico. El principio de trabajo se basa en el transporte selectivo de CO_2 a través de la membrana densa de PDMS seguido de su captura y bioconversión catalítica en el seno de un líquido iónico biocompatible (propionato de colina) que alberga la enzima anhidrasa carbónica. Los resultados de transporte obtenidos para gases puros han demostrado la viabilidad del concepto y su utilidad como plataforma de trabajo de bajo coste para un análisis preliminar con distintos solventes de las principales variables operacionales.

Por último, esta tesis doctoral explora por primera vez el concepto de un dispositivo microfluídico construido en Si/vidrio que integra una membrana de SiO cuya estructura porosa es la impuesta por una geometría fractal en 3D con poros del orden de 100 nm para la permeación de gases a su través. La estructura fractal, embebida en un microcanal, se ha fabricado combinando la técnica de "corner lithography" y al ataque húmedo anisotrópico del Si bajo condiciones controladas. Los chips fabricados se caracterizan por presentar una alta relación S/V y un mecanismo de permeación controlado por difusión Knudsen. Las propiedades de permeación evaluadas han demostrado la viabilidad del concepto para aplicaciones de contacto entre fases a alta temperatura.

Esboço de Resumo e Tese

O objetivo da pesquisa apresentada nesta tese é um projeto, desenvolvimento e fabricação de um dispositivo microfluídico com membrana integrada na forma de um *contactor* de membrana para várias aplicações biológicas. Os dispositivos microfluídicos são fabricados e testados quanto à oxigenação do sangue e à separação do gás anestésico.

Na primeira parte do trabalho, o sistema microfluídico para a oxigenação do sangue, chamado de *lung-on-a-chip*, é introduzido. Em tal sistema, uma câmara é dedicada ao oxigênio puro e a outra câmara é projetada para o sangue e são separadas por uma membrana permeável densa. A modelagem computacional é realizada para projetar a câmara de líquido com fluxo de líquido homogêneo, baixa queda de pressão do sistema e baixo esforço de cisalhamento sem compensação de alta oxigenação. São propostas duas geometrias de microdispositivo diferentes: tipo alveolar e meandro com disposição de membrana *vertical*. Os dispositivos fabricados e as membranas integradas são feitas de PDMS por *soft-lithography* e sua superfície é modificada para torná-las mais hidrofílicas. Os experimentos de oxigenação do sangue são realizados e a concentração de oxigênio é medida por um eletrodo de oxímetro e comparada aos valores modelados matematicamente. A sensibilidade dos parâmetros e as possíveis melhorias das arquiteturas propostas com base nas simulações matemáticas também são apresentadas.

A segunda parte do trabalho é dedicada à aplicação do dispositivo microfluídico com design de tipo alveolar como *contactor* de membrana gás-líquido iônico para a separação seletiva de CO_2 de uma mistura anestésica enriquecida em Xe. Nesta aplicação, a câmara de gás é pressurizada com uma corrente de CO_2 ou Xe e a fase solvente baseada em um líquido iônico é bombeada para dentro da câmara de líquido. O princípio de funcionamento baseia-se no transporte seletivo de CO_2 através da membrana densa do PDMS seguido de captura e bioconversão catalítica em um líquido iônico biocompatível (propionato de colina) que abrigam a enzima anidrase carbônica. Os resultados de transporte obtidos para gases puros demonstraram a viabilidade do conceito e sua utilidade como plataforma de trabalho de baixo custo para uma análise preliminar com diferentes solventes das principais variáveis operacionais.

Finalmente, esta tese de doutorado explora pela primeira vez o conceito de um dispositivo microfluídico construído em Si / vidro que integra uma membrana SiO cuja estrutura porosa é a imposta por uma geometria fractal em 3D com poros da ordem de 100 nm para a permeação de gases através dele. A estrutura fractal, incorporada em um microcanal, foi fabricada

combinando a técnica de litografia de canto e o ataque de Si úmido anisotrópico em condições controladas. Os chips fabricados são caracterizados por uma alta relação S / V e um mecanismo de permeação controlado por difusão Knudsen. As propriedades de permeação avaliadas demonstraram a viabilidade do conceito de contato entre as fases em alta temperatura.

Samenvatting en omvang van dit Proefschrift

Het doel van het onderzoek in dit proefschrift is het ontwerpen, ontwikkelen en fabriceren van een microfluidisch apparaat met geïntegreerd membraan in de vorm van een membraan *contactor* voor verschillende biologische toepassingen. De microfluidische apparaten zijn gefabriceerd en getest voor zuurstofvoorziening van bloed en separatie van verdovingsgassen.

In het eerste deel van dit onderzoek wordt het microfluidische systeem voor zuurstofvoorziening van bloed, de zogenoemde *lung-on-a-chip*, geïntroduceerd. In dit system is een kamer gewijd aan pure zuurstof en is een kamer ontworpen voor bloed. Deze kamers zijn gescheiden door een dicht, permeabel membraan. Om de vloeistofkamer te ontwerpen met een homogene vloeistofstroom, lage drukverschillen en lage schuifspanning zonder compenstatie van hoog zuurstofverbruik, is deze eerst gemodelleerd via een computerprogramma. Twee verschillende microgeometrieën voor het apparaat worden voorgesteld: een alveolaar en een meander type ontwerp met verticaal membraan. Zowel de gefabriceerde apparaten als de geïntegreerde membranen zijn gemaakt met soft-lithography PDMS waarbij het oppervlak gemodificeerd is om zo een hogere hydrofiliteit to creëren. The experimenten met bloedoxygenatie worden uitgevoerd en de zuurstofconcentratie wordt gemeten door een oximeter electrode, waarna deze wordt vergeleken met de gesimuleerde waarden. De op simatie gebaseerde gevoeligheids- en mogelijke beweging variabelen van de voorgestelde ontwerpen worden ook gepresenteerd.

Het tweede deel van het proefschrift introduceert het concept van een alveolaar microfluidisch apparaat als gas-ionische vloeistof contactor voor het verwijderen van CO_2 uit verdovingsgas dat Xe bevat. Het werkende principe heeft te maken met het transporteren van CO_2 door een plat PDMS membraan, gevolgd door het opvangen en enzymatisch converteren van de CO_2 in een vloeibaar oplosmiddel. Als *proof of concept* demonstratie worden simpele gas permeabiliteits experimenten uitgevoerd, gevolgd door experimenten met een ionische vloeistof en een ionische vloeistof met het enzym.

Als laatste wordt een alternatief concept van een microfluïdisch apparaat met geïntegreerd membraan in de vorm van fractale geometrie met nanosproeiers als poriën van het derde niveau octahedra voor de gecontroleerde toevoeging van een gasvormige stof geïntroduceerd. Fractale geometrie, dat wil zeggen een driedimensionale herhaalde vorm, wordt gefabriceerd met een combinatie van anisotropische etsen van silicium en hoek lithografie. Als *proof of concept* worden simpele gas permeatie experimenten uitgevoerd. De resultaten van deze experimenten

worden vervolgens vergeleken met de resultaten van gas permeatie door een dicht PDMS membraan.

Contents

1. Introduction

This chapter introduces the concept of membrane integration in microfluidic devices for various biomedical applications in the form of a membrane contactor. It demonstrates the importance of miniaturization in everyday future utilization. Two main applications involving mass transfer between Gas and Liquid phase are described here: blood oxygenation and anaesthesia gas recovery. State of the art for the artificial commercially available Extracorporeal Membrane Oxygenators as well as lung-on-a-chip under research is presented with main milestones up to date. The importance of the liquid side geometry in the microfluidic device is introduced. On the other hand, the conventional methods and available solvents for carbon dioxide separation from anaesthesia gas together with the G-L membrane contactors being under research are introduced.

1.1. Membrane contactors

Membrane based operations have the potential to replace conventional energy-intensive technologies and provide reliable solutions for sustainable growth [1, 2]. Among those, membrane contactors (MC) have experienced increasing interest over the last decade for diverse applications, some of them validated at an industrial scale: carbonation of beverages [3], degassing of water [4], blood oxygenation [5], solute recovery by liquid-liquid extraction [6], membrane emulsification [7], CO_2 removal and capture [8, 9], ammonia recovery [10] among others. They are considered as an interesting and promising alternative for petrochemical, pharmaceutical, chemical, galvanic and agro-food industries both as end-of-pipe technology for product recovery in water and gas treatment and as an integrated process solution [11]. Although the mass-transfer coefficients achievable in MC systems do not present higher values than those obtained with conventional separation methods, MC provides more surface area per unit volume than conventional packed towers leading to higher mass transfer rates [1]. In many applications, the membrane contactor is not even called a contactor but it is rather referred to the specific functions that it possesses, e.g. blood oxygenator, gas transfer membrane, membrane distillation device, membrane gas absorber etc. For some applications, this approach was found to be cost effective technology; and was anticipated to replace other conventional technologies that may or may not be membrane based [12].

The conventional membrane contactors are commonly based on microporous membranes, which keep two immiscible fluid phases, i.e. L-L, G-L, in contact with each other without dispersion. Avoidance of dispersion is of paramount importance to facilitate the subsequent isolation of two fluids. Both phases are brought into intimate contact at each pore in order to achieve efficient transfer of the solute from one phase to the other; while avoiding their mixing at the same time. This means that, unlike conventional dispersed phase contactors, the liquid as well as gas flow rates can be varied independently over a wide range eliminating the problems of foaming, flooding, channelling, loading and liquid entrainment which usually limit both packed tower and mixer-settler performance. Generally, in case of a gas liquid (G-L) membrane contactor, elevated liquid flow rate results in a reduction of the liquid boundary layer and thus it leads to an augment in the flux of the solute to be separated. On the contrary, as a general rule, the higher is the liquid flow rate, the higher is the risk of membrane wetting which results in an increase of the membrane resistance.

Depending on the particular application, porous membranes in the MC module can be divided into hydrophilic and hydrophobic. It has to be taken into account that, in both cases the

membrane acts as a passive barrier and there is no selectivity for the target component. Hydrophobic membranes are most commonly made of polymers such as: polypropylene (PP), polyethylene (PE), polytetrafluoroethylene (PTFE), poly(tetrafluoroethylene-co-perfluorovinylether (PFA), or polyvinylidene fluoride (PVDF). The working principle of hydrophobic microporous membranes is based on the natural phenomenon of capillary forces. Therefore, the liquid is prevented from entering the micropores due to the surface tension effect, and the membrane is gas filled [1, 13]. When hydrophilic membranes are used, the membrane is liquid filled. This approach is advantageous only if the reaction between the sorbent solution and sorbate species is fast or instantaneous. If this is not the case, it is more beneficial to work with gas-filled membrane, in order to reduce the mass-transfer resistance [12].

Table 1.1 indicates the advantages and drawbacks of membrane contactor technology in comparison to conventional systems. Hollow fibre module is, by far, the most commonly used commercially available membrane contactor. It mainly consists of a bundle of fibres closed in a hard-shelled jacket. In this MC approach, gas flows into the lumen of the fibres while the liquid flows at the shell side. Membrane hollow fibre module systems take advantage of their selectivity, high surface-area-per-unit-volume, and their control of the level of contact and/or mixing between two phases.

Table 1.1 *Main advantages and disadvantages of MC with respect to conventional systems [1]*

Advantages	Disadvantages
-High interfacial area per volume	-Operative pressures dependent on breakthrough ones
-No dispersion between phases	-Additional resistance to mass transfer due to the membrane
-Wide range of operative flow rates	-Shell side bypassing
-No loading or flooding limitations	-Membrane fouling
-No foaming	-Pretreatments to reduce fouling
-No separation of phases after the operation	-Limited lifetime
-Low-pressure drop	
-Constant interfacial area between phases	
-Flexibility and compactness	
-Reduced size and weight	
-No moving parts	
-Easy scale-up due to a modular design	

In spite of the fact that most of the membranes used in MC are microporous, the use of dense membrane for G-L mass transfer was already reported in the 1960s [14]. Dense polymeric films around 100 μm thick, were proposed for wastewater treatment, VOC or artificial gills (underwater breathing equipment). Due to the limitations of membrane preparation technologies at that time, the thickness of the membrane led to elevated mass transfer resistance. Therefore, this idea was abandoned and replaced by porous thin films. Figure 1.1 shows the concentration profile of the solute species "A" in the porous (A) and dense (B) membranes in the G-L contactor.
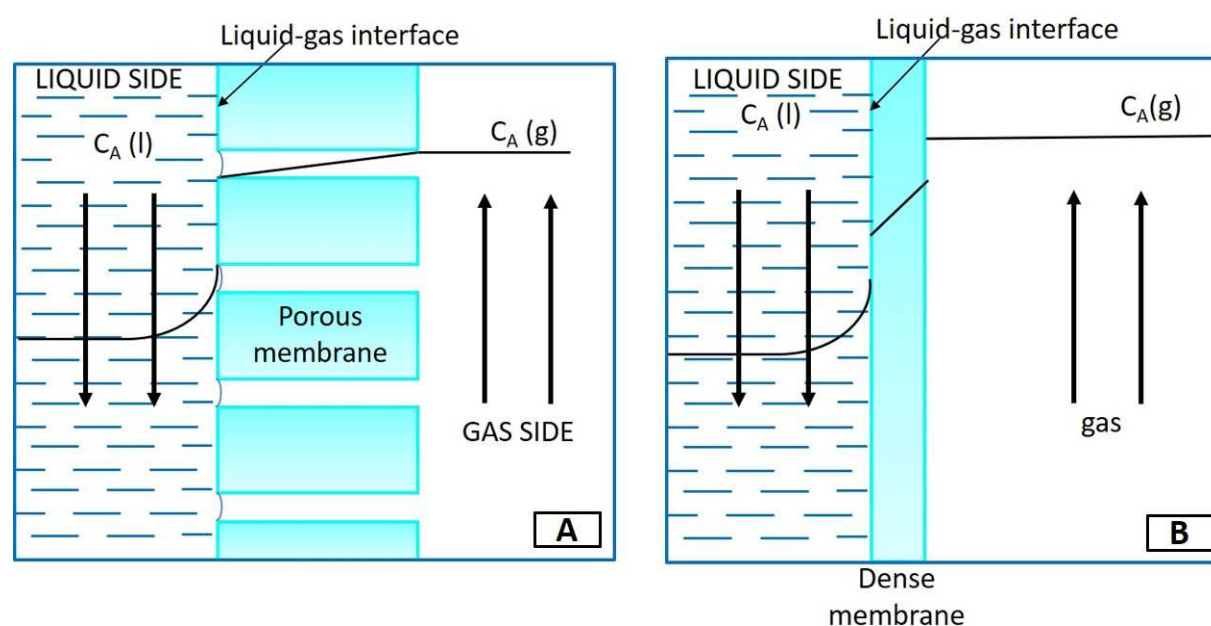
Figure 1.1 Concentration profile of the solute species "A" at the G-L interface for membrane contactors based on A) porous and B) dense membranes

The membrane system approach presented in the following sections comprises a dense-polydimethylsiloxane (PDMS) membrane integrated in the microfluidic device in between two fluid microchambers, i.e. gas-liquid. Thanks to miniaturization of the membrane based system, high interfacial area per volume of the separation unit is provided, and higher mass transfer rates in comparison to the traditional material-agent driven separation processes are expected.

Dense type membranes were chosen to avoid the risk of bubble creation when dealing with blood oxygenation, and to provide selective separation properties for Xe recovery. Furthermore, dense membranes ensure no liquid drainage, avoid flooding, and, in general, they are easier to handle and integrate when compared to porous counterparts.

1.2. Devices for blood oxygenation

The natural lung exhibits exceptional properties for exchange of gas. It possesses branching architecture with alveoli at the end of each airway. Such geometry presents a remarkable possibility to connect inspired gas with blood flowing through capillaries. The magnitude of oxygen and carbon dioxide exchange depends on the surface area available for gas transfer and on the distance between alveolar-capillary channels. The surface area for gas exchange of a natural lung is comparable to the surface of a tennis court, 70-100 m^2. Moreover, it is packed compactly leading to surface area to volume ratio of about 300000 m^{-1}. The thickness of the alveolar-capillary membrane is in the range of 0.5 μm, the effective diffusion distance is 1-2 μm and the gas transfer rate is approximately 200-250 $mL\cdot min^{-1}$ for O_2 and CO_2 respectively in average adult for resting levels and 2000 $mL\cdot min^{-1}$ during exercise [15]. These parameters, among others related to blood fluidodynamics, have to be taken into account to design and fabricate an artificial lung.

The urge of new technologies for blood oxygenation appeared as a result of high morbidity caused by pulmonary disorders. Lung diseases are one of the main causes of death. It was estimated that in 2015, there would be 3 million deaths globally due to Chronic Obstructive Pulmonary Disease (COPD). This results in 5% of all deaths all over the world in that particular year [16, 17]. Only in 2010 the total cost of the medical care of COPD was $2.1 trillion worldwide making it one of the most economically significant diseases. It is expected that by 2030 this amount will be more than double [18]. Lung transplantation is nowadays the only available clinical therapy for patients with the end-stage of chronic lung disease. However, the regular time that the patients need to wait for the organ transplantation is about 2 years, and approximately 10% of them are dying while waiting for the organ to be available [19]. Furthermore, the preterm infants who were born younger than 32 weeks are at a high risk of suffering from severe respiratory problems. Insufficient respiration in new-borns is a result of smaller available surface area for gas exchange or due to the poor diffusion properties of the lung's membrane [20]. The lung transplant cannot be executed due to the fact that implanted organs in infants do not grow with them. Mechanical ventilation is commonly used for delivering sufficient amount of oxygen; however, for small lung tissue which is under development, some serious complications may occur.

This has established a considerable need for artificial lung technologies in order to support gas exchange while waiting for a lung transplant or to improve the quality of life meanwhile the lung transplantation is not possible. Such device is also anticipated during the surgical

operations or the vital organs transplantation where the exchange of gas has to be constantly supported. In case of preterm infants, which cannot be treated with the mechanical ventilation or organ transplant, the market opportunities for artificial lung technologies are quite promising.

1.2.1. Commercially available lung assist devices

One of the first significant attempts which were executed as a replacement to mechanical ventilation during surgical operations was Extracorporeal Membrane Oxygenator (ECMO) developed in 1950. The working principle of ECMO was focused on the blood oxygenation "out" of the body. Venous blood was withdrawn from the organism and was carried throughout the device, next it was oxygenated outside the corpus, and carbon dioxide was removed at the same time. Later, the oxygenated blood returned to the systemic circulation [21]. Most of the artificial lung oxygenators used nowadays are made of porous hollow fibres bundles inside a hard-shelled jacket. Oxygen is carried through the fibres, i.e. lumen side, and it diffuses into venous blood which is flowing around the filaments, i.e. shell side (see Figure 1.2).
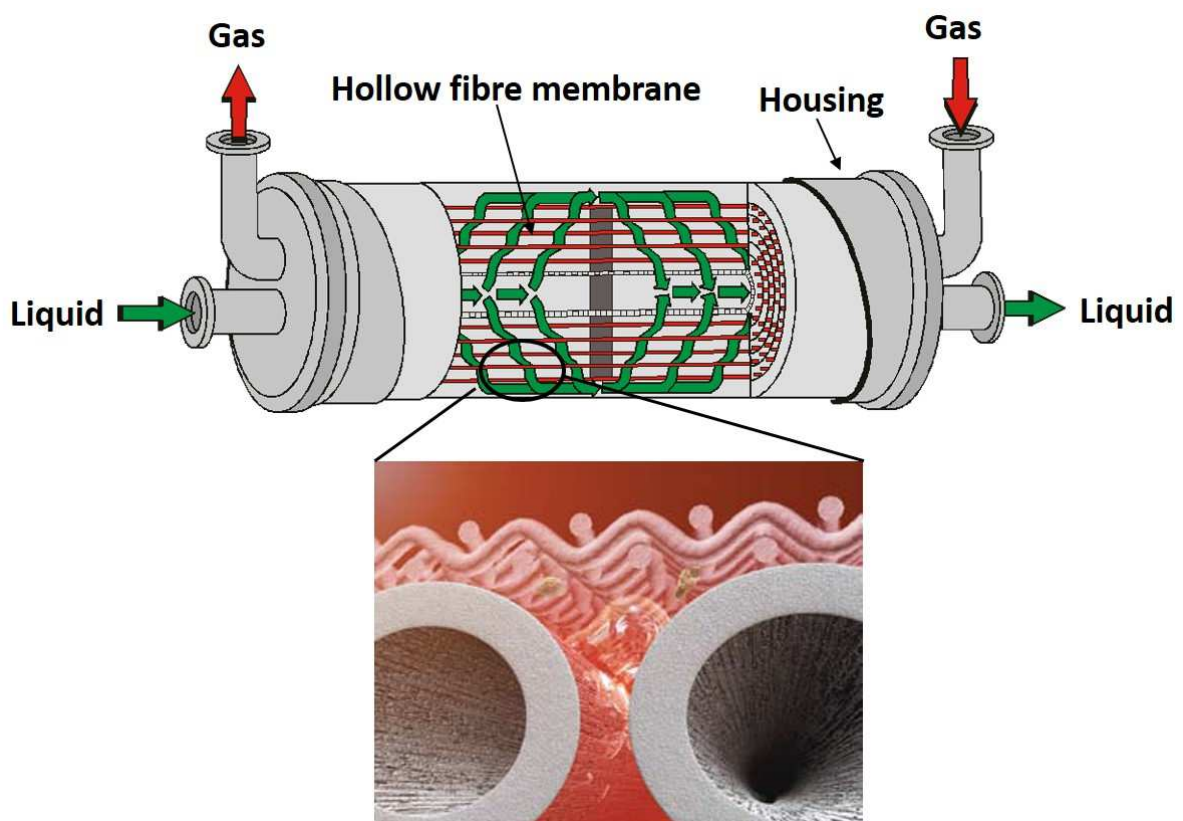
Figure 1.2 Hollow fibre membrane module. Figure adapted from [6]. The magnification represents the additional biocompatible amphiphilic polymer layer added to the ECMO HF of Capiox FX oxygenator

Such configuration allows a better control of the main parameters governing the mass transport of solutes. The membrane is commonly made of microporous polypropylene or polymethylpentene; and sometimes is covered with a thin dense layer of a biocompatible material. For instance, Terumo company that fabricates CAPIOX blood oxygenators uses specific biopassive surface coatings which reduces platelet adhesion and minimizes platelet activation. Moreover, the effective surface area of such devices is in the range of $0.5 - 4.5$ m^2; which leads to a surface to volume ratio twenty times lower than of the natural lung. The S/V ratio for this hollow fibre membrane module, which varies inversely with the fibre diameter, is approximately 15000 m^{-1}[21, 22].

Table 1.2 shows the list of commercially available membrane oxygenators together with their most important parameters. The table is divided into two sections: devices devoted to treat neonates and infants, characterized by lower priming volumes but also by lower blood flow rate, and the other section focused on the devices dedicated to adults.

One of the main concerns around ECMO devices is related to the non – physiological blood flow pathway which leads to highly unpredictable and uncontrolled behaviour [23-25] and complications such as: device clotting, inflammation and haemolysis. Additionally, current systems only allow minimal ambulation. Most of the devices possess short life time and can support respirational needs only of a patient in rest [26].

Table 1.2 Commercially available membrane oxygenators

	Company	Brand	Priming vol [mL]	S/V_{res} ratio [m⁻¹]*	Memb SA [m²]	O₂ transf rate at max blood flow [mL·min⁻¹·m⁻²]	Max blood flow [mL/min·m²]	Memb type**
Neonates/Infants	Maquet	Quadrox-I Neonatal	38	224	0.38	N/A	3947	μporous PP
	Maquet	Quadrox-I Pediatrix	81	471	0.8	N/A	3500	μporous PP
	Medtronic	Affinity Pixie	48	558	0.67	194	3731	μporous PP
	NovaLung	MiniLung Petite	55	N/A	0.32	N/A	2500	PMP
	Sorin	D101 Infant Oxygenator	87	406	0.61	254	4098	μporous PP
	Sorin	D100 Neonatal Oxygenator	31	440	0.22	218	3181	μporous PP
	Terumo	Capiox FX-05	43	500	0.5	200	3000	μporous PP
Adults	Maquet	Quadrox	250	429	1.8	236	3889	μporous PP
	Maquet	Quadrox-D	250	429	1.8	236	3889	PMP
	Medtronic	Affinity	270	625	2.5	172	2800	μporous PP
	Medtronic	Affinity Fusion	260	555	2.5	160	2800	μporous PP
	NovaLung	ILA Active	175	N/A	1.3	N/A	3461	PMP
	Sorin	APEX	310	500	2	250	4000	N/A
	Terumo	Capiox-FX-25	260	625	2.5	200	3200	μporous PP

* V_{res} refers to the entire reservoir volume capacity, **PP=polypropylene; PMP=polymethylpentene

1.3. Microfluidic devices as lung oxygenators-main milestones in 21st century

A biomimetic microfluidic technology has been reported by several authors for the application of lung assist device [20, 23, 25, 27-29] and recently reviewed by J. A. Potkay [26]. In these microchips blood flows through branched vascular microchannels which are separated from flowing oxygen by a gas permeable membrane. Such architecture presents exceptional advantages over conventionally used hollow fibre technology. Mainly, due to controlled dimensions and shape of vascular channels, the physiologic blood flow can be achieved mimicking the natural lung structure and properties. Moreover, such microfluidic devices offer an easier access for cellularization which leads to an improved biocompatibility of the material.

Along the last years, there was a remarkable advancement in the design, fabrication, improvement, test and "in vivo" demonstration [29] of the microchips for blood oxygenation. The first publications about artificial lungs in the form of a microfluidic device started around 1970s. Main milestones of the lung oxygenators in the form of a microfluidic device in the 21st century include: 1) development of soft-lithography and replica moulding in PDMS, 2) computer modelling and parameter study for physiological blood flow, 3) PDMS surface modification to avoid blood clotting and haemolysis, 4) liquid chamber architecture and membrane material and/or morphology evolution, 5) in-vivo experiments, and 6) microfluidic device scale-up. The listed achievements are presented in see Figure 1.3. A short discussion about the main results and contributions presented by the different groups for these milestones is presented below.

The pioneering group of the modern microfluidic artificial lung is the group of Borenstein from Draper Laboratory, Cambridge, MA, USA. In 2002 and 2004, they focused on the establishment of silicon micromachining technology for replica moulding of PDMS. Such technology allowed to control the geometry and dimensions of the microfluidic platforms. Additionally, it was decided to use PDMS for the fabrication of microdevices thanks to its easy handling, transparency, low cost, chemical inertia, high oxygen and carbon dioxide permeability, non-toxic and non-flammable character, and relative biocompatibility. Such fabrication procedure was relatively fast, easy and economical; making the overall process more efficient [30, 31]. Nowadays, thanks to the progress of soft lithography, broader variety of shapes, depths and lengths can be obtained and controlled at the same time.

Microfluidic devices as lung oxygenators – main milestones in 21st century
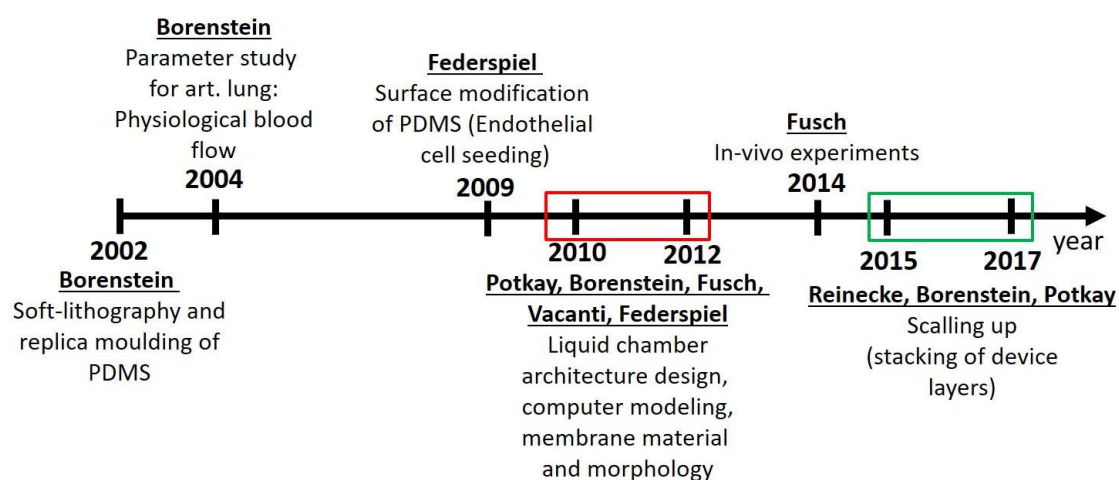
Figure 1.3 Timeline of the main milestones in the design of a lung oxygenator in the form of a microdevice

Over the last decade, the same group continued mastering the design and fabrication of a lung oxygenator in the form of a microfluidic device by studying the crucial parameters that need to be obeyed in order to keep the blood on a physiological level. The parameters were defined and the limits were set. The criterion such as shear stress (which should not overcome the limit of 6 N/m^2), pressure drop (not higher than 20 mmHg) and physiological blood flow were taken into account in the design of the artificial lung chip. This guideline was based on the behaviour of blood inside the natural human lung (for more explanation of the design parameters see section 1.4). Computer modelling was used in order to predict such limits and to design an architecture which will not overcome such limits but which will ensure high level of oxygenation at the same time [30, 31]. Variety of branching human-lung-like geometries were obtained with regulated channel depth, width and length [32].

The next breakthrough was the surface modification. It was noticed that in blood contacting applications, the surface of the chambers as well as the membranes should be haemocompatible, i.e. blood should not react with the surface of the device, hence no blood clotting would be observed. In 2002, the group of Borenstein, and in 2009, the group of Federspiel from the University of Pittsburgh, independently on each other; attempted to modify the surface of PDMS by dynamic cell seeding with immortalized human microvascular endothelial cell line. The decrease of blood clotting was confirmed by the experiments of measuring pressure drop as a function of liquid flow rate [30, 31, 33]. This was the first time, when not only the efficiency

in oxygenation was taken into account; but, also the behaviour of blood after the experiment that has to come back to the systemic circulation in the body.

Along with the improvement of the fabrication procedure and after defining artificial lung parameters, variety of different and more sophisticated architectures of the liquid chamber were constructed with integrated membranes of various materials and morphologies. The group of Vacanti (from the Centre of Regenerative Medicine, Massachusetts General Hospital, USA), tested the blood oxygenation in the devices with different membranes such as: porous polycarbonate (PC), silicone coated with porous PC, silicone commercial MDX4-4210 membrane, ultra – thin free-standing membrane (FSM) from tertiary butyl acrylate (tBA) or n-butyl acrylate (nBA) and composite membrane made of polytetrafluoroethylene (PTFE) and poly maleic anhydride (pMA).The oxygen transfer rate obtained for all the membranes at various thicknesses was comparable [23, 27]. In 2012, the group of Fusch (from the McMaster University, Hamilton, ON, Canada), published the article about different thin polycarbonate (PC) membranes, i.e. 6 μm thick, placed inside the microchip. Two types of PC membranes were examined: with 0.1 μm and 0.05 μm pore size, respectively. Comparable O_2 transfer rate for both membranes was obtained confirming that the main transport resistance is due to the liquid phase [20, 28]. Therefore, the geometry and dimensions of the liquid chamber were emphasized.

The group of Potkay (from the Medical Centre, Cleveland, OH, USA), designed a liquid chamber with very shallow blood channel depths, i.e. 20 μm and 10 μm [34]. It was noticed that the shallower the blood channels the fastest the oxygenation. Nevertheless, blood chamber width should not be decreased too much due to the risk of a high shear stress, elevated pressure drop, collapse of a chamber or channel blockage by red blood cells (RBCs). The big milestone in the design and fabrication of a liquid chamber for blood oxygenation was the architecture constructed by the group of Vacanti which possessed different channel depths along the entire structure, i.e. 700 μm to 100 μm. This procedure, significantly decreased pressure drop and shear stress along the chamber [35]. Along the years, the fabrication procedure was impressively improved. Nowadays, the fabricated devices are not only effective but also the risk of membrane deflection, leaking or chamber collapse decreased significantly.

In 2014, for the first time the in-vivo blood oxygenation experiment was performed. The device, designed previously by the group of Fusch [28], was used for the in vitro and in vivo oxygenation on a newborn piglet model (≈1.6 kg in weight). The system was optimized for gas exchange to raise the O_2 saturation in blood from 70% to 100% for extracorporeal blood flow of 0.5-4 mL/min per device. Five newborn piglets were studied and the average gas exchange

23

for oxygen was 30 mL·min^{-1}·m^{-2} for an extracorporeal blood flow rate up to 24 mL/min. This promising experiment however, did not achieve 100% O_2 saturation of blood due to the operational conditions, i.e. short residence time values. It was suggested that the device with higher volume for the liquid chamber, need to be designed and tested [29].

Finally, the last milestone up to date is the possibility to scale-up the microfluidic devices which increases the throughput and improves the performance. The lung assist device, fabricated by the group of Fusch, consisted of an array of 10 microfluidic single oxygenator units (SOUs) made of PDMS and arranged in parallel [29]. In 2015, the group of Reinecke (from the University of Freiburg, Germany) stacked 21 layers (10 for blood and 11 for gas) of the same device [36] and the group of Borenstein in 2016 stacked 14 layers of the same device one above another [37]. In 2017, the group of Potkay presented a new approach of a microfluidic device with a four-layer structure (blood layer/membrane/air layer/capping layer) that was assembled by rolling a cylindrical substrate over the patterned PDMS substrate, thereby stacking the four layers [38]. This highlighted the straightforward scaling-up when dealing with artificial lung microfluidic technology. However, the authors observed some obstacles connected with stacking one device onto another. The limitations were mainly connected with the interconnections among the platforms and elevated shear stress and pressure drop as the number of platforms and connections increased. Moreover, ensuring physiological blood flow rate is more challenging in the device made of many layers.

The "state of the art" of artificial lung microchips still face some challenges related to gas exchange efficiency, cardiovascular parameters and coagulation and thrombus inhibition that need to be addressed in future in vitro and in vivo trials. First of all, the oxygen transfer rate has to be similar to the assured by the natural lung; 1.9 mL·kg^{-1}·min^{-1} of O_2 at 30 mL·kg^{-1}·min^{-1} of blood, respectively [20]. Extracorporeal bypassing of the systemic circulation at high flow rates could compromise the cardiovascular system, leading to the decreased mean systemic arterial pressure, organ perfusion, and increased heart rate, cardiac output and energy expenditure. Current applications for extracorporeal membrane oxygenation require full-body anticoagulation, which is not feasible for preterm infant population due to the risk for intraventricular haemorrhage [29].

Table 1.3 represents a summary of the microfluidic artificial lungs designed and fabricated by some key research groups with the most important parameters and obtained results. The best results in terms of the oxygen transfer rate up to date were obtained by the group of Borenstein and were in the range of 300 mL·min^{-1}·m^{-2}. The Potkay results are truly outstanding, i.e. 225 mL·min^{-1}·m^{-2} as O_2 transfer rate with air as a supply gas, thanks to the small blood channels

depth, i.e. 10 μm. However, such small channels could result in blood clotting and increased pressure drop inside the liquid side geometry.

Table 1.3 *Key research groups and their microfluidic devices for blood oxygenation*

Source	Blood channel height [μm]	Memb thickness [μm]	Memb surface area [cm^2]	S/V$_{liq}$ ratio [m^{-1}]	O$_2$ transfer [mL/min.m^2]	Memb material	Max blood flow [mL/min.m^2]	Supply gas	Remarks
Vacanti 2010 [23]	200	12	18	5000	136	PC	4444		Porous PC mb
	200	15	18	5000	145	PDMS/PC	4444	O$_2$	
	200	63	18	5000	151	PDMS	4444		
Vacanti 2010 [35]	100	8.7	6.93	10000	41	MDX4-4210 (silicone mb)	9091	O$_2$	
Potkay 2011 [34]	20	15	2.34	40000	137	PDMS	6410	Air	Various blood channel depth in the same chamber
	10	15	2.34	80000	225	PDMS	8974		
Borenstein 2012 [32]	50	30	0.85	20000	329	PDMS	117647	O$_2$	Branching liquid side architecture
	100	30	0.85	10000	317	PDMS	117647		
	50	117	0.85	20000	223	PDMS	117647		
Fusch 2013 [20]	80	15	15.26	12500	12	PDMS	2621	Air	
	80	15	15.26	12500	19	μP PDMS*	2621		
	80	6	15.26	12500	13	PC	2621		
Fusch 2014 [29]	80	20	18.49	12500	104	PDMS	2163	O$_2$	Made of 10 layers of single oxygenator units
	80	20	18.49	12500	30	PDMS	2163	Air	
Borenstein 2016 [37]	80	100	3.3	N/A	190	PDMS	75757	O$_2$	14 layers device
Potkay 2017 [38]	10	66	N/A	83000	153	PDMS	N/A	O$_2$	Made of four layers by rolling

* μP=microporous

1.4. Main Design Parameters of Microfluidic Blood Oxygenators

1.4.1. Physiological blood flow, liquid chamber geometry and pressure drop

Natural lung is made of small alveoli at the end of each airway that possesses membrane thickness of 0.5 μm (see Figure 1.4). These microchannels are dispersed inside the lung in a branching – like conformation. Such architecture results in a high surface area available for oxygenation (approximately 70 m^2) and physiological as well as homogenous blood flow distribution. The branching arrangement of the lung channels obey bifurcation theory introduced by Murray in 1926 [39]. In other words, whenever the channel bifurcates or trifurcates the width must always be 1/2 or 1/3 of the width of the original main channel so the homogenous liquid distribution is kept.
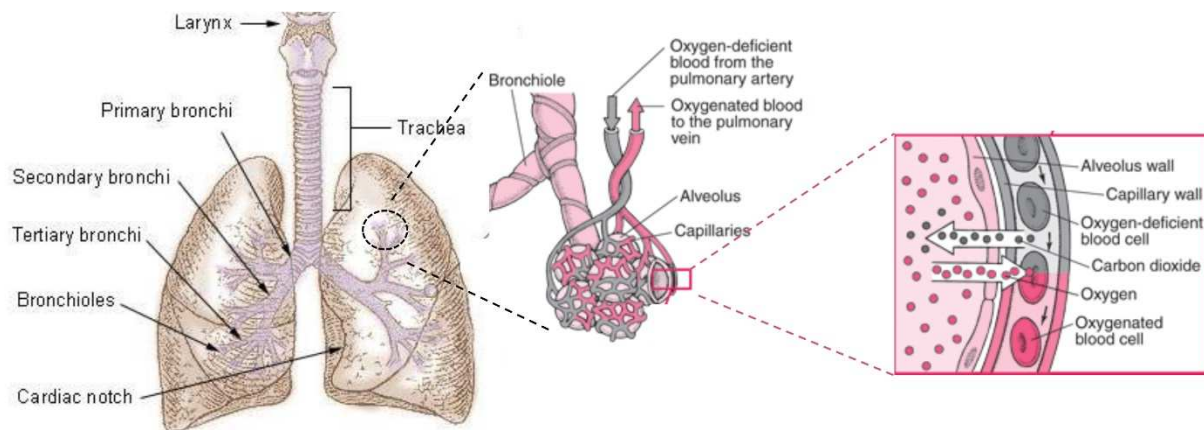
Figure 1.4 Schematic representation of Bronchi, bronchial tree and lungs and gas exchange in the lungs. Figure adapted from [40, 41]

By ensuring laminar flow within the channels, it is simple to keep blood in its physiological levels. That is the reason why the liquid chamber geometry is one of the most important parameter in the design of the artificial lung chip. Therefore, the shape, depth, width and length of the channels are of crucial importance. Moreover, it is important to know what is the blood flow in a human body. The heartbeat of a healthy adult is approximately 72 beats/min, the stroke volume (which is the amount of blood ejected per beat of the heart) is equal to 2 mL/kg thus from the multiplication the blood flow rate is equal to 144 mL/min·kg [20].

Additionally, the device must be constructed in a way that the pressure drop across the branching architecture does not compromise heart rate and blood pressure. Elevated values of ΔP may cause significant obstruction in blood behaviour, such as RBCs deformation or

destruction, clotting and channel blockage. Thrombosis, which is defined as the blood clotting formation inside the blood vessel, occurs at the pressure drop higher than 20 mmHg [32, 34, 35]. Thus, it is of crucial importance not to exceed this value in the design of the liquid chamber of the artificial lung.

Borenstein *et al* first introduced the importance of a pressure drop across the liquid chamber in 2002. The configuration of the channels, in order to mimic the branching conformation, was taken into consideration as well as the possibility of blood clotting on the surface of non – haemocompatible material [30]. This device however, was used only for the monitoring of the liquid distribution and not for the blood oxygenation.

The main platform configurations, for the network architecture presented in the literature by different groups are summarized in Figure 1.5 A – E and discussed in detail below.

Kniazeva *et al*. fabricated two independent platforms, one dedicated for gas in the form of a big, lemon shaped simple chamber, and second platform devoted to liquid in the form of bifurcated small channels [32]. Figure 1.5 A depicts such architectures for the designed platforms. The surface area of the membrane for gas exchange membrane was equal to 0.85 cm^2, depicted in white colour in Figure 1.5 A. The flow distribution in the proposed geometry was homogenous and smooth and no channel blockage was observed.

The group of Vacanti attempted to decrease the pressure drop inside the liquid geometry by designing and fabricating the chamber with various liquid channel depths within one geometry by micro machining technology. In this structure, the deepest channel was in the range of 700 µm at the inlet and the shallowest one was 100 µm. The gas exchange surface was equal to 6.93 cm^2. It is known that the highest pressure is present at the main inlet of the liquid chamber, thus it was decided by the authors to make this channel the deepest one which resulted in a significant decrease of a pressure drop (see Figure 1.5 B) [35]. Another geometry presented by the same group was simple branching design (shown in Figure 1.5 C). The channel depth was constant in the whole structure (200 µm). The area for oxygen diffusion was significantly higher than in other devices and was equal to 18 cm^2 [23].

In 2011, Potkay *et al* tried to extremely minimize the liquid channel depth in order to maximize the O$_2$ transfer rate. A simple geometry (see Figure 1.5 D) with two types of microarchitectures was designed: one with 20 µm and the other with 10 µm liquid channel depth and with the gas exchange surface of 2.34 cm^2. This obviously increased the oxygen transfer rate, although it dramatically elevated pressure drop inside the chamber and decreased the maximum liquid flow rate. In case of 0.5 mL/min of a blood flow rate, the pressure drop was equal to 190 mmHg and 120 mmHg for 10 µm and 20 µm channel depth, respectively. Such

high pressure caused several problems: firstly, when some of the channels were blocked, the total surface area available for oxygenation was not used. Moreover, high pressure was responsible for RBCs deformation or rupture [34].
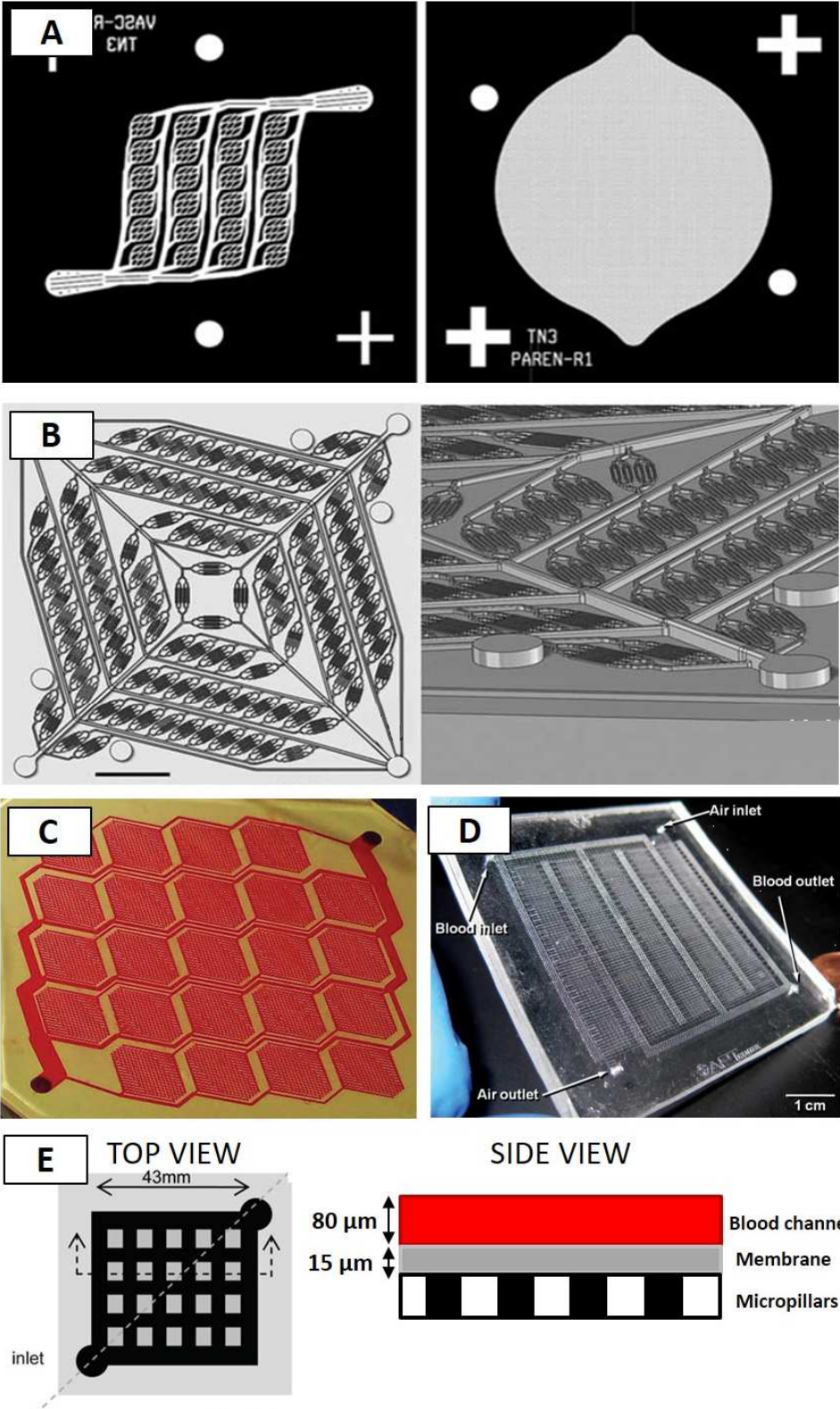
**Figure 1.5** Microfluidic architectures for blood oxygenation. A) adapted from Kniazeva et al [25, 32], B) adapted from Vacanti et al [35], C) adapted from Hoganson et al [23], D) adapted from Potkay et al [34] and E) adapted from Fusch et al [20].

The group of Fusch designed also a very simple architecture, see Figure 1.5 E, where channel depth was equal to 80 μm and the gas exchange surface area was 15.26 cm^2. The

pressure drop in this architecture was 40-60 mmHg for a liquid flow of 1 – 3 mL/min. The chambers were made of PDMS. Four types of membranes were fabricated: dense and porous PDMS, and two etched-through nanoporous PC membranes with 50 nm and 100 nm pore size. Moreover, the same design was used for device scalling-up and in-vitro experiments [20, 28].

Figure 1.6 represents the summary of the exhibited pressure drop values as a function of the blood flow rate obtained by some main research groups.
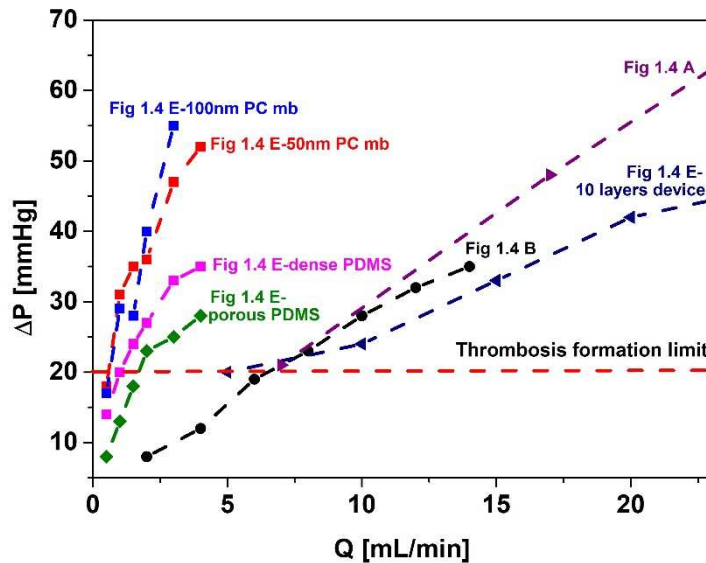
Figure 1.6 Hydraulic losses reported for microfluidic devices. Each curve corresponds to the structure presented in Figure 1.5 A-E.

It was observed by the group of Fusch that lower pressure drop was obtained when PDMS membrane was integrated in between the gas and liquid chambers than it was in the case of PC membrane (see Figure 1.6). The authors concluded that PC membrane is relatively rigid and less elastic than the PDMS membrane, which can expand with pressure.

As it could be observed from the figure, many groups could achieve high blood flow rates (more than 20 mL/min) however, all the devices crossed the limit of thrombus formation (20 mmHg). However, the group of Fusch (Figure 1.5 E) and Vacanti (Figure 1.5 B) obtained the highest blood flow rates and the lowest ΔP (in the range of 30 – 40 mmHg; still over the limit). These two groups achieved the lowest ΔP at highest blood flow rate due to the branching architecture of the liquid side as well as due to the various channel depths inside the same geometry in case of the design of Vacanti. It is then anticipated that in the design of the artificial lung, not only the oxygenation performance will be taken into account but also the pressure drop will be considered in order to protect red blood cells.

31

The devices presented above need to be scale-up, since higher membrane area is needed for the real application of the oxygenation. On the other hand, it has to be taken into account that the priming volume of the device designed for neonates should not exceed 50% of the total blood volume that is approximately 96 mL/kg. Moreover, the oxygenation parameters for neonates should be considered as well. Potkay introduced the term called rated flow (Q) [26] that is the maximum blood flow rate at which an inlet blood saturation of 80% can be oxygenated to an outlet oxygen saturation of 95%.

1.4.2. Device "scale up"

In 2014, the group of Fusch attempted to scale up the microfluidic device for blood oxygenation, presented in Figure 1.5 E. The lung assist device proposed by the group consisted of an array of 10 microfluidic single oxygenator units (SOUs) made of PDMS, arranged in parallel and connected by polymeric interconnects leading to a very low total priming volume, i.e. 4.8 mL/ Each SOU consisted of a vascular network with a thin gas exchange membrane of a surface area equal to 18.49 cm^2. The microchannels in the vascular network were 80 μm in depth and 500 μm in width (see Figure 1.7) [29]. This promising experiment did not achieve 100% O_2 saturation of blood due to the operational conditions, i.e. short residence time values. It was suggested that SOUs with higher volume for the liquid chamber need to be designed and tested. Nevertheless, the increase in the O_2 transfer rate in comparison to the single device designed by this group earlier [20] was visible (see Table 1.3). In case of air as a supply gas, the O_2 transfer increase by approximately a double.
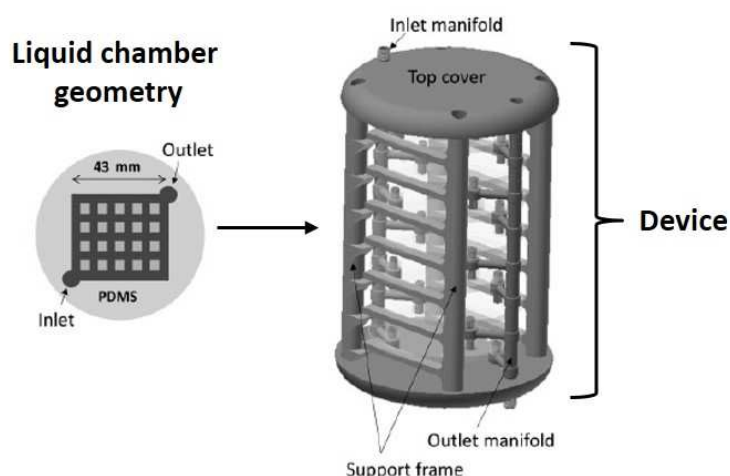

Figure 1.7 Liquid chamber geometry and device made of SOUs. Figure adapted from [29]

In 2015, Reinecke *et al* tried to increase the gas transfer by using straight microchannels in the blood compartment with a width of 1 mm. The structure for the gas and liquid compartments

were not prepared by commonly used soft-lithography, but from the steel frames which were fabricated by wire electrical discharge machining of precision steel sheets. One layer of the blood compartment was made of 40 microchannels with the PDMS membrane thickness of 90 μm. Both, membrane and gas, liquid chambers were connected by curing a thin PDMS layer. The device used for the oxygenation experiments was made of 21 layers (10 for blood and 11 for gas) and had the membrane surface area of 120 cm^2. Pure O_2 was used as the ventilating gas. The O_2 transfer rate obtained by the authors was equal to 2.5 mL/min.m^2 and 1.3 mL/min.m^2 for pure O_2 and air as ventilating gas, respectively at a blood flow rate of 5 mL/min [36]. These authors obtained significantly lower gas exchange rates in comparison to the other groups (see Table 1.3) due to the height of the liquid channels, i.e. 200 μm. It is worthy to mention that the group of Vacanti worked with liquid chamber geometry that possessed 200 μm channel depth as well. This group however, obtained 100 times higher oxygenation [23]. This is related to the design of the liquid chamber itself which in case of Reinecke *et al* did not obey the bifurcation guideline and did not possess branching geometry which clearly affected the device performance (see Figure 1.8).
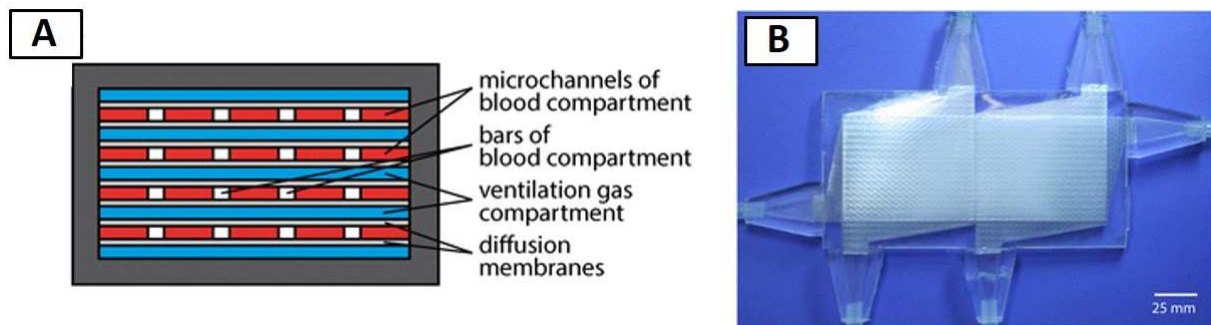
Figure 1.8 Schematic representation of the A) microfluidic channels conformation and B) photograph of the assembled device. Figure adapted from [36]

In 2016 the group of Borenstein tried to further develop already existing alveolar structure presented earlier (see Figure 1.5 A) [32] by stacking more layers (in this case 14 layers) and by increasing the gas exchange area (up to 3.3 cm^2). The resulting device could operate in the range of high liquid flow rates, i.e. up to 25 mL/min, due to blood flow network size expansion and the scaled number of gas transfer modules (see Figure 1.9). Obtained O_2 transfer was equal to 190 mL/min.m^2 of 14 layers device and 90 mL/min.m^2 of 10 layered device (taking into account the footprint of the chip) at liquid flow rate equal to 12 mL/min which is the flow rate at the inlet of the entire structure [37].
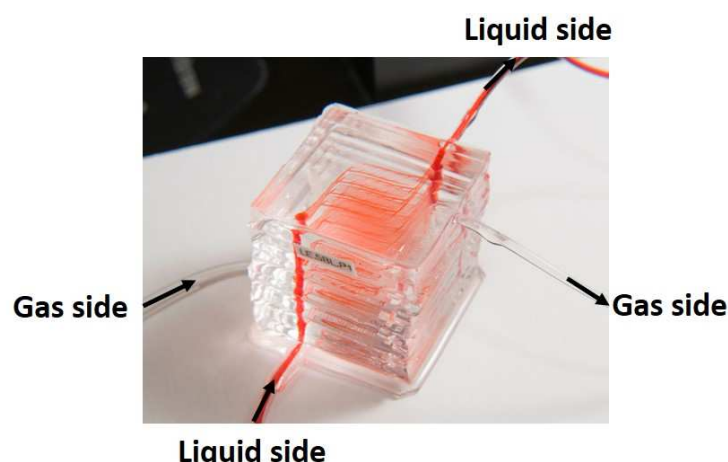
Figure 1.9 Scaled up microfluidic device made of 14 layers. Adapted from [37]

Finally, in 2017 the group of Potkay presented a new approach of a microfluidic device with a four-layer structure (blood layer/membrane/air layer/capping layer) that was assembled by rolling a cylindrical substrate over the patterned PDMS substrate, thereby stacking the four layers (see Figure 1.10).
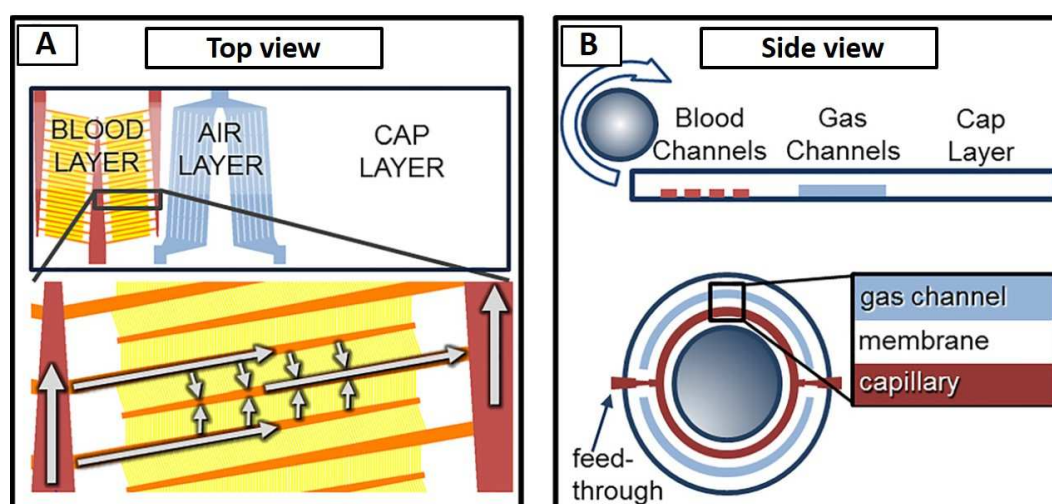
Figure 1.10 Design overview of A) top view and B) side view. Adapted from [38]

The depth of the channels in the presented artificial lung geometry was equal to 10 μm with the membrane thickness of 66 μm. Such a configuration resulted in elevated pressure drop, i.e. at 1 mL/min of blood flow rate, the ΔP was equal to 100 mmHg. The in vitro experiments were performed resulting in high gas exchange rates, i.e. 153 mL·min^{-1}·m^{-2} for O_2. Nevertheless, the authors found some drawbacks connected with the rolled device conformation. They concluded that scaling up the device could be challenging from fabrication point of view due to the number of limitations: 1) the device is made from a single mould thus during scaling up the length of the mould might be too long to manage the fabrication as it is described in the article, 2) as devices are scaled up, the number of layers increased and the fluidic interconnections of all the

layers by a single diameter feedthrough while maintaining physiological shear stress to avoid clotting would become more challenging [38].

Summarizing, the most outstanding results in terms of blood oxygenation were obtained by the group of Borenstein (see Table 1.3) [32]. Even though, the membrane surface area is much smaller than for instance in case of the device designed by the group of Fusch (3.3 cm^2 vs 18.49 cm^2) the oxygen transfer rate is comparable. This is due to the truly branching architecture and imitation of the human lung structure of the design of Borenstein.

1.4.3. Shear stress in the liquid channels

Another important parameter influencing the performance of the device and the condition of blood is the shear stress. Shear stress, defined as the force exerted on the walls of the capillaries for a giving flow rate, depends on the dimensions and the shape of the channel and on the roughness of the wall. The maximum value of this force in the arteries is equal to 70 dynes/cm^2; however, platelet activation and subsequent thrombosis, which disturb the blood flow through the circulatory system, can start at 60 dynes/cm^2 [32]. Therefore, it is desirable and beneficial not to exceed this value in the design of the branching architecture of the liquid chamber. Small number of research institutes working on the development of the artificial lung focused on the control of shear stress up to date. The group of Borenstein emphasized the importance of physiological blood flow and the parameters which control it [30]. After some years, the group continued targeting the importance of the shear stress and made a computer modelling which predicted the value of this force in a given geometry and at a certain inlet pressure, i.e. at 80 mmHg the shear stress was equal to 14.5 dynes/cm^2 [25].

As it was mentioned above, Potkay *et al* designed the structure with very shallow liquid chamber (see Figure 1.5 D). The average shear stress did not exceed the limit values: it was equal to 2.1 dynes/cm^2 and 4.9 dynes/cm^2 for 20 μm and 10 μm channel depth respectively and at the liquid flow rate equal to 1 mL/min. Although the overall shear stress was still below the blood coagulation threshold; the corners of the branching points, where the flow velocity undergoes a sudden direction change, are the regions where the maximum shear stress appeared [34]. The group of Vacanti obtained the value of a shear stress equal to 57 dynes/cm^2 at a liquid flow rate of 6 mL/min (see Figure 1.5 C) [23].

All the above-mentioned parameters, ΔP and shear stress, depends on blood velocity within the channels. Thus, depth, length and shape of the liquid microchannels have to be judiciously chosen to keep the physiological parameters for pressure drop and shear stress, and to ensure homogenous liquid flow distribution capable to provide the required O$_2$ transfer rates.

1.4.4. Haemocompatibility/Biocompatibility of the membrane and platform material

Biomaterial is defined as any material that has been synthesized in order to interact with biological systems for medical purposes. The definition of biocompatibility for blood contacting biological devices is given by IUPAC: "Biocompatibility is the ability to be in contact with a living system without producing an adverse effect" , i.e. uncontrolled activation of cells or plasma protein [42]. The International Organization of Standardization (ISO) and Food and Drug Administration (FDA) established some rules connected with the biocompatibility of a device designed for the blood flowing purposes. For external communicating devices where blood is circulating during prolonged time exposure (24 hours-30 days), the following standards for the materials involved were adopted: 1) haemocompatible, that is not causing inappropriate activation or destruction of blood, 2) non irritative nor reactive; and 3) it should not cause loss of cells viability [43].

In artificial lung assist devices, the adhesion of red blood cells is highly undesired to avoid membrane fouling and blood channels blockage. The protein adsorption is determined by thermodynamic changes within the wall surface-water-protein system. The sorption driving force depends on the surface itself (possible redistribution of charged groups) and on the potential conformational changes of the proteins [44]. Essentially, biomaterials are divided into those with hydrophobic and hydrophilic surfaces, respectively. For protein adsorption, material surface has to partially dehydrate which is thermodynamically favourable in case of a hydrophobic surface (gain of entropy). In the hydrophilic surfaces, there is a displacement of surface-bound water molecules which presents an energy barrier resulting in less protein adsorption to hydrophilic material. Moreover, hydrophilic surfaces generally allow reversible protein adsorption, due to less protein unfolding (see Figure 1.11) [45, 46]. Fibrinogen, a large protein present in blood, has a high affinity to be adsorbed on the hydrophobic, positively charged surfaces [47].

The first scientific research centre which focused on the haemocompatibility of the material for artificial lungs was the Draper Laboratory, (Cambridge, MA, USA) lead by J. T. Borenstein. At the beginning of the year 2000, the group published an article on the vascularized tissue engineering for artificial organs application which was a first small step towards fabricated lung. They developed the dynamic cell seeding in order to minimize blood clotting inside the PDMS chambers. The immortalized human microvascular endothelial cell line (HMEC-1) was used for the culture seeding in order to increase haemocompatibility. Decrease of blood clotting

was confirmed by the experiments of measuring pressure drop as a function of liquid flow rate. The device could withstand a liquid flow rate up to 12 mL/min without rupturing, cracks and leaks [30, 31].
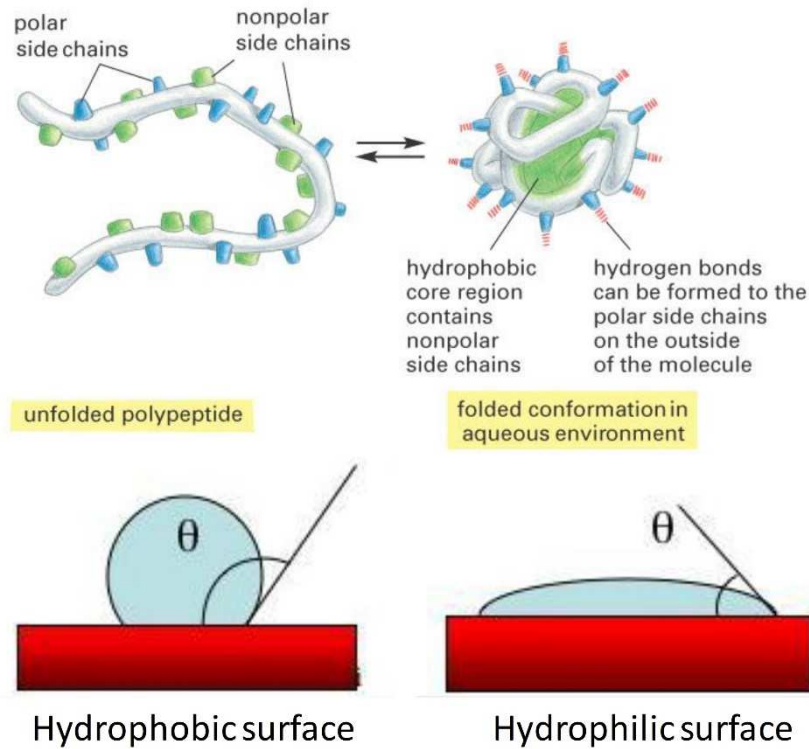
Figure 1.11 Protein conformation on different types of surfaces. Figure adapted from [48]

Burgess *et al* [33] designed and fabricated simple device for blood oxygenation. In this article, the authors did not focus on the sophisticated liquid architecture, but rather on the haemocompatibility and the performance of the device. The vascular PDMS channels were covered with endothelial cells (EC). Briefly, prior to cell seeding, the channels of the device were coated with collagen solution in order to facilitate endothelial cells adhesion. The EC was added to the vascular network at a concentration of 20 million cells/mL. After 3 hours of the incubation, the device was turned upside down in order to ensure cells attachment to the ceiling of the device. Cell attachment and viability were monitored using inverted light microscope. The authors concluded that the endothelial cells play a crucial role in avoiding the coagulation. The experiments of blood perfusion with high amount of anticoagulant inside the bare PDMS channels demonstrated that significant thrombus formation was seen in over half of the channels. In contrast, covering blood channels of a microdevice with EC provides the blood biocompatibility and allows blood perfusion with minor amount or no anticoagulant [33].

The use of polyurethane (PU) as a substitute to hydrophobic PDMS was proposed by Wu *et al* [49]. PU has been widely used in various blood-contact applications such as haemodialysis membranes, heart valves, artificial heart, and intra-aortic balloons. The authors reported a method for fabrication of PU leading to devices with hydrophilic interior surfaces. Additionally, attempts were made to diminish protein adsorption. For these purposes, PU was grafted with polyethylene oxide (PEO). The hydrophobicity/hydrophilicity was measured by contact angle. Unmodified PU was more hydrophilic than PDMS, i.e. contact angle of 63° of PU in comparison to 113° of PDMS. Moreover, the fibrinogen adsorption measurements were performed, indicating that the protein adsorption decreased by approximately 80% in case of PU-PEO surface in comparison to unmodified PU or PDMS [49].

The surface of PDMS was also coated with other polymers to avoid clotting of the liquid channels. Polyethylene glycol (PEG) is well known for its protein and cell resistant properties. It is a linear polymer with repeat unit -CH_2-CH_2-O- which is considered non-toxic. The flexibility and mobility of PEG chains is the mechanism that explains the protein resistance to PEG attached to a surface. When the protein is in close proximity to the PEG modified surface, it compresses the flexible PEG chains. This implies the repulsive interaction, i.e. pushing the protein away from the surface. Such flexibility is due to the conformational freedom of the -C-C-O- backbone of PEG as a result of unrestricted rotation around the C-O bonds. This mechanism is called "excluded volume-steric repulsion" (see Figure 1.12) [50, 51]. The pressure drop of the design of Potkay, decreased significantly upon PEG coating: at the blood flow rate of 0.4 mL/min the ΔP was equal to 6 mmHg in comparison to 190 mmHg before coating, which was a great advancement. Moreover, uncoated device could withstand only 150 min of testing on this configuration while the PEG coated chips were performing the experiment of more than 240 min without collapsing [24]. However, such a shallow liquid channel, i.e. 10-20 µm deep, could cause a number of problems connected with blood itself. Starting from the modification of RBCs (which size is approximately 6-8 µm in diameter) [52, 53], to gradual blocking of the smallest channels. In fact, blood was not analysed after the oxygenation experiments in the device.
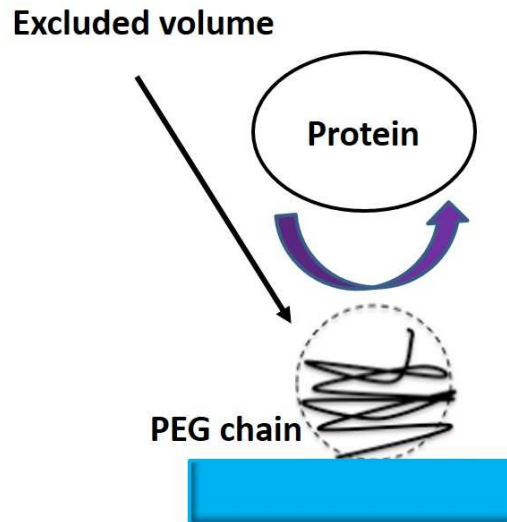
Figure 1.12 Excluded volume-steric repulsion. Figure adapted from [51]

Although tissue engineering has made some significant progress towards creating artificial organs, some challenges are identified: 1) the fabricated structures still differs from the native vessels, i.e. round vessels and rectangular microfluidic channels, 2) demonstration of long-term viability and function of such devices is necessary if clinical applications are considered.

1.4.5. Gas exchange membrane properties

The function of the human lung is to provide oxygen and remove carbon dioxide to and out of the blood respectively. The parameters discussed above are mainly connected with the behaviour of blood while the gas exchange is the parameter which directly influences the performance of the artificial lung chip. Oxygen diffuses through the membrane and connects to blood first as dissolved oxygen and next it binds to haemoglobin (Hb) creating oxyHb (HbO_2) (see Figure 1.13).
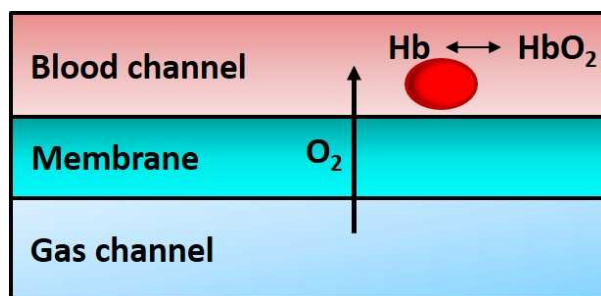
Figure 1.13 Schematic representation of the gas exchange in the artificial lung

In the artificial lung assist device, PDMS film is used as a barrier to avoid direct mixing of blood and gas that may result in bubbles formation inside the liquid causing stroke or heart attack after returning to the systemic circulation. Thus, a durable and highly permeable
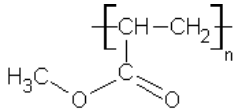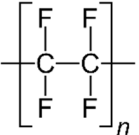
membrane, well attached to the gas and liquid chambers and with high gas exchange area is crucial for successful operation. In case of porous membrane, blood plasma leakage could occur. This would decrease the performance dramatically. Taking all these factors into c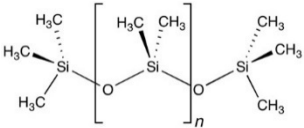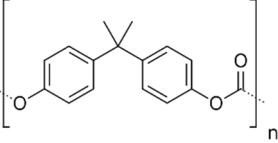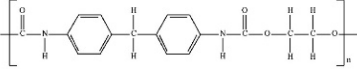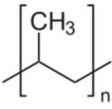onsideration variety of different membrane materials, morphology and thicknesses were examined by different research groups.

<u>Membrane material, morphology and thickness</u>

It was mentioned that for the lung assist device application the membrane should be non-toxic and biocompatible. However, it should also possess high oxygen permeability values. The most commonly used membrane materials integrated in the microfluidic chip for artificial lung applications with their main characteristics are presented in Table 1.4. Out of all the polymers presented in the table, the only one which is oxygen permeable is PDMS. When other polymers are employed, the membranes are porous and thus the oxygen diffuses through these pores. It is also important to notice that the main mass transfer limitations for oxygen transport reside in the liquid phase and not in the membrane. Furthermore, this resistance becomes controlling when increased channel depth. For this reason, as it will be shown below, in most of the cases the increase of the permeance of the membrane is not translated into an increase of the oxygen transfer rate due to its relative low contribution to the total mass transfer resistance.

The group of Vacanti focused on identifying the influence of various membrane types on the oxygenation process [27, 28]. Initially, two types of membranes were fabricated: ultra-thin free-standing membrane (FSM) and composite membrane. The thin film which belonged to FSM was: nBA (n-butyl acrylate) with the thickness ranging from 1-5 μm. For composite membrane, the PTFE (0.1 μm pore diameter and 20 μm thickness) coated with 0.5, 1, 2, 3 μm thick of pMA (poly maleic anhydride) was used. The authors did not notice any significant improvement in gas exchange after coating PTFE with pMA with different thicknesses. In this publication, the oxygenation experiments were not performed, only the permeability was measured (permeability of pMA was 0.3 barrers) [27].

Introduction

Table 1.4 Main characteristics of the most commonly used membrane materials for artificial lung oxygenators

Material	Chemical structure	O_2 perm [Barrer]	Advantages	Disadvantages	Ref
PDMS		620	-Optically transparent -Non-toxic -High gas permeability -Rapid prototyping	-Hydrophobic	[54]
PC		1.4	-Easy moulding -Thermoforming	-Brittle -Low biocompat	[55]
PU		3	-Less hydrophobic than PDMS -Rapid prototyping	-Easy biodegradable	[56]
PP		1.2	-Resistant to many chemical solvents -Flexible and tough	-Low energy surface -Easy biodegradable	[55]
pMA		0.3	-Flexible and tough	-Hydrophobic -Non-stable in alkalies	[27]
PTFE		4.2	-Non-reactive	-Hydrophobic	[55]

The same group also studied different types of membranes inside microfluidic platforms made of PDMS. These membranes included: porous polycarbonate control membrane with 1μm pore size and 12 μm thickness (8% porosity), silicone membrane coated with porous PC (15 μm thick with 3 μm PC coating on the top) and silicone (MDX4-4210) commercial membrane 63 μm thick. Obtained results were comparable among all three membranes in case of O_2 transfer [23].

41

Wu *et al* [20] also analysed different morphologies of a PC thin films placed inside the microchip. The commercial PC membrane with 6 μm thickness was usedTwo types of PC membranes were examined: first with 0.1 μm pore size and 4×10^8 pores/cm^2 as pore density; and, second with 0.05 μm and 6×10^8 pores/cm^2, respectively. The oxygen transfer rate of approximately 20 mL/min.m^2 was significantly lower in comparison to other leading groups due to the usage of air as a supply gas. However, there was no significance difference in gas transport due to the implementation of different membranes due to the controlling mass transfer resistance that was located in the liquid side with 80 μm deep channels [20, 28].

The group of Borenstein focused on the influence of membrane thickness and liquid channel depth, rather than on the membrane material or morphology, for the oxygenation. In 2012, they published the article where two types of dense PDMS membranes were used in order to be integrated in an artificial lung chip. The membranes had two different thicknesses: 30 μm and 117 μm while the depth of the liquid channels inside the chip was 50 μm or 100 μm. Figure 1.14 represents the oxygen transfer rates as a function of blood flow rate for two membrane thicknesses, i.e. 30 and 117 μm [25, 32]. The performance of both devices at low blood flow rates did not change significantly. On the contrary, when increasing blood flow rates, the oxygen demand for full oxygenation also increases; and consequently, the relative contribution of the membrane resistance to O_2 transport. Thus, the lower the membrane thickness, the higher P_{O_2} on the membrane wall and the higher driving force for O_2 diffusion in the liquid phase. Accordingly, the influence of membrane thickness becomes notorious with increasing blood flow rates.
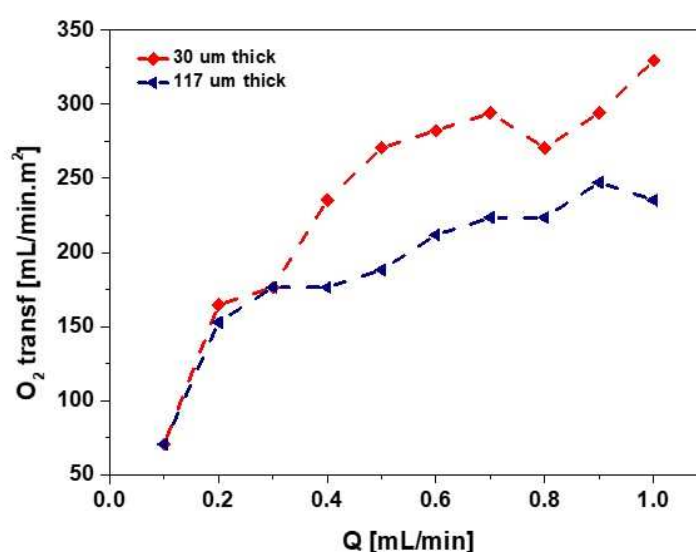
Figure 1.14 O_2 transfer rate for PDMS membrane with different thicknesses obtained by the group of Borenstein [32]

Introduction

The group of Vacanti analysed the influence of the membrane structure, material and thickness on the oxygenation performance. MDX4-4210 commercial silicone membrane was "sandwiched" in between PDMS microfluidic platforms. Three types of membrane configurations were tested: 1) commercial silicon dense membrane, 63 μm thick, 2) commercial silicon dense membrane, 3 μm thick, coated by porous PC layer, 15 μm thick, and 3) porous PC membrane, 12 μm thick. Figure 1.15 represents the comparison of the experimental values of the oxygen transfer rate respectively at various liquid flow rates inside the liquid channels with equal depths, i.e. 200 μm [23, 35]. It can be seen that the oxygen transfer did not change significantly within the operational window studied. Since the geometry of the liquid chamber and depth of the channels were identical in the presented experiments, it can be concluded that the membrane related parameters barely affected oxygen exchange rate.
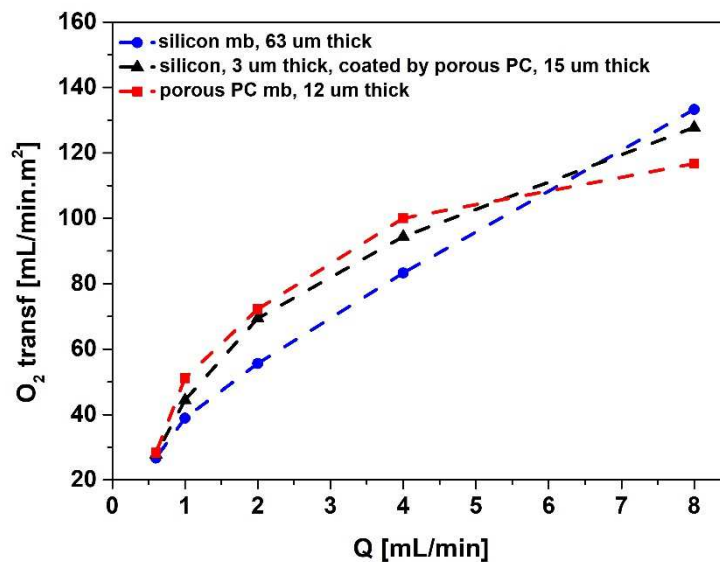
Figure 1.15 O_2 transfer rate obtained by the group of Vacanti as a function of the liquid flow rate and various membrane thickness, material and morphology

From the number of articles presented by the various research groups and from Figure 1.14 and Figure 1.15 it could be concluded that the individual mass transfer resistance of the membrane is not the controlling one for the oxygen transport. Obviously the thinner the membrane the lower its individual resistance and eventually higher oxygen exchange rates could be achieved, especially in case of high liquid flow rates. Whenever mass transfer limitations are located in the membrane it is advantageous to increase membrane permeance, i.e. lower thickness and/or higher permeability values. This should be done without compromising the mechanical stability and durability of the membrane and without changing shear stress (roughness of the membrane surface) in order to increase gas exchange.

1.4.6. Priming volume

One of the significant obstacles connected with the usage of ECMO, mentioned in section 1.2.1, was the high priming volume. Blood priming volume is the amount of blood which must be withdrawn from the body in order to be oxygenated. In case of adults it might not be a significant problem while in case of children or preterm infants this raise to a serious complication. The typical Extracorporeal Membrane Oxygenator devices have priming volumes in the range of 95-310 mL for adults and 31-87 mL for infants. The total volume of blood in an adult is around 5 L, thus the priming volume in the ECMO device accounts for approximately 5% of the total blood volume. On the other hand, the total volume of blood in neonate is about 100 mL/kg, hence the priming volume in the ECMO accounts for around 28%. This shows that the amount of blood which is withdrawn from the preterm infant body is meaningful. Minimizing the amount of blood which is directly exposed to an artificial surface at a given time will lead to an increase of haematocrit values, advance patient recovery and reduce post-operative blood transfusions [26]. Therefore, the target of the artificial lung assist device is to have a portable system with low priming volumes. Priming volumes in microfluidic devices, which considers only a volume of the liquid chamber without considering any external piping, are very small, i.e. from 5 to 400 μL, which accounts for approximately 1% of the total blood volume of the neonate. Fusch *et al*, focused entirely on designing and fabricating the microdevice exclusively addressed to neonates, i.e. with total priming volume of 0.122 mL [20, 28].

1.5. Other applications of microfluidic artificial lungs

The design and fabrication of the artificial lung in the form of a microfluidic device do not always have to be considered as a self-standing artificial organ and be exclusively devoted to blood oxygenation. Nowadays, microfluidic chips are commonly used in drug toxicology as a replacement to animal tests or conventional petri dishes taking into account that certain drugs can behave differently on a flat two dimensional surface than in a three dimensional human capillaries [57, 58]. Microfluidic technology is used to mimic the real structure and properties of the target organ. In 2010, Ingber *et al* developed a multifunctional microdevice that reproduced structural, functional and mechanical properties of the human alveolar-capillary interface (see Figure 1.16). The PDMS device was fabricated by soft-lithography and a membrane with 10 μm thickness was integrated in between the chambers. The membrane was coated with fibronectin, and collagen human pulmonary microvascular endothelial cells were

cultured on the other side of the membrane. The chambers were 1-2 cm long and they were designed in the form of small reservoirs rather than branching architecture. In this approach, vacuum was applied to the gas channel to mimic breathing. Silica nanoparticles which induce cell toxicity were used for the experiments. A surprising result showed that the breathing movement increases the transport of Si NPs from the air to the vascular channel [59, 60].
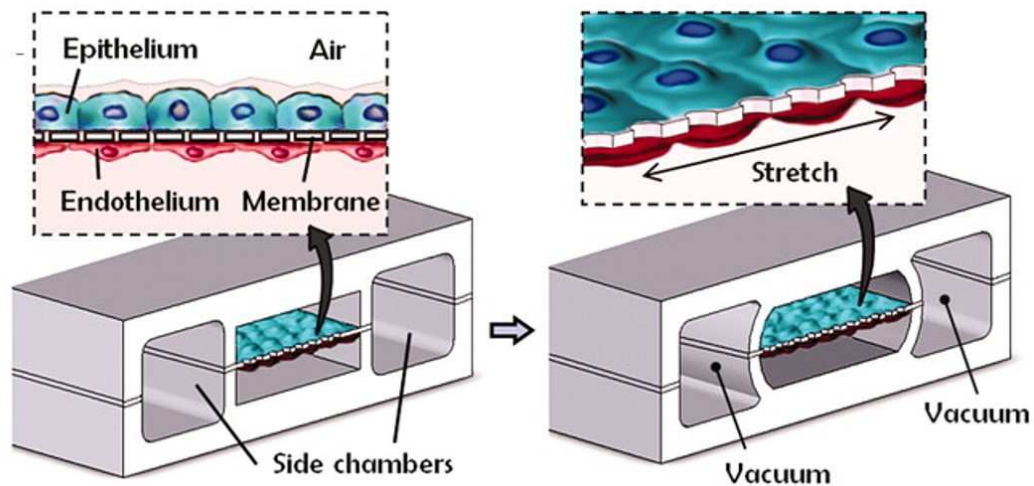
Figure 1.16 Biologically inspired design of a human breathing lung-on-a-chip microdevice. Figure adapted from [59]

In 2015, the group of Guenat also published the article about artificial lung for drug toxicology application. The alveolar barrier is exposed to different xenobiotics of which some portion can enter the bloodstream and can be transported to other organs. The mechanical strain can affect the uptake of such molecules significantly. The microfluidic device proposed by the group of Guenat was designed to enable the investigations of an influence of breathing movements on the uptake of drugs. The microdevice was comprised of the microfluidic chip and a pneumatic system to emulate the respiration. The fluidic part consisted of two PDMS chambers between which a thin, porous and flexible PDMS membrane was sandwiched and bonded. The bottom plate was structured with a cell culture medium reservoir. The pneumatic part was made of a 40 μm thin PDMS layer bonded with the actuation plate in which pneumatic channels were structured. The porous and flexible PDMS membrane was fabricated by a microstructuring-lamination process which gave a final pore of 3 - 8 μm in diameter and thickness of 3.5 – 10 μm. Since this device was not focused on the lung transplantation, no physiological blood flow had to be controlled. Thus, there was no branching architecture in the liquid geometry, as it was observed in the case of previous authors, but only three liquid reservoirs were present (see Figure 1.17). The external force was applied to the device in order to mimic natural process of breathing. In order to stretch the membrane at a frequency of 0.2

Hz, the lung-on-a-chip was connected to an external electro-pneumatic setup. Moreover, the cells were seeded on a PDMS membrane: epithelial cells on the apical side and endothelial cells on the basal side of the membrane. The permeability experiments were performed. It was noticed by the authors that the stretch of the membrane and the dynamic environment increases the permeability of small hydrophilic molecules if they are kept in the dynamic mode, i.e. breathing imitation. Therefore, it was demonstrated that the mechanical stress significantly affects epithelial barrier permeability. Additionally, the metabolic activity of human pulmonary alveolar epithelial cells that were cultured in a dynamic mode was found to be higher than that of cells cultured in static mode. It was also commented that the breathing "movement" did not interfere with the human cells proliferation or cell injury in the first 24 hours [61].
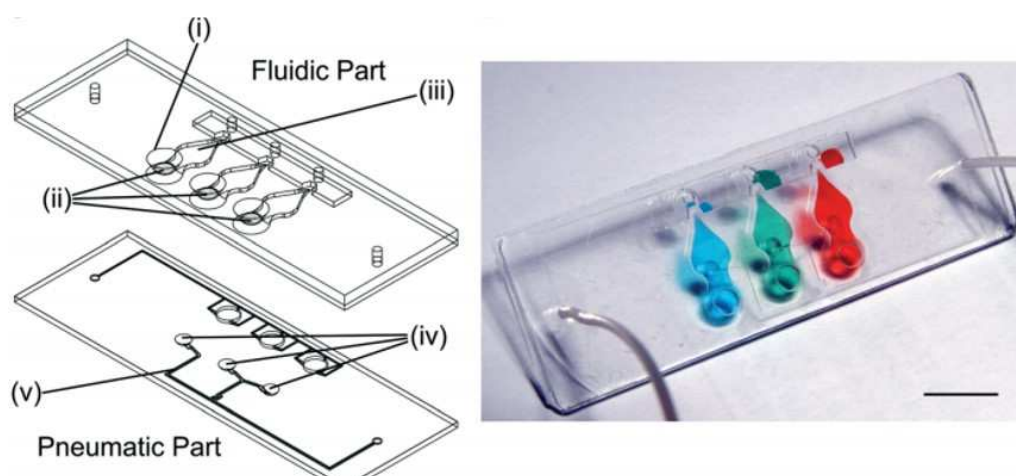
Figure 1.17 Working principle and design of the lung-on-a-chip. The chip is made of (i) fluidic part with 3 cultural vells, (ii) porous and flexible membrane, (iii) lateral chambers, (iv) micro-diaphragms integrated in the pneumatic part, (v) pneumatic microchannels. Figure adapted from reference [61]

1.6. Devices for Anaesthetic Gas Separation

1.6.1. Conventional Anaesthesia Procedure and Commercial Systems

Anaesthesia is a state of unconsciousness that is used to ensure loss of response to pain or muscle relaxation during the surgical operation where the pain would be intolerable for a patient or where being awake is strongly precluded. Anaesthesia results from a treatment with several anaesthetic agents. Nowadays, commonly used anaesthetic gas mixture for surgical operations is composed of: 1) anaesthetic gas, mainly nitrous oxide, 2) oxygen, 3) water vapour and 4) one volatile anaesthetic: isoflurane, sevoflurane or desflurane. In this section, the state of the art of the conventional anaesthesia procedure and its possible drawbacks are presented. The alternatives for controlled anaesthetic gas composition are discussed. Additionally, the desired properties for the liquid phase used as separating agent in the G-L absorption process are described as well.

The most commonly used anaesthetic gas for surgical operations is nitrous oxide (N_2O). The mixture of nitrous oxide (65-70% in the inhaled mixture) and volatile anaesthetic compounds, mainly isoflurane (0.2-0.8%), desflurane (<2.5%) and sevoflurane (0.4-1.2%), is introduced to the closed breathing system [62]. During the patient's respiration, the mixture of anaesthetic gas and carbon dioxide, as the patient breaths out, is introduced to the closed breathing system. Thus, it is of crucial importance to remove CO_2 from the closed circuit.

In the commonly used anaesthetic closed systems (see Figure 1.18), the anaesthetic mixture first flows through the inspiratory part, enters the patient via Y-piece, flows through the expiratory breathing system, passes in and out of the reservoir bag where an excess of the gas is vented out and passes through a sorbent canister where CO_2 is removed. Then, the gas returns to the systemic circulation after addition of fresh anaesthetic gas.
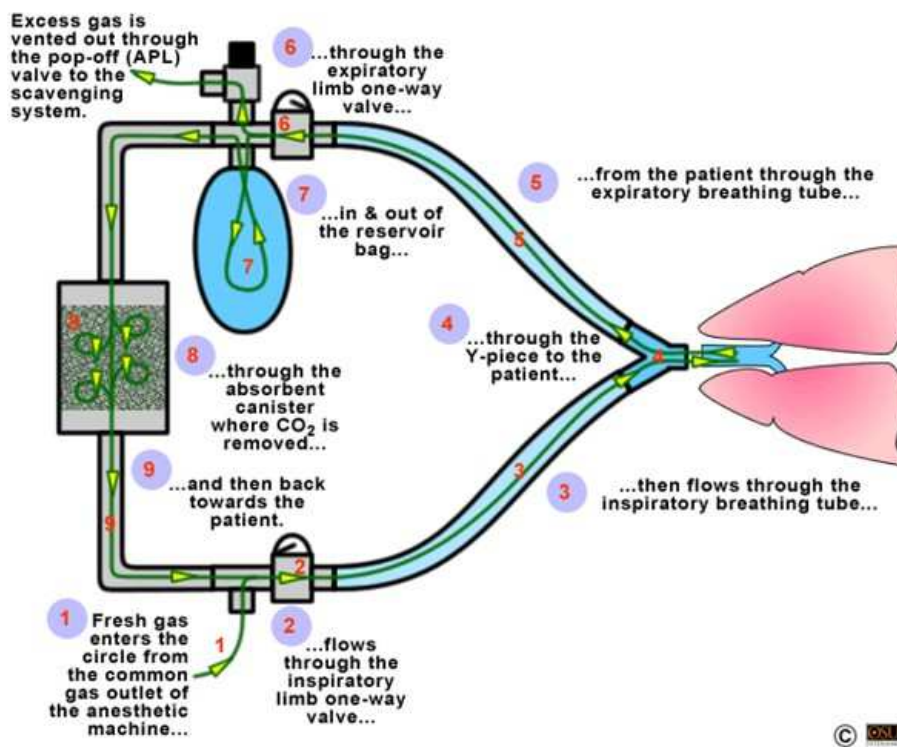
Figure 1.18 The circle of a breathing system under anaesthetic gas treatment [63]

The sorbent canister for separating CO_2 from the exhaled gas mixture in a closed – circuit technology consists of soda lime in granular form (i.e. Drägersorb® [64]) which has a high affinity towards CO_2. Soda consists mainly of: calcium hydroxide, water, sodium hydroxide and potassium hydroxide. The absorption of CO_2 by soda lime occurs as following:

$$CO_{2(g)} \rightarrow CO_{2(aq)}$$ CO_2 dissolves in water- slow and rate-determining (1)

$$CO_{2(aq)} + NaOH \rightarrow NaHCO_3$$ Bicarbonate formation at high pH (2)

$$NaHCO_3 + Ca(OH)_2 \rightarrow CaCO_3 + H_2O + NaOH$$ Carbonate formation and NaOH recovery (3)
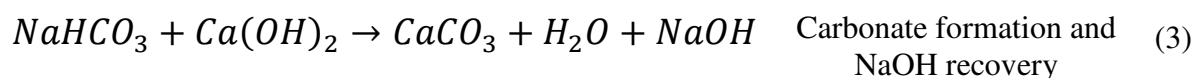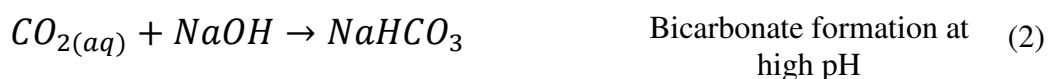
These reaction steps emphasize the catalytic role played by sodium hydroxide in elimination of carbon dioxide from the rebreathing circuit. As expected, the CO_2 sorption recovery is limited by the size of the fixed bed canister, i.e. 0.6 L for standard equipment [65]. Even though the process is relatively efficient and commonly used, it suffers from a number of problems. The canister with caustic material, if allowed to dry up, can produce hydrogen and release heat; resulting in an explosion hazard. Moreover, soda lime can react with volatile anaesthetic compounds producing toxic side products (e.g. fluoromethyl-1-2,2-difluoro-a-(trifluoromethyl) vinyl ether [66] or carbon monoxide [62]) in the gas circuit.

One of the main concerns related to the use of N_2O is the risk of hypoxia. Hypoxia is a condition where the body, or a region of the body, does not possess sufficient amount of oxygen at the tissue level. When high quantity of nitrous oxide, also called a "third gas effect", is present in the alveoli, O_2 and CO_2 are diluted by this gas which leads to the decrease of their respective partial pressures resulting in insufficient blood oxygenation [67]. Taking everything into consideration, alternative, potent and non-toxic, anaesthetic gas together with non-hazardous and more efficient strategies for carbon dioxide separation have to be developed.

1.6.2. Xenon as an alternative anaesthetic gas

The properties of xenon as an anaesthetic gas were described for the first time in 1950s. The concept was created as a response to a diver's report where it was claimed that the mixture containing Xe in their gas bottles made them suffer from fatigue and debility [67]. In 1946 the effect of xenon-oxygen mixture inhalation in mice was firstly reported. The authors noticed that this blend possesses narcotic properties and causes dizziness [68]. The first tests involving humans were performed in early 1950s. Different mixture ratio, various time exposure and distinct Xe concentration were inspected in order to observe the effect on human body. The obtained results were compared to commonly used nitrous oxide and it was concluded that xenon is more potent and less toxic than N_2O.

Xenon is defined as a gas which possesses a number of characteristics making it a perfect anaesthetic compound. It is haemodynamically stable which results in lack of cardiac depression and supress of catecholamine neuromodulator responses. Xe possesses low solubility in liquids, thus the risk of hypoxia is greatly reduced. Additionally, it produces high regional blood flow, which is clearly advantageous because hypoxia may result from the problems with blood flow to the end tissue causing insufficient oxygenation [69]. The minimum alveolar concentration (MAC) of xenon is 71%, indicating that it is more potent than N_2O (approximately 100% of MAC) and the recovery of a patient is faster in that case. MAC is the concentration (normally expressed in %) of the anaesthetic compound in the gas phase that surrounds the alveoli which is needed to obtain anaesthetic effect [62]. Xe is particularly attractive for neonates as it increases neuroprotection. The neuroprotective features of xenon are based on its binding properties to glycine side of glutamatergic N-methyl-D-aspartate (NMDA) receptor which results in blocking it and inhibiting the excitotoxic pathways. NMDA is an ionotropic receptor that is activated by binding of glutamate. The prolonged and excessive activation of this receptor causes neuronal death [70]. Furthermore, xenon is non-flammable and non-toxic in comparison to nitrous oxide based anaesthesia. When compared to isoflurane

49

containing anaesthetic gas, Xe is more environmental friendly [67, 71] as it does not exhibit ozone depleting potential. It was internationally agreed that the manufacture of this volatile compounds will be totally forbidden by the year 2030. Moreover, N_2O is a potent greenhouse gas and its release contributes to approximately 0.1% of the whole global warming. The lifetime of N_2O in the atmosphere is around 120 years [71].

Taking into consideration all the advantages of Xe it might be puzzling why it is not commonly used as an anaesthetic gas. The reason is its price. Xenon is far more expensive than commonly used nitrous oxide. As a noble gas, it is found in the air in small concentration (87 ppb). Therefore, the only meaningful amount of this gas can be obtained by its separation. Xe is manufactured by cryogenic-distillation of liquefied air and after some separation processes it is possible to obtain approximately 99.995% of pure Xe with energy production costs around 17740 kJ/mol [69]. The gas mixture exhaled from the patient during the surgical operation, where xenon is used as an anaesthetic gas, consists mainly of Xe ($\approx$65%), O_2 ($\approx$27%), N_2 (3.3%) and CO_2 (5%) [62]. Hence, recycling of Xe from the anaesthetic exhaled gas rather than wasting it to the atmosphere is the only way to ensure sustainable xenon production. Herein, the main technological challenge is the on-line removal of CO_2 from anaesthetic closed circuits from 5% down to 0.5%.

1.7. Membrane Contactors for Anaesthesia Gas recovery

Membrane contactors are considered as one of the most promising process intensification strategies with devices being possibly between 5 and 20 times smaller than conventional separation processes [14]. In this section, we will particularly focus on the gas-liquid (G-L) membrane contactor for anaesthesia gas recovery by CO_2 separation. A few numbers of manuscripts on non-porous membrane contactors have been published in recent years; and most of them deal with MEA-based absorbents [3, 10, 72]. In this section, the available liquid solvents for CO_2 capture are discussed and recent examples of membrane contactors for anaesthesia gas recovery are described.

1.7.1. Liquid phase for CO_2 absorption in the G-L membrane contactor

The liquid phase for anaesthetic gas recovery should possess high affinity towards CO_2 but no or less interaction with Xe. When aqueous solution is used as a liquid phase for CO_2 absorption, the bicarbonate is produced in the reaction of hydroxylation [73].

Introduction

<u>"Conventional solvents" for CO_2 absorption</u>

The, so called "conventional solvents", which are well-known solvents that present high CO_2 sorption capacity, were commercialized in 1930s. They can be divided into physical and chemical solvents. The physical solvents absorb CO_2 from the feed gas at high pressures, i.e. one of the physical solvent, Selexol, absorbs CO_2 in the pressure of 2.07 to 13.8 MPa [74]. In this process, no chemical reaction is involved in the gas absorption but rather physical conditions such as pressure and temperature are considered. The capacity of physical solvents at low pressure decreases and they have to be replaced by chemical absorbers.

The catalysis of the acid-base reactions in the proximity of the liquid-gas interface in the chemical solvent enhances the absorption rate in comparison to the absorption of CO_2 in water [73]. The aqueous amine solution is used in order to capture CO_2 by chemical absorption process in which the carbon dioxide reacts with the amine in the form of a carbamate through a zwitterion mechanism (see reaction (4)). Table 1.5 shows the main characteristic of some common chemical absorbents based on ethanolamines: -OH group to reduce vapour pressure and increase CO_2 solubility; and $-NH_2$ for the acid-base reaction, i.e. secondary and tertiary amines [75].

(4)
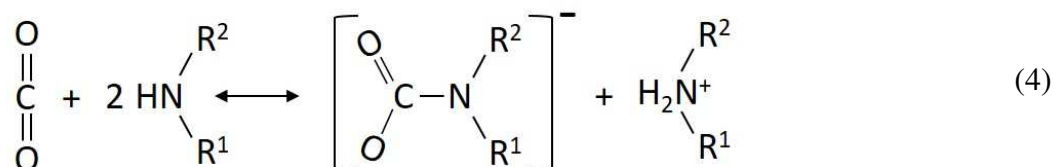
Table 1.5 *Characteristic properties of some representative CO_2 chemical solvents*

Absorbent	Vapour pressure (25°C) [Pa]	Heat of reaction for CO_2 [kJ/kg]	X_{CO_2} [mol/mol]*
MEA[1)]	<133	1920	0.50
DEA[2)]	<1.33	1510	0.32
DIPA[3)]	9300	2180	-
MDEA[4)]	1	1420	0.12

1)Monoethanolamine, 2) Diethanolamine, 3) Diisopropylamine, 4) Methyldiethanolamine; *indicates moles of sour gas per mole of amine for solutions with 1.3 mole of amine per kilogram of water [76]

Even though amines are very effective in CO_2 capture due to high absorbing capacity, high reactivity and selectivity with CO_2, there are some severe disadvantages, i.e. emission of toxic

51

compounds, high vapour pressure, elevated desorption and recycling costs due to high reaction heat. In general, due to its volatility, large amounts of organic amines are present in clean gas which could potentially lead to the formation of dangerous secondary components, i.e. nitrosamines, amides and nitramines, and require additional water washing steps that can increase the cost of the overall capture process. Accordingly, alternative type of solvents and technologies for a more efficient CO_2 separation need to be implemented.

Ionic liquids for CO_2 absorption

Ionic liquids (ILs) are defined as salts comprised of exclusively organic cations and organic/inorganic anions with a melting point lower than 100ºC. These emerging class of novel materials are becoming extremely popular due to their remarkable properties, such as: high thermal and chemical stability, nearly negligible volatility, nonflammability, solvation properties and CO_2 solubility [74, 77].

It was described by several authors that ionic liquids are capable for both physical and chemical CO_2 absorption [74, 75]. The physical absorption occurs where CO_2 occupies the "free space" within the IL structure through Van der Waals forces. However, the solubility of carbon dioxide cannot be entirely explained by the anion-CO_2 interaction. A free volume mechanism is another factor which plays a significant role. Basically, by increasing the free volume, molar volume and alkyl chain length, the carbon dioxide solubility raises as well. This effect correlates well with the elevated volume available for CO_2 interaction [14, 74, 75, 78, 79]. Opposite to the solubility dependence, the diffusion coefficient decreases with the augment of the molar volume [80].

On the other hand, the chemical CO_2 absorption relies on acid-base interactions. The spectroscopic data obtained by Kazarian *et al* [81] revealed that this interaction is a Lewis acid-base type, where the anion, considered as the key player, acts as a Lewis base and CO_2 plays as a Lewis acid.

One of the most widely investigated and reported in the literature ionic liquid family is the imidazolium type due to relatively large CO_2 solubility. For instance, in 1-ethyl-3-methylimidazolium bis(trifluoromethylsulfonyl)imide, [emim][Tf$_2$N], the molar fraction of CO_2 dissolved is 0.209 at 298.15 K and 9.03 bar [75, 82]. Table 1.6 shows CO_2 solubility data for few examples of commonly used ILs. The ionic liquids are comparable in efficiency for CO_2 capture to commercial amine solvents but at the same time are non-volatile, non-toxic and do not need water for the reaction to occur.

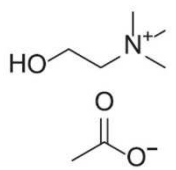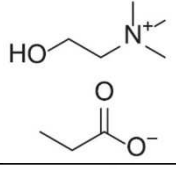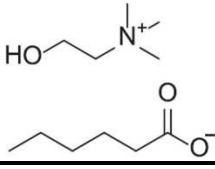*Table 1.6* CO$_2$ *solubility data for imidazolium-based ionic liquids [75]*

Ionic liquid	Acronym	T [K]	P [bar]	X_{CO_2} [mol/mol]
1-buty-3-methylimidazolium tetrafluoroborate	[bmim][BF4]	303	10	0.1461
1-butyl-3-methylimidazolium hexafluorophosphate	[bmim][PF6]	303	10	0.1662
1-ethyl-3-methylimidazolium bis(trifluoromethylsulfonyl)imide	[emim][Tf$_2$N]	298	9.03	0.209
1-hexyl-3-methylimidazolium bis(trifluoromethylsulfonyl)imide	[hmim][Tf$_2$N]	298.1	19.74	0.4330

Even tough, the imidazolium based ILs possessed high affinity to CO$_2$, the biodegradability obstacle appeared. The group of Scammells was the first one which reported poor biodegradability of widely used imidazolium based ILs [83]. The importance of toxicity and biodegradability should not be forgotten, since widespread use of ILs is anticipated. Garcia *et al* evaluated the biodegradability of [bmim][X], where X corresponds to: Br, BF$_4$, PF$_6$, TF$_2$N, DCA, and octylsulphate [OS]. The authors observed that only octysulphate was biodegraded in 25%, while all the other ILs followed the biodegradation of only 5%. Hence, these ILs could not be classified as "readily biodegradable" [84]. Doherty *et al* investigated the biodegradability of six imidazolium and pyridinium based ILs, all containing [Br] anion as the counterion. A longer alkyl chain seems to promote biodegradation in many cases. With the exception of pyridinium IL with the longest alkyl chain, none of the imidazolium based ILs could be classified readily biodegradable [85]. On the contrary, cholinium based ILs shown biodegradable character [86]. In summary, pyridinium and cholinium ILs are more biodegradable than imidazolium and phosphonium counterparts. These biodegradable, biocompatible and environmental-friendly ILs are synthesized by naturally-derived materials such as sugars and aminoacids and are gaining increasing importance since last decade.

Cholinium cations are quaternary ammonium cations ([N,N,N - trimethylethanolammonium]$^+$) fully derived from natural products [87, 88]. It was shown that the cholinium cations combined with a range of alkanoate anions or amino acids provides a media where living cells can actively grow [89, 90]. Moreover, they show high CO$_2$ capturing effect due to absorption plus chemical reaction that take place thanks to their ammonium cations [91]. Table 1.7 shows solubility data for CO$_2$ in case of three most commonly used cholinium

based ionic liquids. Furthermore, this novel class of ILs may provide an optimum media to stabilize proteins (i.e. enzyme) [92] which is of our interest for the increase in CO_2 capturing effect.

Table 1.7 *CO_2 Solubility data for three common cholinium-based ILs* [87]

Ionic Liquid	Molecular structure	T [K]	P [bar]	X_{CO_2}*[mol/mol]
[Cho][Acetate]		303	10	0.085
[Cho][Propionate]		303	10	0.152
[Cho][Hexanoate]		303	10	0.444

* The measurements were performed for ILs at water activity of 0.753

Taking everything into consideration, cholinium based ionic liquids demonstrate comparable carbon dioxide solubility to imidazolium based ILs and commercial chemical solvents. However, cholinium based ILs are biodegradable and possess appropriate environment to be combined with the enzyme in order to increase the CO_2 capturing effect.

Carbonic Anhydrase Enzyme

The ability of carbonic anhydrase (CA) to catalyse CO_2 hydration, as well as its reverse reaction is well known [93]. Carbonic Anhydrase is a naturally occurring thermoresistant metalloenzyme that works as a catalyst for the conversion of CO_2 into bicarbonate (HCO_3^-) at extremely high turnover rates. It regulates important biological processes within humans and other living organisms such as the acid–base balance within the blood [94], the photosynthesis mechanism in plants and the carbon concentration mechanism in microorganisms [64]. The most commonly investigated class of CA is the α form [95] which is generally found in mammals. In α-CA, the enzyme activity is derived from a Zn^{2+} ion that is coordinated to three histidine residues near the centre of the molecule in a cone-shaped cavity (see Figure 1.19).
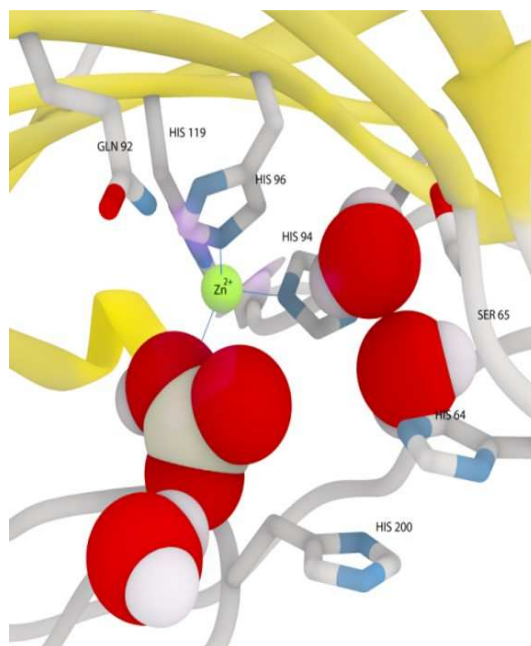
Figure 1.19 3D diagram of α-carbonic anhydrase structure. Active site zinc ion is shown as green space-filled sphere [96]

The hydration of CO_2 occurs when the Zn^{2+} ion abstracts a proton from a surrounding water molecule, creating a hydroxide ion that is negatively charged. Such active site consists of a specificity pocket for CO_2. Thus, the first step of the enzyme catalytic pathway is the nucleophilic attack on carbon dioxide molecule by zinc-bounded hydroxyl group, giving rise to the formation of the enzyme-bicarbonate ion complex. The reaction mechanism can be summarized as follows:

$$Zn^{2+} + H_2O \leftrightarrow H^+ + Zn^{2+} - OH^- \tag{5}$$

$$Zn^{2+} - OH^- + CO_2 \leftrightarrow Zn^{2+} + HCO_3^- \tag{6}$$
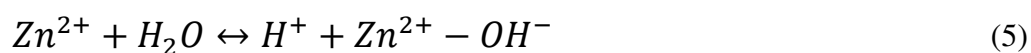
The bicarbonate ion is easily released by the displacement of a water molecule that binds the zinc at the active site followed by the intramolecular proton transfer to imidazole group of the histidine group to restore the active site form zinc-bounded hydroxyl group. Figure 1.20 demonstrates the CA catalytic mechanism for CO_2 reversible hydration.
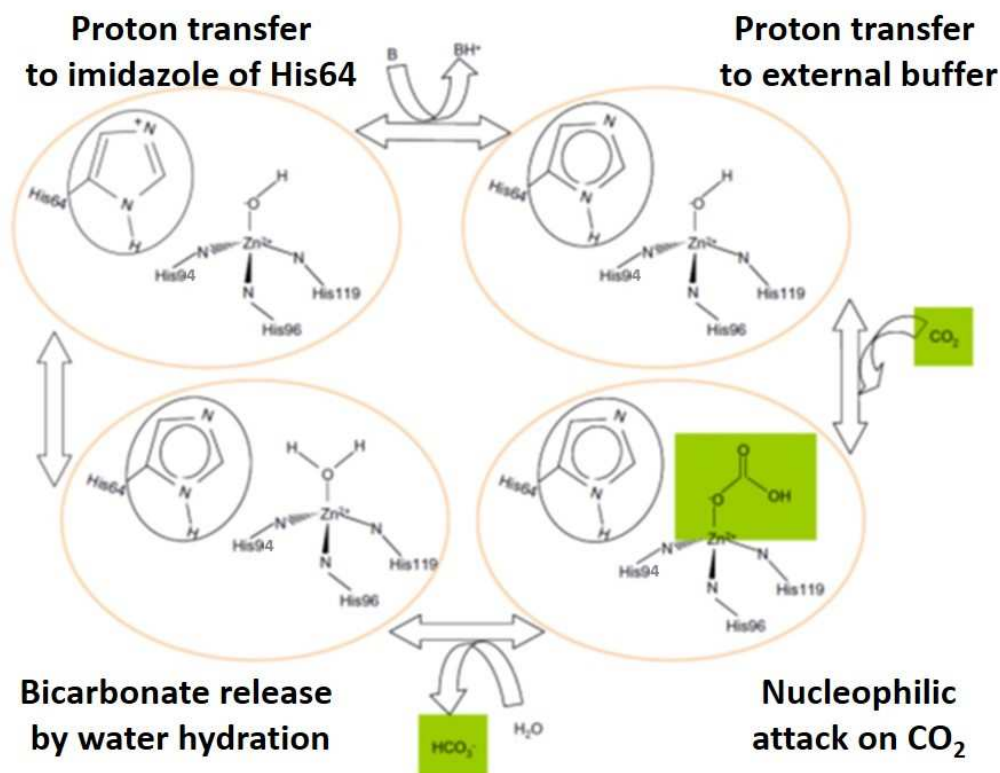
Figure 1.20 Catalytic mechanism of carbonic anhydrase active site during reversible hydration of carbon dioxide. Adapted from reference [73]

Martins *et al* measured the influence of CA at low concentration (0.01% w/w) combined with cholinium priopionate IL on the CO_2 transport and removal. As it was already explained above, water content is an important parameter on enzyme activity and stability. Therefore, by a proper selection of the working conditions, i.e. mainly water activity 0.753 for the IL; the supported liquid membrane contactor enhanced the CO_2 capture by 63% [87, 97].

1.7.2. Membranes for G-L membrane contactors for anaesthesia gas recovery

Mendes *et al* proposed commercial carbon molecular sieve (CMS) hollow fibres [98] and flat sheet porous membranes [62] for on-line removal of CO_2 and N_2 from anaesthetic closed circuits using diamine as CO_2 solvent. High permeabilities (up to 111.4 Barrer for CO_2 and 0.03 Barrer for Xe) and ideal selectivities for CO_2/Xe (up to 6020) and N_2/Xe (up to 180) were obtained. On the other hand, the separation performance with real multicomponent mixtures was adversely affected by Xe. This molecule, with kinetic diameter of 4.04 Å, is able to block the pores close to the CMS membrane surface (with diameters in the range of 3-5 Å) hindering the diffusion of other species.

Introduction

The group of Yong *et al* (2016) used hollow fibre membrane contactor in order to separate CO_2 from the stream gas using potassium carbonate solution [99]. The authors propose the coating of the membrane surface, non-porous polydimethylsiloxane-polysulfone (PDMS-PS) or porous polypropylene (PP), with carbonic anhydrase enzyme by layer-by-layer (LbL) technique to: i) increase mass transfer rates due to the reduction in pore wetting by the adsorbed polyelectrolytes; ii) to promote the CO_2 absorption kinetics into K_2CO_3. However, a slight loss in enzyme activity due to immobilization was observed even during the short term kinetic studies.

The catalytic activity of CA for the integrated CO_2 capture and enzymatic bioconversion has been preliminary tested by Neves *et al* who evaluated pure gas permeability values in supported IL membranes. Commercial hydrophobic porous membrane made of polyvinylidene fluoride (PVDF) was used as a support for the immobilization of CO_2 solvents, i.e. polyethylene glycol (PEG) 300 and 1-butyl-3-methylimidazolium bis(trifluoromethanesulfonyl) imide [bmim][Tf$_2$N] ionic liquid [97]. The CO_2 solubility increased between 20% and 30%, even at low CA enzyme concentration (0.01% w/w) due to the chemical reaction enhancement factor.

A similar G-L membrane contactor has been postulated by Chabanon *et al* [14] for the maximized mass transfer performances of gas-liquid separations application involving physical solvents and ionic liquids. This particular solution, to wetting prevention on hydrophilic microporous membranes, simultaneously offers acceptable mass transfer performance due to the larger viscosity and the lower overall gas-liquid mass transfer coefficients of solvents with extremely low breakthrough pressure. In addition to the above-mentioned advantages, the use of a non-porous thin composite membrane can also be an optimal solution to reduce the solvent evaporation towards the gas phase, thus allowing the use of absorbents with better energy performance but cannot be used in absorption columns due to their high volatility. This idea has been recently explored for volatile-amine based absorbents on Teflon AF2400 self-standing membranes (10-20 um thick) [72].

The G-L membrane contactor scheme herein studied for anaesthesia gas recovery is shown in Figure 1.21. Our concept, based on non-porous membrane for anaesthesia gas recovery by CO_2 absorption on cholinium based ionic liquids in presence of CA enzyme, has to address the main following issues:

- Reduce the membrane mass transfer resistance to fully exploit the advantageous effect of the CO_2 enzymatic reaction in the liquid phase: highly permeable self-standing dense membranes, i.e. high permeability values and/or low membrane thickness are required.

- Use biocompatible solvents and materials capable to withstand the chemically reactive environment of the liquid phase.
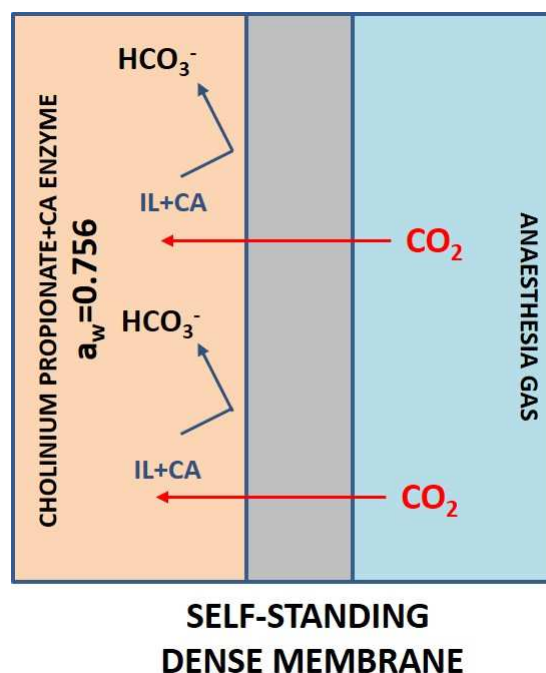
Figure 1.21 Graphical representation of the self-standing dense membrane for anaesthesia gas removal

1.8. Goals of the thesis

The target of the research presented in this thesis is a design, development and fabrication of a microfluidic device with integrated membrane in the form of a membrane contactor for various biological applications. In the first part of the work, the microfluidic system for blood oxygenation, so called lung-on-a-chip, is the first considered application. An implantable lung assist device would augment lung function as a bridge to transplant or possible destination therapy or it would serve as an artificial lung in case of neonates with not well developed natural lung tissue. This current work intends to improve already existing study on microfluidic lung oxygenators both theoretically and experimentally by fulfilling following tasks:

- Providing high blood oxygenation for neonates, i.e. from 80% to 95% O_2, in the fabricated microdevices
- Modification of the liquid side architecture to decrease pressure drop inside the channels (adding liquid flow distributors, changing the dimensions etc.)
- Assurance of blood physiological conditions inside the proposed microfluidic geometries

- Study of the oxygen concentration profile along the liquid chamber geometry and a function of the channel architecture on the speed and goodness of oxygenation by mathematical model that will facilitate chips design and fabrication in the future

Moreover, this study also introduces the concept of an alveolar microfluidic device as gas-ionic liquid contactor for removal of CO_2 from anaesthesia gas, containing Xe. Xenon, which is used as an alternative green anaesthetic gas, has to be separated from CO_2 which is exhaled by a patient during the surgical operation. This task is achieved by:

- Enhanced CO_2 transport by introduction of Ionic Liquids combined with the enzyme that possess high affinity to CO_2,
- Assurance of no effect of the IL+enzyme mixture on Xenon absorption

Additionally, this study also seeks an alternative structure for gas permeation. The three-dimensional fractal geometry with opened apertures at the concave of each layer is tested for simple gas permeation.

2. Microfluidic devices for blood oxygenation

In this chapter, the microfluidic device used as a gas-liquid contactor for blood oxygenation in preterm infants is proposed. The design criteria for the fabricated devices was to increase the oxygen saturation level while ensuring the physiological blood flow in order to avoid thrombus formation and channel blockage. Two different liquid chamber geometries are studied: 1) alveolar type architecture with horizontal membrane arrangement and 2) meander type architecture with vertical membrane arrangement. The aim of our artificial lung is to support the oxygenation process in preterm infants where the membrane of the natural lung is not fully developed. The selection of the geometric parameters, upon analysis of the fluiddynamics by computer modelling of the two architectures and fabrication procedures are described in detail in the following sections. The experimental system, working conditions and calculations are presented and discussed as well. A mathematical description of the oxygen transfer process has been successfully performed. A reasonable agreement among the oxygenation results obtained in the meander type devices and those derived from the mathematical model are obtained. Finally, a parameter sensitivity analysis is carried out to settle the guidelines for future developments.

2.1. Objective

A biomimetic microfluidic technology for the application of artificial organs, especially artificial lungs, has been reported previously by several authors [20, 29, 100-103]. In these microchips blood flows through branched vascular microchannels which mimic the alveolar architecture of a human lung. The oxygen transfer from the gas phase to the blood involves pure oxygen transport through a polymeric dense membrane, diffusion into blood plasma, followed by oxygen binding to haemoglobin. In this work, two different chip conformations and liquid chamber geometries are presented. The main objective of the fabricated devices is to increase the oxygen saturation level while ensuring the physiological blood flow in order to avoid thrombus formation and channel blockage.

2.2. Design of microfluidic devices based on fluiddynamics

In order to design an artificial lung device, that will oxygenate blood, embrace its physiological behaviour, and identify devices operational limitations, the mathematical modelling was performed. The fluiddynamics modelling was carried out in COMSOL Multiphysics 5.0 software. It is one of the most inclusive software used for the CFD computation due to its wide range of applications. It possesses relatively straightforward user interface and allows customizing the model. Additionally, it is compatible with AutoCAD and CleWin softwares that facilitate importing of complicated geometries.

2.2.1. Mathematical model

In order to describe the flow of blood along the designed microchannel, laminar flow adapted for blood inside the liquid chamber geometry has been considered. The momentum conservation for laminar flow of incompressible fluids (eq. 2.1) together with mass conservation (eq. 2.2) were solved:

$$\rho(\mathbf{u} \cdot \nabla)\mathbf{u} = \nabla \cdot \left[-p\mathbf{I} + \mu(\nabla \mathbf{u} + (\nabla \mathbf{u})^T) - \frac{2}{3}\mu(\nabla \cdot \mathbf{u})\mathbf{I} \right] + \mathbf{F} \tag{2.1}$$

$$\nabla \cdot (\rho \mathbf{u}) = 0 \tag{2.2}$$

Where, ρ is the blood density (1060 kg/m^3), $\mathbf{u}$ stands for the flow velocity vector field, p is the pressure, μ is the blood viscosity (0.0035 Pa·s), superscript T is transposed of a matrix, and F is a source term.

In equation 2.1 the terms on the left side are acceleration forces, and on the right side, there are pressure gradient and viscous forces. Following assumptions have been made:

1. No slip conditions, on the walls of the liquid chamber geometry, $\mathbf{u} = 0$

2. No back-flow permitted

3. The flow direction was defined as normal to the chamber inlet and outlet

4. The outlet pressure was set as the atmospheric one

The set of governing equations was solved using a finite volume method for different microdevice geometries presented in the following sections. The convergence criterion was based on the residual error in the momentum equation, which was set to 10^{-3}.

2.2.2. Alveolar design

In this section, two different alveolar designs are presented and discussed, considering possible advantageous and limitations of each. The results of the computational fluid dynamics model inside the liquid chamber are shown and discussed.

Generally, artificial lungs in the form of a microfluidic device consist of two chambers, where one is dedicated to gas and the other to blood, separated by a thin permeable membrane. In such arrangement, pure oxygen is introduced to the gas side of the chip, permeates through the membrane and diffuses into blood (one side gas diffusion), first as dissolved oxygen and then bounded to haemoglobin. As it was discussed in Chapter 1, the oxygen delivery increases linearly with the blood flow, indicating that mass transfer limitations occur in the blood side [20, 102], thus the importance of the proper design of the blood chamber geometry is of crucial importance. The combination of optimized haemodynamics with physiological blood flow and biocompatible material will diminish the risk of thrombus formation which will result in less amount of anticoagulant that must be added to blood.

The first alveolar design, AD1, is based on the liquid side geometry reported previously by the group of Borenstein [100, 104]. It is comprised of branching liquid channels with a depth of approximately 100 μm. The structure consists of a big entrance, i.e. 2 mm wide, 4 main branches with 8 identical single small units in each branch. Each unit possesses set of parallel and perpendicular channels with 50 μm and 100 μm in diameter (Figure 2.1).
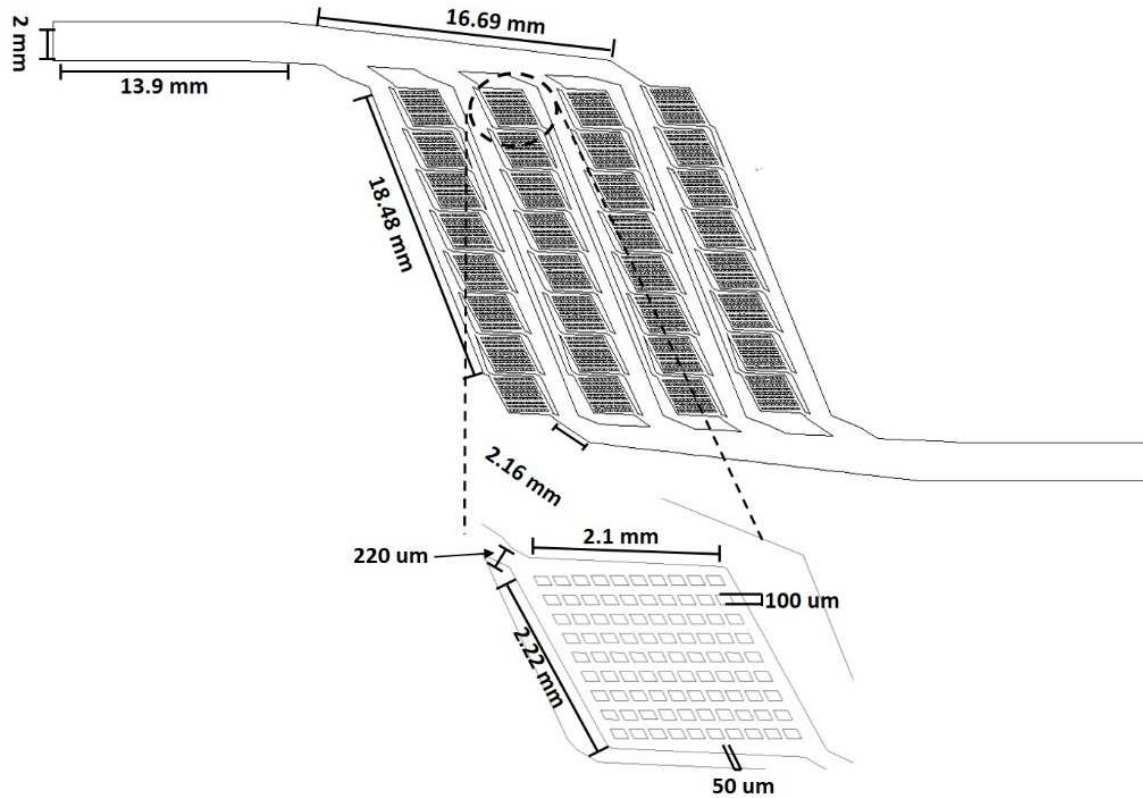
Figure 2.1 AD1 scheme + magnification of a single unit

The computational model described above was performed in order to calculate the shear stress and pressure drop and to visualize the liquid flow path at different liquid flow rates. The size of the mesh used in the simulation was chosen on the basis of computational cost and reproducibility of hydrodynamic results. On this regard, the computational domain was discretized by more than 160 000 triangular elements defining a structured mesh with an edge length in the range 0.3-0.0016 cm. An "opening" boundary of the outlet was applied, which means that the outlet of the structure was opened and the blood was not accumulating inside the chip. The velocity, pressure and shear stress distribution for the entire geometry as well as for the single unit for 1 mL/min blood flow rate are presented in Figure 2.2. The chosen single unit for all the mathematical modelling was the first unit in the first branch of the entire structure. This unit was the most affected one in terms of the highest ΔP and shear stress.
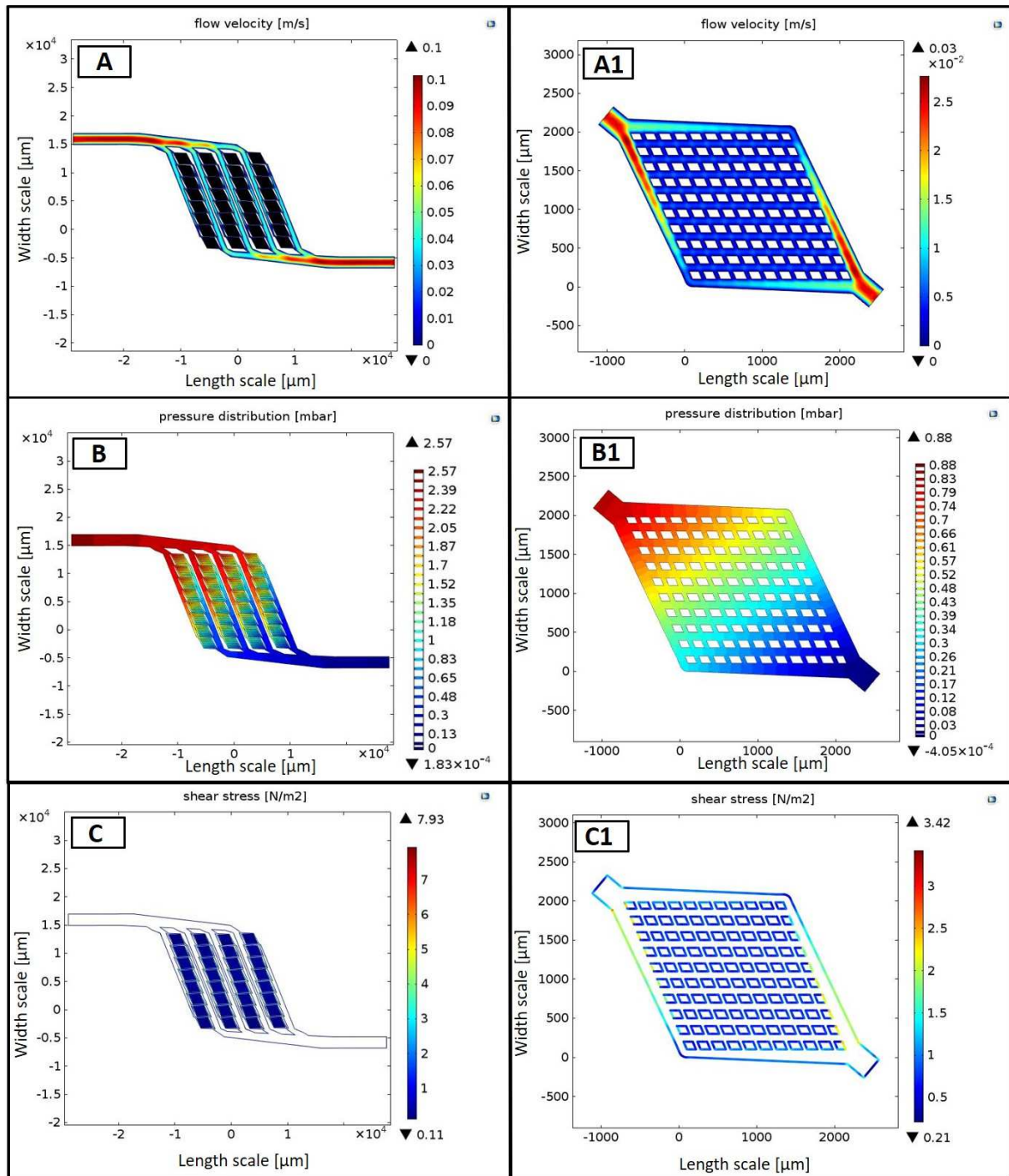
Figure 2.2 Mathematical computation results of A) flow velocity, B) pressure drop and C) shear stress for a —— blood flow rate 1 mL/min. A1, B1 and C1 represent the magnifications of single units

The pressure drop and shear stress at 1 mL/min blood flow rate was equal to 2.57 mbar and 7.93 N/m^2, respectively (see Figure 2.2 B and Figure 2.2 C). However, due to the various dimensions of the perpendicular and parallel channels in a single unit, i.e. 50 μm and 100 μm diameter (see Figure 2.1), the liquid flow distribution lacked some homogeneity that could, eventually result in preferential pathways. Furthermore, elevated ΔP due to accumulation in some zones of the structure and high shear stress is observed in the simulations. This could then

lead to thrombus formation, red blood cells deformation or device ruptures and cracks. As it was discussed in Chapter 1, the consideration of mutual interaction among various parameters is the key factor in the design of the blood oxygenator in the form of a microdevice. In the single unit of the alveolar structure presented, the difference between the highest and lowest flow velocity is approximately 20%. However, the parameter which establishes the homogenous flow distribution is the liquid flow profile. The objective is to obtain the highest flow across the entire unit with the lowest flow velocity located nearby the unit walls. This is clearly not the case in AD1 structure.

Therefore, it was decided to start modifying the single unit design. The target of the proposed modifications was to decrease ΔP and shear stress of the liquid chamber keeping high level of oxygen transfer rate at the same time. A variety of computer simulations with different single unit conformation were performed. Basically, the single perpendicular and parallel channels were removed and flow distributors were incorporated into the reservoir of a single unit. The following variables were taken into account: 1) shape and dimensions of the reservoir, 2) flow distributors shape and size, 3) spacing among them and 4) position. Sometimes, even tough, the pressure drop in the proposed structure was small enough, the shear stress was high and the liquid was not well distributed. Hence, the balance among these parameters had to be considered. As an example, Figure 2.3 shows the pressure drop distribution at 1 mL/min blood flow rate for some of the proposed single unit structures.
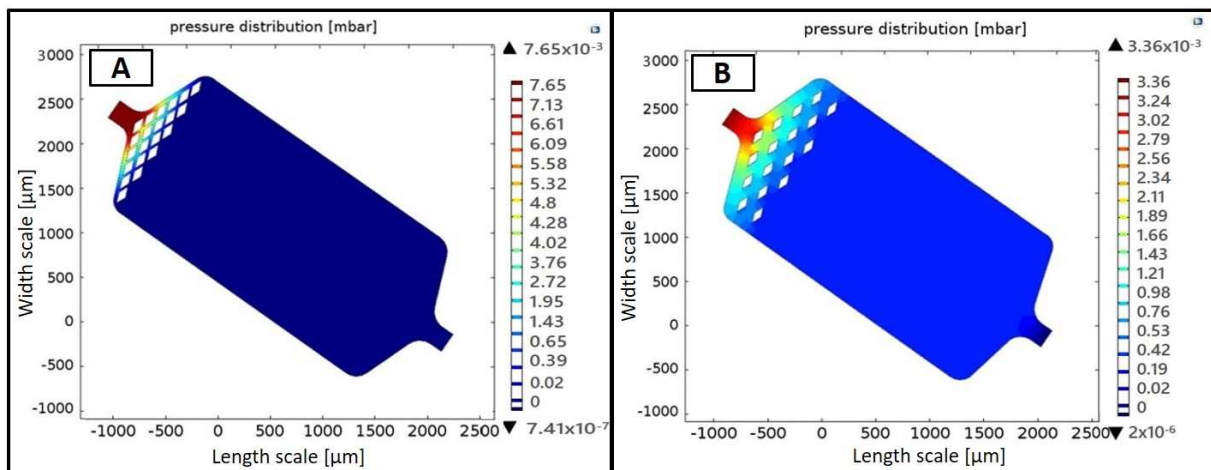
Figure 2.3 Simulation results of pressure drop of AD2 single unit with two different conformations

The calculated values, i.e. 7.65 mbar and 3.36 mbar for structures presented in Figure 2.3 A and B, respectively, are even higher that those previously shown for AD1 design, i.e. 2.57 mbar. High values of ΔP in Figure 2.3 A are related to the big amount of flow distributors which were placed too close to the inlet of the unit and were separated from each other only by 20 µm

spacing. Liquid did not have enough space to circulate through the reservoir; instead it had to enter very small channels which dramatically elevated the pressure. On the other hand, the spacing among the diamonds presented in Figure 2.3 B is much bigger, i.e. 100 μm. This decreased the pressure by approximately a half. Nevertheless, ΔP presented in this unit is still higher than in the AD1 design. This is due to the dimensions of the reservoir, which seem to be too narrow, and the angle of the tapered channel transition at the inlet, i.e. wall inclination (approximately 100°). The lower value of such angle is, the bigger transition of the flow which results in elevated ΔP. As a result of these computer simulations, it was decided to increase the width of the single unit reservoir from 1450 μm to 1700 μm and to elevate the angle of the tapered channel transition from 100° to 130°.

Figure 2.4 shows the computer simulation of the single unit slightly bigger in size, 15% higher, and with bigger angle of wall inclination at the inlet, i.e. approximately 130°, in comparison to the previously shown (100°) with liquid flow distributor at the inlet and outlet, i.e. mirror effect. The calculated pressure drop at 1 mL/min blood flow rate is significantly lower, i.e. 1.82 mbar (see Figure 2.4). Furthermore, identical structure with the flow distributors only at the inlet was simulated as well, resulting in slightly reduced pressure drop, therefore the idea of the mirror diamond effect was abandoned.
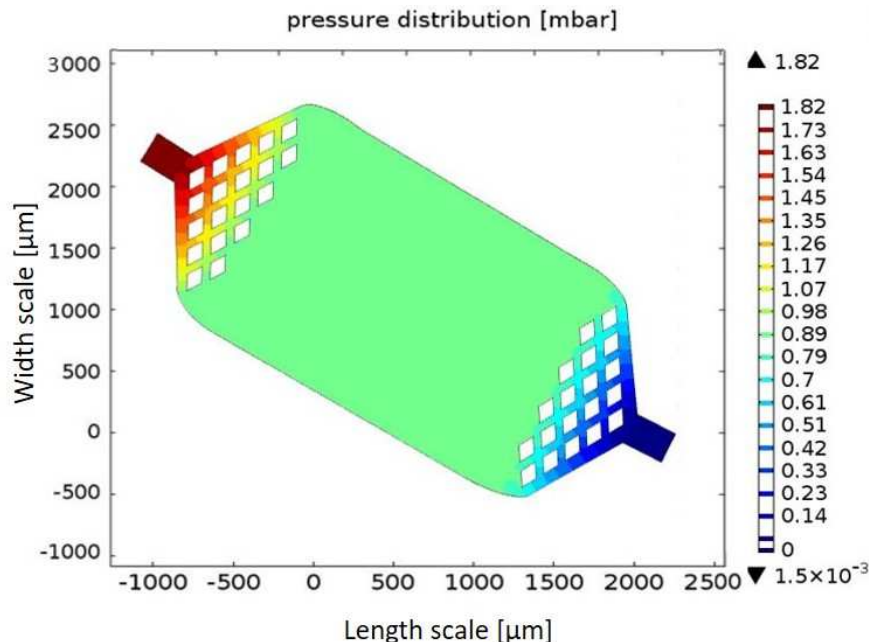
Figure 2.4 Mathematical computational results of pressure of a single unit design with flow distributors at the inlet and outlet

Table 2.1 summarizes the different computer simulations performed with AD2 type design in order to identify the most adequate structure for blood oxygenation testing. Accordingly,

Design 5 was chosen as the final single unit architecture that was placed inside the entire geometry of AD2 chip (see Figure 2.5 and Figure 2.6 B1 for ΔP simulation).

Table 2.1 *Simulation results of pressure drop and shear stress of different single unit for AD2 type design*

Design	ΔP single unit [mbar]	Shear stress [N/m^2]	Remarks
1	7.65	28.2	Small spacing among distributors (20 μm); flatter diamond shape, approx. 100° inlet angle
2	3.36	8.25	Bigger spacing (100 μm), more convex diamond
3	1.82	6.62	Double side distributors; bigger reservoir; 50 μm spacing, approx. 130° inlet angle
4	1.22	6.37	The same as design 3, but one side flow distributors
5	**0.64**	**4.7**	**130 μm spacing, 130° inlet angle, curved angles-Chosen structure**

The selected AD2 type architecture obey the bifurcation theory introduced by Murray [39] which states that the channels for liquid flow should possess equal width and depth (i.e. 100 μm) so the liquid can be dispersed in a homogenous way.

The liquid flow velocity, pressure drop and shear stress for the new proposed geometry were simulated as it was described in case of AD1 geometry. The final mesh used in COMSOL simulations consisted of more than 780 000 triangular elements defining a structured mesh with an edge length in the range 0.4-0.0017 cm.

The graphical representation of such modelling for 1 mL/min blood flow rate is presented in Figure 2.6 It is clearly visible that the pressure drop was significantly reduced by approximately a half (2.57 mbar for AD1 and 1.3 mbar for AD2). This is mainly due to the removal of horizontal and vertical channels. The pressure drop obtained mathematically is way below the limit of a thrombus formation, i.e. 26.6 mbar (see Chapter 1). Moreover, shear stress decreased as well from 7.93 N/m^2 in case of AD1 to 5 N/m^2 in AD2.
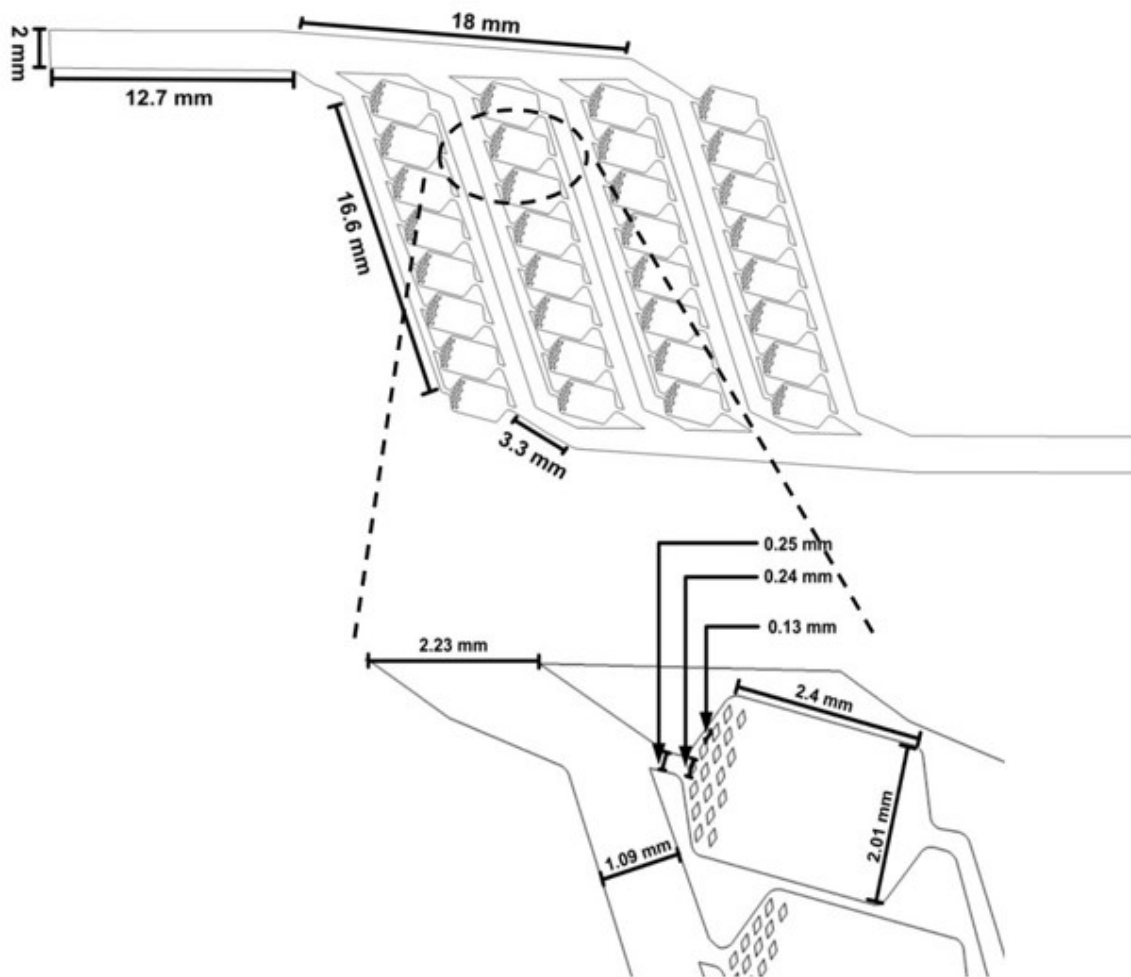
Figure 2.5 AD2 scheme + magnification of a single unit

The mathematically modelled results underline the benefits of AD2-type design which improves such a structure by minimizing the pressure drop inside the liquid chamber. This is a key factor to avoid deformation and/or destruction of red blood cells, leading to the non-physiological blood flow. In both designs, a number of supporting pillars was added to the gas chamber to avoid membrane collapsing and to increase the mechanical stability of the chips. Table 2.2 shows the comparison of simulated parameters for the liquid flow rate in the range of 1-5 mL/min for the two designs, i.e. AD1 and AD2, respectively.
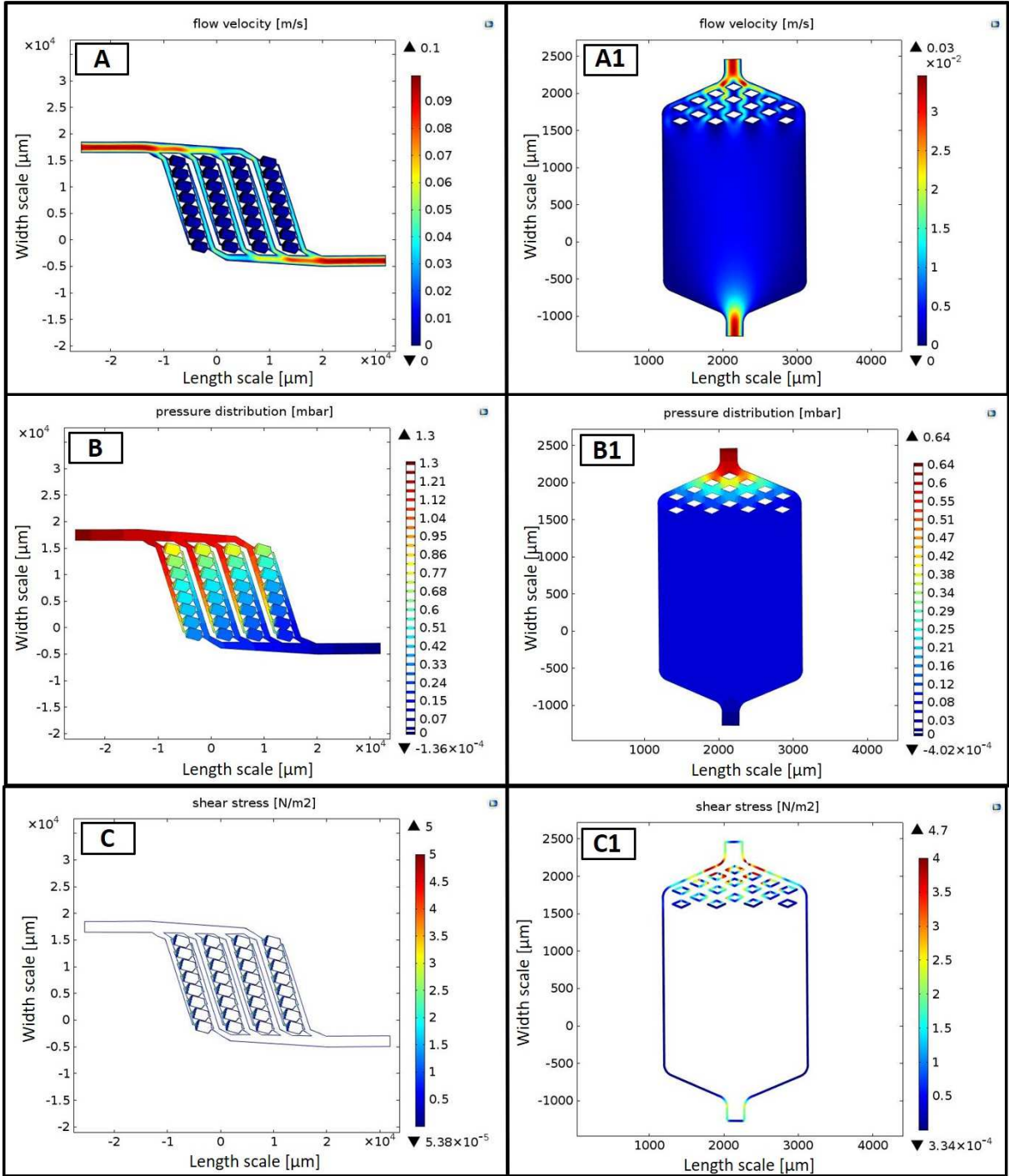
Figure 2.6 Mathematical computation results of A) flow velocity, B) pressure drop and C) shear stress for a blood flow rate 1 mL/min. A1, B1 and C1 represent the magnifications of single units

Table 2.2 *Mathematically modelled results of pressure drop and shear stress of an entire geometry for AD1 and AD2 type designs*

	Blood flow rate [mL/min]	ΔP [mbar]	Shear stress [N/m^2]
Alveolar Design 1	1	3.08	6
	2	6.19	11
	3	9.2	16.4
	4	12.3	22.8
	5	15.4	29
Alveolar Design 2	1	1.57	5
	2	3.16	8.7
	3	4.6	13.2
	4	6.25	18.1
	5	7.8	23.7

The pressure drop and shear stress are not the only parameters affecting the performance of the chip. For a given blood rate, the oxygen saturation mainly depends on the membrane surface area, channel depth and chamber volume. Moreover, our target is the market devoted to neonates, hence low priming volumes as well as compact systems are anticipated. Table 2.3 shows the main parameters of the two alveolar designs that have been fabricated and tested for blood oxygenation.

Table 2.3 *Main parameters of the proposed alveolar-type liquid side geometries*

Alveolar design	Membrane thickness, δ [μm]	Membrane Area, SA [cm^2]	Gas/liquid channel depth [μm]	Chip footprint [cm^2]	Liquid volume[1] [μL]
AD1	120	2.8	100	18.7	28
AD2		3.9			39

[1] similar to priming volume

It is visible that the membrane surface area increased by approximately 40% in AD2 in comparison to AD1 resulting in higher S/V ratio and liquid volume. The membrane thickness as well as the channel depth values were kept equal for both designs.

2.2.3. Meander design with vertical membrane arrangement

Meander design (MD) with vertical membrane arrangement is an alternative configuration for the microfluidic device. This approach consists of a single "mixed" PDMS microfluidic platform comprising a series of meandering flow channels for liquid as well as for a gas, in which the adjacent liquid and gas channels are separated by a dense vertical membrane.

The innovative idea of a vertical membrane chip design relies on the ability to deliver oxygen to blood from both sides of the liquid channel. This approach is also called double side gas diffusion (see Figure 2.7).
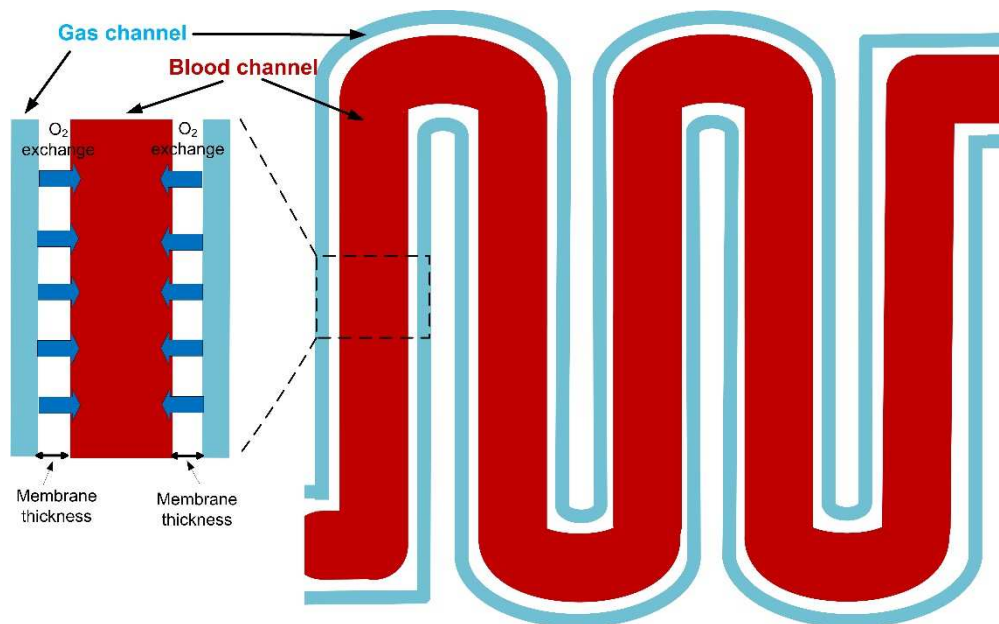
Figure 2.7 Schematic representation of the meandering channels arrangements

In the proposed design, the liquid chamber (red colour) is surrounded by gas channels (blue colour) from both sides. Each meander unit consists of two length section and two half circular lengths of the liquid channel on both sides of a membrane. The total surface area for gas exchange is thus the lateral area of one meander unit multiplied by the number of units and the number of branches. The distance between the gas channel and the liquid channel filled with PDMS is the actual membrane thickness. Gas contact area depends on the depth and the length of the channels. For this reason, the larger channel depth is beneficial. The entire PDMS structure is closed by the glass slide at the bottom. This new idea offers many advantages. Firstly, the presented configuration is clearly valuable due to simplified fabrication process which does not require any separate fabrication of the membrane and peeling off the film of the silicon wafer as it is commonly used in the microfabrication of artificial microfluidic oxygenators [26]. Considering that the oxygen transfer comes from the sides of the channel

71

instead from the top of it, narrowing of the liquid channel will increase the O_2 transfer rate and will decrease the actual dimensions of the chip because the same surface area will be loaded in the smaller chip footprint.

In order to increase the surface for gas exchange it was decided to design a chip with various numbers of branches and meandering units. Moreover, in the meandering arrangement, all the liquid channels possess equal width and length. Thus, it was important to "force" the liquid to enter all the branches with the same velocity. Therefore, each branch possessed a small "loop" at the entrance of each branch in order to force the liquid to follow the same distance and as a result to enter all the branches with the same flow velocity. The same procedure was repeated at the outlet of the geometry in order to make the structure symmetric.

Three distinctive designs were proposed with 9 branches and various number of meandering units. Additionally, different liquid channel width was proposed. Generally, the wider the channels the lower the pressure drop and shear stress in the geometry for a given flow rate; but on the other hand, the narrower the channel the higher the number of liquid channels than can be "packed" in the same chip footprint resulting in a higher gas-liquid contact area. Additionally, thinner liquid channel ensures lower distance for oxygen diffusion to fully oxygenate blood. Moreover, the highest values of the shear stress were present in the half circular lengths as well as at the inlet and outlet. Thus, it was decided to increase the dimensions of the inlet. The final mesh for COMSOL simulations consisted of more than 40 000 elements triangle defining a structured mesh with an edge length in the range 0.04-0.005 cm. The boundary conditions were set equal to the simulation performed for both alveolar arrangements. Table 2.4 shows computational results of pressure drop and shear stress at 1 mL/min liquid flow rate in case of three different designs with various liquid channel width.

Table 2.4 *Simulation results of a pressure drop and shear stress of different meander designs for 1 mL/min blood flow rate*

Design	Liquid channel width [μm]	Liquid volume [μL][1]	ΔP [mbar]	Shear stress [N/m²]
1	200	36.02	66.4	6.7
2	300	47.77	42	5
3	**400**	**57.62**	**16.9**	**3.42**

[1] similar to priming volume

The structure which was finally chosen (Design 3) possesses liquid channel width of 400 μm, gas channel width of 100 μm and the spacing in between (the membrane thickness) of 120 μm.

Microfluidic devices for blood oxygenation

It is made of 19 meandering units and 9 branches loaded on a surface of 35.04 cm² of the total chip footprint with the membrane surface area of 2.9 cm². Figure 2.8 shows the results of the computer modelling for (A) liquid flow velocity, (B) pressure drop and (C) shear stress, respectively at 1 mL/min blood flow rate.
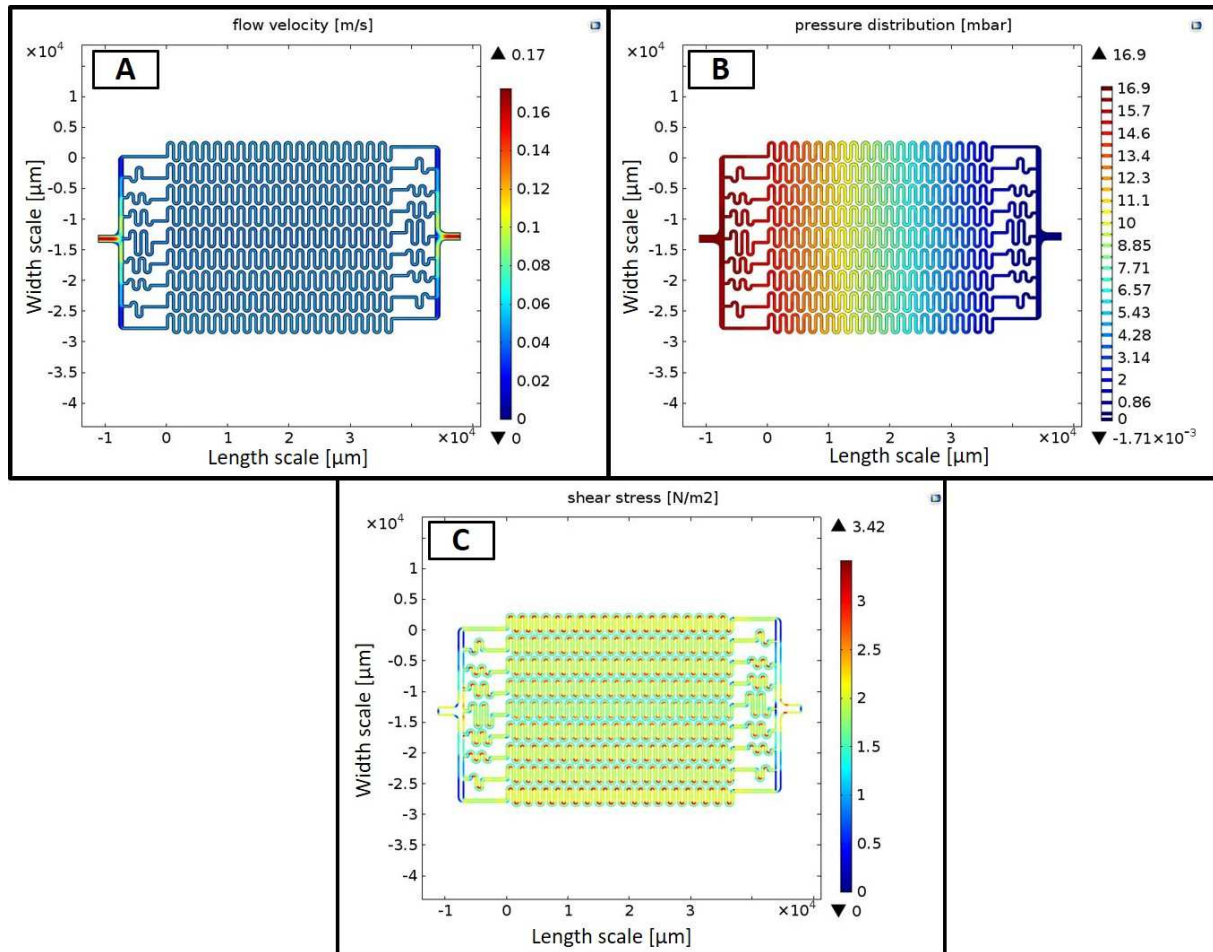
Figure 2.8 Computer modelling results of the meander design of A) liquid flow velocity, B) pressure distribution and C) shear stress

As a result of the flow distributors, the liquid transportation was homogenous which means that the total surface area of the membrane was used, i.e. no dead volume was observed.

Table 2.5 Main parameters of the proposed meander vertical-type geometry

Memb thick., δ [um]	Memb Area, SA [cm²]	Liq. channel width [um]	Gas channel width [um]	Gas/liq channel length [mm]	Gas/liq channel depth [μm]	Liq vol[1) [uL]	Chip footprint [cm²]
120	2.9	400	100	2	100	58	35.0

[1) similar to priming volume,

2.3. Mathematical model for blood oxygenation

After the microfluidic geometries were designed and tested, the mathematical model for blood oxygenation was developed and validated by comparison to the experimental data.

2.3.1. Haemoglobin: oxygen binding protein – structure and properties

Prior to the description of the experimental procedure of blood oxygenation, it is important to understand the structure of haemoglobin and all the processes and modifications that can occur. Haemoglobin (Hb) is the oxygen – binding protein, which enables the red blood cells (RBC) to transport more oxygen. Hb is remarkably efficient in carrying oxygen. It is able to use as much as 90% of its oxygen-carrying capacity due to its structure [105, 106]. Haemoglobin possesses a quaternary structure typical for many multi-subunit globular proteins comprised of four polypeptide chains, two of them called the α chains and the other two named the β chains, attracted to each other by hydrogen bonds. The four polypeptide chains bind oxygen cooperatively, i.e. binding of O_2 to a site in one chain increases the probability of binding oxygen to the remaining chain. The ability of haemoglobin, to bind oxygen depends on the presence of a bound prosthetic group called heme. Figure 2.9 represents the chemical structure of the heme group.
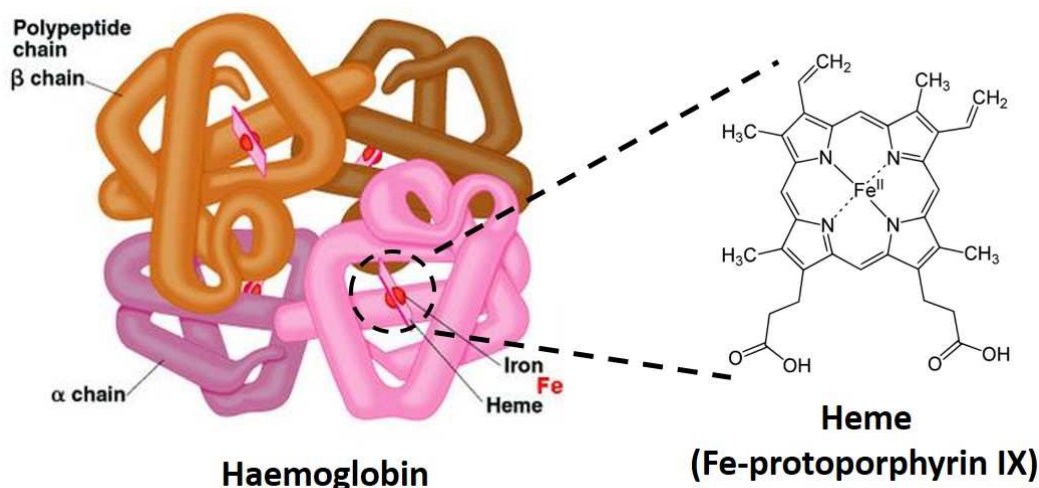
Figure 2.9 Chemical structure of Haemoglobin and Heme group. Figure adapted from [105]

The heme group is responsible for characteristic red colour in muscles and blood. It consists of a central iron atom and an organic component called protoporphyrin. Protoporphyrin is made of four pyrrole rings connected by methane bridges in order to form a tetrapyrrole ring. Heme group also contains of two vinyl groups, four methyl groups, and two propionate side chains. They are well separated by iron-iron distances ranging from 24 to 40 Å [105, 107, 108].

Moreover, the chemical structure of heme group is related to the process of binding oxygen. Figure 2.10 demonstrates the modification of the heme group in case of A) deoxyhaemoglobin and B) oxyhaemoglobin. In case of deoxyHb the iron is placed slightly outside the porphyrin plane while it moves into the plane of the heme in the case of oxyHb. $\alpha1\beta1$ and $\alpha2\beta2$ dimers are easier to move with respect to one another in the oxygenated state than they are in the deoxygenated state. The quaternary structure observed in the deoxy form of Hb is often referred to as the highly unstable T (for tense) state because it is quite constrained by subunit-subunit interactions. The quaternary structure of the fully oxygenated form is named as the R (for relaxed) state. In the R state oxygen-binding sites are free of strain and are capable of binding oxygen with higher affinity than are the sites in the T state. In order to haemoglobin works efficiently it is required that the T state remain stable until sufficient amount of oxygen is bonded and thus converted it to R state [105, 109].
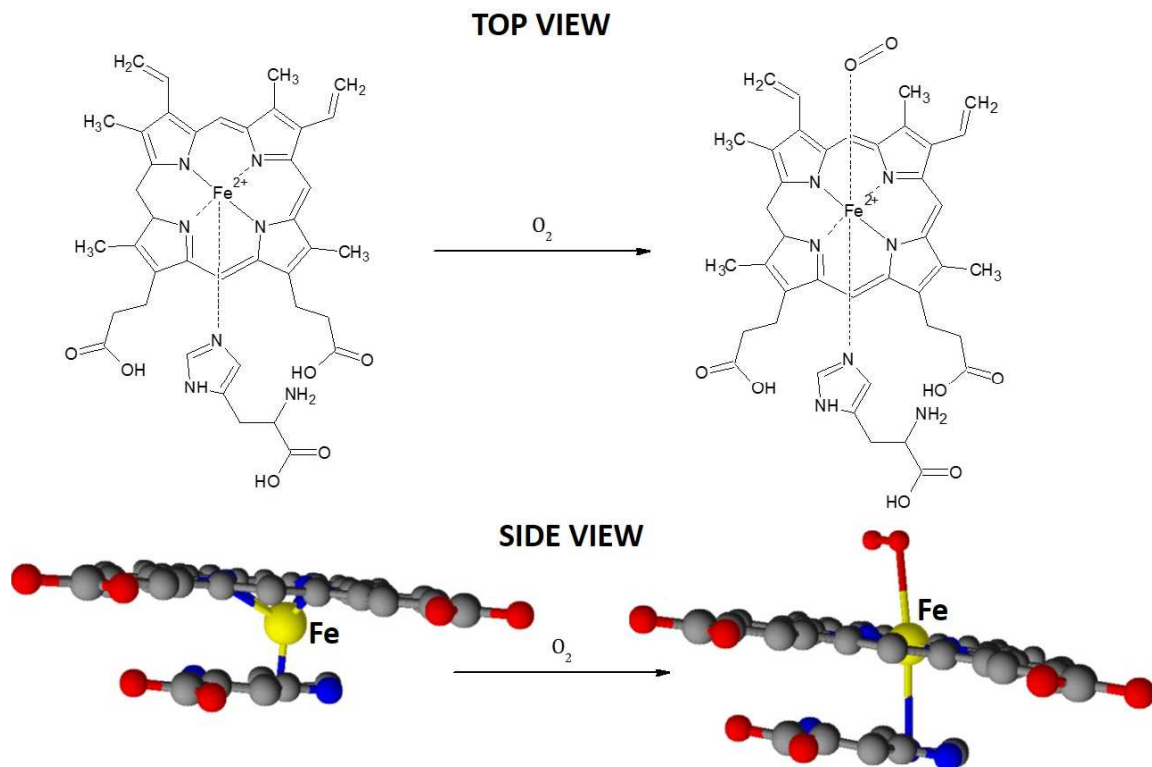
Figure 2.10 Oxygen binding modifies the position of the iron ion in A) deoxyHb and B) oxyHb

2.3.2. Oxygen transport in blood

For purposes of discussing oxygen transport in the blood, it is considered to be composed of two phases: plasma and red blood cells (RBCs). Oxygen is carried in the blood in two forms: dissolved in plasma, denoted as C_{dO2}; and reversibly bounded to haemoglobin (Hb), denoted as C_{O2}.

The oxygen-binding characteristics of Hb are illustrated by an oxygen-binding curve, known as the Hill's curve [110]. The common expression of this equilibrium relationship is the following:

$$S_{O2} = \frac{\left(\frac{P_{O2}}{P_{50}}\right)^n}{1 + \left(\frac{P_{O2}}{P_{50}}\right)^n} \tag{2.3}$$

Where: S_{O2} is the fractional oxygen saturation, P_{O2} is the partial pressure of dissolved oxygen, n is the number of binding sites of haemoglobin (called the Hill coefficient) [-]; and P_{50} is the partial pressure of oxygen when blood is 50% saturated; 26.6 [mmHg] (at 37°C, pH of 7.4 and P_{CO2} of 40 mmHg).

The concentration of oxygen is most conventionally measured by its partial pressure, P_{O2} [105, 106]. Considering that the concentration of dissolved oxygen in the blood, C_{dO2}, is directly proportional to the partial pressure of oxygen, Henry's law could be used for its calculation [106]:

$$c_{dO2} = \alpha \cdot P_{O2} \tag{2.4}$$

Where, α is the solubility coefficient of O_2 in blood.

The fractional saturation of blood, S_{O2}, is described as the fraction of possible binding sites that contain bound oxygen. From S_{O2}, the values of the haemoglobin concentration in blood, [Hb], and the oxygen binding capacity of Hb, denoted as Hbs, the oxygen concentration bound to Hb is calculated as follows:

$$C_{O2} = S_{O2} \cdot [Hb] \cdot Hbs \tag{2.5}$$

If the saturation of blood with oxygen is lower than approximately 80%, the hypoxemia is formed due to the deficiency of O_2 in arterial blood which causes respiratory disorders or damage of the vital tissues.
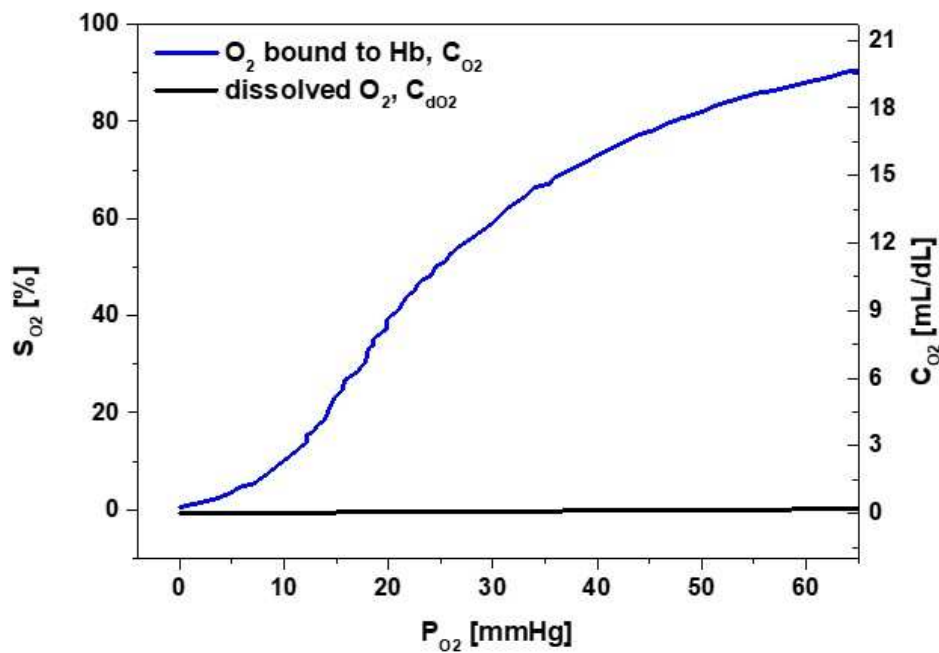
Figure 2.11 Oxygen transport by blood at 37°C and pH of 7.4

Figure 2.11 comparatively shows the oxygen bound to Hb, expressed as fractional saturation, and the oxygen dissolved in plasma as a function of the oxygen partial pressure at 37°C and pH of 7.4. It is clearly seen from the Hill's curve that the concentration of dissolved oxygen in comparison to bound oxygen is negligible.

The sigmoid shape of Hill's curve indicates that Hb shows a special binding behaviour, i.e. the binding of oxygen at one site increases the likelihood that oxygen binds at the remaining unoccupied location. Conversely, the unloading of oxygen at one heme facilitates the unloading of oxygen at the others [105].

There are several factors influencing the efficiency of oxygen transport in haemoglobin, mainly: pO_2, temperature and pH.

Firstly, the partial pressure of oxygen plays a key role in the binding O_2 to Hb. Oxygen is transported in the blood from the lungs, where the pO_2 is quite high, approximately 100 mmHg, to the actively metabolizing tissues, where the pO_2 is much lower, typically 20 mmHg. In the lungs, Hb becomes nearly saturated with O_2 such that approximately 98% of the oxygen-binding sites are occupied. However, immediately upon Hb moves to the tissues and releases O_2, the saturation level drops down to 32%. Thus, a total of 98 − 32 = 66% of the potential oxygen-binding sites contribute to the gas transport.

Another factor affecting the O_2 affinity to bind to Hb is so called the Bohr effect which is the regulation of oxygen binding by hydrogen atoms and CO_2. The oxygen affinity of Hb

decreases with the reduction of pH starting from a value of 7.4. Moreover, as haemoglobin moves into a region of lower pH, its tendency to release O_2 rises. For instance, 77% of oxygen is released when it is transported from lungs, pO_2 of 100 mmHg and pH 7.4, to active muscle, pO_2 of 20 mmHg with a pH of 7.2. However, only 66% of the oxygen would be released in the absence of any change in pH. Two sets of chemical groups are responsible for the pH effect: 1) the α-amino groups and 2) side chains of histidines: β146 and α122, all of which have pKa values near pH 7 [105, 111-113]. Figure 2.12 shows the influence of the pH on the oxygen affinity to haemoglobin.
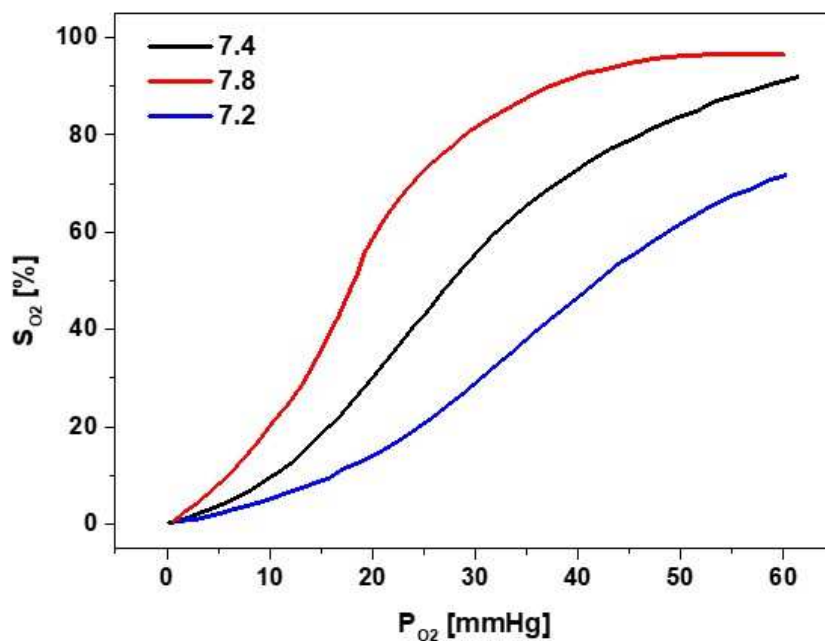
Figure 2.12 Oxygen-haemoglobin dissociation curve as a function of pH

On the other hand, human lungs work as a gas exchange organ, thus there is not only an exchange of oxygen but also carbon dioxide plays a significant role. Carbon dioxide passes through the RBC membrane into the red cell and it stimulates oxygen release by two mechanisms: 1) the presence of high concentrations of CO_2 leads to the drop of H^+ atoms within the RBC, and 2) a direct chemical reaction between CO_2 and Hb that creates carbamates [105]. The visual representation and the explanation of the transport of CO_2 from tissues to lungs is presented in Figure 2.13.

Microfluidic devices for blood oxygenation
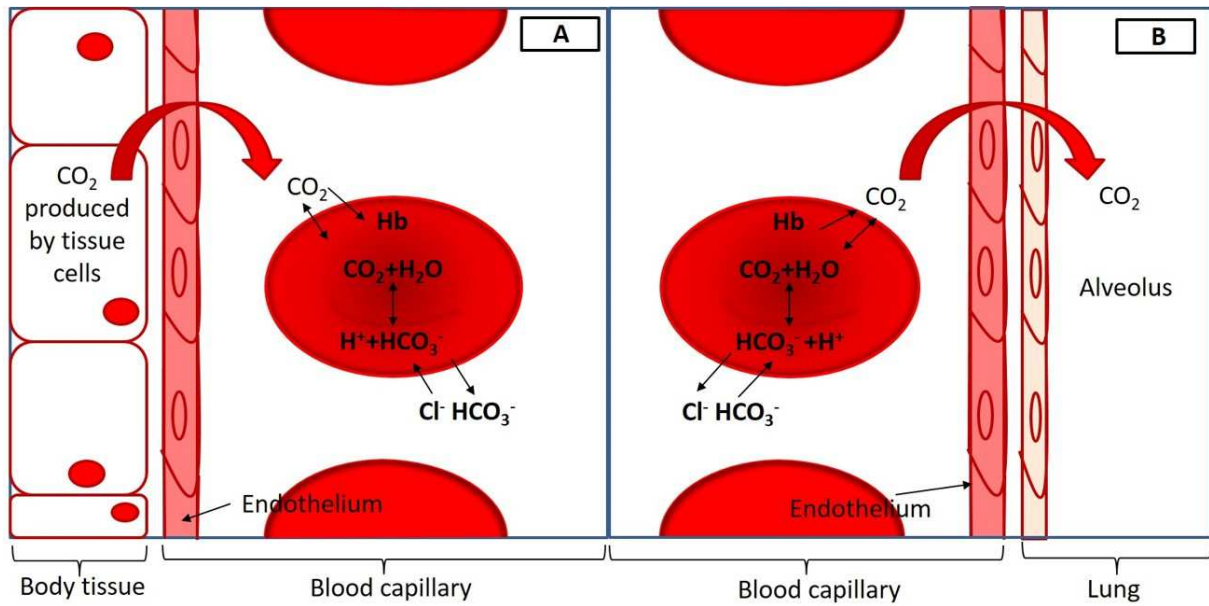
Figure 2.13 Transport of CO_2 from A) tissues to B) lungs. The biggest amount of CO_2 is transported to the lungs in the form of bicarbonate which is produced in RBC and next is released into blood plasma. Smaller amount is transported by Hb as attached carbamate

Another factor influencing the oxygen affinity to Hb is the temperature. Increasing the temperature of Hb decreases its affinity to oxygen and shifts the oxygen-binding curve to the right [113]. The influence of temperature on the oxygen-binding curve is presented in Figure 2.14.
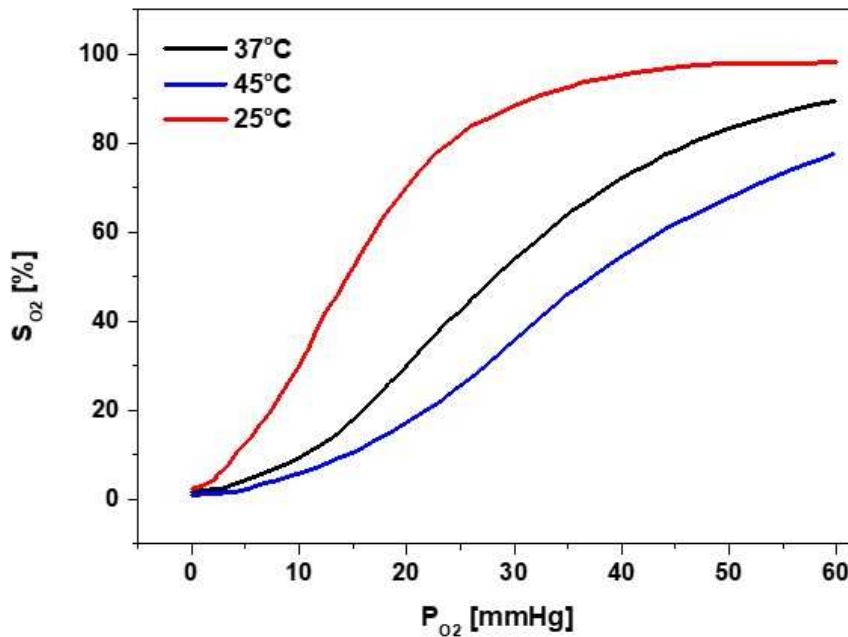
Figure 2.14 Oxygen-haemoglobin dissociation curve and the influence of temperature on the pO_2 and its corresponding saturation

2.3.3. Mathematical equations and development of a model

In addition to the velocity profile solving (described earlier in section **Błąd! Nie można odnaleźć źródła odwołania.**), the mass balance and transport equation for oxygen species in blood was developed from a standard convection-diffusion mass transfer expression [110, 114, 115]:
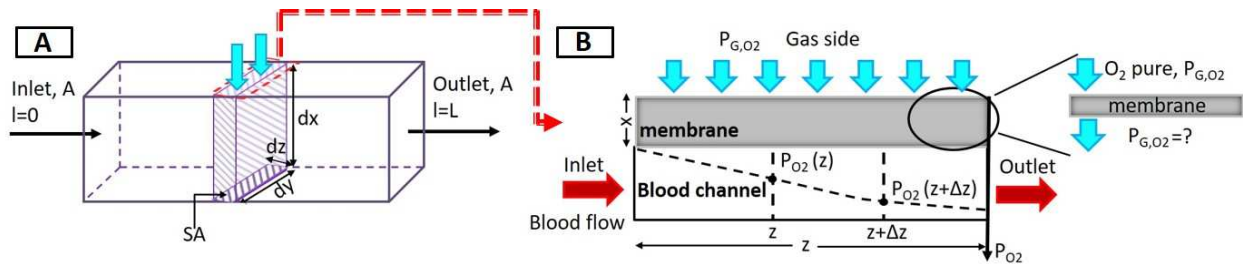
Figure 2.15 Schematic representation of the A) Cartesian control volume for the derivation of the species conservation equation, and B) boundary conditions in the alveolar system

The conservation of a mass balance in the controlled volume can be written as:

$$\sum J_D + \sum J_C = \sum J_\Delta \tag{2.6}$$

Where, J_D is the mass transfer by diffusion, J_C is the mass transfer by convection, and J_Δ is the rate of mass production.

Each term can be derived as follows:

$$J_D = Deff \cdot \nabla^2(\alpha P_{O2})dxdydz \tag{2.7}$$

$$J_C = -\mathbf{u} \cdot \nabla(\alpha P_{O2})dxdydz \tag{2.8}$$

Substituting equations 2.7 and 2.8 to 2.6, dividing and rearranging terms:

$$\alpha \cdot D \cdot \nabla^2 P_{O2} - \mathbf{u} \cdot \alpha \nabla P_{O2} = \alpha \frac{\partial P_{O2}}{\partial t} \tag{2.9}$$

Under steady state, it becomes:

$$\mathbf{u} \cdot \alpha \nabla P_{O2} = \alpha \cdot Deff \cdot \nabla^2 P_{O2} \tag{2.10}$$

Microfluidic devices for blood oxygenation

Where, Deff is the effective diffusivity of oxygen in blood which incorporates the effects of haemoglobin. Such effective diffusivity is calculated from the following relations [114]:

$$Deff = \frac{D_b}{1 + \lambda(P)} \tag{2.11}$$

Where, D_b is the O_2 diffusion coefficient in blood and $\lambda(P)$ is the mathematical term developed to account O_2 bound to Hb. It is expressed as a function of [Hb]:

$$\lambda(P) = \frac{[Hb] \cdot S'_{O2}}{\alpha} \tag{2.12}$$

And S'$_{O2}$ can be derived from equation 2.3 as:

$$S'_{O2} = \frac{n(P_{50})^n \cdot P_{O2}^{n-1}}{(P_{50}^n + P_{O2}^n)^2} \tag{2.13}$$

Rearranging the above equations, the effective diffusivity is calculated as follows:

$$Deff = \frac{D_b}{1 + \dfrac{[Hb] \cdot n(P_{50})^n \cdot (P_{O2})^{n-1}}{\alpha(P_{50}^n + P_{O2}^n)^2}} \tag{2.14}$$

When blood enters the microchannel, the partial pressure of dissolved oxygen is low (see Figure 2.15 B). As the blood flows along the PDMS membrane, oxygen diffuses out of the gas side of the chip, across the membrane, and into the blood, dissolving in blood plasma and then diffusing to and into red blood cells and binding to haemoglobin.

The oxygen pressure on the gas side of the device has been considered constant due to: i) its supply is greater than its gas exchange rate, and ii) the resistance to diffusion on the gas side of the device is negligible compared to that of the membrane and blood.

The oxygen diffusing through PDMS membrane, J$_{O2}$, will be subject to Fick's law, such that [115]:

$$J_{O2} = D_m \cdot \alpha_m \cdot \left(P_{G,O2} - P_{O2,wall}\right) \cdot \frac{1}{t_m}$$

$$\tag{2.14}$$

$$J_{O2} = Perm \cdot \left(P_{G,O2} - P_{O2,wall}\right) \cdot \frac{1}{t_m}$$

Where D_m is the diffusion coefficient for oxygen in the PDMS membrane, α_m is the solubility of oxygen in the PDMS membrane, t_m is the thickness of the PDMS membrane, $P_{O2,wall}$ is the

partial pressure of dissolved oxygen at the membrane wall, and $P_{G,O2}$ is the partial pressure of oxygen in the gas side.

According to the oxygen permeation results of our PDMS membranes (see Chapter 3), the product D_m and α_m, also known as permeability (Perm) through PDMS membrane, is $1.49 \cdot 10^{-11}$ $mol \cdot m \cdot m^{-2} \cdot s^{-1} \cdot mmHg^{-1}$. Table 2.6 shows the main constant parameters which are used in the blood oxygenation calculations.

Table 2.6 *Summary of the main blood and oxygen related parameters used in the calculations*

Parameter	Abbreviation	Value	Units
Solubility coefficient of O_2 in blood	α	$1.25 \cdot 10^{-3}$	$mole_{O2} \cdot m^{-3}_{blood} \cdot mmHg^{-1}$
Diffusion coefficient of O_2 in blood	Db	$1.8 \cdot 10^{-9}$	$m^2 \cdot s^{-1}$
Number of binding sites of Hb	n	2.7	-
Partial pressure of O_2 at 50% blood saturation	P50	26.6*	mmHg
O_2 binding capacity of Hb	Hbs	$1.39 \cdot 10^{-6}$	$m^3 \cdot g^{-1}$
O_2 density	d	1420	$g \cdot m^{-3}$
O_2 molecular weight	M	32	$g \cdot mol^{-1}$
O_2 permeability, PDMS	Perm	$1.49 \cdot 10^{-11}$	$mol \cdot m \cdot m^{-2} \cdot s^{-1} \cdot mmHg^{-1}$

*only at 37°C, pH 7.4 and P_{CO2} of 40 mmHg

2.4. Experimental section

2.4.1. Fabrication process outline

PDMS has been one of the polymers actively developed for microfluidics and prototyping due to its low cost, easy handling, low surface energy and its mechanical properties which facilitate release from moulds. Additionally, it possesses physical and chemical properties (see Table 2.7) which allows device fabrication with useful functionality, thus it is not only a structural material. It belongs to the group of organosilicons, commonly referred as silicones. PDMS consists of a repeating monomer $[SiO(CH_3)_2]$ which appears after the polymerization process [116, 117] (see Figure 2.16).
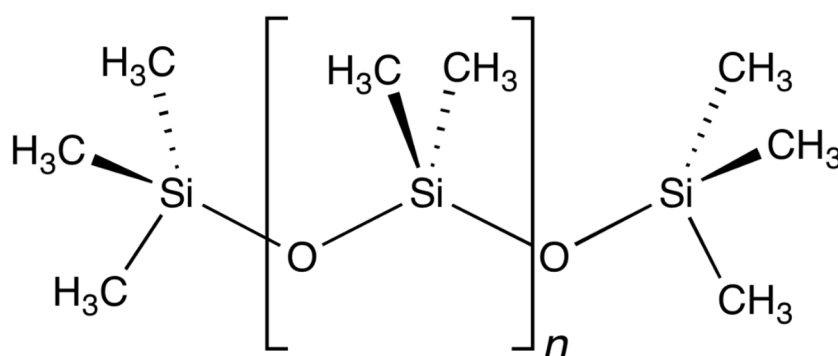
Figure 2.16 Chemical structure of PDMS

Table 2.7 Physical and chemical properties of PDMS with their characteristics and consequences [116, 117]

Property	Characteristic	Effect
Optical	Transparent	Optical detection (240 nm to 1100 nm)
Mechanical	Elastomeric (Young's modulus: 750 kPa)	Conforms to surfaces, allows deformations, easy release from moulds,
Electrical	Insulating	Allows embedded circuits, breakdown voltage $2 \cdot 10^7$ V/m
Thermal	Insulating	Thermal conductivity 0.2 W/(m·K), Can be used to insulate heated solutions
Interfacial	Low Surface Free Energy (20 erg/cm^2)	Easy release of replicas from moulds, can be reversibly sealed to materials
Toxicity	Non-toxic	Can be implanted in vivo, supports cell growth
Permeability	Impermeable to liquid water, permeable to gases	Allows gas transport, incompatible with many organic solvents
Reactivity	Inert; can be oxidized by exposure to plasma	Unreactive towards most reagents; surface can be etched or modified to be hydrophilic

All the above-mentioned properties of the material lead us to select PDMS for the fabrication of the device chambers as well as membrane material.

The fabrication process of two proposed microfluidic PDMS devices, i.e. alveolar-type and meander-type design, is slightly different. In both cases the fabrication involves: 1) chambers construction by replica moulding of rigid masters, and 2) microdevice assembly and attachment. The only difference refers to the PDMS membrane. Alveolar design requires the separate fabrication of the membrane by casting, whereas in meander-type device the membrane is already embedded in the chamber structure.

Chambers construction

The rigid masters for the liquid and/or gas chambers were prepared by standard lithography using SU-8 negative photoresist (SU-8 50 DE MicroChem) as structural layer. 4 in. diameter Si wafers (500±20 um thickness, <100> orientation, "p" doped and resistivity of 5-10 $\Omega \cdot$cm) supplied by Sil'Tronix Silicon Technologies were used. Firstly, the Si wafer was coated with specific SU-8 50 DE MicroChem negative-working photosensitive resist by spin coating at 1250 rpm during 1 min resulting in the thickness of approximately 100 μm. Next, the wafer with the resist was soft baked at 95ºC during 30 min. The photolithography process was carried out on the SU-8 top layer of the wafer to define the chamber geometry. The patterning was transferred from the photomask to SU-8 by exposure to UV (350-400 nm) and post baked at 65ºC during 1 min and later at 95ºC during 10 min. Finally, the patterned structure was developed by immersing the wafer in the developer (SU-8 developer, MicroChem, USA) during 10 min followed by hard baking at 150-200ºC. Next, the entire wafer was silanized by exposure to chlorotrimethylsilane (Sigma Aldrich) vapour for approximately 10 min. This procedure was used for easier removal of PDMS from the patterned SU-8 Si wafer [118]. The schematic view of the lithographical process flow is presented in Figure 2.17.

Next, PDMS prepolymer and curing agent (Sylgard 184 Dow Corning, Midland, MI) were thoroughly mixed in a ratio 10:1 and placed in the degassing chamber. PDMS was poured on the patterned SU8-Si master and placed in the oven at 85ºC for 45 min. The moulds were peeled off from the wafer, cut to the required size and punched for inlet and outlet (TiN Coated Round Punch, Syneo). Fabricated chambers were immersed in the solution of isopropanol (Sigma Aldrich, 99.7%) and placed in the ultrasound bath for approximately 2 minutes in order to remove any possible dust that could be attached to the inside of the channels prior any further procedure (membrane or chamber attachment).
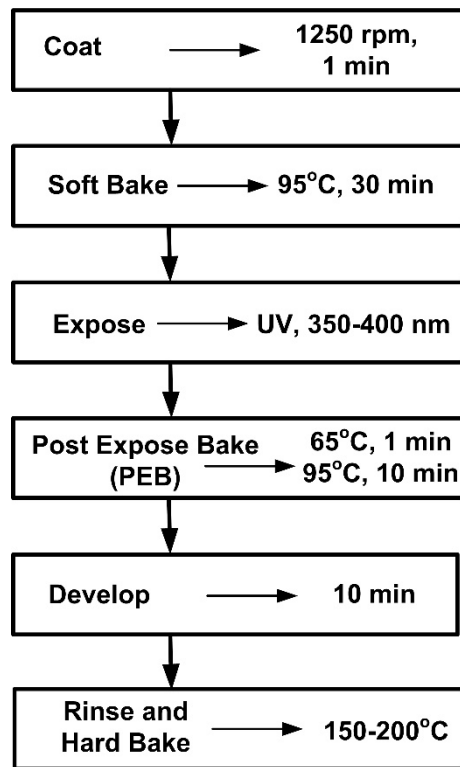
Figure 2.17 SU-8 lithography process flow

2.4.2. Alveolar design device fabrication

Membrane fabrication

The membrane which was integrated in the microdevice was made of PDMS as well. The PDMS membrane was prepared by spin coating (WS-400BZ, Laurell Technologies Corporation Spin Coater) of the PDMS precursor solution on the surface of another wafer at 1000 rpm during 1 min. The so obtained membrane thickness is approximately 120 μm. The Si wafer with the PDMS membrane was placed in the oven at 85°C for approximately 30 min.

Microdevice assembly and attachment

The fabricated PDMS platform dedicated to liquid and the PDMS membrane were placed inside the O_2 plasma chamber (Diener electronic, Plasma-surface-technology) operating at 0.4 mbar, 120 W and 50% of O_2 during 50 sec, in order to activate the surfaces for their subsequent bonding [43]. After the surface was functionalized with O_2 plasma, the PDMS compartment was connected to the membrane and peeled off from the wafer; and finally placed in the oven at 85°C for approximately 1 hour.

The platform dedicated to the gas chamber was prepared following a similar approach. After plasma functionalization, the gas chamber was connected to the membrane-liquid chamber

stack resulting in the three-layer device. The device was placed in the oven again at 85ºC for 1 hour. Figure 2.18 shows the process outline of the whole microdevice fabrication.
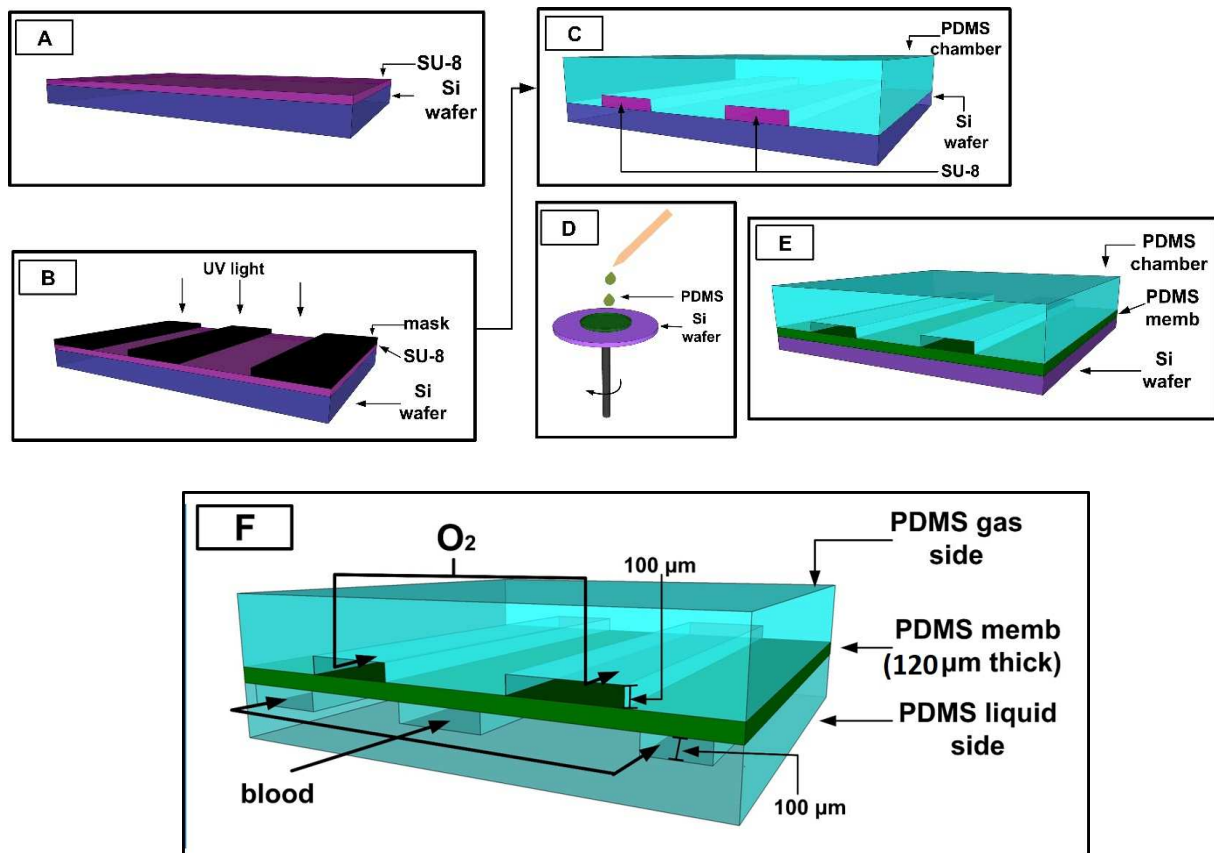
Figure 2.18 Process outline of the microfluidic chip fabrication. Spin coating of the SU-8 negative photoresist on the silicon wafer (A), mask alignment, UV exposure and SU-8 development (B), Pouring of PDMS on a created mould (C) and peeling off after curing. Membrane preparation by spin coating on a silicon wafer (D) and connecting to the PDMS mould by O_2 plasma procedure (E). After curing in the oven, peeling off the membrane and the chamber of the wafer and connecting to the other chamber (F).

2.4.3. Meander type design with vertical membrane arrangement fabrication

Microdevice assembly and attachment

The fabricated "mixed" PDMS platform was placed inside the oxygen plasma chamber at the same conditions as the alveolar design. The chamber and the glass slide were connected and placed in the oven at 85ºC for 1 hour. Next, the metallic pins in the form of "bridges" were inserted at the gas inlets of each branch in order to supply gas to each liquid unit and arm. The fabrication process outline is presented in Figure 2.19.
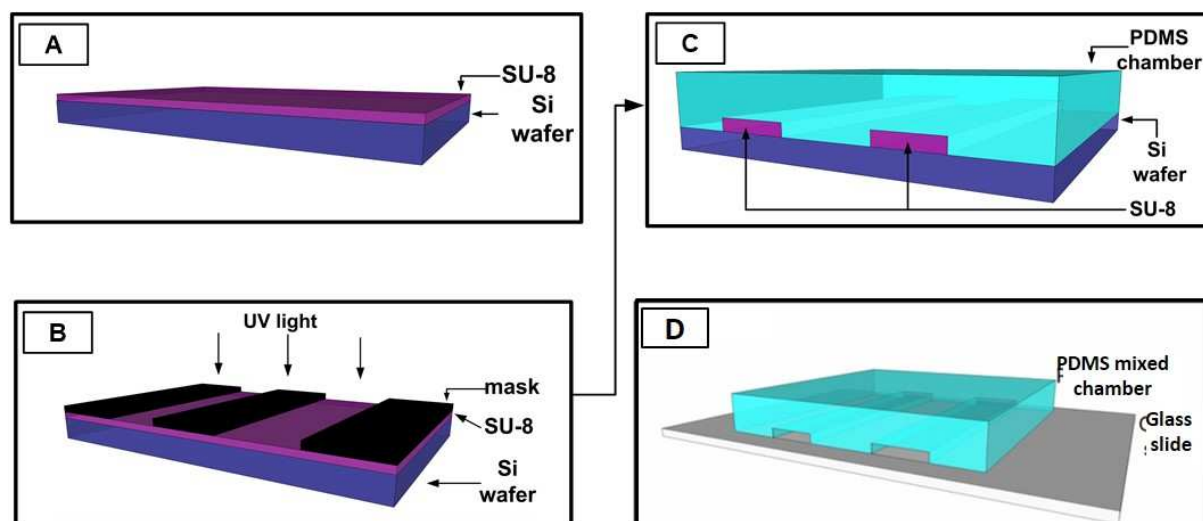
Figure 2.19 Process outline of the meander design chip fabrication. Spin coating of SU-8 negative on the silicon wafer (A), mask alignment, UV exposure and SU-8 development (B), pouring PDMS on a created mould (C) and peeling it off after curing. Connecting the chamber to the glass slide by O_2 plasma procedure (D).

2.4.4. Surface modification of the microdevice

As it was described in Chapter 1, hydrophilic surfaces allow reversible protein adsorption due to less protein unfolding [45, 46]. Accordingly, the surface of PDMS liquid channels as well as the membrane were modified with Pluronic in order to make them more hydrophilic [119, 120].

Pluronic F-68 (Sigma Aldrich) is a block copolymer surfactant which terminates in primary hydroxyl groups (Figure 2.20). Firstly, the surface of the PDMS platforms were activated in the oxygen plasma chamber for 50 seconds at 120 W, 0.4 mbar and 50% of O_2. This treatment leads to the formation of reactive hydroxyl groups on the surface. Next, Pluronic F-68 was thoroughly mixed with DI water in the concentration of 10 mg·mL^{-1} and introduced into the vascular channels with a syringe. The solution was kept inside the channels for 3 hours and subsequently washed with DI water for approximately 15 min [104, 120]. A schematic representation of the PDMS-Pluronic F-68 condensation reactions on the microdevice surface is depicted in Figure 2.20.

The goodness of the PDMS surface modification was evaluated by means of: 1) contact angle measurements, 2) adsorption of fibrinogen, and 3) red blood cells viability after oxygenation in the PDMS chips.

The static contact angle measurements were carried out with NEURTEK OCA 15EC instrument. The drop of distilled water (approximately 5 μL) was injected on the surface of cleaned untreated PDMS and PDMS modified by O_2 plasma and Pluronic F-68.
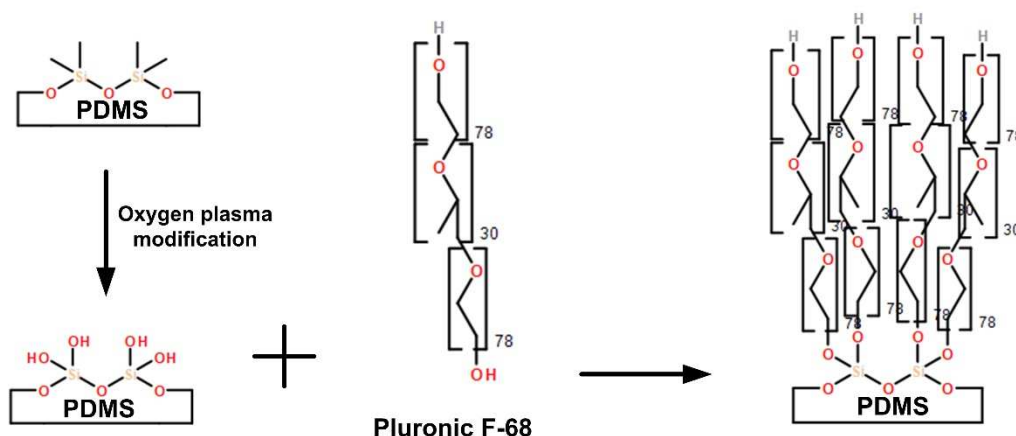
Figure 2.20 Schematic representation of the proposed PDMS surface modification

Fibrinogen, a large protein present in blood, has high affinity to be adsorbed on the hydrophobic, positively charged surfaces [47]. Thanks to this feature fibrinogen is commonly used in the measurements of protein adsorption onto different superficies [44]. Firstly, the surface of PDMS was incubated at 37ºC overnight in PBS to prepare it for further treatment with fibrinogen by maintaining optimal conditions, such as temperature, humidity, oxygen content etc. Next, fibrinogen was added to PBS in the concentration of 0.5 mg/mL and the PDMS surface was incubated for 24 hours. Finally, in order to clean the polymer surface, the PDMS was washed with DI water during approximately 15 minutes. The measurement of the protein adsorption on the PDMS surface was done by a Fluorescence Microscope with the Argon laser of 488 nm wavelength. Fibrinogen was placed on the: 1) untreated PDMS, and 2) PDMS modified by O_2 plasma and Pluronic F-68.

The viability of red blood cells was checked by an observation of the deterioration of the cells under the optical microscope. In order to be able to observe and count the cells under the optical microscope, the cells had to be first stained. A blood smear was performed and stained with hematologic staining (Differential Quik Stain Kit). The kit consists of three reagents: 1) a fixative for air-dried cell, 2) an eosinophilic to stain the cytoplasm, and 3) a basophilic solution to stain the nucleus. The blood smear was immersed 10 times in each solution and rinsed in tap water. After it dried, the smear was visualized in an optical microscope to assess the cell morphology. Additionally, the haemoglobin concentration was also evaluated by gasometry after each oxygenation experiment.

2.4.5. Experimental set-up for blood oxygenation

All the oxygenation experiments were carried out with sheep blood obtained from Faculty of Veterinary at University of Zaragoza without any further modifications. The blood samples

were collected and transferred into 10 mL plastic tubes (Becton Dickinson B.V., Spain) with Ethylenediaminetetraacetic acid (EDTA) as anticoagulant in the concentration of 1.5 mg/mL. The haemoglobin concentration of each batch was measured by gasometry (Vet abc, Animal Blood Counter). Blood was stored in the fridge at approximately 4°C during maximum of 24 hours.

Figure 2.21 shows the experimental system used for blood oxygenation experiments. Firstly, 50 mL of blood was transferred into a glass bottle and placed on a stirring plate inside the climatic chamber in order to maintain the temperature at 37 °C. Obtained blood was a venous blood with the oxygenation of approximately 98%. Hence, it was necessary to deoxygenate it prior to the oxygenation experiment. Thus, the mixture of air and nitrogen with 7.8% of O_2 was bubbled directly to the blood in order to decrease the Hb saturation down to approximately 70%. Afterwards, the deoxygenated blood (for detailed values see Table 2.8) was transferred into a 50 mL syringe (Becton Dickinson B.V., Spain) and placed in the syringe pump (Harvard Apparatus, Spain). The experiments were performed at blood flow rates ranging from 0.1 to 5 mL·min^{-1}. The pressure transducer (Panasonic, DP2-41E) was placed right after the syringe pump to evaluate the pressure drop across the entire system, taking into account the device itself, piping and metallic pins. The gas or liquid was introduced to the microdevice by Tygon microbore tubing (0.020" x 0.060" OD, Cole-Parmer, The Netherlands) and precision stainless steel dispense tip (0.010" ID, 0.020 OD, 45° bend, Nordson, The Netherlands).
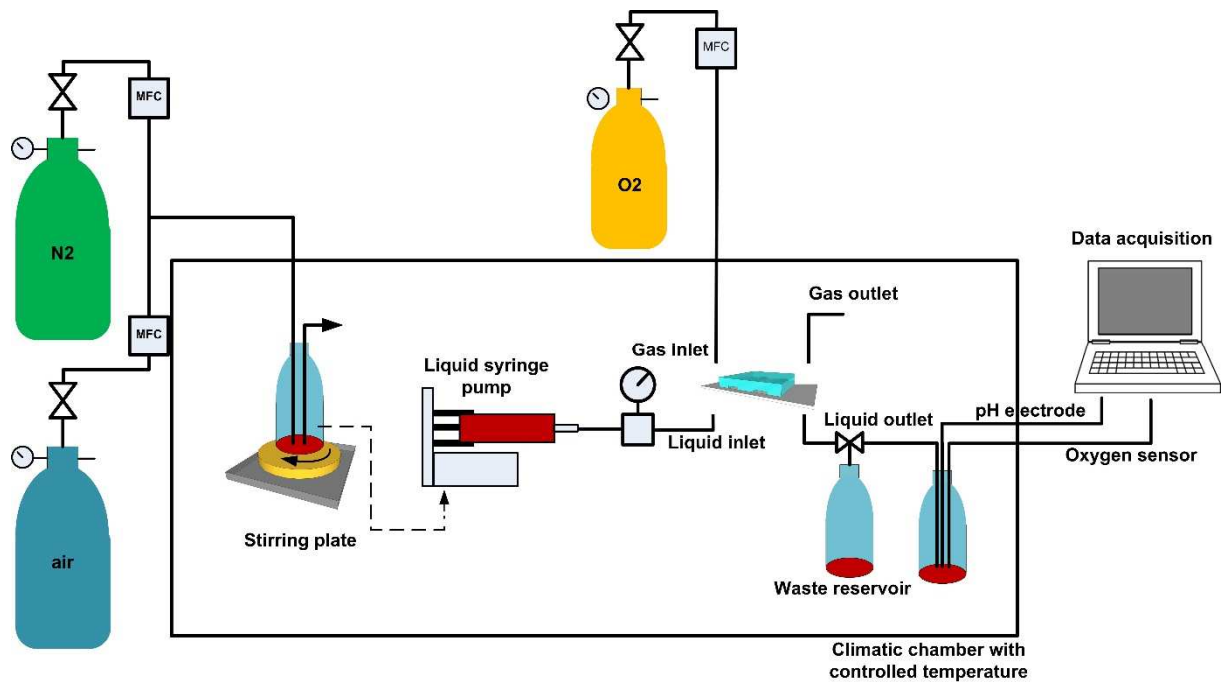
Figure 2.21 Experimental set-up for blood oxygenation experiments

Next, the gas chamber was purged with oxygen while deoxygenated blood entered the microdevice from the liquid chamber side. First part of the outlet blood stream was discarded by pumping to the waste reservoir to ensure steady state conditions. The oxygenated blood was collected in a glass bottle hermetically sealed where pH electrode (Hamilton, Slimtrode 238150, Switzerland) and dissolved oxygen electrode type oximeter (ThermoFisher Scientific, Orion Star A223) were immersed. Before each set of experiments, the control sample measurement was performed by carrying the blood throughout the experimental system without oxygenating it in order to ensure no leaks of the system as well as to measure the exact blood saturation by an oximeter.

As described before, the percentage of blood saturation is calculated from the measurements of the concentration of oxygen dissolved provided by the oximeter according to expressions 2.3 and 2.4, respectively. The evaluation of the oxygenation performance of the microdevice has been assessed by the oxygen transfer rate calculated from the O_2 macroscopic balance in the liquid chamber, i.e. considering both contributions O_2 dissolved and O_2 bound to Hb:

$$O_{2transf} = \frac{\alpha \cdot \Delta P_{O2} + Hbs \cdot \Delta S_{O2} \cdot [Hb]}{SA} \cdot Q \qquad (2.16)$$

Where: ΔP_{O2} and ΔS_{O2} are the differences between the outlet and inlet values of partial pressure of dissolved oxygen in blood and fractional oxygen saturation in blood, respectively. α is the solubility coefficient of oxygen in blood, Hbs is the O_2 binding capacity of haemoglobin, [Hb] is, haemoglobin concentration in blood, Q is the blood flow rate and SA is the membrane surface area.

Three different devices of each design, i.e. AD1, AD2 and meander type device, were used for the oxygenation experiments. Three repetitions at distinctive blood flow rates of each device were performed. The concentration of haemoglobin slightly differed from sample to sample. Therefore, for each experiment, the Hb concentration was measured by gasometry. The main parameters for each oxygenation experiment are shown in Table 2.8.

Table 2.8 *Main parameters of each oxygenation experiment*

	Hb conc [g/mL]	SO_2 inlet [%]
Alveolar Design 1, AD1		
Device 1	0.128	78.6
Device 2	0.129	66.9
Device 3	0.132	57.3
Alveolar Design 2, AD2		
Device 1	0.146	80.2
Device 2	0.141	82.2
Device 3	0.142	68.8
Meander Design with vertical membrane device, MD		
Device 1	0.136	81.4
Device 2	0.145	83.7
Device 3	0.141	77.6

2.5. Results

In this section, the device characterization, as well as the results of the PDMS surface modification, RBC viability and blood oxygenation are presented.

2.5.1. Device characterization

2.5.1.1. Alveolar design

Two types of the microfluidic devices were fabricated: AD1, based on the liquid geometry developed by Kniazeva *et al* [32], and AD2 with liquid flow distributors in the single unit instead of parallel and perpendicular channels. The liquid chamber architecture enabled uniform flow of the blood through the branching construction of the microchannels while supplying pure O_2 permeating through a PDMS membrane to blood from the top side of the chip. Use of PDMS elastomer facilitated chip fabrication and reproduction of the same design with thin non-porous membrane attached to the chambers. Figure 2.22 demonstrates the comparison of two microfluidic devices, A) AD1 and B) AD2, with the liquid chamber filled with blood together with their respective magnifications. The images indicate that the filling of the liquid channels was homogenous, and well distributed without any dead volume inside. Scanning Electron Microscopy (SEM) was used to inspect the chip inside. It was of crucial importance to confirm that the membrane which was "sandwiched" in between two chambers did not deflect, collapse or detached.
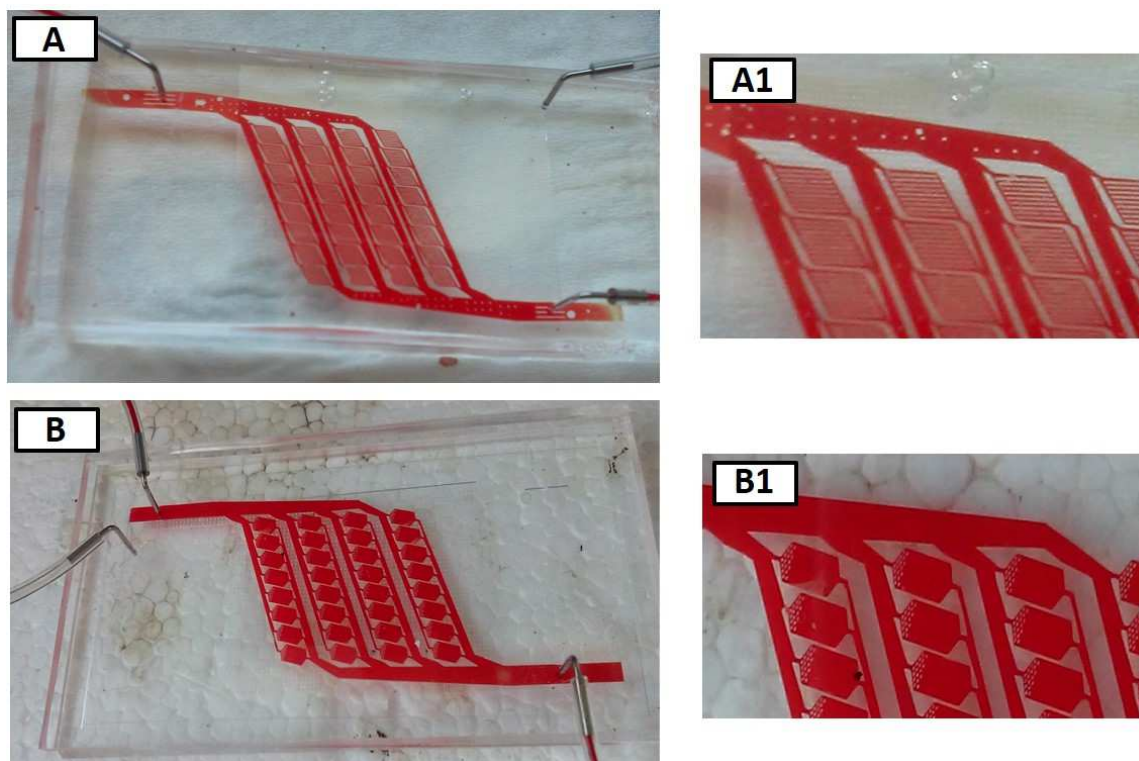
Figure 2.22 Optical images of A) AD1 and B) AD2 PDMS microfluidic devices with sheep blood inside the liquid chamber. A1 and B1 are the magnifications of AD1 and AD2 respectively

Figure 2.23 shows SEM photograph for two different microdevices which indicates that the membrane was well attached to the microfluidic chambers. No leak was observed and each device was capable to work for long time, more than 8 hours, under the experimental conditions. The experimental system with the microfluidic device could withstand liquid flow rate up to 5 mL/min ensuring stable operation and physiological condition, i.e. no thrombosis formation.
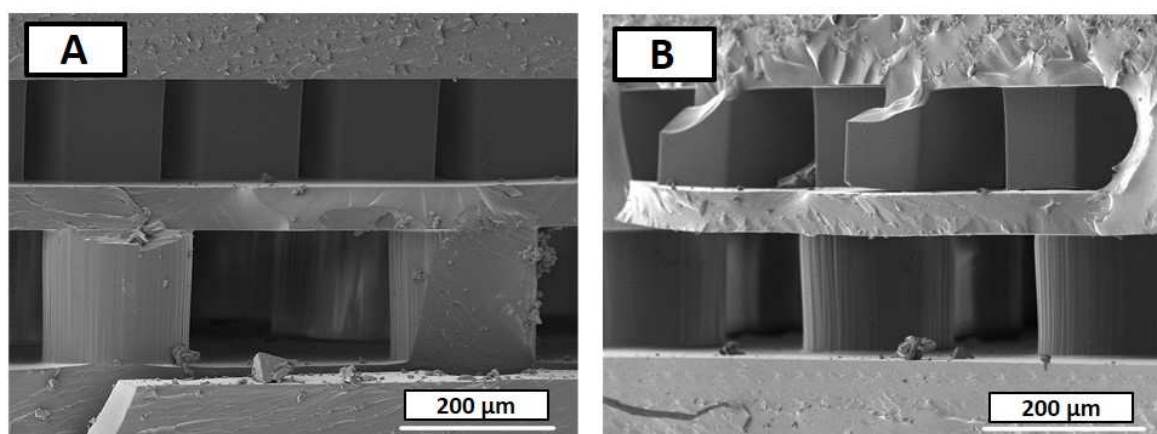
Figure 2.23 Cross section analysis of A) AD1 and B) AD2 type microdevices by SEM

Three different microfluidic devices of each type, AD1 and AD2, were fabricated and tested. The thickness of the PDMS mould for both compartments was 0.8 – 1 cm. The chip

footprint, defined as the total size of the microfluidic device taking into account its width and length, was equal to 18.7 cm^2 making it a very compact system. The volume of the gas chamber was equal to 73 µL for both device types while the volume of the liquid chamber was equal to 28 µL for AD1 and 39 µL for AD2. The depth of each chamber was equal to approximately 100 µm and the membrane surface area was 2.8 cm^2 and 3.9 cm^2, resulting in a S/V$_{liquid+gas}$ ratio of 28 cm^{-1} and 35 cm^{-1} for AD1 and AD2, respectively.

2.5.1.2.   Meander Design with vertical membrane arrangement

The liquid chamber architecture enabled uniform flow of the blood through the meandering microchannels while supplying pure O$_2$ permeating through a PDMS membrane from both lateral sides of the chamber. The gas or liquid was introduced to the chip by Tygon microbore tubing (0.020" x 0.060" OD, Cole-Parmer, The Netherlands) and precision stainless steel dispense tip (0.010" ID, 0.020 OD, 45° bend, Nordson, The Netherlands). The "bridges" which were connecting the gas channels were made of the same precision stainless steel dispense tips. It was measured that at the blood flow rate of 1 mL/min the total ΔP of the entire experimental system was equal to 57 mbar. Figure 2.24 demonstrates the optical microscope images (A, B) and a photograph of a vertical membrane microfluidic device with coloured liquid (red colour) and gas (green colour) channels for better visualisation.
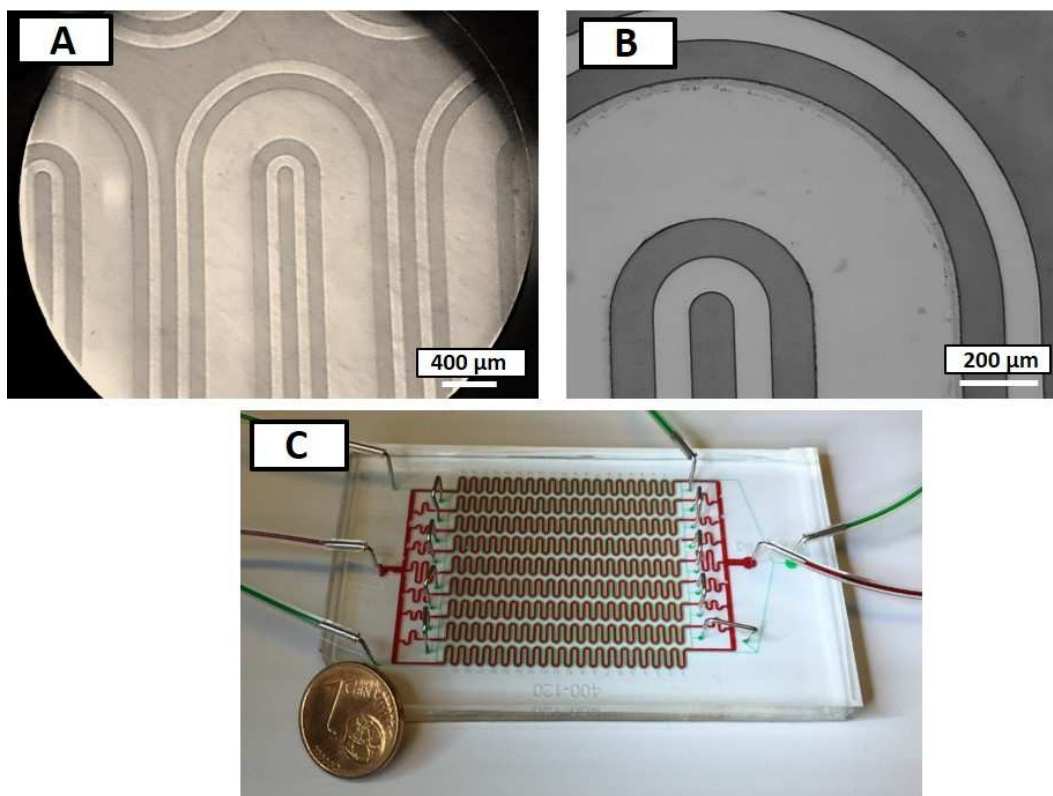
Figure 2.24 MD microfluidic chip. Green and red colours indicate gas and liquid channels, respectively

The image indicates that the filling of the liquid channels was homogenous, and well distributed without any dead volume inside. It is also important to notice that in this architectural conformation there was no risk of membrane deflection or detachment since the membrane was "embedded" in the chamber. Fabricated devices were tested under the experimental conditions described above. No leak was observed or a "mixed" chamber collapse. The device was able to work for many hours at the maximum liquid flow rate of 1 mL/min. Three different meander type microfluidic devices were fabricated and tested. For all of them, the thickness of the PDMS mould for the "mixed" PDMS compartment was approximately 0.8-1 cm and the chip footprint was equal to 35 cm^2 making it a very compact system. The volume of the liquid chamber was equal to 58 μL. The depth of gas and liquid chamber was approximately 100 μm and the membrane surface area was 2.9 cm^2, resulting in a S/V$_{liquid+gas}$ ratio of 50 cm^{-1}.

2.5.2. Blood interaction with PDMS microfluidic systems

Prior to the blood oxygenation experiments it had to be confirmed that the surface of a PDMS microdevice was not altering the physiological properties of blood. The results of the surface modification are presented in the sections below.

Contact angle

The contact angle measurement was performed on the non-modified and modified (O$_2$ plasma + Pluronic F-68) PDMS surfaces. The obtained contact angle of a modified PDMS surface was equal to 10°±3 indicating that the surface was converted to a hydrophilic one, after a comparison with non-treated PDMS surface with contact angle of 115°±0.6. Figure 2.25 shows the graphical representation of a water drop on the A) hydrophobic and B) hydrophilic surface.
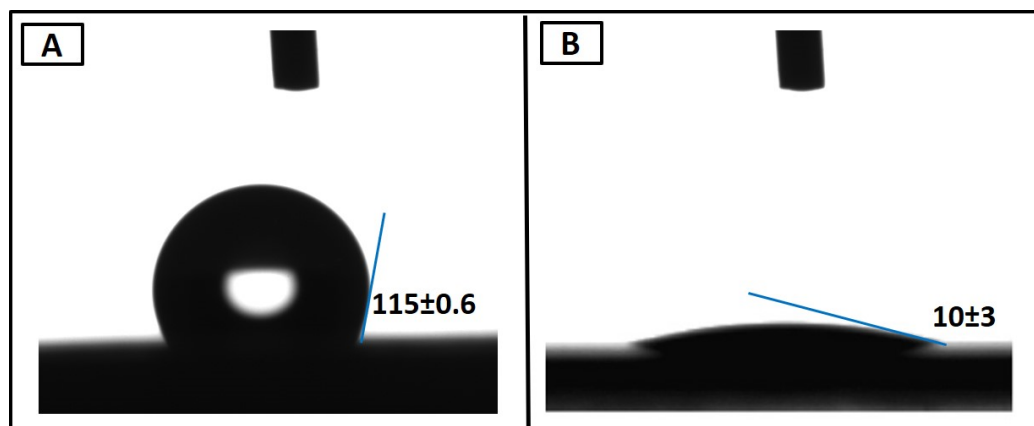
Figure 2.25 Representation of the contact angle in A) hydrophobic and B) hydrophilic surfaces

Visual inspection

The visual inspection of the channels with the optical microscope after perfusion of blood was also executed. Figure 2.26 demonstrates the comparison of the two types of microdevices (Alveolar and Meander type) with the modified hydrophilic PDMS surface (Figure 2.26 A and C) and unmodified hydrophilic superficies (Figure 2.26 B and D) after blood oxygenation experiments. It is visible that chips of which surfaces were modified do not possess any traces of blood inside the channels, while the inside of the non-modified microdevices are contaminated with blood along the entire structure. Moreover, in order to clean the device with modified hydrophilic surface after the experiments with blood, PBS was perfused at 5 mL/min (the higher the flux the better cleaning) for its reuse.
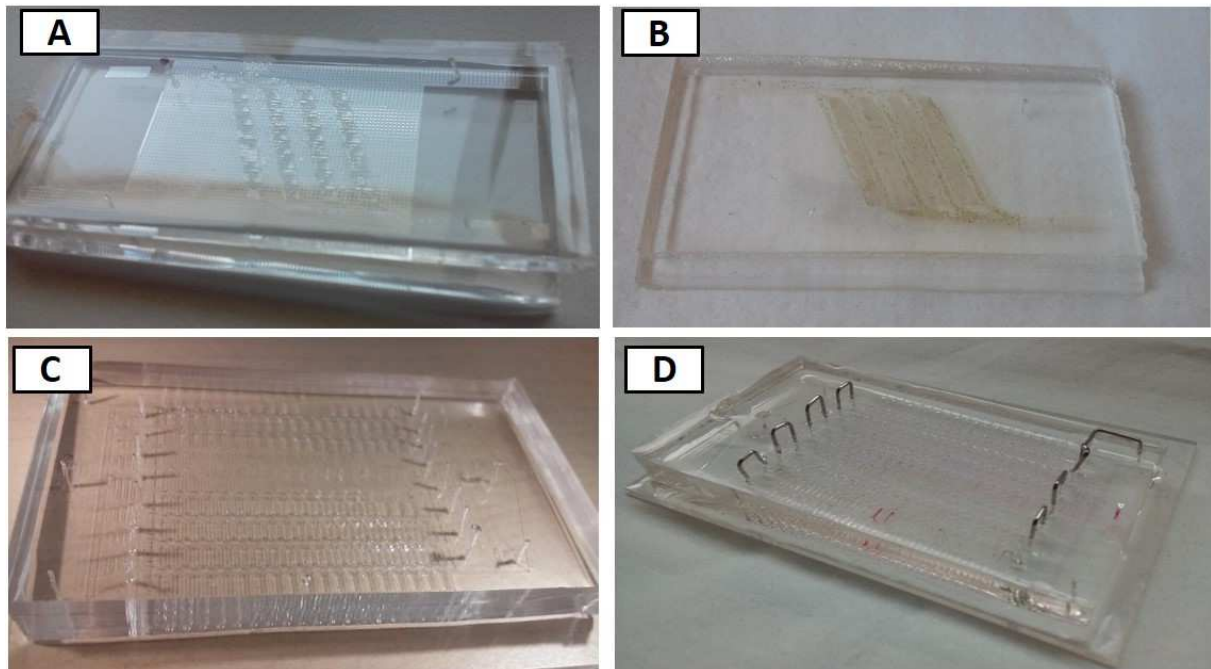
Figure 2.26 Visual inspection of A) surface of AD1 PDMS modified with O_2 plasma and Pluronic, B) non-modified AD1 PDMS surface, C) meander type device with modified surface and D) non-modified meander surface after blood oxygenation experiments

Adsorption of Fibrinogen

The adsorption of Fibrinogen was measured by a fluorescence microscope. The protein adhesion is indicated by green-fluorescence dots, represented in Figure 2.27. It is clearly visible the preferential fibrinogen adhesion on the unmodified PDMS surface. On the other hand, no proteins are distinguished on PDMS modified by O_2 plasma and Pluronic. This observation agrees with the assumption of other authors claiming that the more hydrophilic the surface of a biomaterial, the less protein adsorption and less probability of red blood cells destruction.
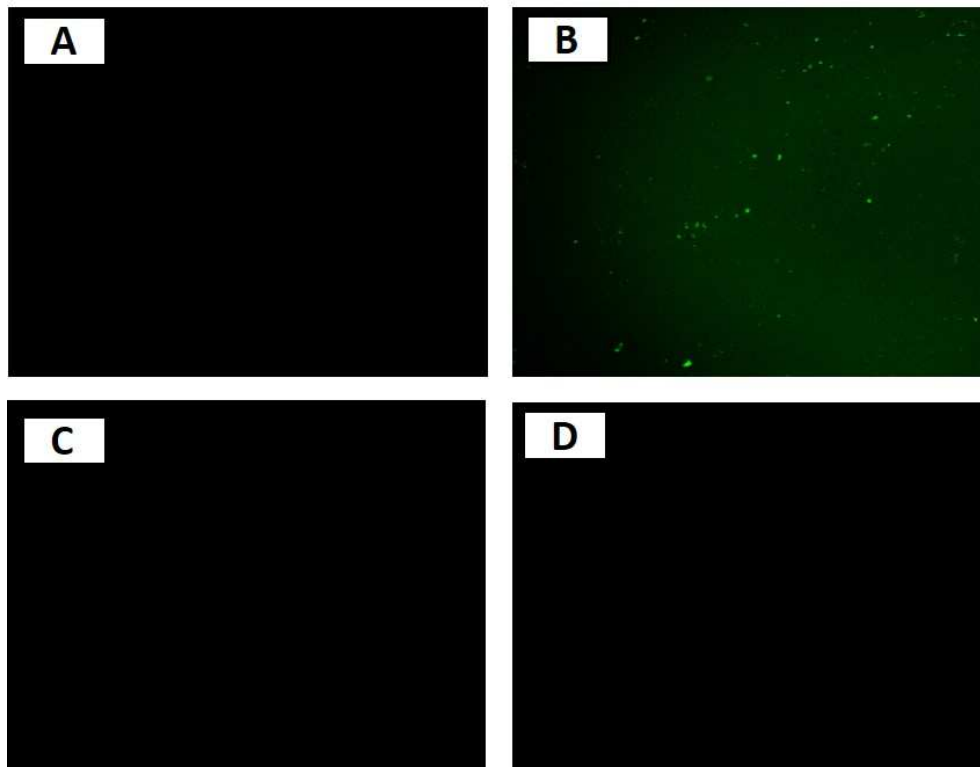
Figure 2.27 Visual representation of the fibrinogen adhesion. A) Untreated PDMS without protein, B) untreated PDMS with protein, C) O_2 plasma + Pluronic without protein and D) O_2 plasma + Pluronic with protein

Blood cell viability

The sample of blood before and after the oxygenation experiments (maximum of 24 hours) was taken for the analysis of red blood cells (RBCs) concentration as well as to check the shape and structure of the erythrocytes by optical microscopy. Figure 2.28 shows the white and red blood cells distribution, shape and structure before and after oxygenation in PDMS microdevices. It is visible that blood did undergo some slight modification, (see Figure 2.28 B and C). Small deterioration of RBCs represented by darker colour and no uniform outer edge in comparison to the cells before the experiment (Figure 2.28 A) is present. Thus, in order to have an overview of the extension of the RBCs deterioration the gasometry analysis was prepared in order to analyse the concentration of erythrocytes before and after the experiment (see Table 2.9).
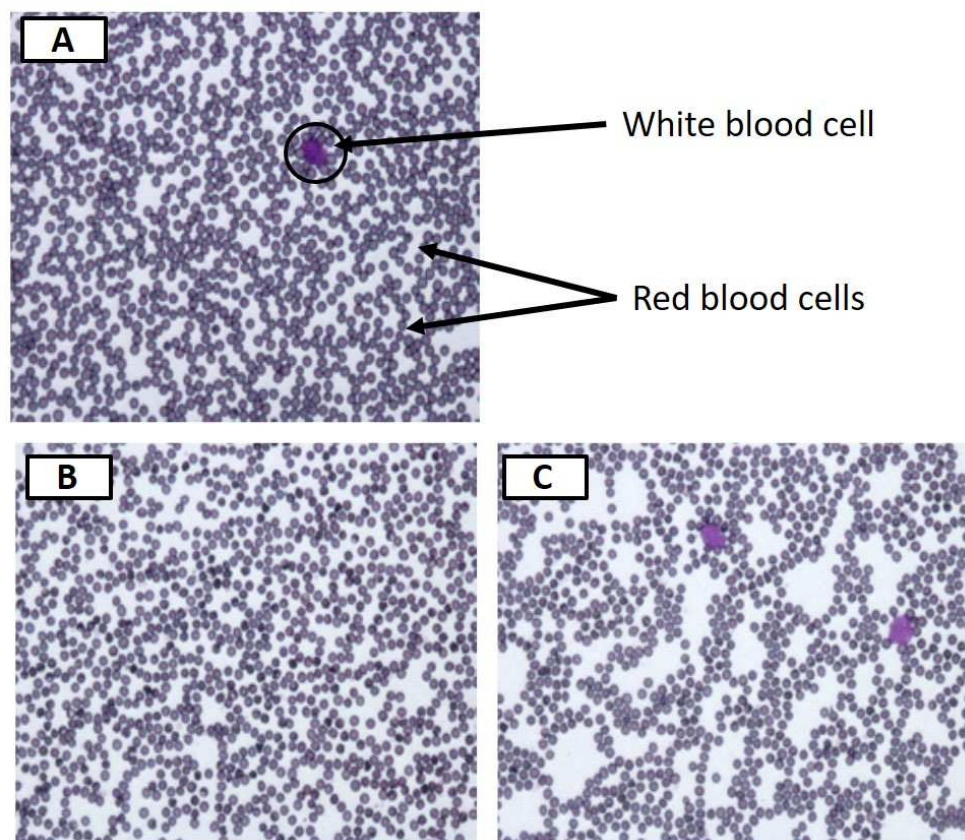
Figure 2.28 Optical microscope images of blood cells A) before and B), C) after the blood oxygenation experiments in the microdevice

Table 2.9 Gasometry results before and after the oxygenation experiments

Measurement	Hb conc [g/dL]	Erythrocytes [mm^{-3}]
Before the experiment	13.5±0.6	13.5±0.3·10^6
After the experiment	13.1±0.7	12.5±0.4·10^6

From the measurements presented above it is visible that some of the red blood cells disappeared or they became deteriorated. Nevertheless, the difference in concentration of erythrocytes before the experiment and after is small enough to assume that there is no significant influence on the blood properties after PDMS surface modification.

2.5.3. Blood oxygenation in alveolar design-experimental results and modelling

2.5.3.1.   Experimental blood oxygenation

Blood saturation [%]

Blood oxygenation experiments were performed in the experimental system presented in Figure 2.21. Dissolved oxygen concentration was measured by an oximeter and recalculated into blood saturation from equation 2.3 and 2.4. Figure 2.29 demonstrates the results of blood saturation with oxygen at different liquid flow rates for two different devices, AD1 and AD2. The figure represents the difference in saturation between a control sample, i.e. approximately 70% blood saturation (see description in section 2.4.5), and standard oxygenation experiment. The error bars represent the standard deviation of three repetitions of the same measurement (see Table 2.8 for details of each experiment).
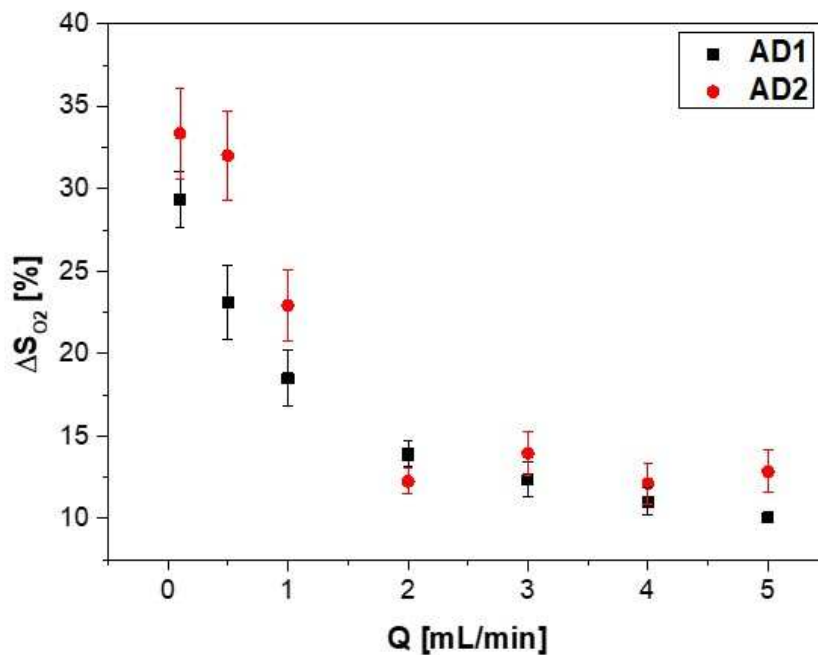
Figure 2.29 Blood saturation with oxygen at different liquid flow rates for AD1 and AD2 type microdevices working under identical operating conditions

It is visible from the figure that the saturation level of blood with oxygen decreases with an increase of the blood flow rate due to the lower residence time. Additionally, the AD2 type design, shows in general better oxygenation performance for a given blood rate than the old

design, AD1. Moreover, the steepest part of the curve is localized at the blood flow rate ranging from 0.1 to 1 mL/min while an almost plateau is obtained at the flow rates from 2 to 5 mL/min.
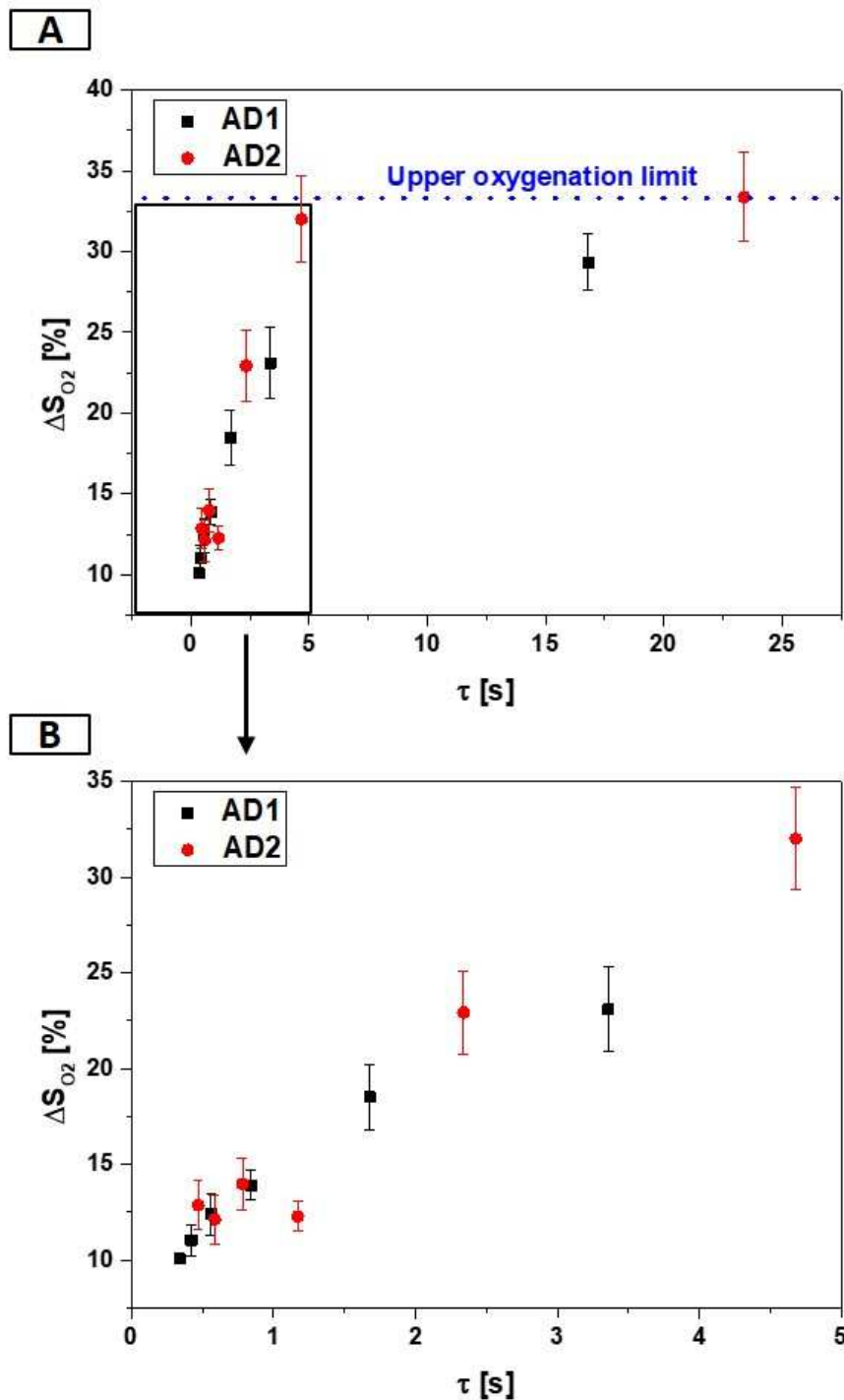
Figure 2.30 Blood saturation with oxygen as a function of residence time (τ) for AD1 and AD2 type microdevices at A) entire range of liquid flow rates and B) magnification of the lowest τ

Figure 2.30 shows the changes in oxygen saturation as a function of residence time, τ, for both AD1 and AD2 chips, respectively. The target of such data representation was to discard the differences of the liquid chamber volume in each device and to focus entirely on the chip

performance resulting from the designed geometry. The figure also indicates the upper oxygenation limit obtained by the alveolar type device.

As it was expected, the higher the τ the higher is the oxygen saturation level. However, this relationship is not linear for the whole operational window herein studied. For lower τ values, i.e. higher blood flow velocities a linear dependence is observed. In this region, the slope is slightly higher for AD2 design. As blood flow decreased, τ increased, the oxygenation saturation eventually levelled off. This behaviour is due to the decay in the driving force for oxygen diffusion in blood as in the proximity of 100% saturation level.

As it was mentioned in section 2.2.2, the target of the alveolar design modification was to be able to work at lower pressure drop values without compensation of high oxygenation levels. Figure 2.31 shows experimentally obtained pressure drops for two proposed designs, AD1 and AD2, measured during oxygenation experiments at various blood flow rates. The registered ΔP values are for the entire experimental set-up resulting from microdevice geometry, pipings, pins etc. The comparison of the mathematically simulated ΔP for both devices that results only from the microfluidic geometry is presented as well.
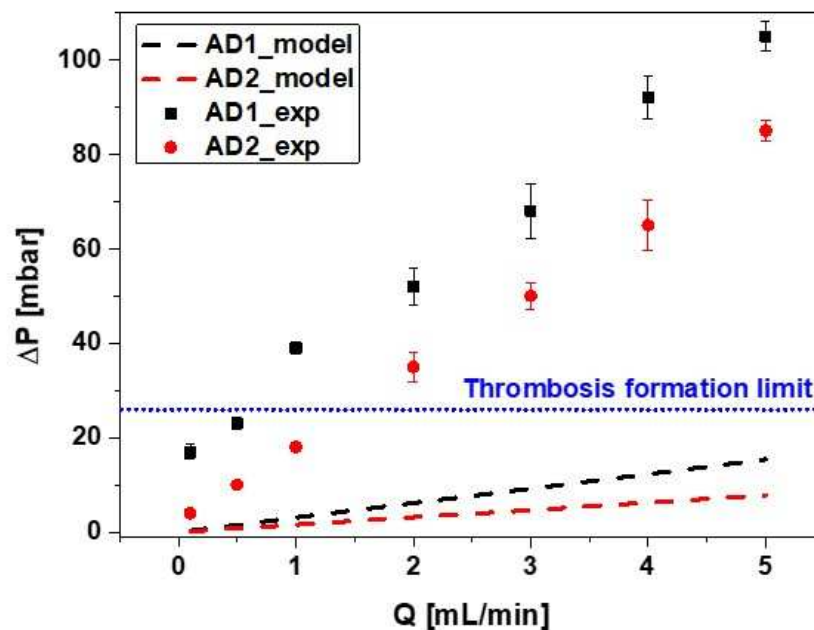
Figure 2.31 Experimental pressure drop of two alveolar designs under identical working conditions

The connections that are used for introducing blood to the microdevice are described in section 2.4.5. The pressure drop, for instance, in the stainless steel dispense tip at 1 mL/min blood flow rate corresponds to 7.9 mbar. Two of these tips are needed for blood inlet and outlet which corresponds to higher ΔP in the system. Moreover, it is observed that the pressure drop

in AD2 is significantly lower than in AD1. This results also in lower shear stress for RBCs. Summarizing, the oxygenation results of two designs are relatively similar, indicating that the pressure drop in AD2 was decreased without lowering the oxygenation performance. The microfluidic connections are being reconsidered to diminish the pressure drop of the capillaries.

2.5.3.2. Mathematically modelled oxygenation results for alveolar designs

<u>Oxygen concentration profile-computer modelling</u>

The governing equations used for the O_2 concentration profile are presented in section 2.3.3. The target of this simulation was to compare the modification of a single unit in terms of better oxygenation. Therefore, due to the long computation time, only the simulations of 3D single units were performed. The computational domain was discretized by more than a 220 0000 tetrahedra defining a structured mesh with an edge length in the range 0.002-0.0005 cm. An "opening" boundary was applied to the 3D single unit. Figure 2.32 shows the oxygen concentration profile across the single unit of AD1 liquid geometry at A) 0.1 mL/min and B) 1 mL/min blood flow rate. The O_2 concentration values obtained from the mathematical modelling correspond to dissolved oxygen in blood, Cd_{O2}, and are given in mol/m^3. Thus, they had to be recalculated to S_{O2} and later to oxygen transfer rate.
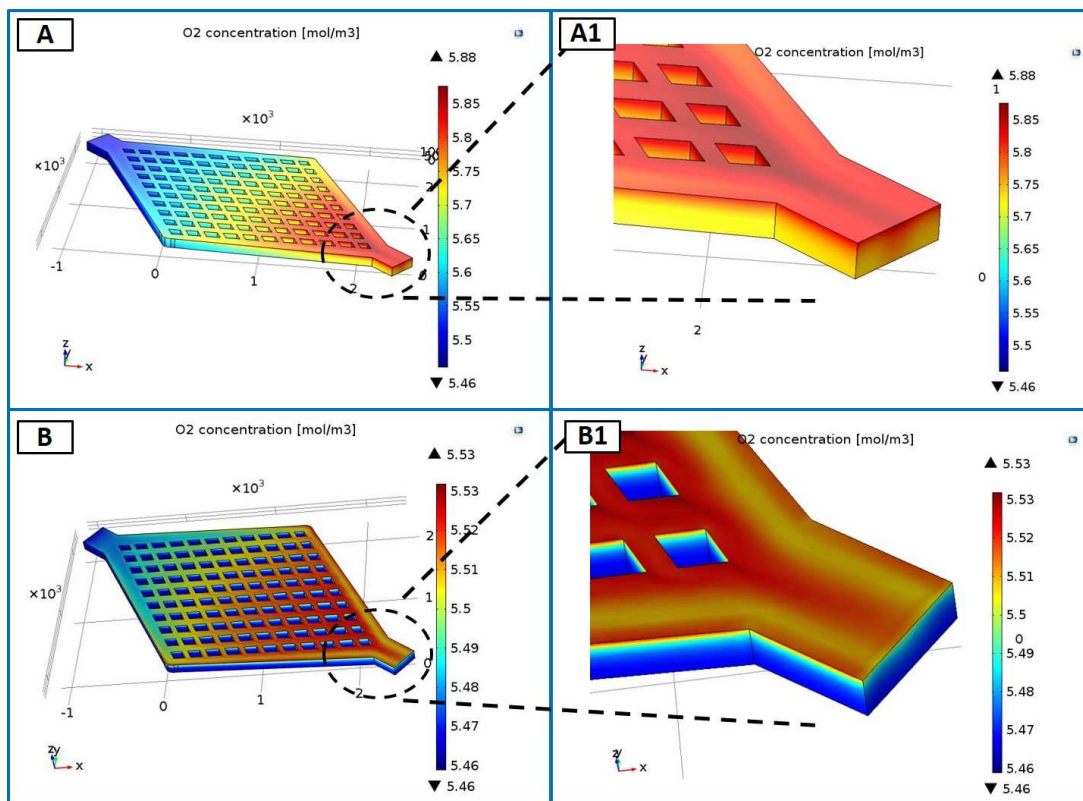
Figure 2.32 Oxygen concentration computer modelling of a single unit D1 at A) 0.1 mL/min blood flow rate and B) 1 mL/min blood flow rate

It is visible that the concentration of oxygen at the outlet of a single unit is higher in case of lower blood flow rate, i.e. 5.75 mole/m^3 and 5.48 mole/m^3 at 0.1 mL/min and 1 mL/min blood flow rate, respectively. Moreover, at low blood flow velocity, the oxygen can penetrate deeper into the liquid channel.

The same type of mathematical modelling was performed for the AD2 structure (Figure 2.33). The final mesh consisted of more than 14 0000 triangular elements defining a structured mesh with an edge length in the range 0.02-0.004 cm. The boundary conditions were set equal to the previous simulation. The new design exhibit high oxygen concentration at the corners situated close to the outlet of the unit. This is connected with the blood flow velocity profiles. This geometry leads to more pronounced oxygen concentration profile in x, y direction for a given z position. However, AD2 single unit renders in higher value for the average O$_2$ concentration dissolved at the outlet, i.e. 5.9 mole/m^3 and 5.53 mole/m^3 for 0.1 mL/min and 1 mL/min blood flow rate, respectively.
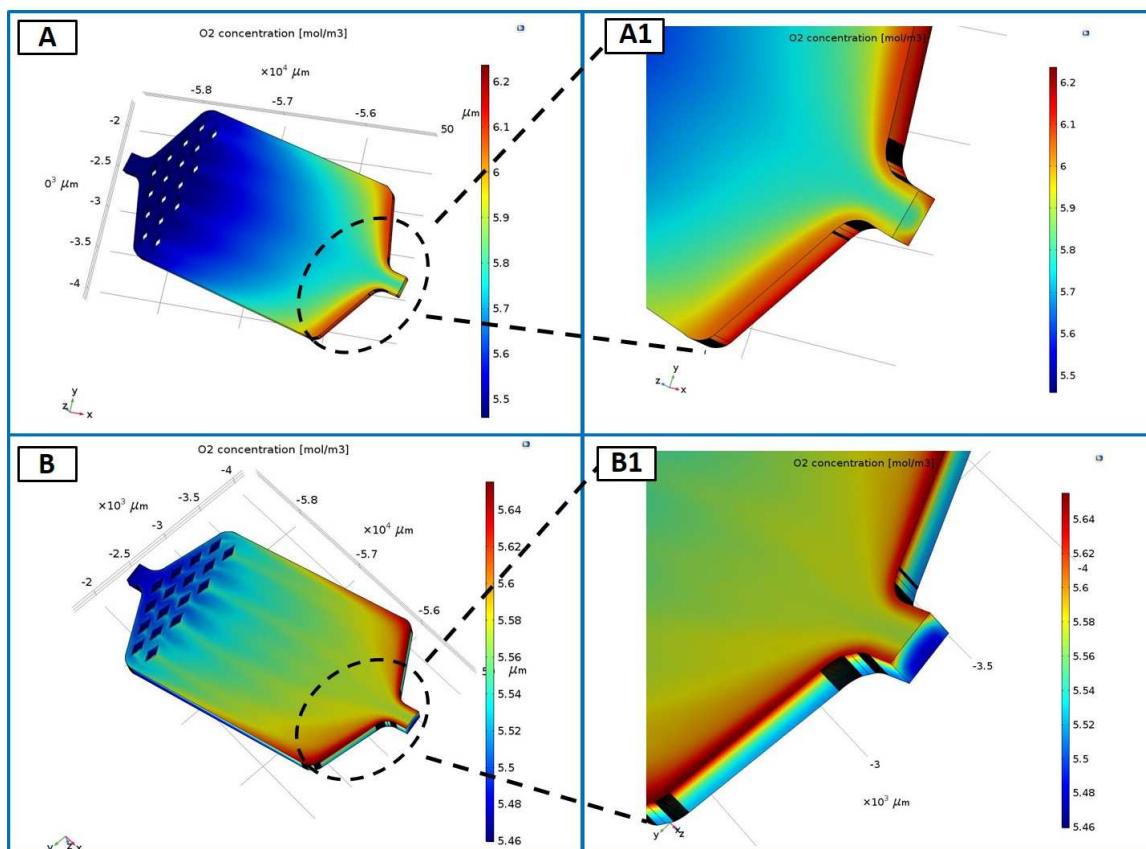
Figure 2.33 Oxygen concentration computer modelling of a single unit D2 at A) 0.1 mL/min blood flow rate and B) 1 mL/min blood flow rate

2.5.4. Blood oxygenation in meander design (MD) with vertical membrane arrangement

2.5.4.1. Experimental blood oxygenation

Blood saturation [%]

In the meander type design, the oxygen enters to the liquid chamber from both sides of the channel (double side diffusion). The changes in oxygen saturation with increasing blood flow rate are presented in Figure 2.34. The observed tendency is similar to the previously shown alveolar devices (see Figure 2.29).
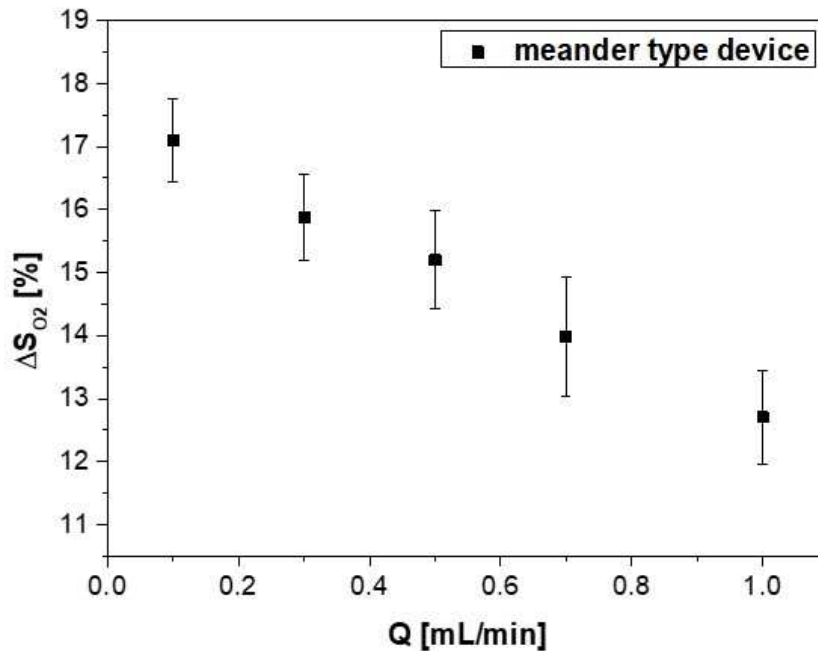
Figure 2.34 Change in saturation in the meander type device with vertical membrane arrangement

Figure 2.35 shows the comparison of ΔS_{O2} in three proposed microdevices: MD, AD1 and AD2 as a function of a residence time (τ) in order to discard the liquid chamber volume differences, i.e. 58 μL, 28 μL, 38 μL, respectively.
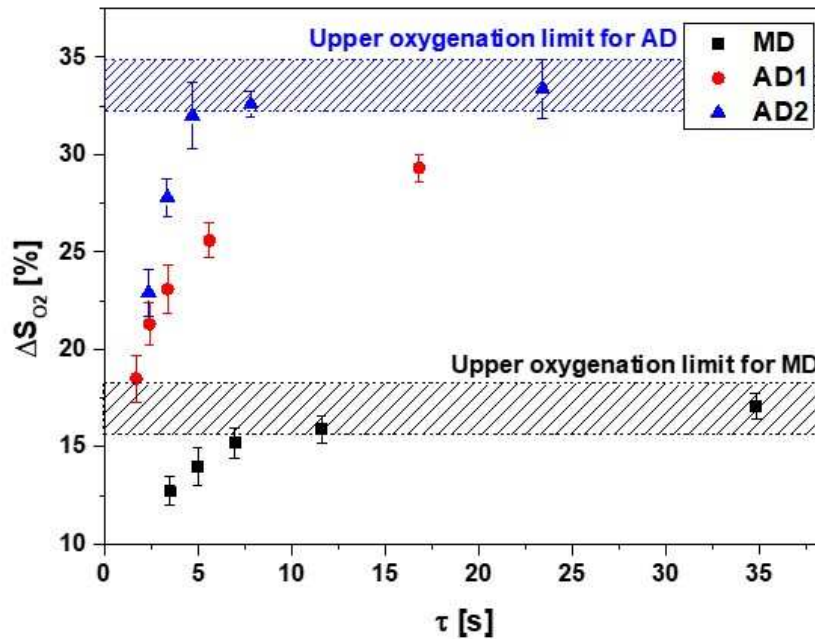
Figure 2.35 Comparison of the change in the saturation in the meander device (MD) and two alveolar geometries (AD1 and AD2) as a function of residence time (τ)

Using similar gas exchange area, alveolar devices with 100 μm channels height, achieve clearly superior O_2 exchange rates than MD devices with 400 μm wide channels at identical τ values. Figure 2.35 underlines the importance of oxygen diffusion along the liquid channel in the overall oxygenation process. At a given residence time, the longer the diffusion pathway in the liquid side, the lower the oxygen saturation level attained. Therefore, AD designs reveal advantages to reduce the diffusion distance limitations. Particularly, AD2 design is clearly outstanding in terms of oxygenation performance and pressure drop (see Figure 2.36) Accordingly, there is plenty of room for improvement by reduction of the liquid chamber height from 100 μm down to approximately 50 μm.

Additionally, in the case of the meander type device, the maximum blood flow rate tested was 1 mL/min due to the pressure drop limitations from the metallic pins inserted in the chip in the form of "bridges". Figure 2.36 shows the experimentally obtained pressure drop during oxygenation experiments resulting from metallic pins, piping and microfluidic geometry as well as the simulation results of the ΔP resulting only from the microfluidic architecture for the three microfluidic devices: MD, AD1 and AD2. As it was mentioned before, the microfluidic connections are being reconsidered to reduce the hydraulic loss in the transfer lines.
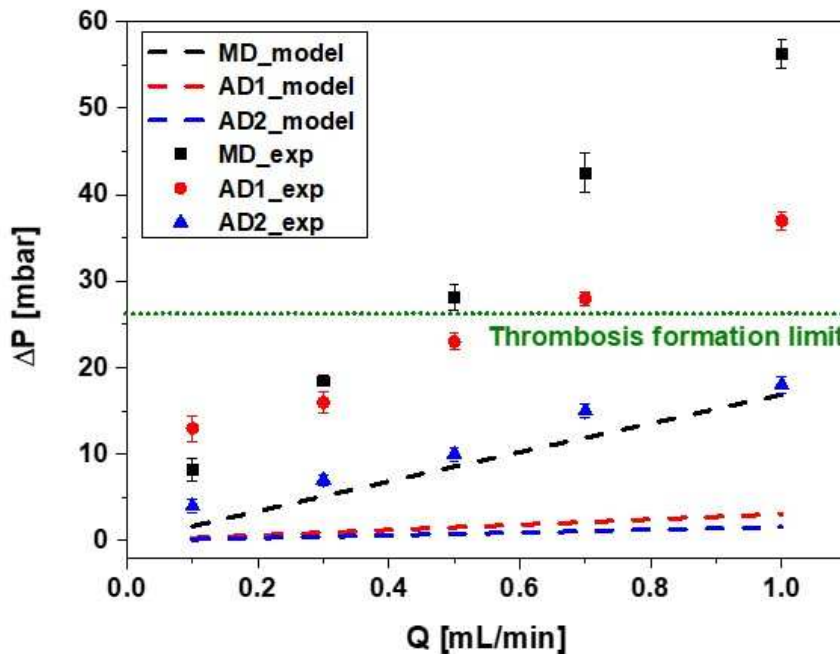
Figure 2.36 Comparison of a pressure drop among three proposed microdevices: MD, AD1 and AD2

Each of the three distinctive liquid side geometries presented in this section, possesses advantages and disadvantages. The comparison of the performance of such devices is shown in Figure 2.35 and Figure 2.36. It is clearly noticed that the performance of the meander device is significantly worse than of both alveolar devices even though the oxygen enters the blood chamber from both sides. This is due to the liquid chamber geometry, i.e. the distribution of the channels and the large diffusion distance in MD with 400 μm width channels in comparison to alveolar design containing 100 μm channel depth.

2.5.4.2. Mathematically modelled oxygenation results in the MD microdevice

As it was performed in case of the alveolar designs, the oxygen concentration profile of the MD geometry was mathematically modelled. The final mesh consisted of more than 40 000 elements triangle defining a structured mesh with an edge length in the range 0.04-0.005 cm. Figure 2.37 demonstrates the oxygen concentration profile across the meander type geometry for two liquid flow rates: A) 0.1 mL/min and B) 1 mL/min with their respective magnifications.
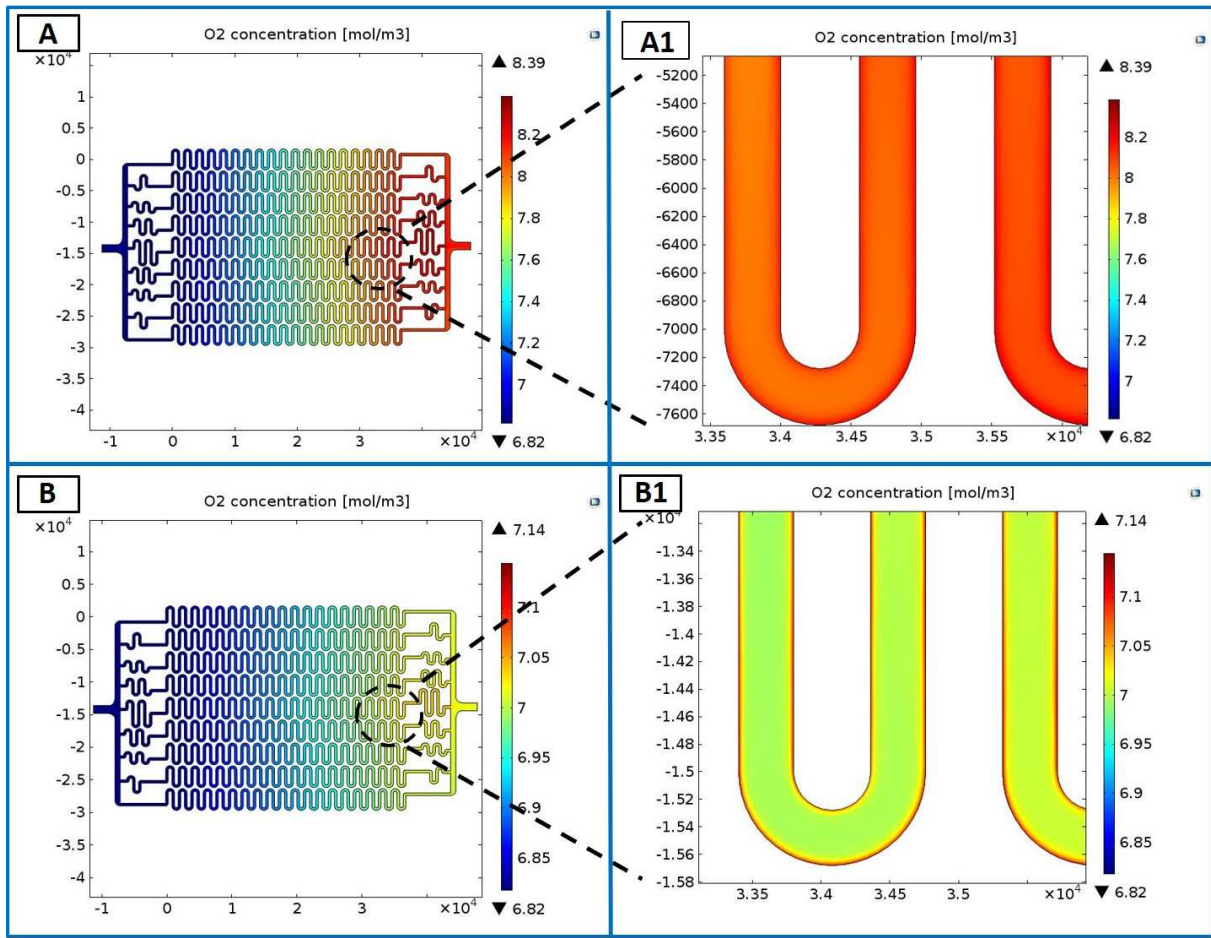
Figure 2.37 Oxygen concentration profile computer modelling of a MD at A) 0.1 mL/min blood flow rate and B) 1 mL/min blood flow rate

As it was expected, higher values of oxygen concentration are obtained with lower blood flow rate. Moreover, it is visible that the highest values of the oxygen concentration dissolved are localized near the membrane wall.

Additionally, Figure 2.38 demonstrates the goodness of the modelling by comparison of experimental as well as simulated results for average values of oxygen saturation level and oxygen transfer rates at the outlet.

In this case, the entire geometry was simulated, therefore the direct comparison to the experimental results could be done. The experimental and theoretical values are in a good agreement except the case of the biggest liquid flow rate, i.e. 1 mL/min. The relative error of the oxygen transfer rate between experiment and model in this blood flow rate is approximately 18%.
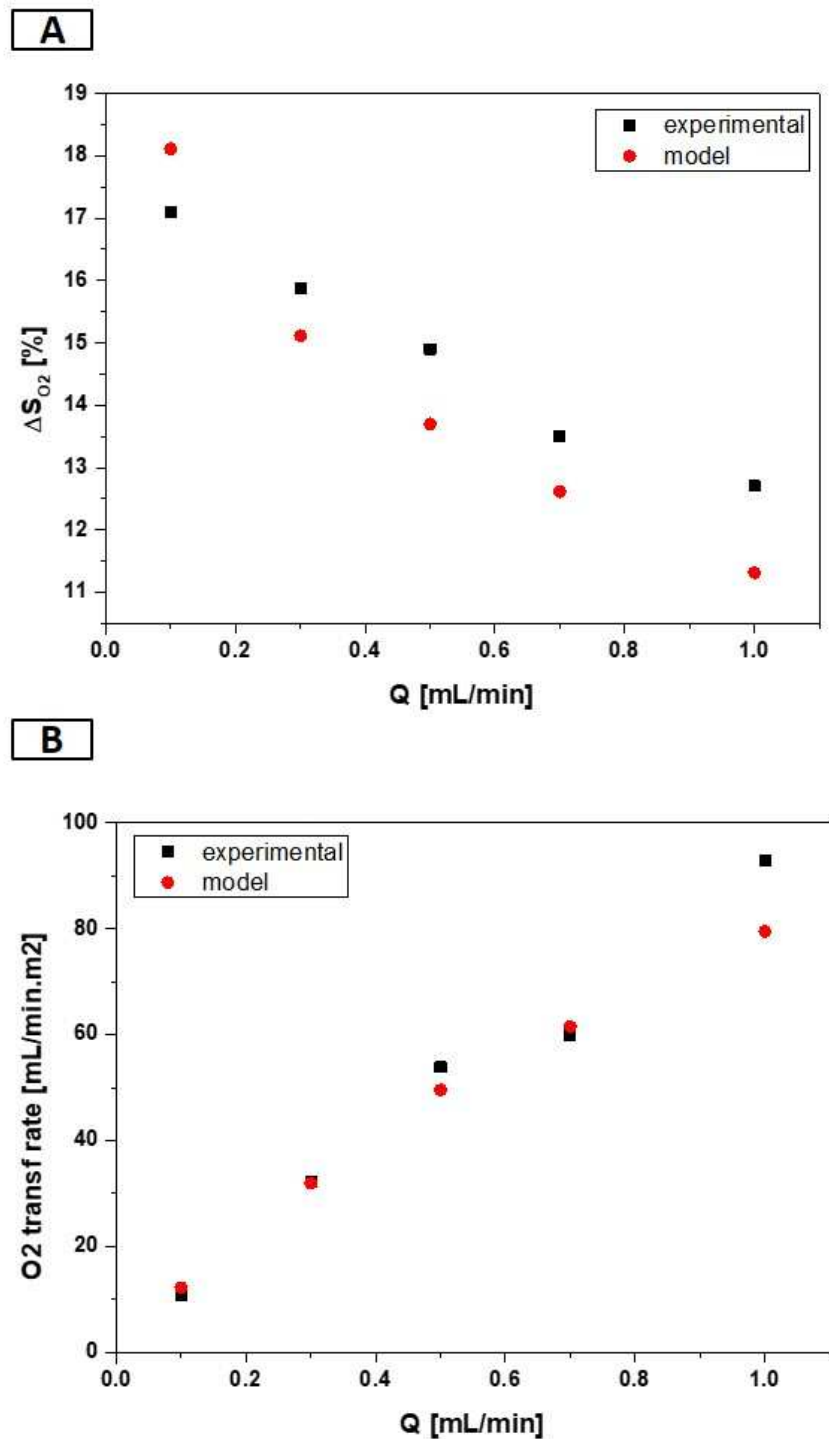
Figure 2.38 The accordance between the mathematical model and experimental values of A) ΔSO2, and B) O2 transfer rate for MD.

Figure 2.39 shows the oxygen saturation profile along the single meander channel for different blood flow rates. The variation of oxygen saturation per unit of length is higher at low blood velocities, i.e. higher τ. For a given experiment, this slope is nearly always the same, with the exception of the first part of the meander that can be seen in the magnification (see Figure

2.39 B). This effect is attributed to the flow development and corresponds to the initial part of the meander channel.
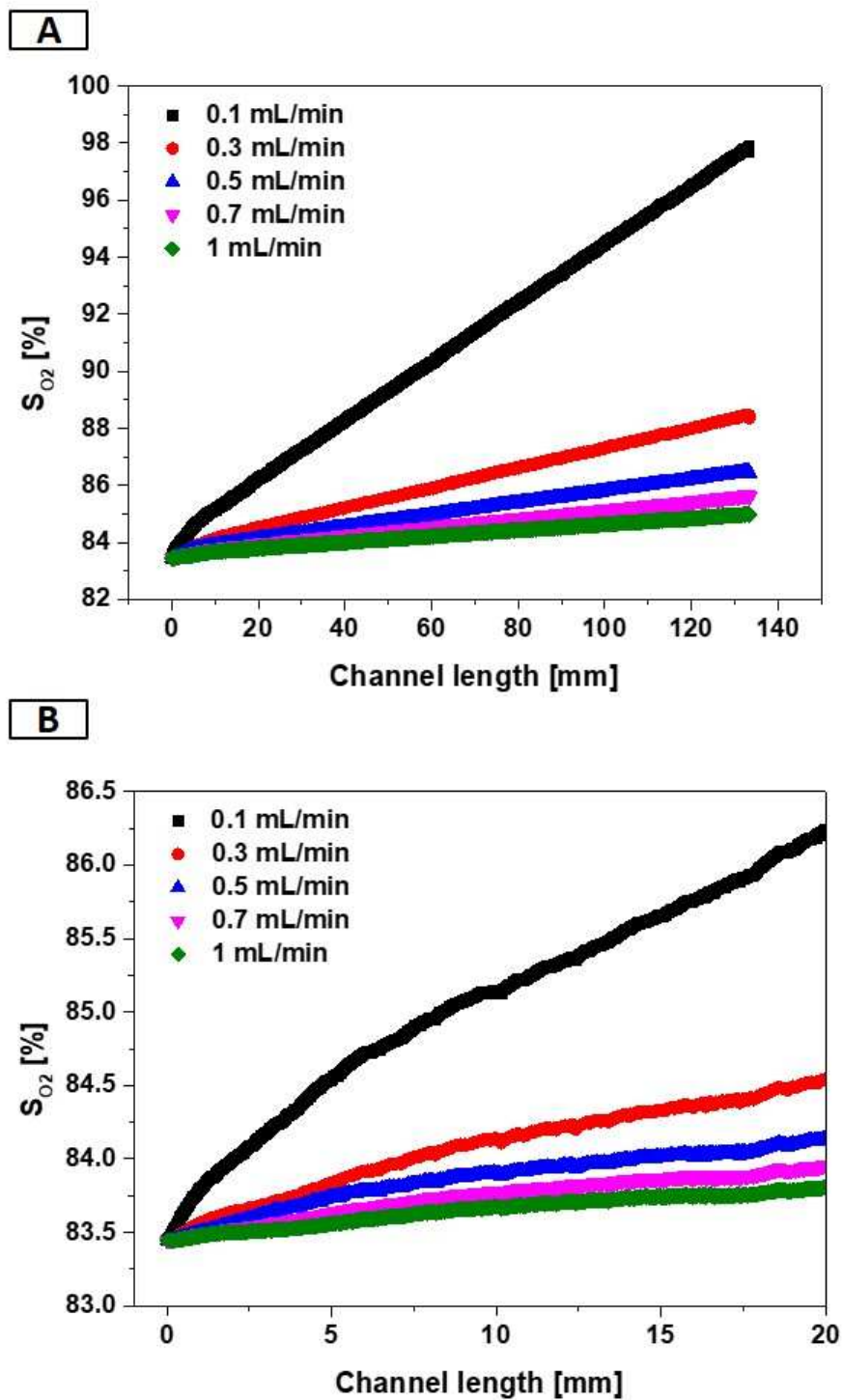
Figure 2.39 Analysis of the oxygenation along the meander type channel

2.5.4.3. Sensitivity analysis of geometric parameters and experimental conditions

The parameter sensitivity simulations for meander device with vertical membrane arrangement were performed in order to quantify the effect of: 1) oxygen concentration from the source gas, 2) membrane thickness, and 3) liquid channel width on the final performance of the device. The target of such parameter sensitivity study was to establish a mathematical equation which will emphasize the importance of a given variable in the oxygenation process. Figure 2.40 shows the sensitivity of the oxygenation to the concentration of the oxygen from the source gas. Three oxygen concentrations were simulated: 100%, 60% and 21% of O_2 entering the system from the gas side. As it was expected, the highest S_{O2} and fastest O_2 transfer is observed in case of pure oxygen. This effect is more important in the case of higher flow, where an increase from 21% to pure oxygen multiply by a factor more than 15% in terms of oxygen transfer rate. Thus, it would be advisable to use pure oxygen to boost the oxygenation process.
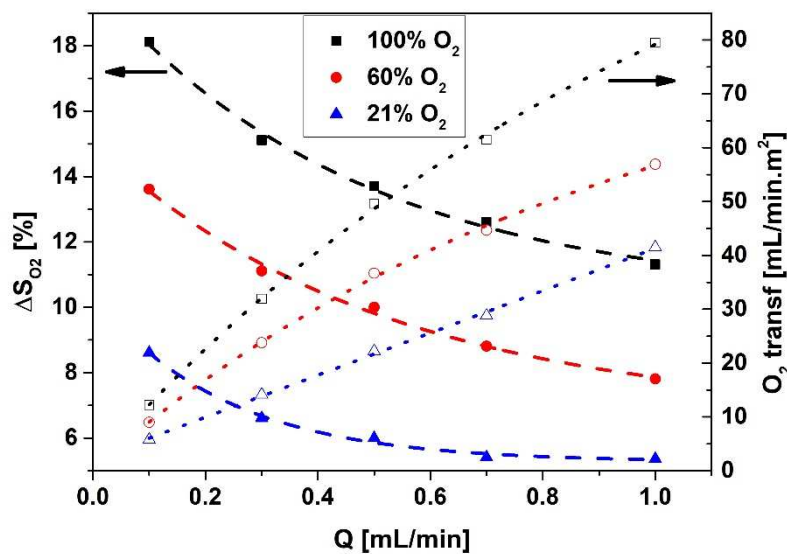
Figure 2.40 Comparison of the oxygen concentration from the source gas on the oxygen transfer rate in the MD at various blood flow rate

Next, Figure 2.41 shows the influence of the membrane thickness on the final performance of the chip. The highest oxygenation was obtained in case of the thinnest membrane due to the minimized resistance for gas diffusion through PDMS and the higher $P_{O2,wall}$ values (partial pressure of oxygen at the membrane wall in contact with blood). This effect is more pronounced in the case of shorter residence time when not only the mass transfer limitations in the liquid phase occur but also there is mass transfer resistance in the membrane side.
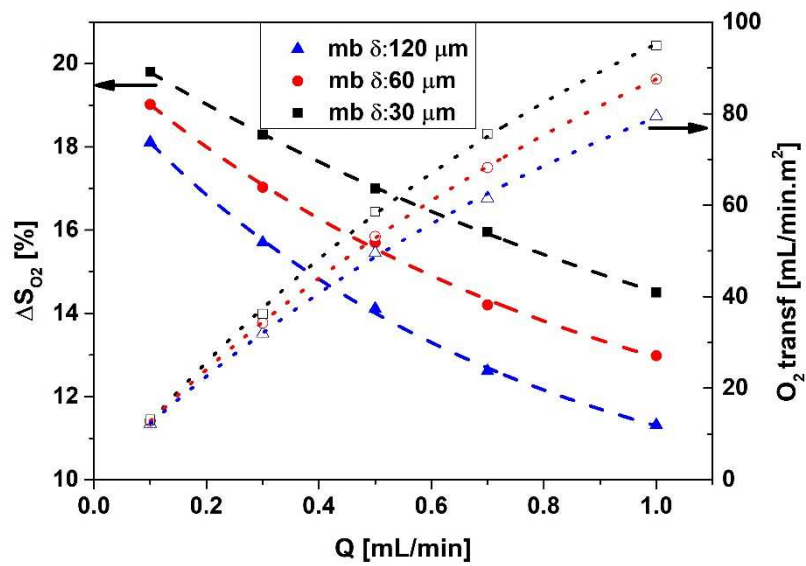
Figure 2.41 Comparison of the influence that membrane thickness possesses on the oxygen transfer rate in the MD at different blood flow rate

The computer simulation presented in Figure 2.42 shows the modification of the oxygen transfer rate and S_{O2} as a function of channel width but keeping constant the cross section of the channels, i.e. the same total volume of the liquid chamber to maintain residence time constant. Four channel widths were simulated: 400 μm, 300 μm, 200 μm, and 100 μm. As it was expected, the thinner the channel the higher O_2 transfer rate due to the smaller pathway that the oxygen has to overcome to bind to Hb.

According to the simulated results, a weight average factor was calculated to illustrate the importance of the different variables studied in the parameter sensitivity analysis on the oxygen saturation values, expressed as ΔS_{O2}. The blood flow rate equal to 0.5 mL/min was chosen for the calculation of these average weight sensitivity factors due to the fact that at this flow rate the blood is in the physiological environment, i.e. ΔP not higher than 20 mmHg.

Microfluidic devices for blood oxygenation
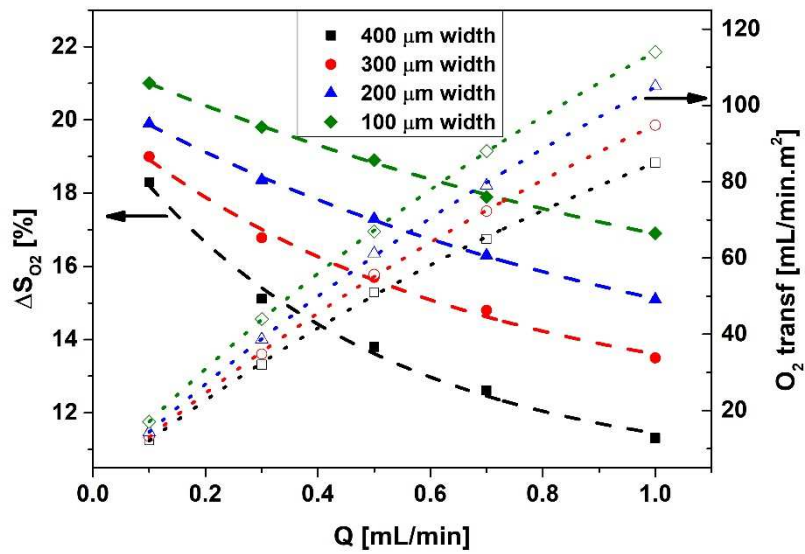
Figure 2.42 Influence of the channel depth in the meander device on the oxygen transfer rate at different blood flow rates

Such average weight sensitivity factors were calculated as follows:

$$a = \frac{\Delta S_{O2_{100\%}} - \Delta S_{O2_{60\%}}}{100 - 60} \tag{2.17}$$

$$b = \frac{\Delta S_{O2_{120\mu m}} - \Delta S_{O2_{60\mu m}}}{120 - 60} \tag{2.18}$$

$$c = \frac{\Delta S_{O2_{400\mu m}} - \Delta S_{O2_{200\mu m}}}{400 - 200} \tag{2.19}$$

Table 2.10 *Average weight sensitivity factors for the MD design*

Value	Description
0.07	Concentration of O_2 in the gas phase [%]
0.03	Membrane thickness [μm]
0.02	Channel width [μm]

The parametric sensitivity analysis showed that the factor which influences the blood oxygenation in the microfluidic meander device is the concentration of oxygen in the gas side. Membrane thickness and channel width are influencing the oxygenation in a comparable way.

To visually demonstrate the parametric sensitivity analysis, Figure 2.43 was developed. It shows the effect of miniaturization on blood oxygenation inside the MD chip. The blood saturation with oxygen in neonates was fixed to be 80% O_2 at the inlet and 95% O_2 at the outlet. The blood flow rate, blood channel depth and membrane surface area were established as well at 0.1 mL/min, 100 μm and 2.9 cm^2, respectively and pure oxygen was used as a supply gas. The computer simulations of the oxygen concentration profile were performed by varying the blood channel width and membrane thickness. The target of Figure 2.43 was to demonstrate the effect that scaling the blood channel width and membrane thickness have on the total volume of the liquid channel for a fixed blood oxygenation.
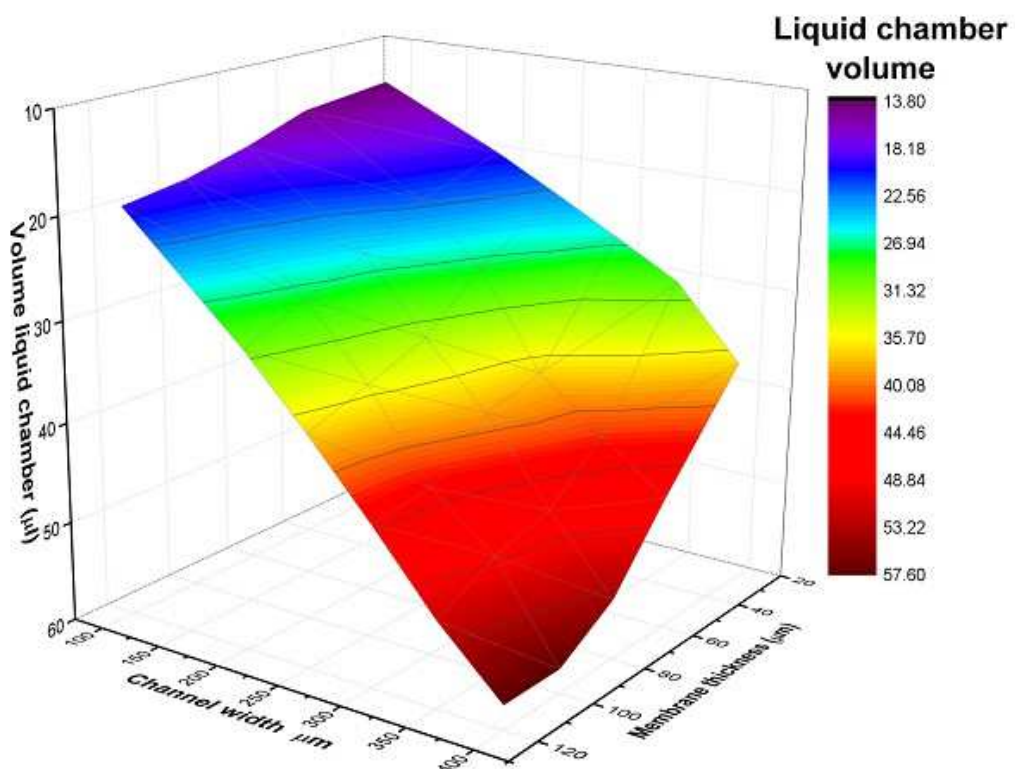
Figure 2.43 A theoretical plot demonstrating the impact of a microfluidic oxygenator device's membrane thickness and blood channel height on its rated blood flow. PDMS was assumed to be the membrane material and pure oxygen was supplied from the gas side

As it is visible in the figure above, the membrane thickness as well as the blood channel width (in the case of the meander type device conformation) have an impact on the liquid volume and on the gas exchange. In order to maximize gas exchange (and gas exchange) both parameters should be minimized as much as possible, without pressure drop and shear stress compensation.

All in all, the mathematical model presented in this section predicted that the performance of the vertical membrane design will be slightly worse than both of the alveolar designs. This might be connected with bigger dimensions of blood channels in case of vertical design, i.e. 400 μm, in comparison to alveolar architecture, i.e. with the smallest width of approximately 50-100 μm. These dimensions influence the diffusion distance of oxygen to blood. Moreover, the alveolar designs demonstrate the alveolar branching architecture, similar to a natural lung which helps in homogenous distribution of a gas. However, the computer simulations show that by decreasing the blood channel width in MD down to 100 μm, the oxygen transfer rate of MD and AD are comparable (see Figure 2.44).

Taking everything into consideration, two different chip conformations and three distinctive liquid side geometries were presented in this chapter, i.e. alveolar and meander type design with vertical membrane arrangement. Each possesses advantageous and disadvantageous. The comparison of the performance of such devices was shown in Figure 2.35 and Figure 2.36. It is visible that the performance of the meander type device is significantly worse than of both alveolar devices even though the oxygen enters the blood chamber from both sides.

2.6. Conclusions

In the presented chapter, two microfluidic chip configurations have been discussed, i.e. alveolar and meander design. The alveolar geometry was successfully modified in order to decrease pressure drop inside the architecture keeping the oxygenation at the same level. The ΔP was decreased by approximately a half without compensation on oxygenation performance. Moreover, AD2 was easier to operate than AD1 due to the lower pressure drop in the system. Computer modelling in COMSOL Multiphysics has enabled to predict the performance of designed structures in terms of pressure drop, homogenous liquid flow and oxygen concentration profile. The fabricated devices exhibit adequate mechanical stability for blood oxygenation applications and the surface modification reveals diminished protein adsorption. The comparison of the oxygen transfer rate obtained in AD and MD to the leading research groups is presented in Figure 2.44. The O_2 transfer rate was calculated from equation 2.16 and normalized with the membrane surface area of each device. The values shown in brackets represent the priming volumes of each microfluidic device. The oxygen transfer velocity increases with an increase of the blood flow rate. However, such increment is not linear, as the ΔS_{O2} dependence. It is visible that especially the performances of the alveolar designs are truly outstanding in comparison to the leading research groups. Moreover, the devices proposed in

this thesis, except high oxygenation performance, possess low pressure drop, can withstand high blood flow rates, i.e. up to 5 mL/min, and have biocompatible surface.
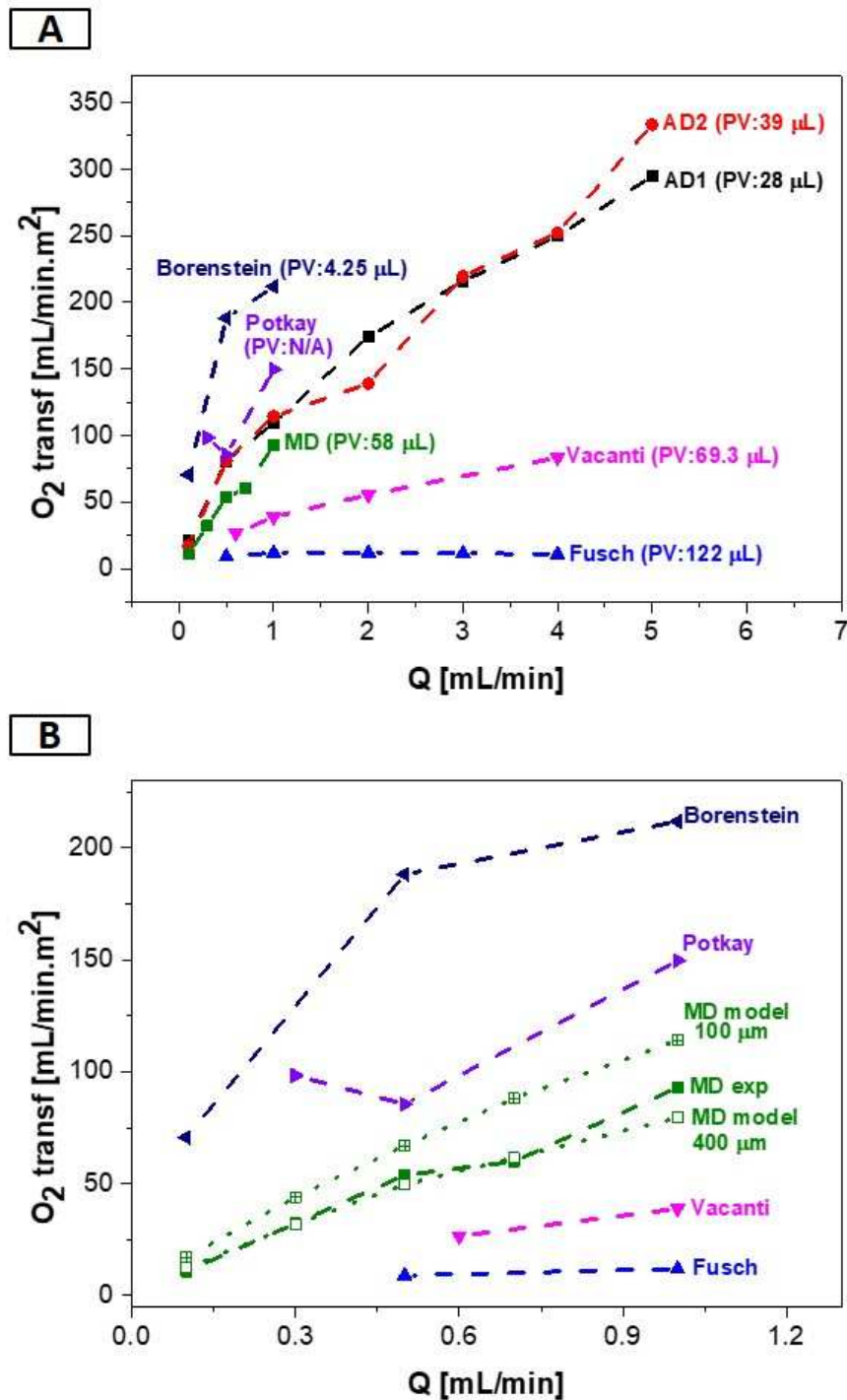
Figure 2.44 Oxygen transfer rate at various liquid flow rates for three different geometries: MD, AD1 and AD2 in comparison to the leading groups at A) entire range of blood flow rates and B) blood flow in the range of 0.1-1 mL/min together with the computer simulations for 100 μm and 400 μm channel width of MD. PV indicates priming volume

Figure 2.44 B shows the O_2 transfer rate for a blood flow rate of 0.1 to 1 mL/min for leading research groups and our MD chips in comparison to the mathematical model of MD with 400 μm and 100 μm channel width, respectively. The oxygen transfer model was validated by means of intercomparison to the experimental results of the meander design. The O_2 transfer rate increases by decreasing the blood channel width down to 100 μm.

Additionally, parameter sensitivity analysis was also performed in order to envision the possible guidelines and to be aware of the importance of each parameter. The chip performance would improve notably by minimizing the values of membrane thickness, channel width and depth.

3. Microfluidic device for Anaesthetic Gas Separation

The concept of a microfluidic device as gas – ionic liquid contactor for CO_2 removal from anaesthesia gas (containing Xe) is introduced. The working principle involves the transport of CO_2 through a flat PDMS membrane followed by the capture and enzymatic bioconversion in the ionic liquid solvent. Thanks to miniaturization, the volume of ionic liquid required to fill the micro-chamber and the amount of CA are notably reduced while providing high throughput for the preliminary screening of different ionic liquids and operational conditions. As proof of concept demonstration, simple gas permeability experiments were performed followed by the experiments with ionic liquid and ionic liquid combined with the enzyme.

3.1. Objectives

The target of the experiments presented in this chapter was to validate a PDMS based gas-liquid membrane contactor in the form of a microfluidic device for CO_2 separation from anaesthetic gas. In the liquid side, the stream of either cholinium propionate ionic liquid (CP) as CO_2 chemical solvent or CP solution containing carbonic anhydrase enzyme (CA) acting as a catalyst was carried out.

3.2. Microfluidic device as G-L Membrane Contactor

As it was described in Chapter 1 section 3.4, the miniaturization of the G-L membrane contactor for anaesthetic gas recovery will be beneficial from fabricating and economical point of view. The manufacture of such chip is inexpensive and easy to scale up. Moreover, the volume of a liquid phase required to fill the micro-chamber is notably reduced.
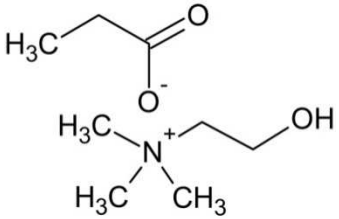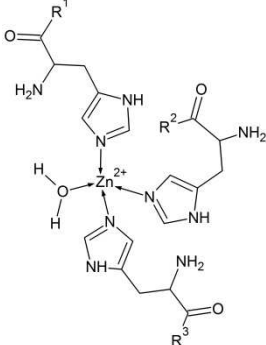
3.2.1. Liquid phase in the G-L microfluidic membrane contactor

It was described that ionic liquids possess high CO_2 absorption properties (see Chapter 1, section 3.3.1). Moreover, cholinium based ILs acquire elevated CO_2 capturing effect and high biodegradability. Based on the work of Martins *et al* [87] it was decided to use cholinium propionate ionic liquid as a liquid phase in the G-L microfluidic membrane contactor for anaesthetic gas recovery. Cholinium propionate IL was prepared by neutralization of propionic acid (purchased from Sigma-Aldrich, USA) in choline hydroxide in the University Nova de Lisboa. One of the significant parameters of IL affecting its viscosity and diffusion of CO_2 is the water activity (a_w). Water activity is defined as the partial pressure of water in a substance divided by the standard state partial vapour pressure of water at the same temperature. It is related to water content in a non-linear relationship named a moisture sorption isotherm curve. Basically, the gas diffusion through an ionic liquid depends on: 1) temperature, 2) molecular size of the gas and 3) viscosity of the IL. Keeping in mind that the molecular size of a gas is constant as well as the temperature of the experiment, the only variable is the viscosity of IL which is related to its a_w. The viscosity of cholinium based IL decreases with the elevated values of water activity due to the molecular interactions promoted by water inside IL and thus, the diffusion of CO_2 increases. Additionally, Henry's constant increases with higher water activity which results in lower CO_2 solubility values due to diminished ability of IL to solubilize CO_2 because of weak affinity between water and carbon dioxide. The water activity of CP IL selected for the CO_2 separation experiments was equal to 0.753 based on the results obtained

by Martins *et al* [87]. Therefore, CP IL was equilibrated into a chosen water activity by sodium chloride salt (Applichem, Panreac, Germany) [121]. Briefly, CP was placed in the gas dessicator with sodium chloride salt at the bottom. The dessicator was placed in the room with controlled temperature equal to 30°C. The water content corresponding to a given water activity was measured by Karl-Fisher coulometer (Metrohm, model 831 KF coulometer).

In order to increase the CO_2 capturing effect, carbonic anhydrase enzyme was added to the cholinium propionate IL. Carbonic anhydrase lyophilized from bovine erythrocytes (ref: C3934, Sigma-Aldrich, USA), was used without any further purification. 0.1 mg of the enzyme was added to 1 g of ionic liquid, and the resulting mixture was placed on the mixing plate till complete dissolution. Enhanced CO_2 transport was expected due to the high solubility of CO_2 in cholinium propionate assisted by the enzymatic CO_2 conversion, that was a chemical reaction, due to the presence of CA that lead to greater driving force. Table 3.1 represents the parameters of the liquid phase selected for the experiments herein described.

Table 3.1 *Parameters of the liquid phase used for CO_2 capturing experiments*

Ionic Liquid	Cholinium propionate (CP) [9]	
Density [$g \cdot cm^{-3}$]	1.07	
Molecular weight [$g \cdot mol^{-1}$]	177	
Viscosity [$Pa \cdot s^{-1}$]	0.039	
Water activity	0.753	
Water content [%]	35.7	
Henry Constant CO_2 [bar]	65.59	
CO_2 Diffusivity [$m^2 \cdot s^{-1}$]	$3.3 \cdot 10^{-10}$	
Enzyme	Carbonic Anhydrase (CA)	
CA conc in IL [$mg \cdot g^{-1}_{IL}$]	0.1	
Water activity	0.753	
Water content for CP [%]	40.9	
Henry constant CO_2 [bar]	74.23	

3.2.2. Microfluidic chip design

The microdevice, proposed for the G-L membrane contactor for anaesthesia gas recovery, consists of two independent chambers, one dedicated to the CO_2 capturing liquid phase and the second one devoted to a gas, separated by the PDMS dense membrane, 60 μm thick. Simple dense membrane was chosen for the proof of concept demonstration in the G-L membrane contactor in order to ensure the stability of the chip and no problems with leakage or membrane detachment. Entire chip was fabricated from PDMS by soft-lithography as it was described in Chapter 2 section (to be defined). Similarly, to blood oxygenation, the mass transfer limitations are mainly attributed to the liquid side; therefore, the key factor in the design of the microfluidic gas-liquid membrane contactor is the liquid side geometry. Hence, liquid channels were arranged in a branching-like-architecture, as it was described before, so the ionic liquid could be distributed in a homogenous flow regime in order to reduce dead volume and to avoid high pressure drop across the structure. The depth of the liquid channel, i.e. 100 μm, also aimed to minimize the mass transfer limitations in the liquid side. On the other hand, the gas chamber, in the form of an empty reservoir, possessed a number of supporting pillars in order to reduce the risk of membrane and chip collapse.

The alveolar design with liquid flow distributors, i.e. D2 (see Chapter 2 section-to be defined) has been mainly adopted for the liquid chamber to ensure that mass transfer of carbon dioxide through the liquid phase, in order to reach the CA active reaction sites, does not become rate controlling. Figure 3.1 shows the conformation of the PDMS microfluidic device for anaesthetic gas recovery.
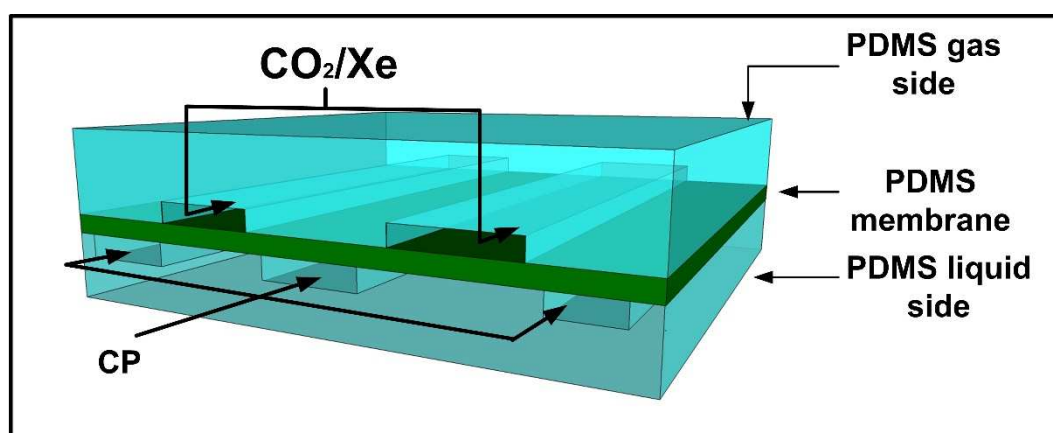
Figure 3.1 Schematic representation of the gas-ionic liquid membrane contactor

The gas, CO_2 or xenon, was introduced in one of the microfluidic chambers. The IL was continuously fed to the liquid chamber with a low flow rate, i.e. 0.01 mL/min, in order to maintain constant and high driving force while the membrane deflection and/or liquid

microchannels blockage are avoided. CO_2 permeated through the membrane and was captured by the liquid side.

Computer modelling in COMSOL Multiphysics 5.0 was performed to calculate the pressure exerted on the walls of the liquid chamber and the homogeneity of the cholinium propionate (CP) ionic liquid flow. Such computer simulation enabled to predict the ionic liquid behaviour inside the microfluidic device and it also helped to define the operational conditions for the IL flow rates. As an example, Figure 3.2 shows the ionic liquid flow distribution in the liquid chamber at standard working conditions (0.01 mL·min^{-1}) for which the resulting ΔP estimated by CFD was equal to 0.014 mbar. However, it had to be taken into account that the tubing and metallic pins used to connect the microdevice to the macro world resulted in elevated pressure drop. Hence, it was observed that the maximum ΔP of the total experimental system before the membrane started to be deflected was approximately 60 mbar at a liquid flow rate indicated above. Detailed explanation and discussion of pressure drop that corresponds to each part of the system is described in Chapter 2 section 2.4.5.
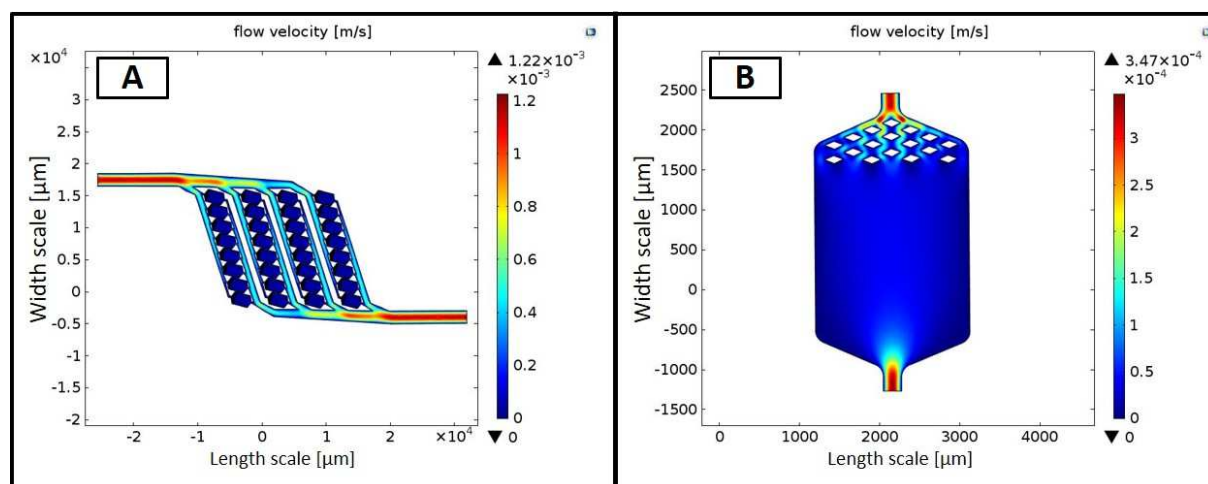
Figure 3.2 CFD simulation of ionic liquid flow distribution in the A) entire geometry of a microdevice and B) single unit of the total geometry at standard working conditions

3.3. Theoretical calculations

The equations presented in this section were used for the evaluation of the gas permeation through the membrane as well as the CO_2 transport from the gas phase to the liquid phase. The expressions to calculate mass transfer coefficients are introduced together with the enhancement factor equation.

3.3.1. Membrane Permeability for Single Components

The gas permeation measurements were carried out by monitoring the pressure changes with time in the feed and permeate side respectively. Thus, pure gas permeability was calculated according to the expression (3.1) which was derived from the mass balance equation under non-steady state conditions [122] and which was also adapted to the experimental system described by Neves et al [97] and used in this work (see section 3.4.1):

$$\frac{1}{\beta} ln\left(\frac{[P_{feed} - P_{perm}]_0}{[P_{feed} - P_{perm}]}\right) = p\frac{t}{l} \tag{3.1}$$

where P_{feed} and P_{perm} are the pressures in the feed and permeate side, respectively [bar], t is time [s], l corresponds to membrane thickness [m], p is the membrane permeability [m^2 s^{-1}] and β [m^{-1}] is the parameter which depends on the geometry of the compartment and is given by:

$$\beta = A\left(\frac{1}{V_{feed}} + \frac{1}{V_{perm}}\right) \tag{3.2}$$

where V_{feed} and V_{perm} are the volumes of the feed and permeate chambers, respectively [m^3], and A is the membrane surface area [m^2]. In the experimental system used for our measurements the value of β was equal to 106.38 [m^{-1}].

The equation (3.1) results in a permeability with the units of m^2 s^{-1}. In order to convert this value into commonly used barrer units, the conversion factor (Conv_Factor) introduced by Cussler [122] was used:

$$Conv\_Factor = \frac{10^{-10}cm^3(STP) \cdot cm}{cm^2 \cdot s \cdot cmHg}\left|\frac{1\,mol\,at\,STP}{22.4 \cdot 10^3 cm^3}\right|\left|\frac{0.082\,atm \cdot L}{mol \cdot K}\right|$$
$$\cdot \left|\frac{76\,cmHg}{1\,atm}\right| \cdot \left|\frac{10^3 cm^3}{1\,L}\right| \cdot \left|\frac{1\quad m^2}{10^4\,cm^2}\right| \cdot T\,[K] \tag{3.3}$$

The conversion factor depends on the temperature. The temperature in each of the experiment was equal to 30ºC. Thus, the Conv_Factor for all the presented experiments calculated from the formula (3.3) is equal to $8.3 \cdot 10^{-13}$. Then, the permeability expressed in m^2 s^{-1} can be converted to barrer unit simply by dividing it by the Conv_Factor:

$$Permeability \ (barrer) = \frac{p \ (m^2 \cdot s^{-1})}{Conv\_Factor} \tag{3.4}$$

3.3.2. Mass Transport in Membrane Contactors

The CO_2 mass transfer in G-L membrane contactors occurs due to the CO_2 permeation across the membrane [123]. In order to evaluate the supplementary mass transfer resistance opposed by the membrane in the G-L absorption process, the overall mass transfer coefficient, denoted as K, and individual mas transfer coefficient in the liquid phase denoted as k_L, were evaluated with and without CA.

The flux of CO_2, denoted as J [mol·m^{-2}·s^{-1}], from the gas to the liquid side in a membrane contactor [99] was calculated from the equation (3.5):

$$J = K\Delta C = K(C_G - C_G^*) \tag{3.5}$$

where K [m·s^{-1}], is the overall mass transfer coefficient for CO_2 transport, ΔC is the driving force: C_G is the CO_2 concentration in the gas phase and C_G^* is the hypothetical CO_2 concentration in the gas phase that is in equilibrium with the CO_2 concentration in the bulk liquid phase.

Under the experimental conditions used in this work (see section 3.3.2) for the evaluation of K_{CO2}, the hypothetical concentration of CO_2 in equilibrium with the CO_2 dissolved in the CP (C_G^*), has been considered negligible due to the CO_2 Henry constant values of the selected cholinium based ionic liquid and the continuous feeding of fresh solvent to the system. Thus, the global mass transfer coefficient was calculated from the exponential fit of the normalized pressure decay in the gas chamber according to the following:

$$-V\frac{dC_G}{dt} = K \cdot A \cdot (C_G - C^*) \tag{3.6}$$

Where, V is the volume of the pressurized gas chamber filled with the single component [m^3] and A is the membrane surface area [m^2]. Since C* is assumed 0, then:

$$\frac{C}{C_0} = e^{-\frac{KA}{V}t} \qquad (3.7) \qquad \text{or} \qquad \frac{P}{P_0} = e^{-\frac{KA}{V}t} \qquad (3.8)$$

The exponential fit of the normalized pressure decrease provides the value of KA/V. The value of global mass transfer K, can be next divided into individual resistances or individual

mass transfer coefficients for each experimental configuration from equation (3.9) which describes the resistance in series model [99] as shown below:

$$\frac{1}{K} = \frac{1}{k_G} + \frac{1}{k_M} + \frac{1}{mEk_L^0} \tag{3.9}$$

where k_G is the individual mass transfer coefficient in the gas phase [m s^{-1}], k_M is the individual mass transfer coefficient opposed by the membrane [m s^{-1}], k_L is the individual liquid phase mass transfer coefficient [m s^{-1}]; k_L^0 is the individual liquid phase mass transfer coefficient [m s^{-1}] in absence of enzyme, m is the Henry's law constant [-] and E is the enhancement factor due to the presence of CA [-].

The membrane resistance (R_M) is calculated simply by the inverse of the individual mass transfer coefficient inside the membrane ($\frac{1}{k_M}$). Similarly, the resistances resulting from the presence of ionic liquid (R_{CP}) or ionic liquid with the enzyme (R_{CP+CA}) are calculated from the inverse of the mass transfer coefficient of the IL $\left(\frac{1}{k_L^0}\right)$ and mass transfer coefficient with the enzyme ($\frac{1}{Ek_L^0}$) respectively.

The overall mass transfer coefficient expression can be simplified further to be solely dependent on k_M and k_L because all the experiments herein performed have been carried out with pure gases resulting in:

$$\frac{1}{K} = \frac{1}{k_M} + \frac{1}{Ek_L^0} \tag{3.10}$$

3.4. Anaesthetic gas separation experiments – principle of the measurements and experimental procedure

The principle of the xenon recovery from the anaesthetic gas is based on the separation of CO_2 from the gas mixture exhaled by the patient during the surgical operation (~65% volume of Xe). Basically, the experiments carried out in this chapter are:

1) Single gas permeation measurements for CO_2, O_2 and Xe on the free – standing PDMS membranes;

2) CO_2 and Xe transport measurements on the microfluidic devices working as G-L membrane contactors with continuous feeding of CP as liquid phase;

3) CO_2 and Xe transport measurements on the microfluidic devices working as G-L membrane contactors with continuous feeding of CP+CA as liquid phase;

In the following sections, the experimental set-ups for each type of experiments together with the working routines are described.

3.4.1. Single Gas Permeability of PDMS free – standing membranes

The permeability of a free-standing PDMS membrane was evaluated, according to the method previously described by Neves *et al* [97]. The target of this set of experiments was to measure the permeation through non – commercial membranes fabricated in our laboratory.

The membranes were fabricated by mixing PDMS pre – polymer with a curing agent in a ratio 10:1 and placed in the vacuum chamber for degassing. Next, the PDMS precursor solution was placed on the silicon wafer and spin coated (WS-400BZ, Laurell Technologies Corporation Spin Coater) at 1000 or 500 revolutions per minute (rpm) for 1 minute resulting in a membrane thickness of 60 μm or 126 μm respectively. The wafer with spin coated membrane was placed in the oven for 45 minutes at 80ºC. The thickness of the fabricated membranes was measured in the Clean Room by a profiler (P-6 Stylus Profiler, Kla Tencor). The PDMS thin films were gently removed from the wafer, cut to the required size, placed on the top of one of the gas compartment and covered with second gas compartment. The membrane was secured by the O-ring in between the stainless – steel compartments.

The gas permeation measurements mainly involved the pressure monitoring with time in both gas compartments, which was related to the gas permeation through the membrane. The experimental system used for the experiments was composed of a: 1) gas source, 2) two identical gas compartments (GC1 and GC2) dedicated to feed and permeate side respectively, and made of stainless – steel (volume: 6cm^3) with the 3) PDMS membrane placed in between, 4) two pressure transducers (Druck PDCR 910 models 99166 and 991675, England) and 5) temperature controller which was immersed in a 6) water bath. The membrane module was placed in a water bath at constant temperature (30ºC) monitored by temperature controller (TC). **Błąd! Nie można odnaleźć źródła odwołania.** shows the schematic representation of the experimental system for the free – standing membrane permeation measurements. The permeability of three different pure gases was evaluated: CO_2, O_2 and Xe. The gas was introduced on the feed side (V1 and V2 opened) and the chamber was pressurized up to approximately 0.7 barg (V3, V4 and V5 closed). As soon as the gas pressure reached 0.7 barg

V1 and V2 were closed. The pressure decay on the feed side and the pressure increase on the permeate side were recorded using the two pressure transducers.
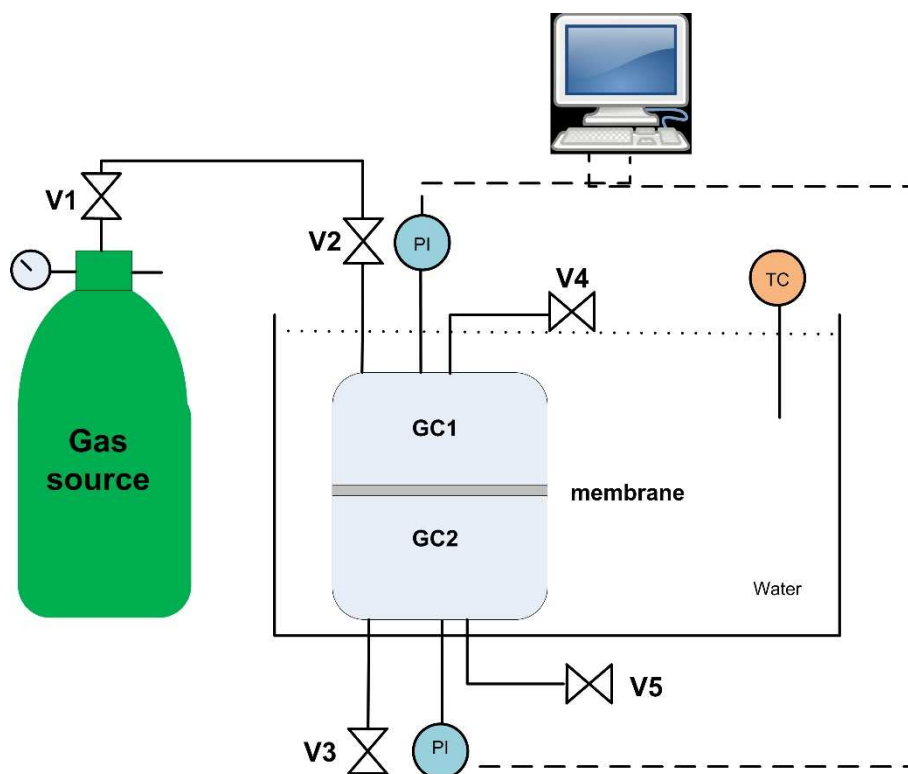
Figure 3.3 Experimental system for the measurement of the gas permeability in the free-standing membrane

3.4.2. Single Gas Transport Measurements on the Microfluidic Devices

The single gas transport measurements on the microfluidic devices working as G-L membrane contactors were carried out in the experimental system shown in Figure 3.4. In this case, the system consisted of: 1) gas source, 2) one pressure transducer connected to the 3) one stainless-steel gas compartment (volume: 72 cm^3), 4) microfluidic device, 5) syringe pump for the liquid phase feeding (NE-1000, New Era Pump Systems Inc. USA), and 6) temperature controller (TC). The gas compartment together with the microfluidic device was immersed in the water bath at 30°C. The gas (xenon or carbon dioxide) was introduced on the feed side with V1 and V2 opened while valves 3 and 4 were closed. The feed side was pressurized up to 0.1 barg, after equilibrium V1 and V2 were closed and V3 was opened. The liquid phase was fed by a syringe pump connected to the liquid chamber (permeate side) at 0.01 cm^3·min^{-1}. The outlet of the liquid side was left open to the atmosphere so there was always a fresh portion of ionic liquid entering the compartment.
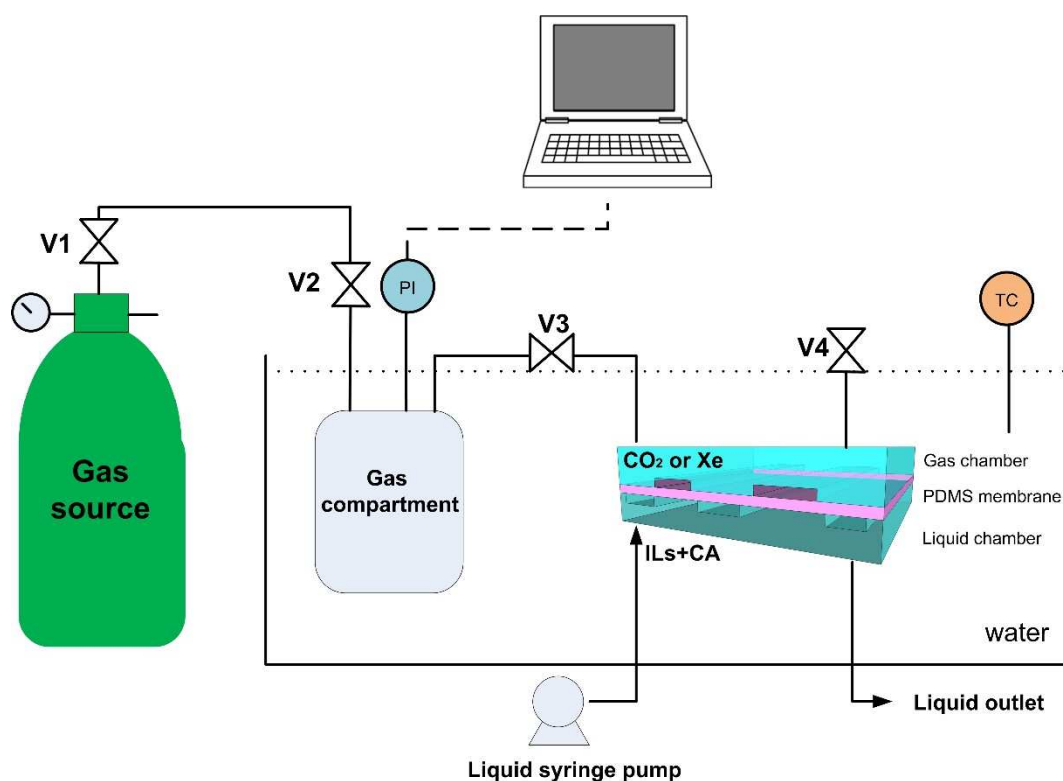
Figure 3.4 Experimental system for measuring the transport rate of CO_2 or Xe in the microfluidic device working as G-L membrane contactor

3.5. Results

In this section, the microfluidic devices working as a gas – liquid membrane contactor are fully characterized. Firstly, proper connections and absence of leaks are checked to ensure reliable results. Then, the permeability results of free – standing membranes are presented. From this information, the effective mass transfer coefficient of the dense PDMS membrane, k_M is calculated for being implemented in equation [3.9]. Next, the mass transfer performance of the microfluidic devices for CO_2 and Xe is studied for CP and CP+CA as liquid media, respectively. The evaluated values for the performance descriptors are discussed and opportunities for further improvement are identified.

3.5.1. Device characterization

Figure 3.5 A shows the photograph of a microchip with liquid chamber (blue dye) and a gas compartment (pink dye) in order to visualize the flow path. The image indicates that the filling of the gas and liquid channels was homogenous, demonstrating that there was no dead volume. Metallic pins were inserted at the inlet and outlet of gas and liquid compartments in order to facilitate introducing the piping into the microchip. In particular, the gas or liquid was introduced to the chip by Tygon microbore tubing (0.020" x 0.060" OD, Cole-Parmer, The

Netherlands) and precision stainless steel dispense tip (0.010" ID, 0.020 OD, 45° bend, Nordson, The Netherlands). To avoid deformations or leaks in the chip, the maximum allowable pressure in the gas side was 0.1 barg. On the other hand, the maximum allowable liquid flow rate was equal to $0.01 mL \cdot min^{-1}$, leading to the pressure drop of the liquid side, considering piping, pins and the chamber, to approximately 60 mbar. Although the use of PDMS elastomer facilitated chip fabrication and reproduction of the same design with thin non – porous membrane attached to the chambers; one of its main limitations is precisely the narrow working conditions for stable operation.

SEM picture of a cross section of a microdevice (Figure 3.5 B) indicates that the membrane was well attached to the microfluidic chambers, resulting in no leaks or deformation of the membrane or the microfluidic chambers. Four chips, with approximately 60 μm membrane thickness, were built and tested. Each microdevice was capable to work for many hours under the standard conditions for this work: 0.1 barg as pressure on the feed side at t=0 and 0.01 $mL \cdot min^{-1}$ as liquid flow rate.
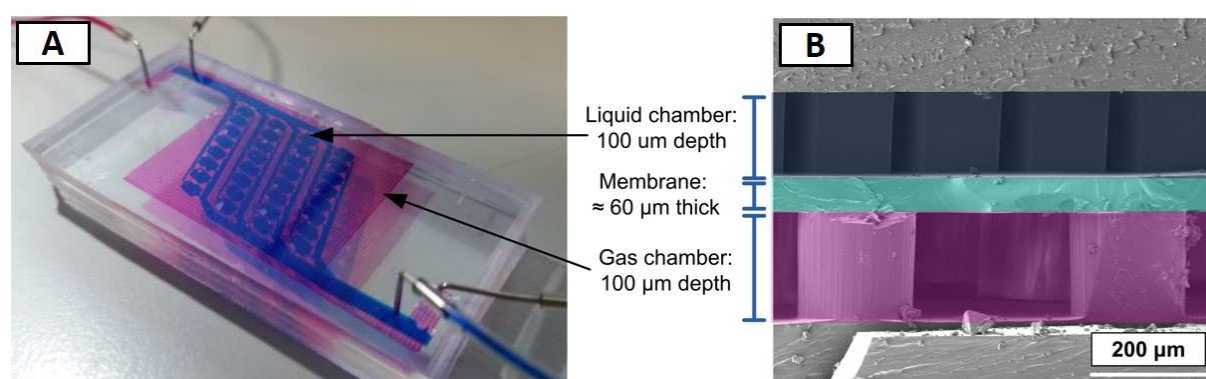
Figure 3.5 PDMS microfluidic device: A) liquid and gas chambers filled with food dye for better visualisation; B) SEM cross section of the chip

The membrane surface area in the chip was equal to 3.9 cm^2. The chip footprint, defined as the total size of the microfluidic device taking into account its width and length, was equal to 18.9 cm^2 making it a very compact system. The thickness of the PDMS mould, where the liquid or gas geometry was embedded, for both compartments was in the range of 0.8 – 1 cm. The depth of the gas as well as liquid chamber was equal to 100 μm resulting in the volume of the gas geometry of 0.073 cm^3 and volume of the liquid 0.038 cm^3, considering only the volumes of the chambers (without any external connections). Hence, the resulting S/V ratio, also denoted as specific gas-liquid interfacial area in absorption processes, is 3500 m^2/m^3, which is higher than the 30-330 m^2/m^3 offered by packed/tray towers and 160-500 m^2/m^3 for mechanically agitated absorption columns. The S/V ratio for the hollow fibre membrane module varies

127

inversely with the fibre diameter, nevertheless the ratio is approximately 15000 m^2/m^3 which exhibits higher values than a microfluidic device [124]. The liquid geometry of the microdevice used for the anaesthesia gas recovery was the alveolar design 2 (AD2) described in detail in Chapter 2 section. Table 3.2 shows the main parameters of the microfluidic device used for CO_2 gas separation.

Table 3.2 *Geometry of the microfluidic chip used as G-L membrane contactor*

Parameter	Value
Membrane thickness [μm]	60
Membrane surface area [cm^2]	3.9
Chip footprint [cm^2]	18.9
Gas chamber volume [μL]	73
Liquid chamber volume [μL]	38
Depth of the liquid/gas channels [μm]	100
S/V ratio [m^{-1}]	3500

3.5.2. Single Gas Permeation Results

The gas permeation experiments of a free – standing membrane (FSM) were performed in the experimental system shown in previous section in Figure 3.3. Pressure decrease at the feed and pressure increase at the permeate side were measured and the resulting permeability was calculated using equation (3.1). Figure 3.6 A shows the pressure variation for two different FSMs (60 μm thick and 126 μm thick) for a typical carbon dioxide experiment. The raw data shows that the pressure decrease of the feed is proportional to the increase of pressure at the permeate indicating that the volumes of the feed and permeate chambers are equal and that there is no leak in the system. The measurements were performed for oxygen, xenon and carbon dioxide and the same behaviour of the gas was observed in all the cases satisfying the mass balance with ±5%. Figure 3.6 B shows the normalized ΔP decay (defined using t=0 as reference) versus time divided by the thickness for three different gases in two earlier mentioned membranes. As it was expected, the slowest normalized pressure drop ($\Delta P/\Delta P_0$) decay rate was

observed in case of oxygen which has the lowest permeability through PDMS membrane, i.e. 310-357 barrer. In contrast, the higher slope was shown for carbon dioxide with highest permeability through PDMS, i.e. 854-843 barrer. Additionally, the decay is overlapped for two different thicknesses of the membranes in the case of oxygen and xenon which do not interact or absorb in the PDMS. However, in the case of CO_2, the decay is faster for the thinner membrane, indicating that CO_2 has a specific absorption on the PDMS. This effect will be considered later in the experiments with the ionic liquid.
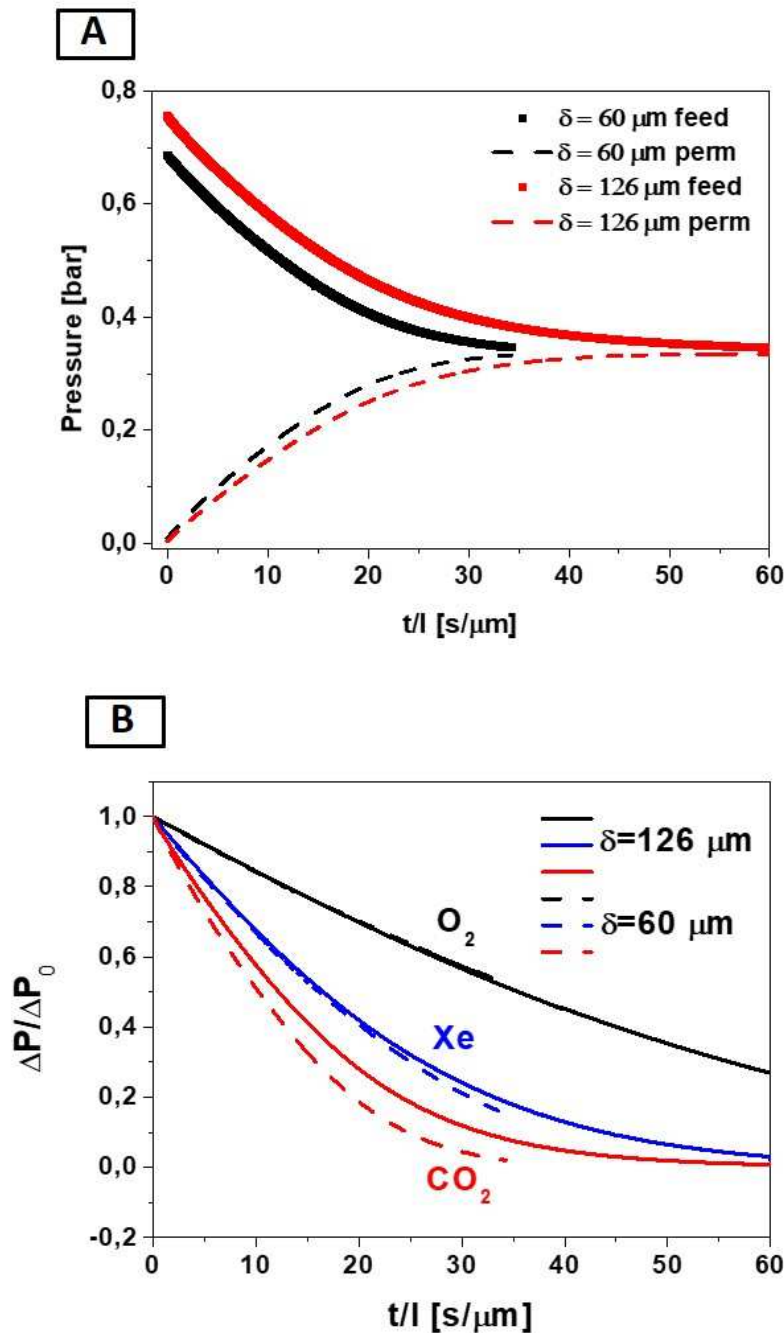
Figure 3.6 Two distinctive free-standing membranes (60 μm and 126 μm thick) and their A) feed pressure decay and permeate pressure increase of CO_2; and B) normalized pressure drop of three different pure gases (O_2, Xe and CO_2)

There are several factors influencing the gas permeation properties of PDMS membranes; mainly mixing ratio and curing temperature. The mixing ratio used in this work of the PDMS prepolymer to the curing agent was 10:1. This ratio is suggested by the producer and it represents a good balance between permeability and mechanical stability of a material. The crosslinking process is defined by the Si – H groups (silicon hydride) and it has a direct influence on the resulting elastomeric network. The higher the mixing ratio, the larger the permeability because less of a curing agent is added to the mixture, which means that the cross linking between the polymer chains is weaker, the polymer matrix is more relaxed and the free volume increases so the gas molecules can move easily within the polymer matrix. Lamberti *et al* analysed the influence of the mixing ratio on the permeability of air through the PDMS membrane. The permeability of this gas increased from approximately 600 barrer at the mixing ratio 10:1 to about 1600 barrer at the ratio 20:1 [125]. However, during membrane fabrication the mechanical stability has to be taken into account for peeling off the membrane from the Si wafer. It was observed that the mixing ratio has an impact on the mechanical properties of the cross – linked material. The elastic modulus (Young's modulus) was examined by tensile measurements. Young's modulus escalates with the higher amount of a curing agent due to a stronger network formation. Summarizing, the bigger amount of a cross – linker the more mechanically stable the structure is with lower permeability at the same time [125-128]. Thus, the optimal prepolymer: curing agent ratio depends on the final application.

The obtained permeability values for three different gases are presented in Table 3.3. As it was expected, the permeability values remain almost constant with the membrane thickness. In the recovery of the anaesthetic gas, we consider only the separation of CO_2 and Xe, thus the ideal selectivity $\alpha_{CO2/Xe}$, calculated as the permeability ratio, was presented in the table. It is also noteworthy that the ideal selectivity $\alpha_{CO2/O2}$, i.e. 2.5, is quite similar to those values published in the literature. Lagorsse et al obtained the $\alpha_{CO2/O2}$ selectivity of 2.69 and 4.55 for two commercially fabricated thin films: Blue Membrane and Carbon Membrane, respectively [62].

Table 3.3 *O_2, CO_2 and Xe permeability values for the prepared free-standing membranes*

Thickness [μm]	Permeability O_2 [barrer]	Permeability CO_2 [barrer]	Permeability Xe [barrer]	Ideal Selectivity $\alpha_{CO2/Xe}$
60	357	854	620	1.4
126	310	843	612	1.4

Moreover, it is concluded from Table 3.3 that the permeability of Xe is only slightly lower than of CO_2 with ideal selectivity of 1.38. In fact the values of the Lennard – Jones kinetic diameter are similar, 3.94 Å and 4.04 Å for CO_2 and Xe respectively [129]. Merkel *et al* studied the permeability of different gases in PDMS and they concluded that even though the kinetic diameters of gases are similar, permeabilities can be different as a result of relative solubility of a gas in PDMS. Typically, gases with higher critical temperatures, 31.1ºCfor CO_2 vs. 16.6ºC for Xe, exhibit high condensability and are more soluble in polymers as well as in liquids.

3.5.3. Single Gas Transport Results in the Microfluidic Device

In this section, the influence of the ionic liquid and ionic liquid combined with the enzyme on the transport rate of xenon and carbon dioxide inside the microfluidic chips are presented and discussed. Special emphasis has been devoted to the comparative analyses of the following processes: 1) CO_2 transport through the PDMS membrane in the absence of solvents in the liquid chamber, 2) CO_2 transport from the gas phase to the liquid phase due to gas permeation followed by chemical reaction in the bulk ionic liquid, and 3) in the bulk ionic liquid containing CA enzyme as catalyst. The global mass transfer resistances resulting from the three procedures and the overall mass transfer coefficients are calculated and interpreted.

The gas permeation experiments through the membrane integrated in the microfluidic chip was carried out in the experimental system shown in Figure 3.4 in section 3.4.2. In this case, the liquid chamber was empty and the valves connecting the chamber to the atmosphere were closed. The pressure decay was recorded for xenon and carbon dioxide. Figure 3.7 A shows the raw data of a pressure decrease at the feed and pressure increase at the permeate side for CO_2 inside one of the chip, while Figure 3.7 B shows the comparison of normalized pressure drop for four different chips, containing membranes with the same thickness 60±2 μm, in case of carbon dioxide. It is visible from Figure 3.7 A that the pressure at the feed decreases slower than the pressure at the permeate increases. This is related to the difference in the volume of two chambers. Taking into account that the feed chamber consists of a gas compartment made of a stainless steel connected to the gas chamber of a microdevice and considering all the pins, piping and valves the total volume of the feed side is 72.83 cm^3. On the other hand, the permeate side consists only of a liquid chamber of a microfluidic device and the piping leading to the volume of 0.12 cm^3.
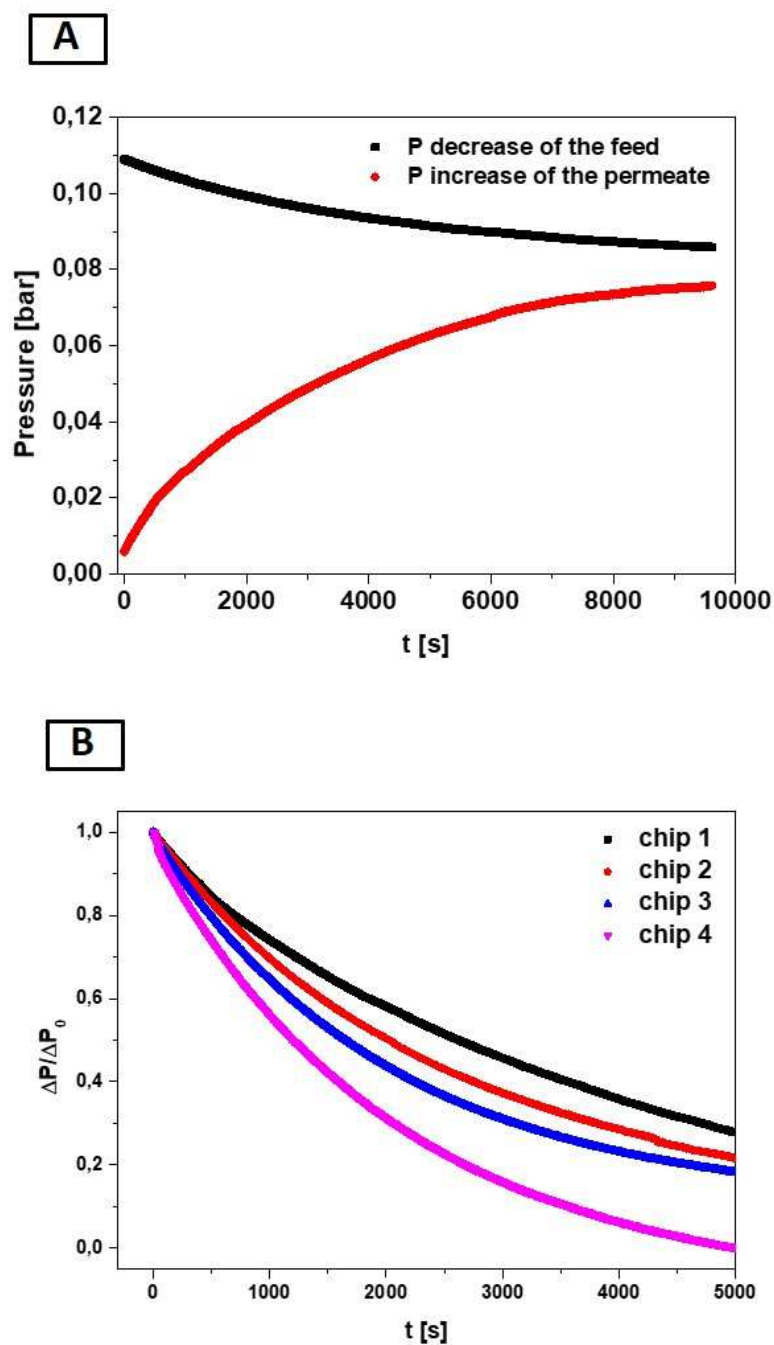
Figure 3.7 A PDMS membrane integrated in the microfluidic device and its (A) feed pressure decay and permeate pressure increase of CO_2 and (B) normalized CO_2 pressure drop recorded for the four different chips prepared in this work.

Additionally, in a proposed microdevice there is not only a membrane which is made of PDMS but also both chambers. The thickness of the PDMS mould of all four chips is comparable, i.e. 0.8-1 cm. Unlike FSMs experiments, shown in section 3.5.2, the amount of CO_2 moles permeating from the feed side significantly differed from the amount of CO_2 moles appearing on the permeate side. The contribution of CO_2 sorption on the PDMS side walls accounts up to 15%. In other words, the gas permeates not only through the membrane but

through the chamber walls, as well, resulting in modified gas transport values. In this scenario, a significant contribution of the PDMS walls effect on the recorded pressure variation in the feed side is expected. To corroborate such hypothesis, the CO_2 permeability measurements of the last chip (chip 4) were carried out slightly different: before the pressure decay measurement, the microfluidic device was saturated with carbon dioxide for about 3 hours. After that time, the measurement was executed as it was described above. The aim of this procedure was to saturate the PDMS walls with CO_2 in order to avoid the effect of the PDMS sink for a gas. Thus, the total transport of a gas occurred through the membrane rather than in the PDMS walls. This is visible in Figure 3.7 B where the biggest decay of a normalized pressure is observed in Chip 4. Hence, it was decided that to avoid the PDMS walls effect, the values of the membrane permeability and a membrane resistance for a given gas will be taken from the experiments presented in the previous section for a free – standing membrane.

In order to increase the driving force for CO_2 transport and CO_2/Xe selectivity, cholinium propionate ionic liquid, CP; alone or combined with carbonic anhydrase enzyme, CA, was introduced to the liquid chamber by a syringe pump with the flow rate of 0.01 mL min^{-1} as it is presented in the experimental set – up in Figure 3.4. The experiments were carried out for the four different chips with PDMS dense membrane, 60±2 μm thick. To confirm that CP and CP+CA does not have any influence on the transport rate of xenon, an identical set of experiments were carried out in the case of Xe as well. As it was done in the previous measurements, pressure decay in the gas chamber was recorded and the calculation of the total resistance for each single experiment was performed.

Figure 3.8 comparatively shows the normalized pressure decay in the feed side for all three experimental configurations as a function of time for CO_2 (A) and Xe (B), respectively. There is no visible effect of ionic liquid and the enzyme on the affinity of xenon in comparison to the measurements with the empty liquid chamber. Additionally, there is a slight enhancement in the CO_2 pressure decay rate in presence of the CP. The carbon dioxide pressure decreases even more rapidly as a result of the catalytic chemical reaction due to the presence of the CA in the CP.

Figure 3.9 represents the final decay of gas pressure in the feed side of four different chips at the three experimental configurations in the form of a bar graph. It is visible that the ionic liquid has a positive influence on the CO_2 transport and it increases it slightly. However, the biggest rise in the gas transport is obtained when the catalytic enzyme is added to the CP, which is in agreement with previous works and results obtained by Martins *et al* after addition of CA in CP in a bulk system [87, 97].
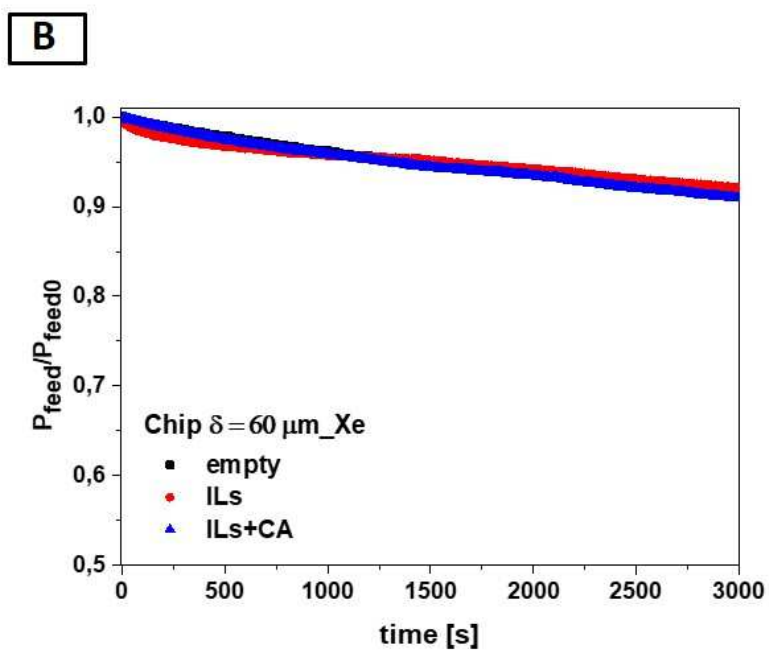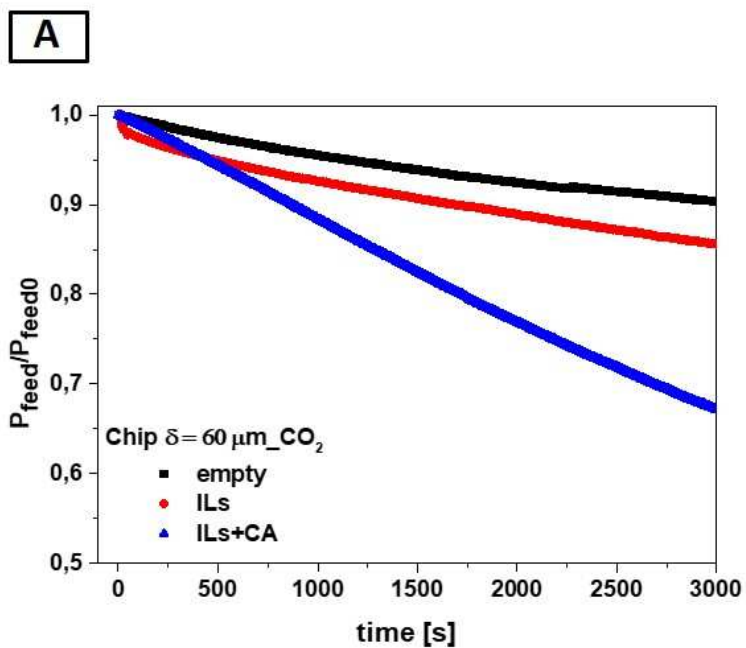
Figure 3.8 Normalized pressure decay in the feed side over time in the empty chip (no IL), the chip with CP and the chip filled with CP and CA for A) CO_2 and B) Xe
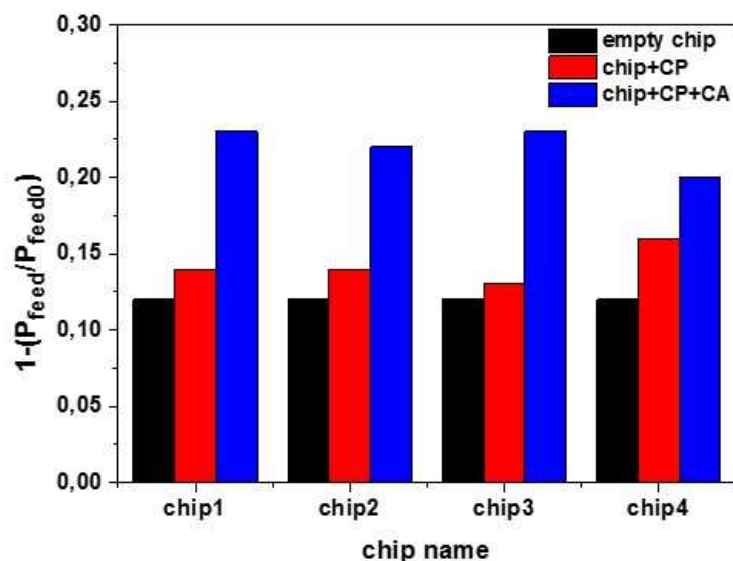
Figure 3.9 Enhanced CO_2 transport due to the presence of ionic liquid and the enzyme: results for the four different chips prepared in this work

Table 3.4 compiles the estimated values for the mass transfer coefficients at the three experimental configurations. In particular, for the estimation of the K_{CO_2} in absence of solvents in the liquid chamber, i.e. k_M, the registered permeability value for the FSMs (see Table 3.3) and the specific thickness of the PDMS membrane were used. The enhancement factor due to the addition of the enzyme is also presented in the table together with the CO_2/Xe transport selectivity for the CP+CA configuration, which was calculated as a quotient of K_{CO_2}/K_{Xe}.

***Table 3.4** Microfluidic Device Performance for CO_2/Xe separation.*

Chip	Chip	Chip+CP		Chip+CP+CA			
	$K_{CO_2} = k_M$	$K_{CO_2} = \dfrac{1}{\dfrac{1}{k_M} + \dfrac{1}{mk_L^0}}$ $[\text{m·s}^{-1}]$	$R_{CP}\,[\%]$	$K_{CO_2} = \dfrac{1}{\dfrac{1}{k_M} + \dfrac{1}{mEk_L^0}}$ $[\text{m·s}^{-1}]$	R_{CP+CA} $[\%]$	E	Transport Selectivity CO_2/Xe
1	$1.19 \cdot 10^{-5}$	$1.24 \cdot 10^{-6}$	89.6	$2.11 \cdot 10^{-6}$	82.3	1.9	3.5
2	$1.17 \cdot 10^{-5}$	$1.25 \cdot 10^{-6}$	89.3	$2.07 \cdot 10^{-6}$	82.3	1.8	2.9
3	$1.10 \cdot 10^{-5}$	$1.58 \cdot 10^{-6}$	85.6	$2.11 \cdot 10^{-6}$	80.8	1.4	3.8
4	$1.14 \cdot 10^{-5}$	$1.51 \cdot 10^{-6}$	86.8	$1.87 \cdot 10^{-6}$	83.6	1.3	3.0

As it was expected, the obtained results are indicating that the main controlling resistance to CO_2 transport in the gas – liquid membrane contactor is located in the liquid phase. When a membrane contactor is used in place of a direct contact G-L absorption column, the intensification factor (i.e. size reduction effect) essentially depends on the product of the overall mass transfer coefficient by the specific gas–liquid interfacial area S/V. In general, compared to packed columns, a large increase of the interfacial area is offered by the membrane contactor. For the microdevices herein used, this value scales up to 3500 m^{-1}. In contrast, the overall mass transfer coefficient K necessarily decreases almost one order of magnitude due to the supplementary mass transfer resistance opposed by the membrane, which is directly related to the membrane thickness. In this work, the membrane mass transfer coefficient, thanks to the PDMS permeability and the thickness of the spin-coated membrane, is comparable to the range of coefficients when a direct gas-ionic liquid contact applies, i.e. 10^{-4} -10^{-5} $m \cdot s^{-1}$ [14].

We found that individual liquid phase resistance values R_{CP} are in the range of 85-90% of the total resistance. The overall mass transfer coefficients are two orders of magnitude lower than the ones presented by Yong *et al* due to higher viscosity of the ionic liquid (39 mPa·s vs 2 mPa·s) and the lower solvent Reynolds number, (0.001 vs. 20) used in this work. Additionally, in our case, we were not able to increase the flow rate of the IL because this would augment the pressure drop in the entire system, above the limit of 0.1 bar, leading to deformation and leaks in the chambers. The enhancement factor on CO_2 transport due to the presence of the enzyme increases up to 1.9. This value is clearly outstanding compared to published results [99] due to the lower amount of free enzyme in the microfluidic device, i.e. 4 μg. The enhancement factor (E) results after addition of carbonic anhydrase to cholinium propionate ionic liquid are in agreement with the results obtained by Martins *et al.* for bulk experiments [87] where an enhancement of 1.6 was obtained. This observation supports the benefits of the alveolar type design for ensuring the facile access to the catalytic CA active reaction sites. Finally, the CO_2/Xe transport selectivity after addition of the ionic liquid and the enzyme increased up to 3.8.

3.6. Conclusions and Future Work

In summary, we have investigated the effect of CP ionic liquid and its combination with CA catalyst on the CO_2 transport properties in a PDMS microfluidic device working as G-L membrane contactor. The microfluidic experimental system, compatible with the solvents used, was tested at semi-continuous operation mode, i.e. continuous for the liquid phase but discontinuous for the gas phase. Even though the permeability of PDMS for Xe and CO_2 was

similar, the cholinium propionate and cholinium propionate in combination with carbonic anhydrase led to a significant improvement on the CO_2/Xe transport selectivity due to the distinctive chemical absorption of CO_2 by the liquid phase.

This work serves as the proof of concept demonstration for CO_2 removal from the anaesthesia gas through a membrane contactor in the form of a microfluidic device. Thanks to miniaturization, the consumption of the chemicals, i.e. ionic liquid and enzyme, is notably reduced; whereas the S/V ratio overpasses the standards for direct G-L contact systems. At the same time, it provides noticeable enhancement factor due the reduction of the diffusion pathways to access to the catalytic CA active: up to 1.9 in the presence of 4 µg of the enzyme. Additionally, this type of liquid side geometry and device assembly could be successfully used for the xenon recirculatory machines for neonates where the low capacity is mandatory.

Further research in a close future should also consider:

-Alternative materials for the fabrication of the microfluidic chambers compatible with the IL phase, in order to avoid the sink effect on the walls and to enlarge the operational working window ensuring the chip integrity. Ideally, large transmembrane pressure difference is desired in order to be used for the regeneration step. In this sense, the use of thicker membranes would be more convenient.

-The exploration of novel membrane architectures (porous, corrugated) to enlarge the S/V ratio and, consequently the overall transport rate.

-The use of higher concentrations of the CA enzyme, playing as catalyst, and solvent flow – rates to enlarge the mass transfer coefficients in the liquid phase.

4. 3D Fractal Geometry for gas permeation in microchannels

This chapter introduces an alternative concept of a silicon/glass microfluidic chip with an integrated nanoporous siliconoxide membrane in the form of three-dimensional fractal geometries with nanopores for gas permeation. The fractal structures, that are fabricated by oxide corner lithography, are hollow which enables the gas to enter to the 3D geometry and to permeate through the nanopore. The chips possess extraordinarily high surface-to-volume ratio, i.e. 2000 m^{-1}, and are characterized by controlling diffusion distances, in the order of 100 nm. As a proof of concept, simple gas permeation experiments are performed to identify the permeation mechanism. The obtained results are compared to the gas permeation properties of dense PDMS membrane as benchmark in order to assess about their potentiality. The developed chip, emerge as an alternative for G-L or G-G contactors that require harsh conditions.

4.1. Introduction

The importance of membranes in microfluidic systems is reflected in the diversity of applications where they are deployed. Among them, it is worthy to mention the detection of chemical reagents and gases, drug screening, cell growing, protein separation, microreactors, electrokinetic ion and fluid transport and pumps and valves for fluid or chip handling [130, 131]. In particular, when the role of the membrane is to act as a gas-liquid interface, effective gas permeation and minimal leakage is required [132].

The key step for the combination of membranes and microfluidics is the sealing for avoiding leakages, especially in the case of gases. The most convenient strategies for the incorporation of membranes in microfluidics, which solve the key issue of sealing, include: i) the preparation of the membrane as a part of the silicon chip, and ii) the use of the permeation properties of chip polymeric material itself [130]. In the case of biological applications, this last option has been adopted in most of the cases using PDMS chips. It is well known that this polymer possesses high oxygen permeability [133]. However, when chemical or temperature resistance is needed, the use of silicon chips would be preferred. Therefore, the replacement of a conventionally used gas permeable PDMS chips by silicon structure and the concept of porous membrane made of fractals containing nanoapertures would result in effective, compact and inert gas permeation device. Moreover, the elevated surface to volume ratio is emphasized to improve efficiency of the process and chip throughput.

4.2. Fractal geometry

Fractal geometry describes disciplines that consider broken structures where, after magnification, the shape appears identical. In other words, the magnified piece is an almost copy of the whole [134]. Recently, Berenschot *et al* from the University of Twente has developed the fabrication method, based on a combination of anisotropic etching of silicon and corner lithography, to create small nanoapertures of approximately 80-100 nm [134, 135]. Briefly, conformal deposition of layers of silicon nitride by low-pressure chemical vapor deposition (LPCVD), and thermal oxide and partly back-etching of a silicon nitride layer that is placed inside the octahedral silicon pits is used in order to form dots in sharp concave corners. The crystalline property of silicon and a gradual etching characteristic of its (111) planes result in the formation of octahedral cavities. Repeated corner lithography, in combination with anisotropic etching, results in the construction of 3D octahedral fractals which are hollow inside

and where the number of layers can be controlled (for more detailed fabrication procedure see Appendix 1).

The important features of this process are the possibility to scale up to wafer level and the ability to tailor the number of apertures and thus control the diffusion of gases through them. These apertures are distributed on the corners of pyramids which are part of a 3D fractal structure that could be replicated (see Figure 4.1). To decrease mass transfer limitations, which often are encountered in the liquid side of the channels, the 3D fractal structure could be embedded in a microfluidic channel which results in larger interfacial area and higher surface to volume ratio. The schematic drawing of this structure and how it evolves is presented in Figure 4.1 B. The blue octahedral structures in the fractal correspond to 1st and 2nd generation and the transparent structures correspond to 3rd generation that will be created after a corner lithography process, containing pores represented by the yellow dots.
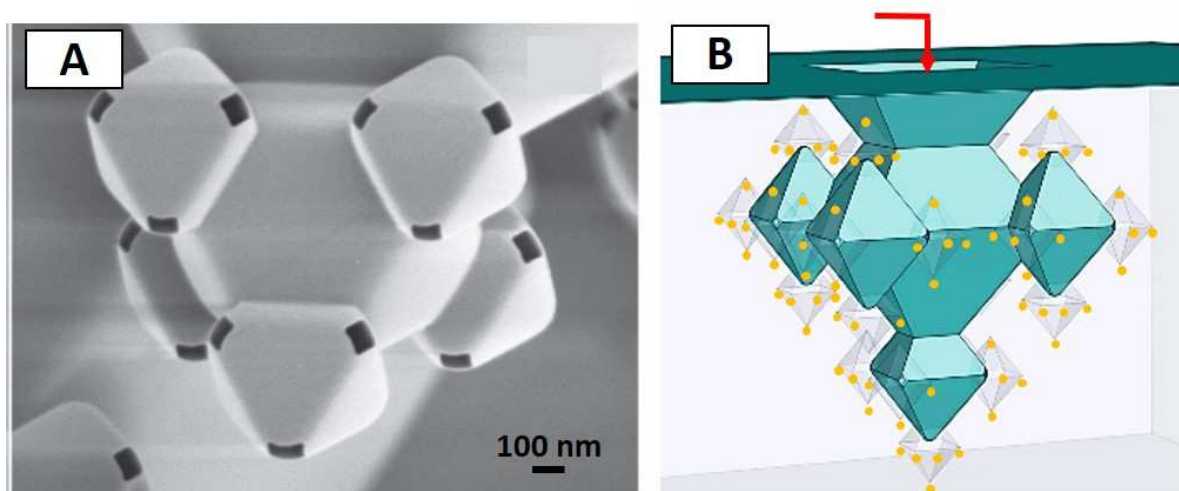
Figure 4.1 A) SEM image of 3rd generation open fractals, B) Schematic representation of fractal

In order to maximize gas diffusion and increase surface to volume ratio, the fractals with three generations have been selected for this work. Figure 4.2 shows the SEM photograph of three fabrication stages of the fractal geometry (the apertures of the 3rd generation fractals are not visible in this SEM image).
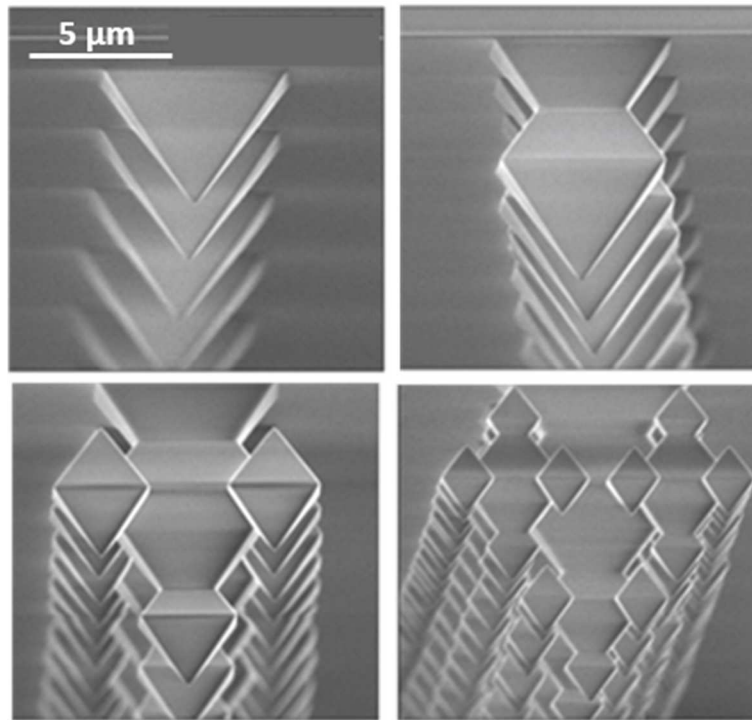
Figure 4.2 SEM image of 0th, 1st, 2nd and 3rd fabrication stage

4.3. Experimental procedure

4.3.1. Chip design and assembly

The main considerations in the design of a proposed chip for gas diffusion in a channel are: 1) the number of fractal levels fabricated, that is directly connected with the number of openings, 2) the number of fractals in the channel, 3) the space among them and 4) the distance from one phase to another, i.e. the depth of the channel which is related to the diffusion distance. Moreover, it had to be considered that the size and density of the fabricated fractals had to be extremely precise in order to avoid merging of fractals during its expansion. Therefore, the octahedral size of the next level should never be bigger than the half size of the previous fractal geometry. The etch rate should be monitored and nanonozzle size should be minimized, when the maximum density is anticipated (for detailed fabrication procedure of fractal three-dimensional architecture based on the corner lithography see Appendix I).

In this work the fabricated structures were integrated in the microfluidic chip that will be adopted for the gas diffusion through the nanonozzles for the first time. In particular, the fractal structures were fabricated in a channel 3.5 cm long and 300 (Chip 1) or 500 (Chip 2) microns wide, containing a total of 244 (Chip 1) and 308 (Chip 2), 3rd generation fractals, unevenly

distributed along the channel. Before the experiments, the total number of fractals containing open pores was evaluated by optical microscopy; the final number of estimated pores and characteristics of the chips is presented in Table 4.1. The total surface area of the channel was assumed as the active surface area of the membrane. The porosity was calculated as the volumetric porosity by dividing the volume of the 3rd generation entities by total volume of the structure, i.e. the microchannel on the permeate side (see Figure 4.3).

Table 4.1 *Properties of fabricated fractal chips*

	Chip 1	**Chip 2**
Channel width (µm)	500	300
Number open fractal structures	244	308
Surface area [m^2]	1.75·10^{-5}	1.05·10^{-5}
Volumetric porosity, ε	3.72·10^{-6}	7.67·10^{-6}
Size of the starting groove of fractal, 0th level (µm)	25	

The channel containing fractal structures was anodically bonded to a glass wafer with powder blasted holes and assembled together with another wafer containing a single channel 500 µm in height and same width and length as the fractal channels. Figure 4.3 shows a schematic representation of the final chip, containing a single freehanging fractal for simplicity.
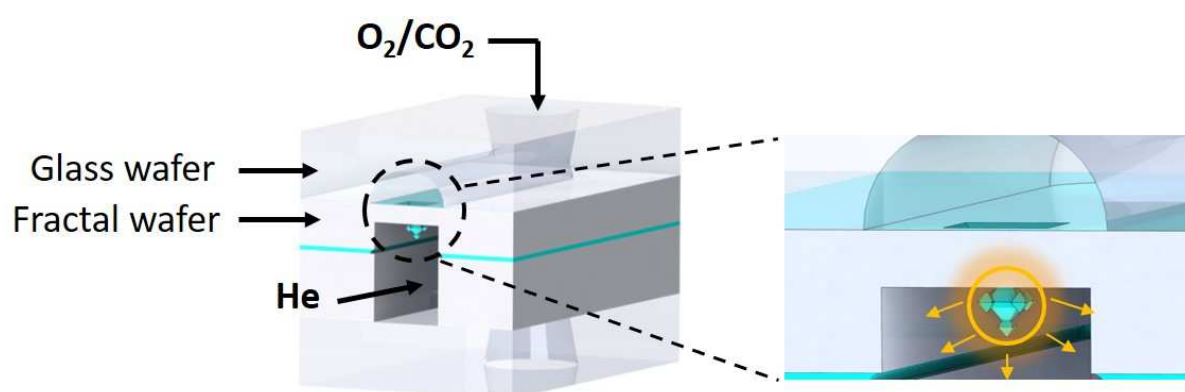
Figure 4.3 Schematic representation of the silicon nanonozzle chip vertical cross-section

Moreover, it was necessary to connect the microchip to the external piping in order to be able to perform the permeation experiments. Therefore, the fractal holder was designed and printed by a 3D printer (RapidShape S30L) at the University of Twente. Four identical parts

were printed from a photopolymer resin and the chip was "sandwiched" in between two parts at the inlet and two parts at the outlet of the chip. The holder parts were connected to each other by two pins with 1.5 mm diameter. Each fractal holder part consisted of a thread (3.95 mm diameter, 0.7938 threading and 32 pitch) in order to connect the external capillary, 360 μm diameter (Teknokroma, Tubing Fused Silica) through the nanoport fittings (IDEX Health&Science, Nanoport Fittings) to enable the transfer lime (3.2 mm diameter) connection of a feed and sweep gases at the inlet as well as retentate and permeate gases at the outlet (see Figure 4.4).
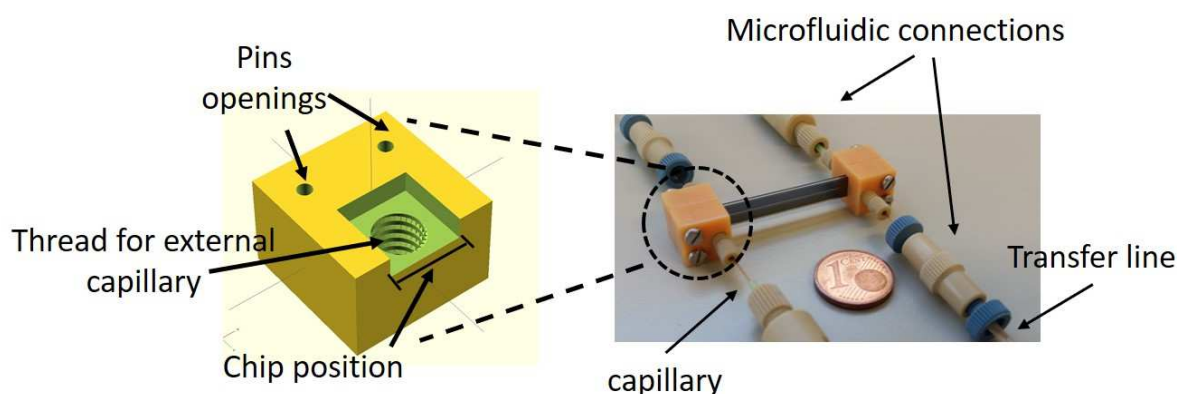
Figure 4.4 Fractal holder and chip assembly

4.3.2. Gas permeation measurements

The experimental system for gas permeation (see Figure 4.5) consists of: 1) gas source, 2) mass flow controllers (Brooks, 5850 TR, USA), 3) pressure transducer (Panasonic, DP2-41E, Spain), 4) microfluidic fractal chip, and 5) micro – Gas Chromatograph (Micro – GC, Varian CP-4900, EVISA, USA). Two bubble meters were placed at the retentate and permeate side, respectively in order to measure the gas flow rates to ensure that there were no leaks in the system.

The permeation of two gases was measured: O_2 (purity grade 99.999% Praxair, USA) and CO_2 (high-purity grade 99.998% Praxair, USA). One of these two gases was introduced to the feed chamber at a given flow rate, controlled by mass flow controller (MFC). The pressure on this side was measured by a pressure transducer (PI). The ΔP between two chambers was in the range of $2 \cdot 10^5$ Pa. The sweep gas (He, purity grade 99.999% Praxair, USA) was introduced to the permeate chamber of the fractal microfluidic chip at a constant flow rate, 10 mL STP/min. The gas permeated through the nanoapertures to the permeate side and the mixture He + gas (CO_2 or O_2) was analysed in the Micro GC equipped with two modules, one with a M5A mole-

sieve column and the other with Pora PLOT Q (PPQ) column. He was used as a carrier gas in both columns. The micro-GC was calibrated in the range of 2.5 to 4.5% in volume for CO_2 and O_2, respectively.
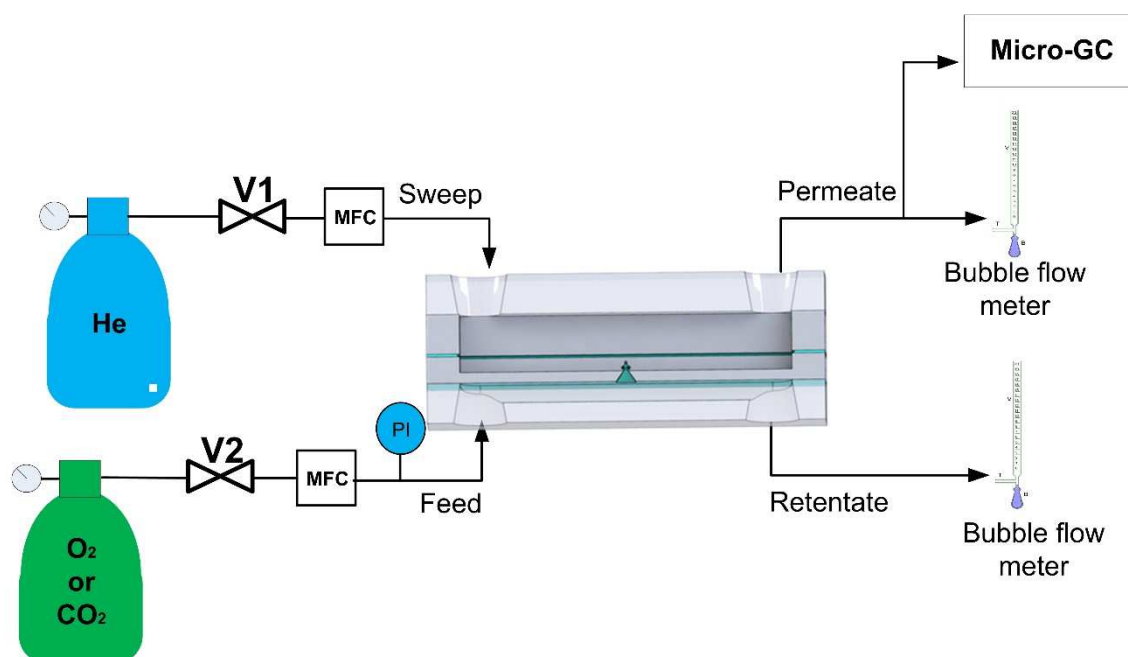
Figure 4.5 Experimental system for gas permeation

The permeation was calculated according to equation (4.1):

$$P_i = \frac{Q_{perm}\, Y_i}{A\, \Delta P_i} \tag{4.1}$$

Where P_i is the permeance of the gas (i.e. O_2 or CO_2) [mole/m^2·s·Pa], Q_{perm} is the total molar flow of the permeate [mole/s], Y_i is the molar fraction in the permeate side, and ΔP_i corresponds to the driving force for permeation of "i" species and is the difference between the partial pressure in the feed side and the permeate side, respectively.

4.4. Results

To evaluate the permeation through the pores of the fractal geometry two possible permeation mechanisms occurring simultaneously could be considered: molecular flow (or Knudsen) and viscous flow (or Poiseuille) (see Figure 4.6) [136, 137].
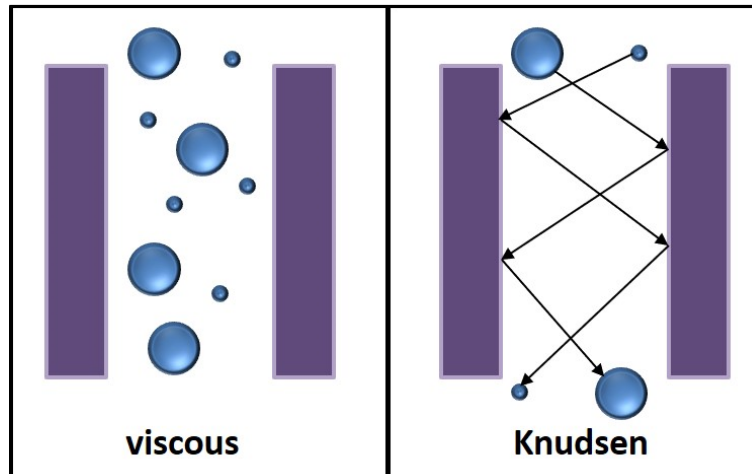
Figure 4.6 Visual demonstration of viscous and Knudsen transport mechanisms

Viscous flow occurs when the size of the pore that the gas is flowing through is significantly larger than the mean free path of the gas (e.g. $d_p \gg \lambda$), defined as the average distance the particle travels between collisions with other moving particles. If the pore diameter decreases and becomes smaller than mean free path, (e.g. $d_p \ll \lambda$), the flow regime gradually starts to change. The mean free path can be calculated from the kinetic theory of ideal gases. Gas molecules are immediately adsorbed after each collision, and they are reflected in a random direction. The collisions of molecule-molecule are rare, and thus each gas molecule moves independently of each other. This type of gas permeation is called Knudsen diffusion. A lower limit for the significance of the Knudsen mechanism has usually been set at $d_p > 20$ Å. Different flow regimes were described by Knudsen who introduced the dimensionless Knudsen number: $Kn = \lambda/d$, being λ the mean free path of the molecule and d the diameter of the pore. According to the Kn number, the gas flow behaviour can be divided into viscous (Kn < 0.01), transition (0.01 < Kn < 1) and molecular (Kn > 1) flow regime. In our case, the Knudsen number is around 1.4 thus we considered that molecular flow will be more important.

Figure 4.7 shows two different sets of experimental points for permeation of oxygen versus mean pressure obtained for Chip 1 and Figure 4.8 corresponds to the permeation of oxygen and carbon dioxide in Chip 2. In both figures the dashed line corresponds to the theoretical model used for the description of the permeation in the nanonozzles presented below.

All the permeation experiments show that there is no significant increase in the permeance with the mean pressure, which means that the viscous flow is negligible through these small nanoapertures [138]. Therefore, the molecular (Knudsen) flow regime was considered as the dominant flow through the nanonozzles, similar to previous work describing the flow through nanopillars of 45 nm height and 62 nm in diameter described by equation (4.2) [137]:

$$F_{mol} = \frac{A \cdot \varepsilon \, w(x)}{\sqrt{2\pi MRT}}$$

(4.2)

Where, F_{mol} is the flow conductance in the molecular flow regime, i.e. [mole·s^{-1}·Pa^{-1}], A is the total membrane surface area [m^2], ε is the porosity, M is the gas molecular weight [kg·mole^{-1}], R is the gas constant [J·mol^{-1}·K^{-1}], T is the temperature [K] and w(x) is the Clausing function that considers the collisions of gas molecules with the walls of the pore and it is related to its geometry. The Clausing function, w(x) is the probability, or more precisely the reciprocal of this probability, $\eta(x) = 1 - w(x)$, that is related to the distribution of collisions of molecules with the walls of the system, related to the geometry of the pore. In other words, it estimates how easy it is for a molecule to exit the geometry. In our case we have considered a pyramidal geometry corresponding to the 3rd generation open fractal structure. The Clausing function, w(x), for conical orifices according to the conical geometry described by Lobo *et al*. with the angle of the pyramid 30 degrees, and L=495 nm, R$_0$=100 nm, has a value of 0.90814 [136, 139]. This value is higher compared to the one for cylinders, which means that the probability to exit the cone is higher compared to cylinder.
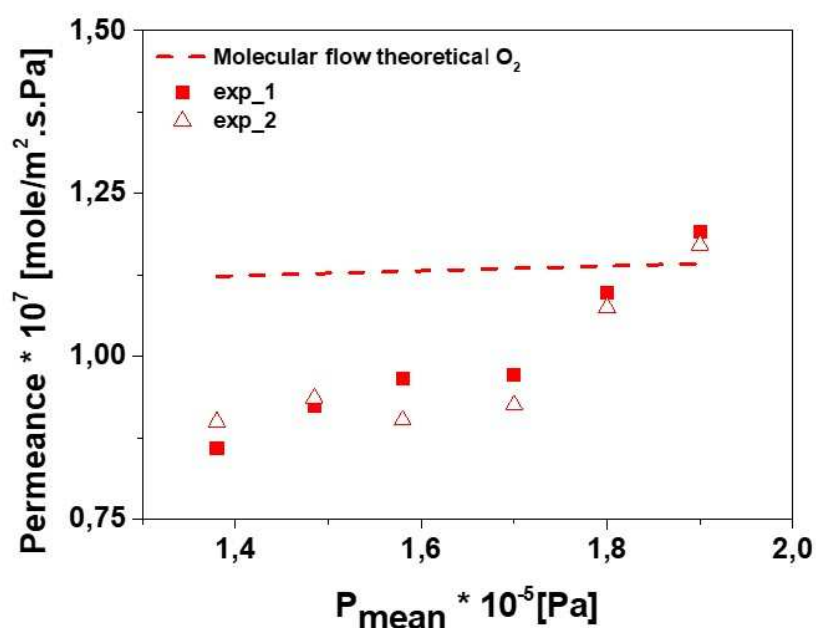
Figure 4.7 Experimental and theoretical permeation of O$_2$ in Chip 1
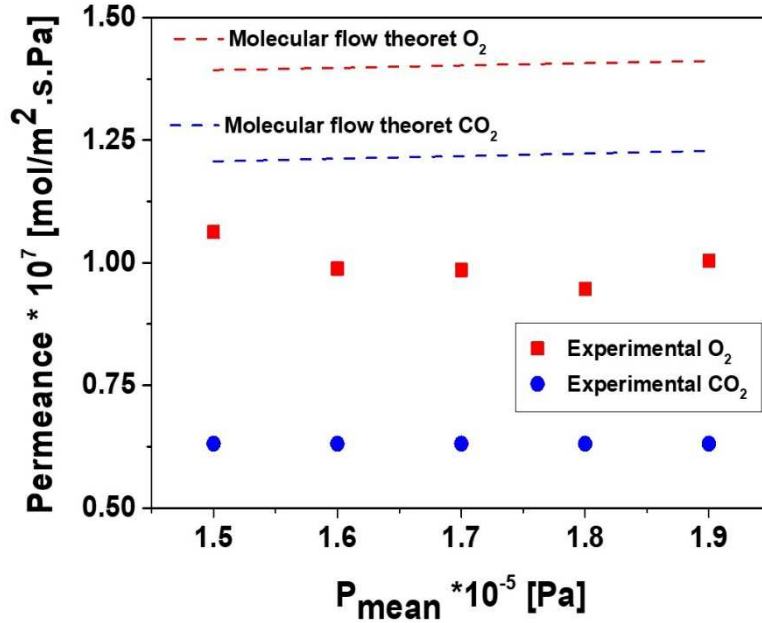
Figure 4.8 Experimental and theoretical permeation of O_2 and CO_2 in Chip 2

The theoretical calculations showed that the experimental values are approximately 30-40% lower than the predictions (see Figure 4.7 and Figure 4.8). This might be due to the difficulty in estimating the real amount of truly open apertures/nanonozzles. Some nanonozzles could be closed or not fully opened due to the fabrication procedure.

Also, in case of Knudsen diffusion mechanism (see equation 4.2), the permeation of the gas depends on its type, particularly on its molecular weight (M) because the flow is inversely proportional to the square root of the M. As expected in the Knudsen regime, the diffusion of smaller molecules through the pores is faster than larger molecules, i.e. oxygen is faster than carbon dioxide. According to equation (4.3) the ideal selectivity of O_2 over CO_2 should be 1.2, whereas we found a slightly higher value of 1.6.

$$\alpha_{\frac{O_2}{CO_2}} = \sqrt{\frac{M_{O_2}}{M_{CO_2}}} = \sqrt{\frac{44}{32}} = 1.2 \qquad (4.3)$$

The permeation values obtained, in the order of 10^{-7} mole/m²·s·Pa are high in comparison to polymeric materials such as PDMS, with a permeability values of 334 Barrer and 849 Barrer for O_2 and CO_2, respectively [133]. Table 4.2 shows the experimentally obtained fluxes of O_2 and CO_2 in two chips as a function of P_{mean} and their corresponding theoretical thicknesses of the PDMS film. It is seen from the Table that a membrane film of just 1-4 micrometers would be required to get the same permeation flux as the nanonozzles presented here (but such thin PDMS membrane cannot be handled).

147

Table 4.2 *O_2 and CO_2 permeation fluxes in the 3D fractal nanonozzles as a function of mean pressure and corresponding theoretical PDMS membrane thickness*

$P_{mean} \cdot 10^{-5}$ [Pa]	P_{O2} [mol/m²·s·Pa]		Equivalent PDMS thickness [μm]	P_{CO2} [mol/m²·s·Pa]	Equivalent PDMS thickness [μm]
	Chip 1	**Chip 2**	**O_2**	**Chip 2**	**CO_2**
1.38	$8.79 \cdot 10^{-8}$	$1.02 \cdot 10^{-7}$	1.12	$6.48 \cdot 10^{-8}$	4.1
1.48	$9.31 \cdot 10^{-8}$	$1.06 \cdot 10^{-7}$	1.07	$6.31 \cdot 10^{-8}$	4.2
1.58	$9.34 \cdot 10^{-8}$	$9.88 \cdot 10^{-8}$	1.09	$6.10 \cdot 10^{-8}$	4.3
1.7	$9.48 \cdot 10^{-8}$	$9.85 \cdot 10^{-8}$	1.08	$6.46 \cdot 10^{-8}$	4.1
1.8	$1.08 \cdot 10^{-7}$	$9.46 \cdot 10^{-8}$	1.00	$6.26 \cdot 10^{-8}$	4.2
1.9	$1.18 \cdot 10^{-7}$	$1.01 \cdot 10^{-7}$	0.93	$5.96 \cdot 10^{-8}$	4.4

Furthermore, if, theoretically, the fractal chip could be used as an alternative to PDMS microdevice for blood oxygenation, some theoretical calculations would have to be performed in order to fulfil the artificial lung approach. For instance, in order to achieve 1.9 mL of O_2 per minute in blood at a blood flow rate of 30 mL/min (see blood oxygenation requirements in Chapter 1 section 1.3) that is $1.4 \cdot 10^{-11}$ mole/s·Pa, it is necessary to have approximately 2500 fractals in the chip, taking into account the permeation of O_2 that was obtained through fractal nanoapertures. The example of such calculation is presented below:

$$SA_{AL} = \frac{blood\_requirement}{Perm\_O2_{Chip2}} \qquad (4.4)$$

$$nr_{fractals\_AL} = \frac{nr_{fractals} \cdot SA_{AL}}{SA} \qquad (4.5)$$

Where, SA_{AL} is the surface area Artificial Lung [cm²], $nr_{fractals\_AL}$- number of fractals in Artificial Lung, $nr_{fractals}$ are the fractlas in the fabricated chip (Chip 1 or Chip 2) and SA is the surface area of the current chip (Chip 1 or Chip 2) [cm²]

Finally, 2500 of fractals would have to be embedded in the channel in order to fulfil the requirements presented above.

4.5. Conclusions

In this chapter, we have validated the concept of a new 3D membrane structure incorporated in a chip for gas transfer to a microfluidic channel. We measured experimentally and calculated theoretically the permeation of oxygen and carbon dioxide. The chip presented by our group is characterized by portability, low consumption of reagents, increased contact surface area,

mechanical stability since the membrane is made of a silicon wafer. Thus, there is no risk of a thin film deflection or material swelling. Moreover, due to the compactness of the system, the distance for diffusion was extremely reduced which resulted in decreased travelling time and path. This approach could work as an alternative to PDMS membranes since the permeation flux obtained through the nanonozzles in the 3D fractals is high.

Other applications apart from the single gas permeation tested here include gas-liquid contactors, where the 3D structure presents an advantage due to the higher surface to volume ratio compared to 2D membranes, and also application requiring high temperatures and gas distribution or removal such as micromembrane microreactors [140].

5. Conclusions

5.1. Conclusions: how far we have reached?

The main scope of the work conducted in this thesis was to design and fabricate microdevices with integrated membrane and to test them for various biomedical applications. The gained experience and results brought us to the following conclusions:

- In the design of lung-on-a-chip, the synergistic effect of various parameters was noticed. The microfluidic liquid structure plays a crucial role in the oxygenation and general performance of the microdevice. High oxygen transfer rate, low pressure drop, and shear stress, homogenous liquid flow, biocompatibility, low priming volume and high surface to volume ratio are the main parameters that define a perfect artificial lung.

- The liquid chamber of the PDMS devices fabricated in this thesis exhibited homogenous blood flow profile, low pressure drop and shear stress. Red blood cells were not modified after the oxygenation experiments which proofs that the haemodynamics of the designed devices, i.e. shape and dimensions of the liquid channels, did not negatively affect the blood. Thanks to miniaturization, the microdevice was characterized by low priming volume and high surface to volume ratio which is an advantage for the artificial lung devoted to neonates.

- Computer modelling that was performed, indicated the influence of the branching architecture and flow distributors in the liquid geometry on the oxygenation process. We have learnt that the main limiting parameter in blood oxygenation is the geometry of the liquid side (i.e. gas diffusion distance). Moreover, it was noticed that the membrane permeation properties play a secondary role in the oxygenation process that become more notorious when shortening the diffusion pathways. In general, the thinner the membrane and the narrower the blood channel, the faster and more profound the oxygenation. Nevertheless, pressure drop across the geometry and fabrication limits have to be taken into account in the design of the future chip.

- The surface properties of microfluidic channels or membrane integrated in the chip play a key role in biomedical applications. The PDMS surface could be easily post-modified depending on the desired function. In the lung-on-a-chip, the PDMS surface was successfully modified into more hydrophilic one to prevent the fibrinogen adhesion. On the other hand, in the anaesthesia gas recovery measurements it was more advantageous to have hydrophobic surface due to the prevention of membrane wetting.

- In anaesthesia gas recovery process, it was observed that cholinium propionate ionic liquid in combination with carbonic anhydrase enzyme possesses high CO_2 capturing

effect and provided a significant enhancement factor in CO_2 removal and molar flux ratio of CO_2/Xe using very small concentration of enzyme 0.1 mgCA/gIL. Such minor addition of enzyme in the liquid phase led to significant enhancement of CO_2 transport due to the stabilizing role of cholinium based ionic liquid.

- The use of a gas-ionic liquid membrane microcontactor for the on-line removal of CO_2 demonstrated how efficient the miniaturized devices can be. The individual mass transfer resistance of the dense PDMS membrane for the CO_2 transport through the PDMS microfluidic device accounts for less than 20% of the total value. Thanks to miniaturization, the volume of ionic liquid required to fill the micro – chamber and the amount of enzyme were notably reduced while providing high throughput for the preliminary screening of different ionic liquid-enzyme formulations at several working conditions.

- It was confirmed that the use of microfluidic devices as membrane contactors possess variety of advantages in comparison to commonly used hollow fibres, i.e. portability, easier access for cellularization in case of necessary surface modification, low priming volume, possibility to mimic the branching architecture by adopting simple fabrication process and low cost.

- The integration of non-leaky membranes in microfluidic devices avoiding leaks is a challenging task, in particular in case of gas-systems. The concept of a microfluidic silicon/glass chip with an integrated silicon oxide membrane in the form of three-dimensional fractal geometry geometries with nanopores was presented as an interesting alternative for gas-liquid contactors that require harsh conditions such as microreactors or microdevices for energy applications. Lower resistance to mass transfer in comparison to commonly used PDMS dense membranes was obtained, due to the hierarchical branched structure of the fractals, and infinitesimal thickness of the opened pores. Furthermore, the high number of opened pores in the fractal structure resulted in high permeation flux through Si fractals. The obtained results shown that the mechanism for gas permeation through the nanonozzles in the form of fractal geometry is governed by Knudsen diffusion.

5.2. Future scope: where can we go from here?

Further research should consider improvements of the microfluidic device designs, materials development as well as additional experimental procedures to increase the reproducibility of the results.

- In the microfluidic device, designing and fabricating the chamber with various liquid channel depths within one geometry would be beneficial. The liquid chamber fabricated by micro machining technology used by Hoganson *et al* [35] demonstrated significantly lower pressure drop and shear stress due to the controlled depth of the channels, especially at the inlet of the structure, in comparison to the geometries with constant depths.

- Exploring novel liquid channels and membrane architectures which would further increase the surface-to-volume ratio, i.e. porous or corrugated membranes, branching channel architectures would be beneficial.

- In the anaesthetic gas recovery experiments, alternative non-permeable materials with higher mechanical resistance for the fabrication of microfluidic chambers should be considered. This would avoid the gas permeation from the system through the PDMS chambers to the surroundings. Moreover, the experimental system could be upgraded in order to allow the regeneration and recirculation of ionic liquid for closed loop operation. The selectivity of CO_2/N_2 as well as the recovery of Xe in the real anaesthetic gas mixture should be also measured. Moreover, it would be beneficial to monitor the CO_2 capturing effect of higher concentration of CA enzyme.

- Fractal geometry could be used for the preliminary blood oxygenation experiments. However, the chip design should be modified according to the parameters which are beneficial for blood contacting applications, i.e. low shear stress and pressure drop and homogenous liquid flow distribution. Computer modelling would help to predict the advantageous fractal distribution across the channel and the necessary number of opened apertures in order to supply sufficient amount of oxygen to oxygenate blood up to approximately 95%.

Conclusiones: ¿Hasta donde hemos llegado?

El objetivo principal del trabajo realizado en esta tesis fue diseñar y fabricar dispositivos microfluídicos con membrana integrada y evaluar su comporamiento como contactores gas-líquido en dos aplicaciones biomédicas. Así pues, la experiencia adquirida y los resultados obtenidos han permitido formular las siguientes conclusiones:

- El diseño del microdispositvo *"lung-on-a-chip"* ha de considerar microcanales en los que las células y plaquetas experimenten presiones, esfuerzos rasantes y ángulos de ramificación que emulen las del cuerpo humano. La estructura microfluídica para la cámara del líquido desempeña un papel clave en el proceso de oxigenación y en el rendimiento global del dispositivo. Las principales características que definen un pulmón artificial perfecto son: alta tasa de transferencia de oxígeno, baja caída de presión y esfuerzo cortante, flujo homogéneo de sangre, biocompatibilidad, bajo volumen de cebado y alta relación superficie /volumen.

- Los microdispositivos de PDMS fabricados en esta tesis se caracterizaron por presentar una distribución de flujo de sangre homogéneo, bajos valores para la caída de presión y el esfuerzo rasante. Gracias a la miniaturización, los microdispositivos presentaron un volumen bajo de cebado (priming volume) y una elevada relación superficie a volumen. Este rasgo los hace especialmente atractivos para el desarrollo de un pulmón artificial para recién nacidos y prematuros. Se observó experimentalmente que la forma y tamaño de los glóbulos rojos no se modificaron después de los experimentos de oxigenación realizados. Este comportamiento demuestra que la hemodinámica de los microdispositivos diseñados, es decir, la forma y las dimensiones de los canales líquidos, es adecuada.

- El modelado matemático realizado destaca la influencia de la arquitectura de ramificación de canales en la cámara del líquido y de los distribuidores de flujo sobre el proceso de oxigenación. El principal parámetro que limita el transporte de O_2, bajo las condiciones experimentales ensayadas, es la distancia de difusión para el oxígeno disuelto. Las propiedades de permeación de la membrana densa, que separa ambos compartimentos, juegan un papel secundario en el proceso de oxigenación; si bien este se hace más notorio a medida que los caminos de difusión para el oxígeno disuelto se acortan. En general, cuanto más fina es la membrana y más estrecho es el microcanal sanguíneo, más rápida y profunda es la oxigenación a expensas de un aumento de las

pérdidas de carga. Por lo tanto, el diseño del futuro chip ha de resultar de un compromiso que también tenga en cuenta las limitaciones derivadas de las propias técnicas de microfabricación utilizadas.

- La superficie de los microcanales y de la membrana integrada en contacto con el flujo sanguíneo tiene una relevancia especial en aplicaciones biomédicas ya que ejerce una influencia importante sobre las interacciones con las proteínas presentes en el medio. En el microdispositivo *lung-on-a-chip*, la hidrofilicidad de la superficie del PDMS se modificó satisfactoriamente para evitar la adhesión del fibrinógeno.

- En el microdispositivo con diseño alveolar utilizado como microcontactor G-L para la separación de CO_2 de gas de anestesia, el empleo como solvente de propionato de colinio con 0.753 de a_w en combinación con la enzima anhidrasa carbónica condujo a una captura elevada y selectiva de CO_2 por el solvente a muy bajas concentraciones de enzima, i.e. 0.1 mgCA / gIL. Las mejoras significativas en el transporte de CO_2 introducidas con la adición de esta pequeña cantidad de enzima se atribuyeron a la función estabilizadora del líquido iónico biocompatible basado en el catión colinio.

- El empleo del *microcontactor* gas-líquido iónico de membrana densa para la eliminación en línea de CO_2 demostró cuán eficientes pueden ser los dispositivos miniaturizados. La resistencia individual al transporte de CO_2 ofrecida por la membrana densa de PDMS representa menos del 20% del valor de la resistencia total. Gracias a la miniaturización, el volumen de líquido iónico requerido para llenar la microcámara así como la cantidad de enzima se reducen notablemente. Al mismo tiempo, el microcontactor de membrana proporciona una elevada relación S/V en comparación con los sistemas convencionales de dispersión de fases. Por lo tanto, esta plataforma microfluídica se constittuye como una herramienta de baja coste, sencilla y versátil para la estudio preliminar de la viabilidad de diferentes formulaciones de líquidos iónicos-enzimas a condiciones de trabajo variables.

- De la evaluación de los dispositivos microfluídicos fabricados como contactores de membrana en las dos aplicaciones seleccionadas se pueden derivar las siguientes ventajas en comparación con las membranas de fibras huecas comúnmente utilizadas: portabilidad, acceso más fácil para celularización en caso de ser necesaria una modificación superficial, bajo volumen de cebado, posibilidad de imitar la arquitectura de ramificación mediante procesos simples de fabricación y de bajo coste.

Conclusions

- La integración de membranas en microdispositivos asegurando ausencia de fugas es una tarea desafiante, especialmente en el caso de los sistemas que operan con gases a temperaturas elevadas como son microrreactores o microdispositivos para aplicaciones energéticas. En este contexto, el chip de microfluídica construido en Si/ vidrio que integra una membrana de SiO en forma de geometría fractal 3D con nanoporos se presentó como alternativa de elevada S/V, baja resistencia al flujo de gas a su través (en comparación con las membranas densas de PDMS) y selectividad tipo Knudsen, debido a la estructura ramificada de los fractales, y al espesor infinitesimal y diámetro nanométrico de sus poros abiertos.

Trabajo futuro

La investigación futura debería considerar mejoras en los diseños de los microdispositivos, en la propuesta y desarrollo de nuevos materiales y experimentación adicional para corroborar la reproducibilidad y representatividad de los resultados ya obtenidos. Algunas de estas propuestas se comentan a continuación:

- En el microdispositivo, sería beneficioso diseñar y fabricar la cámara de la fase líquida con varias profundidades dentro del mismo microcanal conforme el fluido avanza. La cámara de líquido fabricada por la tecnología de micro mecanizado utilizada por Hoganson et al [35] demostró una caída de presión y un esfuerzo cortante significativamente más bajos debido a la profundidad controlada de los canales, especialmente en la entrada de la estructura, en comparación con las geometrías comúnmente estudiadas de profundidad constante.

- La exploración de nuevas configuraciones fabricadas por técnicas de impresión 3D que mimeticen el pulmón, así como nuevas arquitecturas de membrana con topología micro y nano estructurada que permitan aumentar la relación superficie-volumen y asegurar hidrofilicidad.

- Para la aplicación en recuperación de gas de anestesia, se deben considerar materiales alternativos no permeables y con mayor resistencia mecánica en la fabricación de las cámaras microfluidicas. Esto evitaría la adsorción del gas del sistema por las paredes y su eventual transporte al entorno. Una segunda fase podría abordar el estudio del sistema en ciclo cerrado, es decir, bajo alimentación continua de fas gas y la regeneración y recirculación completa del líquido iónico. Además, sería necesario evaluar el efecto de la concentración de enzima sobre el grado de separación alcanzado.

- A la vista de los resultados de permeación y la fiabilidad y versatilidad del proceso de fabricación del chip construido en Si/vidrio con membrana de SiO en forma de geometría fractal 3D, este podría ser evaluado en oxigenación de la sangre. El modelado matemático previo permitiría identificar el valor óptimo de profundidad del fractal embebido en el microcanal de líquido, su distribución y tamaño para asegurar condiciones hemodinámicas y una saturación de O_2 en sangre hasta aproximadamente el 95%.

Conclusões: até onde chegamos?

O escopo principal do trabalho realizado nesta tese foi projetar e fabricar microdispositivos com membrana integrada e testá-los para várias aplicações biomédicas. A experiência adquirida e os resultados nos trouxeram as seguintes conclusões:

- No design do *lung-on-a-chip*, observou-se o efeito sinérgico de vários parâmetros. A estrutura líquida microfluídica desempenha um papel crucial na oxigenação e no desempenho geral do microdispositivo. A alta taxa de transferência de oxigênio, baixa queda de pressão e tensão de cisalhamento, fluxo de líquido homogêneo, biocompatibilidade, baixo volume de iniciação e alta relação superfície / volume são os principais parâmetros que definem um pulmão artificial perfeito.

- A câmara líquida dos dispositivos PDMS fabricados nesta tese exibiu perfil de fluxo sanguíneo homogêneo, baixa queda de pressão e tensão de cisalhamento. Os glóbulos vermelhos não foram modificados após os experimentos de oxigenação que comprovam que a hemodinâmica dos dispositivos projetados, isto é, a forma e as dimensões dos canais líquidos, não afetaram negativamente o sangue. Graças à miniaturização, o microdispositivo foi caracterizado por baixo volume de iniciação e alta relação superfície / volume, que é uma vantagem para o pulmão artificial dedicado aos neonatos.

- Modelagem de computador que foi realizada, indicou a influência da arquitetura de ramificação e distribuidores de fluxo na geometria do líquido no processo de oxigenação. Aprendemos que o principal parâmetro limitante na oxigenação do sangue é a geometria do lado líquido (isto é, distância de difusão do gás). Além disso, observou-se que as propriedades de permeação da membrana desempenham um papel secundário no processo de oxigenação que se tornam mais notáveis ao encurtar as vias de difusão. Em geral, quanto mais fina a membrana e mais estreita o canal de sangue, mais rápida e profunda é a oxigenação. No entanto, a queda de pressão através da geometria e os limites de fabricação devem ser levados em consideração no projeto do futuro chip.

- As propriedades superficiais dos canais microfluídicos ou da membrana integrada no chip desempenham um papel fundamental nas aplicações biomédicas. A superfície do PDMS pode ser facilmente modificada após a função desejada. No *lung-on-a-chip*, a superfície do PDMS foi modificada com sucesso em mais hidrofílico para evitar a adesão do fibrinogênio. Por outro lado, nas medidas de recuperação de gás de anestesia

foi mais vantajoso ter superfície hidrofóbica devido à prevenção da molhagem da membrana.

- No processo de recuperação de gás de anestesia, observou-se que o líquido iónico de propionato de cololio em combinação com a enzima de anidrase carbônica possui alto efeito de captura de CO_2 e forneceu um fator de aprimoramento significativo na remoção de CO_2 e na razão de fluxo molar de CO_2 / Xe usando uma concentração muito pequena de enzima, 0.1 mgCA / gIL. Essa menor adição de enzima na fase líquida levou a um aumento significativo do transporte de CO_2 devido ao papel estabilizador do líquido iónico baseado em colinol.

- O uso de um *microcontactor* de membrana gás- líquido iônico para a remoção on-line de CO_2 demonstrou a eficiência dos dispositivos miniaturizados. A resistência individual à transferência de massa da membrana PDMS densa para o transporte de CO_2 através do dispositivo microfluídico PDMS representa menos de 20% do valor total. Graças à miniaturização, o volume de líquido iónico necessário para preencher a microcámara e a quantidade de enzima foram notadamente reduzidos, proporcionando alta produção para a triagem preliminar de diferentes formulações de enzimas líquidas iónicas em várias condições de trabalho.

- Foi confirmado que o uso de dispositivos microfluídicos como contatores de membrana possui várias vantagens em comparação com fibras ocasmente usadas, isto é, portabilidade, acesso mais fácil para celularização em caso de modificação de superfície necessária, baixo volume de iniciação, possibilidade de imitar a arquitetura ramificada por adotando processo de fabricação simples e baixo custo.

- A integração de membranas não vazadas em dispositivos microfluídicos que evitam vazamentos é uma tarefa desafiadora, especialmente no caso de sistemas de gás. O conceito de chip de microfluídica de Si/vidro com uma membrana integrada de óxido de silício na forma de geometrias tridimensionais de geometria fractal com nanoporos foi apresentado como uma alternativa interessante para contatores gás-líquidos que requerem condições severas como microrreatores ou microdispositivos para aplicações de energia . Foi obtida menor resistência à transferência de massa em comparação com as membranas densas PDMS comumente utilizadas, devido à estrutura hierárquica ramificada dos *fractals* e à espessura infinitesimal dos poros abertos. Além disso, o elevado número de poros abertos na estrutura fractal resultou em um alto fluxo de permeação através de *fractals* de Si. Os resultados obtidos mostraram que o mecanismo

de permeação de gás através dos nanoaberturas sob a forma de geometria fractal é governado pela difusão de Knudsen.

Trabalho futuro

Outras pesquisas devem considerar melhorias nos projetos de dispositivos microfluídicos, desenvolvimento de materiais e procedimentos experimentais adicionais para aumentar a reprodutibilidade dos resultados.

- No dispositivo microfluídico, o projeto e fabricação da câmara com várias profundidades de canais líquidos dentro de uma geometria seria benéfico. A câmara de líquido fabricada pela tecnologia de micro-usinagem utilizada por Hoganson *et al* [35] demonstrou queda de pressão e tensão de cisalhamento significativamente menores devido à profundidade controlada dos canais, especialmente na entrada da estrutura, em comparação com as geometrias com profundidades constantes.

- Explorando novos canais de líquido e arquiteturas de membrana que aumentarão ainda mais a relação superfície para volume, isto é, membranas porosas ou onduladas, as arquiteturas de canal de ramificação seriam benéficas.

- Nas experiências de recuperação de gás anestésico, devem ser considerados materiais alternativos não permeáveis com maior resistência mecânica para a fabricação de câmaras microfluídicas. Isso evitaria a permeação do gás do sistema através das câmaras de PDMS para os ambientes. Além disso, o sistema experimental pode ser atualizado para permitir a regeneração e recirculação do líquido iônico para operação em circuito fechado. A selectividade de CO_2/N_2, bem como a recuperação de Xe na mistura de gás anestésico real também devem ser medidas. Além disso, seria benéfico controlar o efeito de captura de CO_2 de maior concentração de enzima CA.

- A geometria do *fractal* pode ser usada para os experimentos preliminares de oxigenação no sangue. No entanto, o design do chip deve ser modificado de acordo com os parâmetros que são benéficos para aplicações de contato com o sangue, isto é, baixa tensão de cisalhamento e queda de pressão e distribuição de fluxo de líquido homogêneo. A modelagem por computador ajudaria a prever a distribuição fractal vantajosa através do canal e o número necessário de aberturas abertas para fornecer quantidade suficiente de oxigênio para oxigenar o sangue até aproximadamente 95%.

Conclusies: hoe ver zijn we gekomen?

Het hoofddoel van het uitgevoerde werk in dit proefschrift was het ontwerpen en fabriceren van microapparaten met een geïntegreerd membraan en het testen van deze apparaten voor een aantal biomedische applicaties. The opgedane ervaring en resultaten brengt ons tot de volgende conclusies:

- In het ontwerp van *lung-on-a-chip* is het synergetische effect van verschillende variabelen opgemerkt. De microfluidische vloeistofstructuur speelt een cruciale rol in het oxygeniseren en de algemene werking van het microapparaat. Hoge zuurstof transfersnelheid, laag verlies van druk en schuifspanning, homogene vloeistofstroom, biocompatibiliteit, een laag vulvolume en een hoge oppervlakte-volume verhouding zijn de voornaamste variabelen die een perfecte kunstlong definieren.

- De vloeistofkamer van de in dit proefschrift gefabriceerde PDMS apparaten lieten een homogeen bloed vloeiprofiel, laag drukverlies en een lage schuifspanning zien. Rode bloedcellen werden niet aangetast na oxygenatie-experimenten, wat bewijst dat de hemodynamiek van de ontworpen apparaten, dat wil zeggen de vorm en dimensies van de vloeistofkanalen, het bloed niet negatief beïnvloeden. Dankzij de miniaturisatie wordt het microapparaat gekenmerkt door een laag vulvolume en een hoge oppervlakte-volume verhouding. Dit is positief voor de kunstlong gewijd aan prematuur geboren kinderen.

- De uitgevoerde simulaties duiden de invloed van een vertakkende architectuur en stroomverdelers in de vloeistoefgeometrie aan. We hebben geleerd dat vloeistof geometrie (dat wil zeggen, gasdiffusie afstand) de voornaamste limiterende factor in het oxygeneren van bloed is. Bovendien werd opgemerkt dat de membraan permeatie-eigenschappen een secundaire rol spelen in het oxygenatieproces. Deze worden zelfs nog minder invloedrijk wanneer de diffusie paden worden verkort. In het algemeen geldt: hoe dunner het membraan en smaller het bloedkanaal, hoe sneller en diepgaander de oxygenatie. Echter, er moet rekening gehouden worden met drukverlies over de gehele geometrie en fabricage limieten bij het ontwerpen van een toekomstige chip.

- De oppervlakte eigenschappen van de microfluïdische kanalen en van het in de chip geïntegreerde membraan spelen een belangrijke rol in biomedische applicaties. Het PDMS oppervlak kan makkelijk achteraf gemodificeerd worden voor de gewenste functie. In de *lung-on-a-chip* is het PDMS oppervlak succesvol gemodificeerd tot een

meer hydrofiel oppervlak om fibrogen aanhechting te voorkomen. Echter, tijdens de verdovingsgas experimenten bleek een hydrofoob oppervlak voordelig. Dit vanwege het voorkomen van membraan benatting.

- Tijdens het verdovingsgas herwinnings proces werd geobserveerd dat een choliniumpropionaat ionische vloeistof in combinatie met een koolzuuranhydrase enzym een hoog CO_2 opvang effect heeft. Dit gaf een significante verbetering in de CO_2 verwijdering en molaire flux ration van CO_2/Xe door gebruik van een zeer lage concentratie van enzym: 0,1 mg CA/gIL. Dit minimale gebruik van enzym tijdens de vloeistoffase leidde tot een significante verbering van CO_2 transport, vanwege het stabiliserende effect van cholinium gebaseerde ionische vloeistof.

- Het gebruik van een gas-ionische vloeistof membraan microcontactor voor het on-line verwijderen van CO_2 demonstreerde hoe efficiënt geminiaturiseerde apparaten kunnen zijn. De individuele massa transportweerstand van het dichte PDMS membraan voor CO_2 transport door het PDMS microfluïdische apparaat is minder dan 20% van de totale waarde. Dankzij miniaturisatie is het benodigde volume om de microkamer te vullen en de benodigde hoeveelheid enzym merkbaar gereduceerd, terwijl er gezorgd wordt voor een hoge doorloop voor de eerste screening van verschillende ionische vloeistof-enzym formulaties onder verschillende werkcondities.

- Het werd bevestigd dat het gebruik van microfluïdische apparaten als membraan contactors een hoeveelheid voordelen heeft ten opzicht van het gebruik van holle vezels, zoals draagbaarheid, laag vulvolume, de mogelijkheid om een vertakkende architectuur te imiteren via een eenvoudig fabricageproces en lage kosten.

- Het vermijden van lekken tijdens de integratie van niet-lekkende membranen in microfluïdische apparaten is een uitdagende handeling, met name bij gassystemen. Het concept van een microfluïdische silicium/glas chip met een geïntegreerd siliciumoxide membraan in de vorm van een driedimensionale fractale geometrie met nanoporiën werd voorgesteld als een interessant alternatief voor gas-vloeistof contactors onder zware condities, zoals microreactoren of micro apparaten voor energie applicaties. Lagere massa transport weerstand ten opzichte van veelgebruikte PDMS dichte membranen werd bereikt, vanwege de hiërarchisch vertakte structuur van de fractalen en de minieme dikte van de geopende poriën. Bovendien resulteerde het hoge aantal geopende poriën in de fractale structuur in een hoge permeatie flux door de Si fractalen. De ontvangen resultaten laten zien dat het mechanisme van de gas permeatie door de

nano spuitstukken in de fractale geometrie vorm zich onderwerpt aan de Knudsen diffusie.

Toekomstige rijkwijdte: Waar kunnen we vanaf hier gaan?

Toekomstig onderzoek dient te kijken naar verbeteringen van het microfluïdisch apparaat ontwerp en materiaal ontwikkeling. Ook dient er gekeken te worden naar verder experimenten om de reproduceerbaarheid van de resultaten te vergroten.

- Het kan voordelig zijn om de kamer in het microfluïdische apparaat met verschillende kanaaldieptes en geometrieën te ontwerpen. De door Hoganson *et al* [35] gebruikte microverspaning technologie liet significant minder drukverlies en schuifspanning zien door de gecontroleerde diepte van de kanalen, met name bij de inlet van de structuur, ten opzichte van de geometrieën met constante dieptes.

- Het verkennen van nieuwe vloeistoefkanalen en membraan ontwerpen om een grotere oppervlakte-volume verhouding te verkrijgen, bijvoorbeeld door poreuze of gegolfde membranen of vertakkende kanaal architecturen is voordelig.

- In de verdovingsgas herwinnings experimenten zouden alternatieve, non-permeabele materialen met hogere mechanische weerstand overwogen kunnen worden voor de fabricage van microfluïdische kamers. Bovendien kan het experimentele systeem verbeterd worden om zo de regeneratie en recirculatie van de ionische vloeistof aan te kunnen voor een gesloten circuit gebruik. De selectiviteit van CO_2/N_2, alsmede de herwinning van Xe in het echte verdovingsgas mengsel dient ook gemeten te worden. Ook kan het voordelig zijn om het CO_2 opvang effect van een hogere concentratie CA enzym te bestuderen.

- Fractale geometrie zou gebruikt kunnen worden voor inleidende bloed oxygenatie experimenten. Echter, het chip design dient dan aangepast te worden volgens de variabelen die voordelig zijn voor bloedcontact toepassingen. Dat wil zeggen: lage schuifspanning en laag drukverlies, alsmede homogene vloeistof stroom distributie. Computermodellering zou helpen om de voordelige fractale verdeling over het kanaal en het benodigde aantal geopende openingen te voorspellen om voldoende zuurstof te leveren om bloed tot zuurstof van ongeveer 95% te kunnen oxygeneren.

Appendix I

3D fractal structure fabrication

Corner lithography

The method of engineering of a 3D fractal structure is based on a combination of anisotropic etching of silicon and corner lithography. Corner lithography is a technique that allows production of truly three-dimensional features. It uses conformal deposition of layers of silicon nitride by low-pressure chemical vapour deposition (LPCVD), and thermal oxide and partly back-etching of a silicon nitride layer that is placed inside the octahedral silicon pits in order to form dots in sharp concave corners. The crystalline property of silicon and a gradual etching characteristic of its (111) planes result in the formation of octahedral cavities. Repeated corner lithography, in combination with anisotropic etching, results in the construction of 3D octahedral fractals where the number of layers can be controlled.

Fractal fabrication procedure

Silicon dioxide (SiO$_2$) thermal growing

The fractal fabrication procedure starts with a (100) plane single crystalline silicon wafer having a layer of thermally grown silicon dioxide (SiO$_2$). The thickness of the grown oxide layer should be equal on the silicon (100) and (111) crystal planes because it affects the oxide growth speed.

The oxidation of silicon is achieved by (dry) thermal oxidation at 1100°C. Such high oxidation temperature leads to the differences in grown oxide in terms of layer thickness on (100) and (111) silicon crystal planes in comparison to low oxidation temperatures ($\leq$ 950°C). At temperatures lower or equal to 950°C, the oxide thickness is thinner at convex and concave corners than a flat (100) Si planes. However, there is a difference in oxide growth speed on the main crystal directions of silicon. The amount of intersecting (111) planes influences the degree of sharpening of the thermal oxide layer in the concave corners. Generally, the more the intersecting planes, the thinner the grown oxide layer. Therefore, in ribbons – i.e. two intersecting (111) planes – less oxide sharpening occurs in comparison to an intersection of three or four (111) planes (i.e. apices). Such process is presented in Figure A.0.*1*.
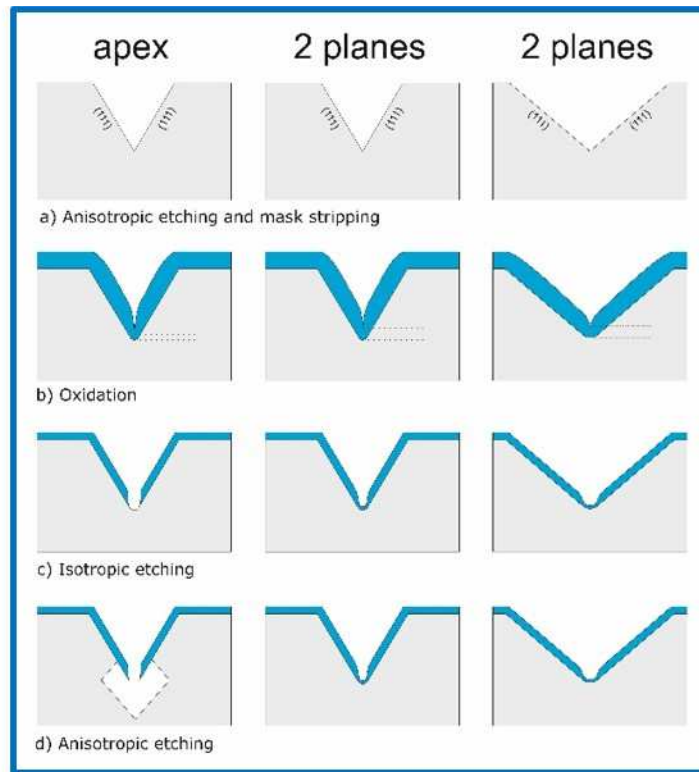
Figure A.0.1 Selective opening of the thermally grown silicon oxide at the apex of the pyramidal pit after HF etching [141]

Patterning and creating 3D structures

Silicon wafer with thermally grown silicon dioxide was patterned in buffered hydrofluoric acid (BHF) using a resist mask with a regular pattern of holes (25 μm diameter and 25 μm periodicity). The silicon which was unprotected, was anisotropically etched in a potassium hydroxide (KOH) in order to create a pyramidal etch pits. The remaining oxide mask was stripped. Next, the wafer was uniformly coated with 160 nm of low-pressure chemical vapour deposited silicon nitride. The next step, called corner lithography, was used to remove the nitride in hot phosphoric acid (H_3PO_4) and to leave it only in the corner of the pyramid (see Figure A.0.*2* C). The thin oxide was used to protect the silicon from erosion by the H_3PO_4. The following step was the process called LOCOS (LOCal Oxidation of Silicon). In this stage silicon was locally oxidized at 1100°C during 45 min into 77 nm SiO_2 using the nitride as a mask. The nitride in the corner of a pyramid was stripped and it created a single nanonozzle. Next, the unprotected silicon in the pyramidal apex was etched anisotropically during 125 min using tetra methyl ammonium hydroxide (TMAH) which formed a single octahedral shape feature at the vertex of the pyramid (Figure A.0.*2* D). The size of the single octahedral feature was determined by the (111) silicon etch rate that was approximately 15-20 nm min^{-1}. The zeroth level of processing was finished by stripping of SiO_2 and depositing around 88 nm of

nitride. The entire process was repeated in order to create the first generation of substructures. To do that, the nitride was partly etched (Figure A.0.*2* E), 77 nm of LOCOS was grown, and thin oxide and nitride were stripped in the vertices. Silicon was etched again in TMAH but this time only the half of the etching time was used. This procedure created five octahedra at the vertex corners of each octahedron of the previous step. However, the size of new created octahedra decreased by a half in comparison to the previous generation (Figure A.0.*2* F). The cycle was repeated for the second and third level always creating the octahedra half in size in comparison to previous generation. The octahedral fractal fabrication scheme in the crystalline silicon is presented in Figure A.0.*2*.
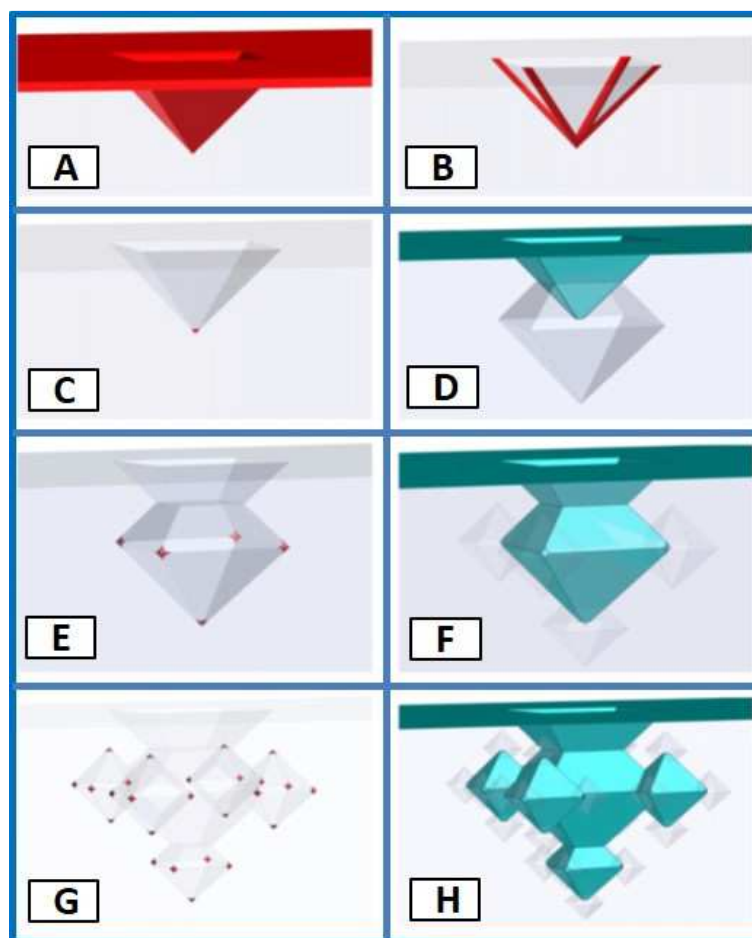
Figure A.0.2 Octahedral 3D fractal fabrication scheme in the crystalline silicon [134]

References

References

1.	A. K. Pabby, J. V. Sonawane, A. M. Sastre, and Y. Kulkarni, *Chapter 4: Industrial Applications of Membrane Contactors*, in *Handbook of Membrane Separations. Chemical, Pharmaceutical, Food, and Biotechnological Applications*, A. K. Pabby, S. S. H. Rizvi, and A.M. Sastre, Editors. 2015.
2.	Baker, R.W., *Chapter 1: Overview of membrane science and technology*, in *Membrane Technology and Applications*, R.W. Baker, Editor. 2004.
3.	E. Drioli, A. Criscuoli, and E. Curcio, *Membrane Contactors: fundamentals, applications and potentialities*, ed. M.S. Technology. Vol. 11. 2006, New York: Elsevier.
4.	Murata, H., Y. Tomita, M. Miyashita, K. Sakai, M. Toda, and T. Ohmi, "Mass transfer of water vapor in a hollow fiber for degassing processes" *AIChE Journal,* 1999, 45, 681-690.
5.	Gaylor, J.D.S., "Membrane oxygenators: current developments in design and application" *Journal of Biomedical Engineering,* 1988, 10, 541-547.
6.	Gabelman, A. and S.-T. Hwang, "Hollow fiber membrane contactors" *Journal of Membrane Science,* 1999, 159, 61-106.
7.	Joscelyne, S.M. and G. Trägårdh, "Membrane emulsification - A literature review" *Journal of Membrane Science,* 2000, 169, 107-117.
8.	Dai, Z., L. Ansaloni, and L. Deng, "Precombustion CO_2 Capture in Polymeric Hollow Fiber Membrane Contactors Using Ionic Liquids: Porous Membrane versus Nonporous Composite Membrane" *Industrial and Engineering Chemistry Research,* 2016, 55, 5983-5992.
9.	Dindore, V.Y., D.W.F. Brilman, R.H. Geuzebroek, and G.F. Versteeg, "Membrane-solvent selection for CO_2 removal using membrane gas-liquid contactors" *Separation and Purification Technology,* 2004, 40, 133-145.
10.	Klaassen, R., P.H.M. Feron, and A.E. Jansen, "Membrane contactors in industrial applications" *Chemical Engineering Research and Design,* 2005, 83, 234-246.
11.	Pabby, A.K. and A.M. Sastre, "State-of-the-art review on hollow fibre contactor technology and membrane-based extraction processes" *Journal of Membrane Science,* 2013, 430, 263-303.
12.	A. Criscuoli and E. Drioli, *Chapter 30. Membrane Contactors for the Absorption of Carbon Dioxide from Gaseous Streams. State of the Art on Membrane Improvements.*, in *Handbook of Membrane Separations. Chemical, Pharmaceutical, Food, and Biotechnological Applications*, A. K. Pabby, S. S. H. Rizvi, and A.M. Sastre, Editors. 2015.
13.	A. Criscuoli and E. Drioli, *Chapter 38. Membrane contactors for gaseous stream treatments*, in *Handbook of Membrane Separations. Chemical, Pharmaceutical, Food, and Biotechnological Applications*, A. K. Pabby, S. S. H. Rizvi, and A.M. Sastre, Editors. 2009.
14.	Chabanon, E., B. Belaissaoui, and E. Favre, "Gas-liquid separation processes based on physical solvents: Opportunities for membranes" *Journal of Membrane Science,* 2014, 459, 52-61.
15.	W. J. Federspiel and K.A. Henchir, *Lung, Artificial: Basic principles and current applications*, in *Encyclopedia of Biomaterials and Biomedical Engineering*, 2004, 910-920.
16.	"Chronic obstructive pulmonary disease" *World Health Organization,* Retrieved December 2016, from http://www.who.int/mediacentre/factsheets/fs315/en/,
17.	C. D. Mathers, D.L., "Projections of Global Mortality and Burden of Disease from 2002 to 2030" *Plos Medicine,* 2006,
18.	"The global economic burden of non-communicable diseases" *World Economic Forum,* Retrieved January 2017, from http://www3.weforum.org/docs/WEF_Harvard_HE_GlobalEconomicBurdenNonCommunicableDiseases_2011.pdf,
19.	E. K. Bassett, D.M.H., J. H. Lo, E. J. N. Penson, J. P. Vacanti, "Influence of vascular network design on gas transfer in lung assist device technology" *American society of artificial organs,* 2011, 533-538.

20. W. I. Wu, N. Rochow, E. Chan, G. Fusch, A. Manan, D. Nagpal, P. R. Selvaganapathy, and C. Fusch, "Lung assist device: development of microfluidic oxygenators for preterm infatnts with respiratory failure" *Lab on a Chip,* 2013, 13, 2641-2650.

21. K. J. Rehder, D.A.T., D. Bonadonna, R. J. Walczak, R. J. Rudder, I. M. Cheifetz, "Technological advances in extracorporeal membrane oxygenation for respiratory failure" *Expert review of respiratory medicine,* 2012, 6, 377-384.

22. G. P. Gravlee, M. Kurusz, and J.R. Utley, "Cardiopulmonary Bypass" *Lippincott Williams&Wilkins,* 2000,

23. D. M. Hoganson, J.L.A., E. F. Weinberg, E. J. Swart, B. K. Orrick, J. T. Borenstein, J. P. Vacanti, "Branched vascular network architecture: A new approach to lung assist device technology " *The Journal of Thoracic and cardiovascular surgery,* 2010, 140, 990-995.

24. K. M. Kovach, M.A.L., M. C. Moyer, B. L. Cmolik, E. van Lunteren, A. Sen Gupta, J. R. Capadona, J. A. Potkay, "In vitro evaluation and in vivo demonstration of a biomimetic, hemocompatible, microfluidic artificial lung" *Lab on a Chip,* 2015,

25. T. Kniazeva, J.C.H., J. L. Charest, J. T. Borenstein, "A microfluidic respiratory assist device with high gas permeance for artificial lung applications" *Biomedical Microdevices,* 2011, 13, 315-323.

26. Potkay, J.A., "The promise of a microfluidic artificial lungs" *Lab on a Chip,* 2014, 14, 4122-4138.

27. R. Screenivasan, E.K.B., D. M. Hoganson, J. Vacanti, K. K. Gleanson, "Ultra-thin, gas permeable free-standing and composite membranes for microfluidic lung assist device" *Biomaterials,* 2011, 32, 3883-3889.

28. N. Rochow, W.I.W., E. Chan, D. Nagpal, G. Fusch, P. R. Selvaganapathy, S. Monkman, C. Fusch, "Integrated microfluidic oxygenatr bundless for blood gas exchange in premature infants" *Micro Electro Mechanical systems (MEMS),* 2012, 2012 IEEE 25th International Conference on January 29 to February 2, 957-960.

29. N. Rochow, A.M., W. I. Wu, G. Fusch, S. Monkman, J. Leung, E. Chan, D. Nagpal, D. Predescu, J. Brash, P. R. Selvaganapathy, C. Fusch, "An integrated array of microfluidic oxygenators as a neonatal lung assist device: In vitro characterization and In vivo demonstration" *Artificial organs,* 2014,

30. J. T. Borenstein, H.T., K. R. King, E. J. Weinberg, M. R. Kaazempur-Mofrad, J. P. Vacanti, "Microfabrication technology for vascularized tissue engineering" *Biomedical Microdevices,* 2002, 4, 167-175.

31. M. Shin, K.M., O. Ishii, H. Terai, M. Kaazempur-Mofrad, J. Borenstein, M. Detmar J. P. Vacanti, "Endothelialized networks with a vascular geometry in microfabricated Poly (dimethyl siloxane)" *Biomedical Microdevices,* 2004, 6, 269-278.

32. T. Kniazeva, A.E.E., J. C. Hsiao, E. S. Kim, V. B. Kolachalama, J. L. Charest, J. T. Borenstein, "Performance and scalling effects in a multilayer microfluidic extracorporeal lung oxygenation device" *Lab on a Chip,* 2012, 12, 1686-1695.

33. K. A. Burgess, H.H., W. R. Wagner, W. J. Federspiel, "Towards microfabricated biohybrid artificial lung modules for chronic respiratory support" *Biomedical Microdevices,* 2009, 11, 117-127.

34. J. A. Potkay, M.M., A. Vinson, B. Cmolik, "Bio-inspired, efficient, artificial lung employing air as the ventilating gas" *Lab on a Chip,* 2011, 11, 2901-2909.

35. D. M. Hoganson, H.I.P., E. K. Bassett, I. D. Spool, J. P. Vacanti, "Lung assist device technology with physiologic blood flow developed on a tissue engineered scaffold platform" *Lab on a Chip,* 2010, 11, 700-707.

36. T. Rieper, C.M., H. Reinecke, "Novel scalable and monolithically integrated extracorporeal gas exchange device" *Biomedical Microdevices,* 2015, 17, 86.

37. A. A. Gimbel, E.F., A. Koo, G. Garcia-Cardena, J. T. Borenstein, "Development of a biomimetic microfluidic oxygen transfer device" *Lab on a Chip,* 2016, 16,

References

38. Thompson, A.J., L.H. Marks, M.J. Goudie, A. Rojas-Pena, H. Handa, and J.A. Potkay, "A small-scale, rolled-membrane microfluidic artificial lung designed towards future large area manufacturing" *Biomicrofluidics,* 2017, 11,

39. Murray, C.D., "The physiological prnciple of minimum work I. The vascular system and the cost of blood volume" *Proceedings of the national academy of sciences of the united states of america,* 1926, 12, 207-214.

40. Bronchi, B.T.a.L., National Cancer Institute, (2011), Available at and R.O. http://training.seer.cancer.gov/anatomy/respiratory/passages/bronchi.html.

41. Brain JD, E.O.a.C.D., The Merck Manuals Online, A. Medical Library, Available at:, and R.O. http://www.merck.com/mmhe/sec04/ch038/ch038d.html,

42. M. Vert, Y. Doi, K-H. Hellwich, M. Hess, P. Hodge, P. Kubisa, M. Rinaudo, and F. Schue, "Terminology for biorelated polymers and applications (IUPAC Recommendations 2012)" *Pure Appl. Chem.,* 2012, 84, 377-410.

43. Bhattacharya, S., A. Datta, J.M. Berg, and S. Gangopadhyay, "Studies on surface wettability of poly(dimethyl) siloxane (PDMS) and glass under oxygen-plasma treatment and correlation with bond strength" *Journal of Microelectromechanical Systems,* 2005, 14, 590-597.

44. C. J. Wilson, R.E.C., D. I. Leavesley, M. J. Pearcy, "Mediation of Biomaterial-Cell interactions by adsorbed proteins: a review" *Tissue Engineering,* 2005, 11, 1-18.

45. J. D. Andrade, V.H., A-P. Wei, C-H. Ho, A. S. Lea, S. I. Jeon, Y. S. Lin, E. Stroup, "Proteins at Interfaces: Principles, Multivariate Aspects, protein resistant surfaces, and direct imaging and manipulation of adsorbed proteins" *Clinical Materials,* 1992, 11, 67-84.

46. L. Yeong-Shang, V.H., J. Janatova, "Adsorption of complement proteins on surfaces with a hydrophobicity gradient" *Biomaterials,* 1992, 13, 497-504.

47. R. S. Kane, P.D., G. M. Whitesides, "Kosmotropes from the basis of protein-resistant surfaces" *Langmuir,* 2003, 19, 2388-2391.

48. Poot, A.A., "Cell-Biomaterial Interactions" 2014,

49. W. I. Wu, K.N.S., J. L. Brash, P. R. Selvaganapathy, "Polyurethane-based microfluidic devices for blood contacting applications" *Lab on a Chip,* 2012, 12, 960-970.

50. Kim, Y.H., D.K. Han, K.D. Park, and S.H. Kim, "Enhanced blood compatibility of polymers grafted by sulfonated PEO via a negative cilia concept" *Biomaterials,* 2003, 24, 2213-2223.

51. Alibeik, S., *Surface modification with polyethylene glycol-protein conjugates for improved blood compatibility*, in *School of Graduate Studies*, 2011, McMaster University, Canada.

52. www.healthhype.com, r.S.

53. www.labce.com, O.l.c.e.f.c.l.a.m.t., retrieved September 2017.

54. Ahn, J., W.-J. Chung, I. Pinnau, J. Song, N. Du, G.P. Robertson, and M.D. Guiver, "Gas transport behavior of mixed-matrix membranes composed of silica nanoparticles in a polymer of intrinsic microporosity (PIM-1)" *Journal of Membrane Science,* 2010, 346, 280-287.

55. http://www.faybutler.com/pdf_files/HowHoseMaterialsAffectGas3.pdf, r.J.

56. G. Shamini and K. Yusoh, "Gas permeability properties of thermoplastic polyurethane modified clay nanocomposites" *International Journal of Chemical Engineering and Applications,* 2014, 5,

57. J. El-Ali, P.K.S., K. F. Jensen, "Cells on chips" *Nature,* 2006, 442, 403-411.

58. Esch, E.W., A. Bahinski, and D. Huh, "Organs-on-chips at the frontiers of drug discovery" *Nat Rev Drug Discov,* 2015, 14, 248-260.

59. D. Huh, B.D.M., A. Mammoto, M. Montoya-Zavala, H. Y. Hsin, D. E. Ingber, "Reconstituting Organ-Level Lung Functions on a Chip" *Science,* 2010, 328, 1662-1667.

60. D. Huh, G.A.H., D. E. Ingber, "From 3D cell culture to organs-on-chips" *Trends in Cell Biology,* 2011, 21, 745-752.

61. A. O. Stucki, S.R.R.H., M. Felder, Y. Mermoud, R. A. Schmid, T. Geiser, O. T. Guenat, "A lung-on-a-chip array with an integrated bio-inspired respiration mechanism" *Lab on a Chip,* 2015, 15, 1302-1310.

62. Lagorsse, S., F.D. Magalhães, and A. Mendes, "Xenon recycling in an anaesthetic closed-system using carbon molecular sieve membranes" *Journal of Membrane Science,* 2007, 301, 29-38.

63. Lee, L. *Anaesthesia Equipment: Breathing Circuits & Scavenging System. https://instruction.cvhs.okstate.edu/vmed5412/Lecture09.htm,*

64. S. Bhattacharya, A. Nayak, M. Schiavone, and S.K. Bhattacharya, "Solubilization and concentration of carbon dioxide: novel spray reactors with immobilized carbonic anhydrase" *Biotechnology and Bioengineering,* 2004, 86, 37-46.

65. S. D. Faulkner, N. A. Downie, Ch. J. Mercer, S. A. Kerr, R. D. Sanders, and N.J. Robertson, "A xenon recilculating ventilator for the newborn piglet: developing clinical applications of xenon for neonates" *European Journal of Anaesthesiology,* 2012, 29, 577-585.

66. Frink Jr, E.J., W.B. Green Jr, E.A. Brown, M. Malcomson, L.C. Hammond, F.G. Valencia, and B.R. Brown Jr, "Compound A concentrations during sevoflurane anesthesia in children" *Anesthesiology,* 1996, 84, 566-571.

67. Hecker, K., J.H. Baumert, N. Horn, and R. Rossaint, "Xenon, a modern anaesthesia gas" *Minerva Anestesiologica,* 2004, 70, 255-260.

68. Cullen, S.C. and E.G. Gross, "The anesthetic properties of xenon in animals and human beings, with additional observations on krypton" *Science,* 1951, 113, 580-582.

69. Singh, S., "Xenon: A modern anaesthetic" *Healthcare Management,* 2005,

70. Esencan, E., S. Yuksel, Y.B. Tosun, A. Robinot, I. Solaroglu, and J.H. Zhang, "XENON in medical area: emphasis on neuroprotection in hypoxia and anesthesia" *Medical Gas Research,* 2013, 3, 4-4.

71. Goto, T., "Is there a future for xenon anesthesia" *Canadian Journal of Anesthesia,* 2002, 49, 335-338.

72. Ansaloni, L., R. Rennemo, H.K. Knuutila, and L. Deng, "Development of membrane contactors using volatile amine-based absorbents for CO2 capture: Amine permeation through the membrane" *Journal of Membrane Science,* 2017, 537, 272-282.

73. Russo, M.E., G. Olivieri, A. Marzocchella, P. Salatino, P. Caramuscio, and C. Cavaleiro, "Post-combustion carbon capture mediated by carbonic anhydrase" *Separation and Purification Technology,* 2013, 107, 331-339.

74. Ramdin, M., T.W. de Loos, and T.J.H. Vlugt, "State-of-the-Art of CO2 Capture with Ionic Liquids" *Industrial & Engineering Chemistry Research,* 2012, 51, 8149-8177.

75. Torralba-Calleja, E., J. Skinner, and D. Gutiérrez-Tauste, "CO2 capture in ionic liquids: A review of solubilities and experimental methods" *Journal of Chemistry,* 2013,

76. *Ullmann's Energy: Resources, Processes, Products-Volume 1,* ed. B. Elvers. 2015: Wiley-VCH.

77. Liu, X., Z. Li, Y. Pei, H. Wang, and J. Wang, "(Liquid+liquid) equilibria for (cholinium-based ionic liquids+polymers) aqueous two-phase systems" *The Journal of Chemical Thermodynamics,* 2013, 60, 1-8.

78. Yong, J.K.J., G.W. Stevens, F. Caruso, and S.E. Kentish, "The use of carbonic anhydrase to accelerate carbon dioxide capture processes" *Journal of Chemical Technology and Biotechnology,* 2015, 90, 3-10.

79. Muldoon, M.J., S.N.V.K. Aki, J.L. Anderson, J.K. Dixon, and J.F. Brennecke, "Improving carbon dioxide solubility in ionic liquids" *Journal of Physical Chemistry B,* 2007, 111, 9001-9009.

80. J. Huang and T. Ruther, "Why are ionic liquids attractive for CO2 absorption? - an overview" *Australian Journal of Chemistry,* 2009, 62, 298-308.

81. Kazarian, S.G., B.J. Briscoe, and T. Welton, "Combining ionic liquids and supercritical fluids: In situ ATR-IR study of CO2 dissolved in two ionic liquids at high pressures" *Chemical Communications,* 2000, 2047-2048.

82. D. T. Arazawa, J.D.K., W. J. Federspiel, "Kinetics of CO2 exchange with carbonic anhydrase immobilized on fiber membranes in artificial lungs" *Journal of Material Science: Mater Med,* 2015, 26, 193.

References

83. Gathergood, N., M.T. Garcia, and P.J. Scammells, "Biodegradable ionic liquids: Part I. Concept, preliminary targets and evaluation" *Green Chemistry,* 2004, 6, 166-175.

84. Garcia, M.T., N. Gathergood, and P.J. Scammells, "Biodegradable ionic liquids Part II. Effect of the anion and toxicology" *Green Chemistry,* 2005, 7, 9-14.

85. Docherty, K.M., J.K. Dixon, and C.F. Kulpa Jr, "Biodegradability of imidazolium and pyridinium ionic liquids by an activated sludge microbial community" *Biodegradation,* 2007, 18, 481-493.

86. Yu, Y., X. Lu, Q. Zhou, K. Dong, H. Yao, and S. Zhang, "Biodegradable naphthenic acid ionic liquids: Synthesis, characterization, and quantitative structure-biodegradation relationship" *Chemistry - A European Journal,* 2008, 14, 11174-11182.

87. Martins, C.F., L.A. Neves, M. Estevão, A. Rosatella, V.D. Alves, C.A.M. Afonso, J.G. Crespo, and I.M. Coelhoso, "Effect of water activity on carbon dioxide transport in cholinium-based ionic liquids with carbonic anhydrase" *Separation and Purification Technology,* 2016, 168, 74-82.

88. Blusztajn, J.K., "Choline, a vital amine" *Science,* 1998, 281, 794-795.

89. Petkovic, M., J.L. Ferguson, H.Q.N. Gunaratne, R. Ferreira, M.C. Leitão, K.R. Seddon, L.P.N. Rebelo, and C.S. Pereira, "Novel biocompatible cholinium-based ionic liquids - Toxicity and biodegradability" *Green Chemistry,* 2010, 12, 643-649.

90. e Silva, F.A., F. Siopa, B.F.H.T. Figueiredo, A.M.M. Gonçalves, J.L. Pereira, F. Gonçalves, J.A.P. Coutinho, C.A.M. Afonso, and S.P.M. Ventura, "Sustainable design for environment-friendly mono and dicationic cholinium-based ionic liquids" *Ecotoxicology and Environmental Safety,* 2014, 108, 302-310.

91. Wu, C., T.P. Senftle, and W.F. Schneider, "First-principles-guided design of ionic liquids for CO2 capture" *Physical Chemistry Chemical Physics,* 2012, 14, 13163-13170.

92. Jia, X., Y. Yang, C. Wang, C. Zhao, R. Vijayaraghavan, D.R. Macfarlane, M. Forsyth, and G.G. Wallace, "Biocompatible ionic liquid-biopolymer electrolyte-enabled thin and compact magnesium-Air batteries" *ACS Applied Materials and Interfaces,* 2014, 6, 21110-21117.

93. B. C. Tripp, K. Smith, and J.G. Ferry, "Carbonic Anhydrase: En insights for an ancient enzyme" *Journal of Biological Chemistry,* 2001, 276, 48615-48618.

94. da Costa Ores, J., L. Sala, G.P. Cerveira, and S.J. Kalil, "Purification of carbonic anhydrase from bovine erythrocytes and its application in the enzymic capture of carbon dioxide" *Chemosphere,* 2012, 88, 255-259.

95. Shekh, A.Y., K. Krishnamurthi, S.N. Mudliar, R.R. Yadav, A.B. Fulke, S.S. Devi, and T. Chakrabarti, "Recent Advancements in Carbonic Anhydrase–Driven Processes for CO2 Sequestration: Minireview" *Critical Reviews in Environmental Science and Technology,* 2012, 42, 1419-1440.

96. 3dciencia.com, S.i., animation&multimedia, Retrieved July 2017.

97. Neves, L.A., C. Afonso, I.M. Coelhoso, and J.G. Crespo, "Integrated CO 2 capture and enzymatic bioconversion in supported ionic liquid membranes" *Separation and Purification Technology,* 2012, 97, 34-41.

98. Mendes, A., "Development of an adsorption/membrane based system for carbon dioxide, nitrogen and spur gases removal from a nitrous oxide and xenon anaesthetic closed loop" *Applied Cardiopulmonary Pathopysiol,* 2000, 9, 156-163.

99. Yong, J.K.J., G.W. Stevens, F. Caruso, and S.E. Kentish, "In situ layer-by-layer assembled carbonic anhydrase-coated hollow fiber membrane contactor for rapid CO2 absorption" *Journal of Membrane Science,* 2016, 514, 556-565.

100. Hoganson, D.M., J.L. Anderson, E.F. Weinberg, E.J. Swart, B.K. Orrick, J.T. Borenstein, and J.P. Vacanti, "Branched vascular network architecture: A new approach to lung assist device technology" *Journal of Thoracic and Cardiovascular Surgery,* 2010, 140, 990-995.

101. Sreenivasan, R., E.K. Bassett, D.M. Hoganson, J.P. Vacanti, and K.K. Gleason, "Ultra-thin, gas permeable free-standing and composite membranes for microfluidic lung assist devices" *Biomaterials,* 2011, 32, 3883-3889.

102. Rochow, N., W.I. Wu, E. Chan, D. Nagpal, G. Fusch, P.R. Selvaganapathy, S. Monkman, and C. Fusch, "Integrated microfluidic oxygenatr bundless for blood gas exchange in premature infants" *Micro Electro Mechanical systems (MEMS),* 2012, 2012 IEEE 25th International Conference on January 29 to February 2, 957-960.

103. Kniazeva, T., J.C. Hsiao, J.L. Charest, and J.T. Borenstein, "A microfluidic respiratory assist device with high gas permeance for artificial lung applications" *Biomedical Microdevices,* 2011, 13, 315-323.

104. Kniazeva, T., A.E. Epshteyn, J.C. Hsiao, E.S. Kim, V.B. Kolachalama, J.L. Charest, and J.T. Borenstein, "Performance and scalling effects in a multilayer microfluidic extracorporeal lung oxygenation device" *Lab on a Chip,* 2012, 12, 1686-1695.

105. J. M. Berg, J. L. Tymoczko, and L. Stryer, *Biochemistry. Chapter 7: Hemoglobin: Portrait of a Protein in Action*.

106. D. Saddawi-Konefka and B. Bryner. *Dissolved oxygen in the blood,* http://www.umich.edu/~projbnb/cvr/o2.html,

107. McCarthy, M.R., K.D. Vandegriff, and R.M. Winslow, "The role of facilitated diffusion in oxygen transport by cell-free hemoglobins: Implications for the design of hemoglobin-based oxygen carriers" *Biophysical Chemistry,* 2001, 92, 103-117.

108. Kutchai, H., J.A. Jacquez, and F.J. Mather, "Nonequilibrium facilitated oxygen transport in hemoglobin solution" *Biophysical Journal,* 1970, 10, 38-54.

109. Zijlstra, W.G. and A. Buursma, "Spectrophotometry of hemoglobin: Absorption spectra of bovine oxyhemoglobin, deoxyhemoglobin, carboxyhemoglobin, and methemoglobin" *Comparative Biochemistry and Physiology - B Biochemistry and Molecular Biology,* 1997, 118, 743-749.

110. Potkay, J.A., "A simple, closed-form, mathematical model for gas exchange in microchannel artificial lungs" *Biomedical Microdevices,* 2013, 15, 397-406.

111. Rettich, T.R., R. Battino, and E. Wilhelm, "Solubility of gases in liquids. 22. High-precision determination of Henry's law constants of oxygen in liquid water from T = 274 K to t d 328 Ka" *Journal of Chemical Thermodynamics,* 2000, 32, 1145-1156.

112. Perry, R.H., *Perry's chemical engineers handbook. Chapter3 Physical and chemical data*, ed. M.-H.i. editions.

113. Pittman, R.N., *Regulation of Tissue Oxygenation. Chapter 4, Oxygen Transport*, ed. M.C.L. Sciences. 2011.

114. J. Zhang, T. D. C. Nolan, T. Zhang, B. P. Griffith, and Z. J. Wu, "Characterization of membrane blood oxygenation devices using computational fluid dynamics" *Journal of Membrane Science,* 2007, 288, 268-279.

115. S. McKee, E. A. Dougall, and N. J. Mottram, "Analytic solutions of a simple advection-diffusion model of an oxygen transfer device" *Journal of Mathematics in Industry,* 2016, 6, 1-22.

116. McDonald, J.C. and G.M. Whitesides, "Poly(dimethylsiloxane) as a material for fabricating microfluidic devices" *Accounts of Chemical Research,* 2002, 35, 491-499.

117. Duffy, D.C., J.C. McDonald, O.J.A. Schueller, and G.M. Whitesides, "Rapid prototyping of microfluidic systems in poly(dimethylsiloxane)" *Analytical Chemistry,* 1998, 70, 4974-4984.

118. Rea, I., E. Orabona, A. Lamberti, I. Rendina, and L. De Stefano, "A microfluidics assisted porous silicon array for optical label-free biochemical sensing" *Biomicrofluidics,* 2011, 5, 034120-034120-10.

119. Wu, M.-H., "Simple poly(dimethylsiloxane) surface modification to control cell adhesion" *Surface and Interface Analysis,* 2009, 41, 11-16.

120. Wu, Z. and K. Hjort, "Surface modification of PDMS by gradient-induced migration of embedded Pluronic" *Lab on a Chip - Miniaturisation for Chemistry and Biology,* 2009, 9, 1500-1503.

121. Greenspan, L., "HUMIDITY FIXED POINTS OF BINARY SATURATED AQUEOUS SOLUTIONS" *J Res Natl Bur Stand Sect A Phys Chem,* 1977, 81 A, 89-96.

References

122. Cussler, E.L., "Diffusion. Mass Transfer in Fluid Systems, third edition" *Press Syndicate of The University of Cambridge, Cambridge,* 2009,

123. Gabelman, A. and S.T. Hwang, "Hollow fiber membrane contactors" *Journal of Membrane Science,* 1999, 159, 61-106.

124. *Encyclopedia of Desalination and Water Resources,* http://www.desware.net/Sample-Chapters/D05/, *Retrieved May 2017,*

125. Lamberti, A., S.L. Marasso, and M. Cocuzza, "PDMS membranes with tunable gas permeability for microfluidic applications" *RSC Advances,* 2014, 4, 61415-61419.

126. Singh, A., B.D. Freeman, and I. Pinnau, "Pure and mixed gas acetone/nitrogen permeation properties of polydimethylsiloxane [PDMS]" *Journal of Polymer Science, Part B: Polymer Physics,* 1998, 36, 289-301.

127. Khanafer, K., A. Duprey, M. Schlicht, and R. Berguer, "Effects of strain rate, mixing ratio, and stress–strain definition on the mechanical behavior of the polydimethylsiloxane (PDMS) material as related to its biological applications" *Biomedical Microdevices,* 2008, 11, 503.

128. Liu, M., J. Sun, and Q. Chen, "Influences of heating temperature on mechanical properties of polydimethylsiloxane" *Sensors and Actuators, A: Physical,* 2009, 151, 42-45.

129. Poling, B.E., J.M. Prausnitz, and J.P. O'Connell, "The properties of gases and liquids, fifth edition" 2004,

130. De Jong, J., R.G.H. Lammertink, and M. Wessling, "Membranes and microfluidics: A review" *Lab on a Chip,* 2006, 6, 1125-1139.

131. Chen, X. and J. Shen, "Review of membranes in microfluidics" *Journal of Chemical Technology and Biotechnology,* 2017, 92, 271-282.

132. Ren, X., H. Lu, J.G. Zhou, P.L.G. Chong, W. Yuan, and M. Noh, "Porous Polydimethylsiloxane as a Gas-Liquid Interface for Microfluidic Applications" *Journal of Microelectromechanical Systems,* 2017, 26, 120-126.

133. Houston, K.S., D.H. Weinkauf, and F.F. Stewart, "Gas transport characteristics of plasma treated poly(dimethylsiloxane) and polyphosphazene membrane materials" *Journal of Membrane Science,* 2002, 205, 103-112.

134. E. J. W. Berenschot, H.V.J., N. R. Tas, "Fabrication of 3D fractal structures using nanoscale anisotropic etching of single crystalline silicon" *Journal of Micromechanics and Microengineering,* 2013, 23, 1-10.

135. Burouni, N., E. Berenschot, M. Elwenspoek, E. Sarajlic, P. Leussink, H. Jansen, and N. Tas, "Wafer-scale fabrication of nanoapertures using corner lithography" *Nanotechnology,* 2013, 24,

136. R. P. Iczkowski, J.L.M., S. M. Robinson, "Effusion of gases through conical orifices" 1963, 229-233.

137. S. Unnikrishnan, H.V.J., F. H. Falke, N. R. Tas, H. A. G. M. Van Wolferen, M. J. De Boer, R. G. P. Sanders, M. C. Elwenspoek, "Transition flow through an ultra-thin nanosieve" *Nanotechnology,* 2009, 20, 1-6.

138. K. Keizer, R.J.R.U., R. J. van Vuren, A. J. Burggraaf, "Gas separation mechanisms in microporous modified γ-Al_2O_3 membranes" *Journal of Membrane Science,* 1988, 39, 285-300.

139. Gómez-Goñi, J. and P.J. Lobo, "Comparison between Monte Carlo and analytical calculation of the conductance of cylindrical and conical tubes" *Journal of Vacuum Science and Technology A: Vacuum, Surfaces and Films,* 2003, 21, 1452-1457.

140. Zhang, X., E.S.M. Lai, R. Martin-Aranda, and K.L. Yeung, "An investigation of Knoevenagel condensation reaction in microreactors using a new zeolite catalyst" *Applied Catalysis A: General,* 2004, 261, 109-118.

141. Berenschot, J.W., R.M. Tiggelaar, J. Geerlings, J.G.E. Gardeniers, N.R. Tas, M. Malankowska, M.P. Pina, and R. Mallada. *3D-fractal engineering based on oxide-only corner lithography*. in *Symposium on Design, Test, Integration and Packaging of MEMS/MOEMS, DTIP 2016*. 2016.

175